The University of Nottingham

UNITED KINGDOM · CHINA · MALAYSIA

Discrete Element Modelling of constant strain rate and creep tests on a graded asphalt mixture

By

Wei Cai

Thesis submitted to the University of Nottingham for

the degree of Doctor of Philosophy

May 2013

TO MY FAMILY

ABSTRACT

This thesis investigates the use of Discrete Element Modelling (DEM) to simulate the elastic and viscoelastic deformation behaviour of an asphalt mixture. A numerical specimen preparation procedure has been developed to produce specimens with an isotropic stress and correct volumetrics. Stone mastic asphalt has been chosen in this project because of its high content of coarse aggregate and binder-rich mortar. A range of uniaxial compression tests have been undertaken in the laboratory under various loading speeds and stresses. The axial stress, axial strain and radial strain were recorded during the tests. The peak stress is found to be as a power-law function of the strain rates for the asphaltic material.

Elastic contact properties have been used to investigate the effect of particle number and location, loading speed, normal and shear contact stiffness. The Poisson's ratio was found to increase with the ratio of normal to shear contact stiffness but was independent of the stiffnesses. The Young's modulus was found to be dependent on both normal and shear stiffnesses, in agreement with previous work on idealised asphalt mixtures.

The Burger's model was introduced to give time-dependent stiffness for the viscoelastic modelling. The Burger's model was implemented to give moment and torsional resistance as well as in direct tension and compression. To reduce the computational time in the creep simulations, the effect of scaling both viscosities in the Burger's model to simulate a shorter time, have been investigated. The effects of each parameter on the deformation of asphalt mixture were also investigated.

ABSTRACT

The stress-strain response for the laboratory tests and the simulations were recorded. The results show good agreement when the bond strengths in the model are made to be a function of strain rate for both constant strain rate and creep conditions. Both normal and Weibull distributions have been used for the bond strengths between the aggregate particles. The constant strain rate tests results were proved to be independent of the bond strength variability and position of particles, while the creep tests results were dependent on the bond strength variability and position of particles. This is in good agreement with experimental tests: different specimens at the same stress level gave variability in the creep behaviour, at higher stress levels.

Bond breakages were recorded during the simulations to investigate the micro-mechanical deformation behaviour of asphalt mixtures. It was found that a well-defined rupture at higher stress levels coincided with the maximum rate of bond breakage. The modified Burger's model has therefore proven to be a useful tool in modelling the moment and torsional resistance at particle contacts in an asphalt mixtures, in order to correctly predict observed behaviour.

ACKNOWLEDGEMENTS

TABLE OF CONTENTS

TABLE OF CONTENTS

TABLE OF CONTENTS

LIST OF TABLES

LIST OF FIGURES

LIST OF FIGURES

LIST OF FIGURES

LIST OF FIGURES

LIST OF FIGURES

LIST OF FIGURES

LIST OF FIGURES

1 Introduction

1.1 Problem definition

An effective transport system is essential for the economic and social development of any nation. Roads are the most popular form of transportation system. Asphaltic materials became popular as the road material at the end of the 19th Century eg. (Read et al., 2003). Asphalt is a complex multi-part material that comprises three parts: bitumen, aggregate and air. A range of asphalt mixtures can be produced by varying the proportions of these components and the grading of aggregate. These components have different physical and mechanical properties and behaviours that have a significant effect on the performance of asphalt mixtures. It is important to understand the link between the mix-composition and the overall properties or performance, since micromechanical behaviour is an important factor in terms of overall material performance.

The most common forms of structural failure of asphalt roads are permanent deformation (i.e. rutting) and fatigue cracking. Experimental methods are used to explain the damage mechanisms of asphalt mixtures from a macroscopic perspective. However they are usually very costly and the micromechanics among the three components are not known. Moreover, experimental methods are limited by safety requirements. Probably the most successful approach has been to conduct a limited number of laboratory or field tests to provided actual track performance data to validate computer simulation programs. These

computer simulation programs are then used to extrapolate the experimental results over the range of test conditions where experimentation would be too dangerous or too expensive (Todd et al., 1989). Uniaxial tests are among the simplest tests used to determine the representative parameters for modelling and to supply results to compare with the modelling results.

The traditional approach to modelling asphalt mixtures is to treat them at the macro scale using continuum-based models. This usually involves undertaking careful experiments over a range of conditions (e.g. stress levels, loading rates, and temperature), measuring the macroscopic response of the material and fitting continuum-based constitutive models to the measured behaviour. The continuum approach implemented into a Finite Element Program can incorporate nonlinear constitutive equations. However, in the continuum approach the micromechanical behaviour of the mixture is typically not included which means it is not easy to relate observed behaviour to the micromechanics of the material (Lee, 2006).

The three-dimensional micromechanics based discrete element model can be used to simulate the mechanical behaviour of asphalt mixtures from a micromechanical perspective. Particle Flow Code in Three Dimensions (PFC3D) is used to model materials that consist of individual particles and the particles are allowed to roll or slide relative to other particles. PFC3D has been used in this project to give a more fundamental understanding of the constitutive behaviour of asphalt mixtures.

As a first step towards modelling the micromechanical behaviour of asphalt mixtures, Lee (2006) and Wu (2009) used the PFC3D to model idealised

asphalt mixtures. The idealised asphalt mixture comprised approximately single-sized sand mixed with bitumen. They have successfully modelled the time-dependent behaviour of the idealised sand asphalt mixture under uniaxial and triaxial compression tests. The dilation behaviour was also modelled, and a computation time optimisation has been introduced to speed up the constant strain rate simulations.

Following on from the work of Lee and Wu, the next step is the development of the Discrete Element Method for modelling the constitutive behaviour of the asphalt mixtures with graded aggregate under different uniaxial compression loading conditions. The scope of this research involves both undertaking compression tests and developing the discrete element model to model the constitutive behaviour of asphalt mixtures. The responses of the uniaxial compression tests on asphalt mixtures under various test conditions have been carefully measured and used to validate the discrete element modelling. The overall aims of this research are to:

- Develop a validated means of using Discrete Element Method for simulating graded asphalt mixtures;
- Improve the understanding of the micromechanical deformation behaviour of asphaltic mixtures.

In order to achieve these aims the following objectives are required:

- Development of a numerical speimen preparation procedure for producing representative graded asphalt mixtures;
- Laboratory testing of a similar asphalt mixture with computer simulation at various loading conditions;

- Investigation of the stress-strain response of the asphalt mixture;

- Production of user-defined time-dependent contact models in the simulation to give a better prediction;

- Numerical simulation of the uniaxial compression test for the asphalt mixtures;

- Calibration of the predictions using existing experimental data to determine Discrete Element Method contact properties;

- Production of guidelines related to the parameter determination procedures and testing required to characterise an asphalt mixture for Discrete Element Method simulations for different loading conditions;

- Investigation and simulation of the strain rate dependence of the asphalt mixture and comparison with laboratory results;

- Simulation of the creep tests under different stress levels and comparison with laboratory results.

1.2 **Thesis structure**

This thesis is organised as follows:

Chapter 1: an introduction to the project (the current chapter), and the aims and objectives of this research.

Chapter 2: a review of the literature concerning the type of asphalt mixtures that are used in road construction. The mechanical properties of asphalt mixtures including the permanent deformation and fatigue cracking are also described. This is followed by a brief review of the constitutive relationships for monotonic behaviour of bitumen and asphalt mixtures. Several constitutive

models based on continuum mechanics are also introduced in this chapter. Then, a brief introduction of the uniaxial constant strain rate and creep tests is presented followed by a review of micromechanical model for asphalt.

Chapter 3 begins with a review of the Discrete Element Method and the development and application of the Discrete Element Method in granular materials and asphalt mixtures. This is then followed by the introduction of the software package Particle Flow Code in Three Dimensions (PFC3D). This chapter also reviews the theory and background of the modelling using PFC3D. Finally, there is a review of the user-defined model in PFC3D which is very important in this project.

Chapter 4 introduces the procedure to generate a numerical specimen in PFC3D. The numerical specimen is required to replicate the volumetric characteristics of the asphalt mixtures. A measurement method is established to quantify the stress and strain quantities of the numerical specimen during simulations. A modified servo control method is also introduced for the constant stress creep tests.

Chapter 5 contains information about the tests of uniaxial creep and constant strain rate on asphalt mixtures over a wide range of stresses and strain rates. An asphalt mixture with the same component contents and similar grading of particles based on the numerical specimen was produced. The selection and preparation of this asphalt mixture are also presented in this chapter followed by a brief introduction of the test equipment and instruments. A series of uniaxial compression tests were performed and the stress-stain responses are presented.

Chapter 1 Introduction

Chapter 6 presents the elastic response of asphalt mixture modelling by using an elastic contact model in the Discrete Element Method. The parallel bond has been successfully used to simulate the mechanics of bitumen. The effect of number and position of particles, loading speed, normal to shear contact stiffness, the parallel bond radius are examined.

Chapter 7 presents the simulation of the viscoelastic behaviour of asphalt mixtures. The modified Burger's model is used to simulate the time-dependent behaviour with moment and torsional resistance. The effect of the Burger's model parameters, the ratios of normal to shear contact stiffness, the inter-particle friction coefficient and the bond strength distribution (uniform, normal and Weibull) in the viscoelastic simulations under constant strain rate loading conditions are investigated. The bond breakages are recorded during the simulations to explain the internal damage within the specimen. The modified Burger's model has been used for simulating uniaxial constant strain rate and creep tests in the laboratory and proved to be a useful tool in modelling the moment and torsional resistance at particle contacts in an asphalt mixture.

Chapter 8 presents the analysis of the results, summaries and conclusions from this research and presents recommendations for future research.

2 Literature review

2.1 Introduction

Asphalt mixtures have complex microstructural and mechanical properties. A typical asphalt mixture comprises aggregate, bitumen and air. Aggregates have a wide range of sizes, irregular shapes, and various values of roughness, frictional properties and other characteristics. Bitumen has time and temperature dependency. Therefore, the constitutive behaviour of different asphalt mixtures are drastically different in nature (Liu, 2011). The load carrying mechanism within this material is dependent on the load transfer within the aggregate skeleton, while bitumen serves as an adherent that enables the mix to withstand tensile and shear stresses.

Experimental testing procedures are well developed for asphalt mixtures. The Superpave (SUperior PERforming Asphalt PAVEment) system was developed as a tool to design asphalt pavement for better perform under extremes of temperatures and heavy traffic loads. The effects of temperature and loading frequency have been extensively studied and methodologies have been developed for shifting the properties obtained under different conditions in the laboratory to produce functions of dynamic shear modulus or phase angle versus loading frequency at reference temperature. This is known as the time-temperature superposition principle, e. g. (Abbas, 2004).

A range of laboratory test simulations can be used to reduce the amount of expensive and time consuming experimental tests required for mechanistic

empirical design and analysis programs. The two main numerical simulation techniques are the finite element method (continuum approach) and the discrete element method (discrete approach). Simulations using the finite element method have been successful in capturing the stress-strain distribution within the asphalt mixtures and its effect on the stiffness anisotropy. However, the interaction between aggregate particles, which has been identified as one of the most important mechanisms resulting in permanent deformation, is not explicity taken into account. Such limitation can be surmounted by the discrete element method.

Image analysis techniques are used to capture the internal structure of asphalt mixtures to offer a realistic numerical representation. Particle simulations are often regarded as intellectually unsatisfying compared to elegant and simple continuum formulations. However, in solving practical problems, the continuum formulations can become overloaded with ad hoc assumptions and parameters inflation, while particle formulations usually need simple laws and few parameters to govern interactions at the particle level (Cundall, 2001).

This chapter begins by reviewing three main types of asphalt mixtures followed by a review of the mechanical properties of asphalt mixtures. Typical constitutive models for asphalt, the uniaxial compression tests on asphalt and the micromechanical models for asphalt mixtures are also included.

2.2 Asphalt mixtures

Asphalt mixture is a complex multipart material comprising at least three main parts: bitumen, graded mineral aggregate and air. A range of mixture types can

be produced depending on the types and proportions of these components and on the aggregate grading. Bitumen plays an important part in determining the characteristics of road asphalts and is responsible for the viscoelastic behaviour characteristic of asphalts, e.g. (Thom, 2008). Various types of asphalt mixtures are used in pavement construction. A typical continuously graded mixture (e.g. Asphalt Concrete) relies on an interlocking aggregate skeleton for its strength with the binder primarily acting as a lubricant to aid compaction and "glue" the mixture together. At the other extreme, a typical gap-graded mixture (e.g. Hot Rolled Asphalt) has a discontinuous aggregate grading (i.e. some stone sizes will not be present) and relies on a coarse aggregate skeleton bound by a bitumen/filler mortar for its strength (Wu, 2009). For both these mixture types the micromechanical behaviour, at the scale of an aggregate particle (e.g. particle size distribution, angularity), will be an important factor in terms of overall material performance eg. (Thom, 2008). Typical hot-mixed asphaltic mixtures used in the UK pavement industry are Asphalt Concrete (AC), Hot Rolled Asphalt (HRA) and Stone Mastic Asphalt (SMA). Brief explanations for those mixtures will be given in the following sections.

2.2.1 **Asphalt concrete**

Asphalt concrete is continuously graded and is manufactured with relatively low bitumen content. A typical grading and an idealised section through this mixture are shown in Figure 2.1. Its strength is derived from the interlock of coated aggregate. Asphalt concrete is designed by the Marshall method. A specification for asphalt concrete can be found in BS EN 13108-1:2006.
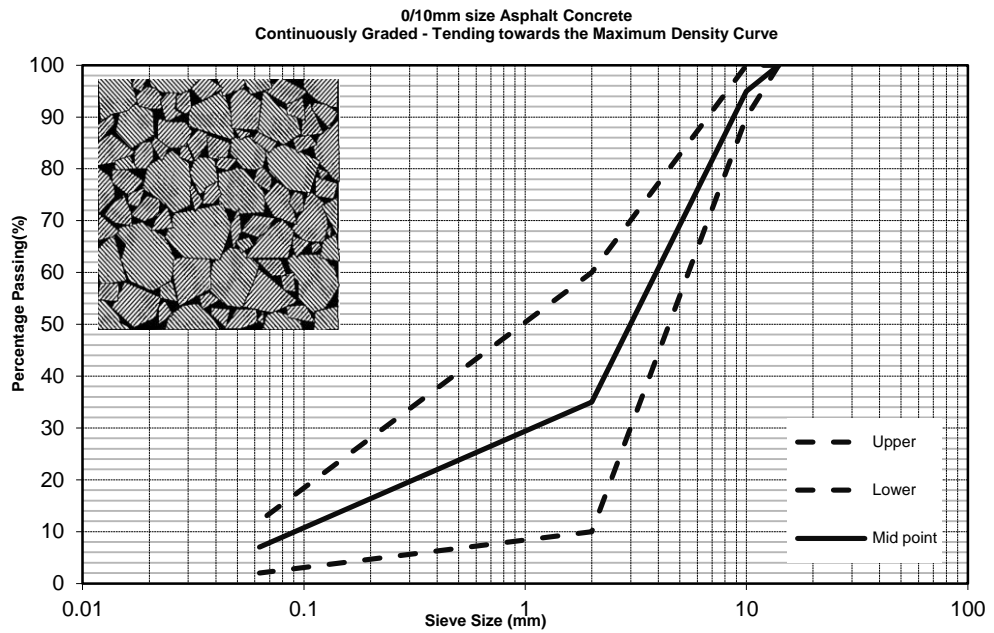
Figure 2.1 0/10mm size asphalt concrete

2.2.2 **Hot rolled asphalt**

Hot Rolled Asphalt (HRA) is a gap-graded mixture with very little medium-sized aggregate and consists of a matrix of sand, filler and bitumen. Therefore the bitumen content is higher than asphalt concrete. Bitumen and fine aggregate are assumed to mix together as a special "asphalt mastic". In hot rolled asphalt there is a lack of direct contact between the coarse aggregate particles, so the load is primarily transmitted by asphalt mastic. HRA is an asphaltic product with very good durability compared to many asphaltic mixtures. Figure 2.2 shows a typical aggregate grading curve, and a cross section of the HRA mixture. A specification for HRA can be found in BS EN 13108-4:2006.
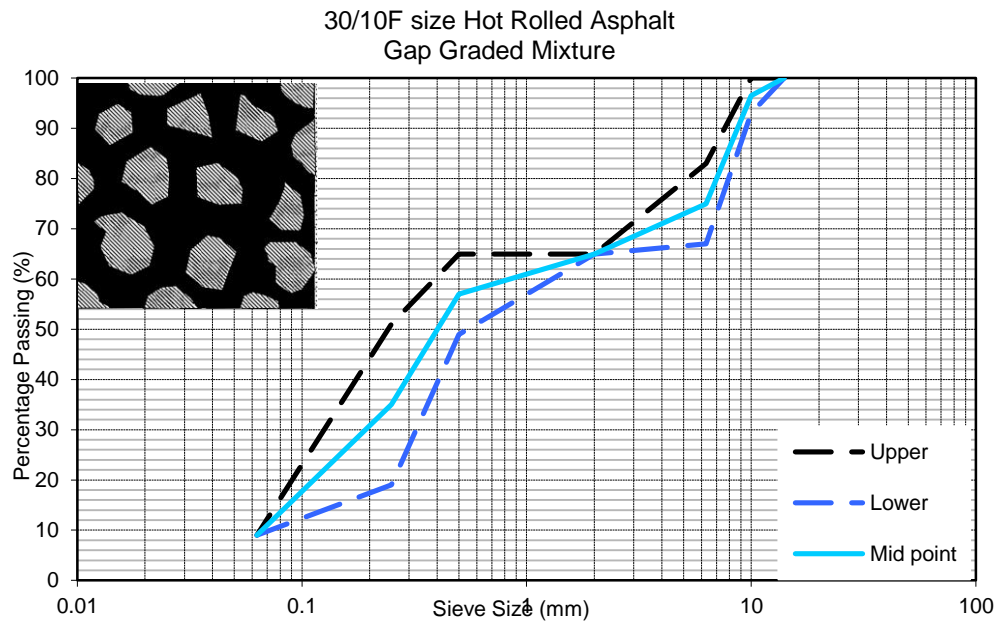
Figure 2.2 30/10F size hot rolled asphalt

2.2.3 **Stone mastic asphalt**

Bellin (1992) reported the use of a new type of hot mix asphalt during 1960's in Germany which later became known as the stone mastic asphalt (SMA) because of its high resistance to rutting. SMA is a dense gap-graded asphaltic mixture with high content of coarse aggregate (>70%) and a binder rich mortar (filler and bitumen). By comparison with other asphalt mixtures, SMA performed better in resistance to deformation and cracking, delivered high durability, harder wearing and travelling resistance, insensitivity to water, good skid resistance, low surface noise and superior surface finish (Taherkhani, 2006). This is mainly due to the gap-graded coarse aggregate skeleton which is able to carry loads without permanent deformation through direct stone to stone contact. The cracking resistance is improved by an increased binder of about 6.5 to 7.5 %, and the good durability is attained by thick binder films minimizing the air void content which makes the mix less susceptible to

oxidative ageing (Partl et al., 1994). Figure 2.3 shows a typical aggregate grading curve, and a cross section of the SMA mixture. A specification for SMA can be found in BS EN 13108-5:2006.

The characteristics of SMA are derived based on the following principles: its stability and rutting resistance which is best derived from coarse aggregate stone to stone contact and proper aggregate packing; its durability which is best attained with proper mixture design in relation to the volumetrics, including air voids, voids in the mineral aggregate, asphalt film thickness and mineral filler proportion, e.g. (Qiu et al., 2006).
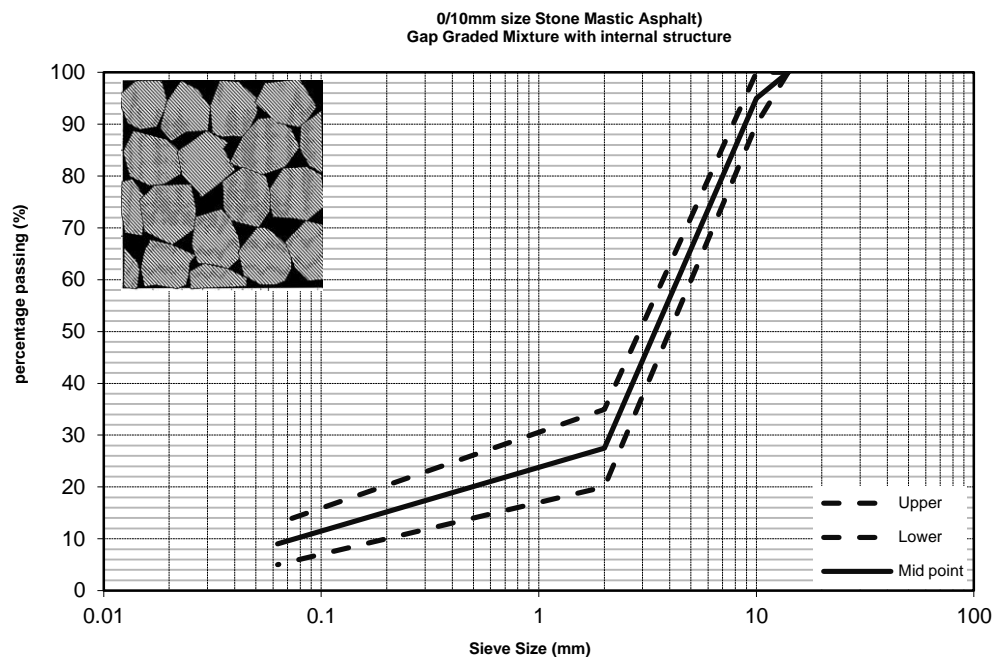
Figure 2.3 0/10mm size stone mastic asphalt

2.3 **Review of mechanical properties of asphalt**

As a viscous liquid, even at the normal service temperatures, bitumen has some particular features: it can "flow" at high temperature, leading to pavement

rutting; it can fracture at low temperature, leading to pavement cracking; and the adhesion between bitumen and aggregate can break down under a combination of aging and water attack (Thom, 2008). The following sections present the stiffness of asphalt and the two main types of load failure in asphalt pavement: cracking (fatigue) and rutting (permanent deformation).

2.3.1 **Stiffness of asphalt**

The stiffness of an asphalt mixture in a pavement is an indication of its ability to spread the load-induced stress to the lower layers. Van der Poel (1954) introduced the Van der Poel nomograph which use "stiffness" to describe the mechanical behaviour of pure bitumen as a function of temperature and loading time. In 1955, (Van der Poel) extended the stiffness concept to experimentally map the dynamic behaviour of various bitumen mixtures by assuming that the stiffness of the mixture is a function of the stiffness of the bitumen and the volume fraction of the aggregate. Later, Heukelom and Klomp (1964) proposed the following relationship for predicting the stiffness of a bitumen mixture:

$$\frac{S_{mix}}{S_{bit}} = \left[1 + \frac{2.5C_v}{p(1-C_v)}\right]^p \tag{2.1}$$

where S_{mix} and S_{bit} are the stiffnesses of the mixture and bitumen, respectively. The quantities C_v (volume concentration of the aggregate) and p are defined by:

$$C_v = \frac{V_{ag}}{V_{mix}} \tag{2.2}$$

$$p = 0.83 \log \left[\frac{4 \times 10^{10}}{S_{bit}(Pa)} \right] \tag{2.3}$$

where V_{ag} is the volume of aggregate; V_{mix} is the Volume of aggregate and bitumen in the mixture and Pa means the unite Pascals. The equations above were derived from empirical fits to test data obtained from static and dynamic tests on well compacted mixtures containing about 3% of air voids and C_v values ranging from 0.7-0.9.

Brown (1992) redefined the above equations to

$$\frac{S_{mix}}{S_{bit}} = \left[1 + \frac{257.5 - 2.5VMA}{p(VMA - 3)} \right]^{P} \tag{2.4}$$

where VMA is the percentage of voids in mixed aggregate and p is the same as in equation (2.3). It should be noted that equation (2.4) is valid for VMA values from 12-30% and $S_{bit} \geq 5$ Mpa At higher values of bitumen stiffness ($S_{bit} \approx 1$ Gpa), bitumen behaves as an elastic solid and the stiffness ratio is a measure of the stiffening effect when rigid aggregate is included in an elastic matrix. However, for lower values of S_{bit} the stiffness ratio becomes a function of the elastic, viscoelastic and viscous response of the material.

Stiffness is simply defined as the ability of a material to resist deflection by an applied load. In the lab, the elastic stiffness is generally evaluated using a uniaxial stress-strain relationship, see equation (2.5). Although the bitumen mixtures behave in a visco-elastic manner, the elastic stiffness has been found to be suitable provided that a number of boundary conditions are applied (British Standards Institution (1993)).

$$E = \frac{\sigma}{\varepsilon} \tag{2.5}$$

where E is the elastic stiffness; σ is the applied stress; and ε is the resultant strain.

The method used to measure the elastic stiffness in this project will be presented in chapter 6.

2.3.2 **Permanent deformation of asphalt**

Permanent deformation of asphalt mixtures is caused by the two major mechanisms: densification and shear deformation. Densification is due to the aggregate skeleton becoming more closely packed and it tends to occur relatively early in the life of pavement caused by the poor compaction during construction (Stroup-Gardiner et al., 1997). Shear deformation is the primary factor lead to rutting. It can result in the development of shoulders on either side of a rut due to the process of lateral material flow (Hofstra et al., 1972). Permanent deformation behaviour can be affected by the following factors: type of aggregate, gradation of aggregate, binder type and content, degree of compaction (air void content), method of compaction, temperature and magnitude and frequency of loading and so on.

It is well known that bitumen is a thermoplastic material. It behaves as an elastic solid at low temperature and/or short loading times, as a viscous fluid at high temperatures and/or long loading times and exhibits both elastic and viscoelastic behaviour and displays a time-dependent relationship between applied stress and resultant strain in the intermediate range. The magnitude of

deformation caused by applied load depends on the material properties, load level, temperature and loading time. The material deforms with an instantaneous elastic response after which the deformation gradually increases with loading time. Upon remove of load, part of the deformation will be recovered but with some permanent deformation remaining in the material. The recovered deformation is a result of the elastic and delayed elastic properties, and the permanent deformation is due to the plastic and viscous properties of the material. Figure 2.4 shows an idealised strain response to an applied stress pulse of an asphalt mixture.

The permanent deformation accumulated under each loading application will lead to the rutting of the pavement. Figure 2.5 shows the accumulation of permanent strain under repeated loading.
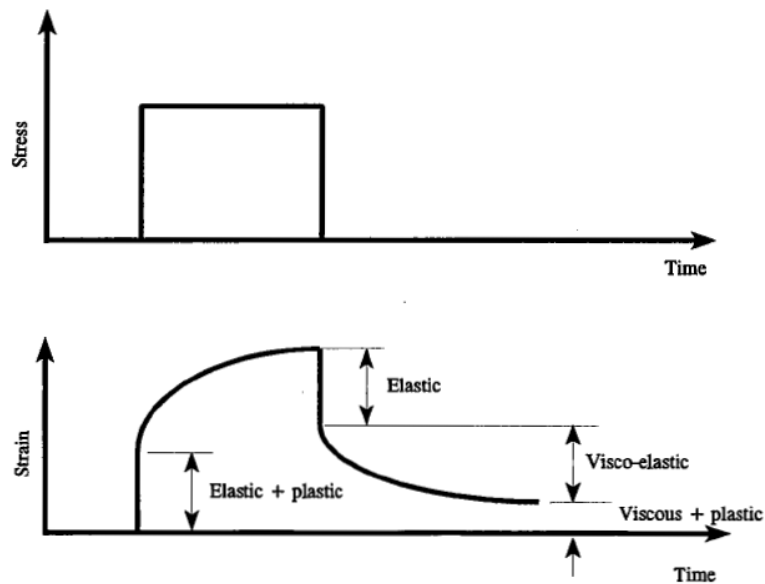
Figure 2.4 Idealised strain response of an asphalt mixture (Gibb, 1996)

25
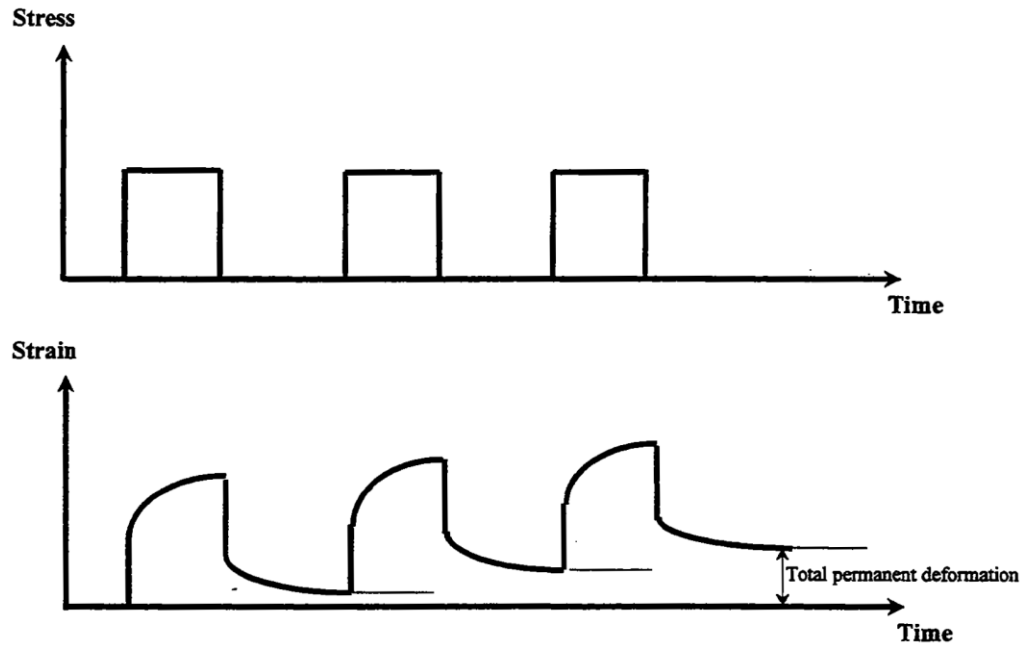
Figure 2.5 Accumulation of permanent deformation of asphalt mixture under repeated load (Khanzada, 2000)

2.3.3 **Fatigue characteristics of asphalt**

The fatigue characteristics of asphalt are defined as fatigue cracking which is caused by tensile strains generated in the pavement not only by traffic loading but also by temperature variations and construction practices. Fatigue cracking consists of two phases: crack initiation which is generally described as the coalescence of micro-cracks to form a macro-crack under the repeated application of tensile strains; and crack propagation which concerns the growth of the macro-crack through the material under further application of tensile strains, e.g. (Read, 1996).

Fatigue cracking is usually initiated at the bottom of the asphalt layer and grows upwards due to the traffic loading according to structural analysis. A suitable design procedure based on the mechanical properties of the structure

26

can be used to reduce this phenomenon. More fatigue theories and laboratory testing on fatigue cracking can be found in Read (1996).

2.4 Review of monotonic constitutive behaviour of realistic asphalt mixtures

Ossa et al. (2005) indicated that constitutive behaviour of asphalt mixture is strongly dependent on the bitumen even though the mixture contains less than 10% by volume of asphalt. Understanding the mechanical behaviour of asphalt mixtures relies on an understanding of the behaviour of the bitumen. Cheung (1995) performed a serious uniaxial tension and shear tests for pure bitumen over a wide range of stress, strain rate, and temperature conditions and found that the steady-state behaviour of bitumen at a particular temperature can be represented by a power law equation; the temperature dependence of the steady-state deformation behaviour of the bitumen at low temperature ($T \leq 20$ ^{o}C) can be represented by the Arrhenius equation (energy controlled); at higher temperature ($T \geq 20$ ^{o}C) the temperature dependence was free volume controlled and can be expressed by the WLF equation (see (Cheung, 1995)). The Power Law Model was obtained by combining these two theories as

$$\frac{\dot{\varepsilon}}{\dot{\varepsilon}_{op}} = \left(\frac{\sigma}{\sigma_{op}}\right)^{n} \exp\left(-\frac{Q_p}{RT}\right) \qquad (2.6)$$

where $\dot{\varepsilon}$ and σ are uniaxial strain rate and stress, respectively; n is the creep exponent; $\dot{\varepsilon}_{op}$ is the reference strain rate at a reference stress σ_{op}; Q_p is the thermal activation energy; R is the universal gas constant; the temperature T

is in degrees Kelvin. In addition he described the steady state uniaxial behaviour of the bitumen by the Modified Cross Model (MCM):

$$\frac{\sigma}{\sigma_0} = \frac{\dot{\varepsilon}}{\dot{\varepsilon}_0}\left(\frac{1}{1+\left(\dfrac{\dot{\varepsilon}}{\dot{\varepsilon}_0}\right)^n}\right) \tag{2.7}$$

Cheung (1995) also found that, at temperatures above the glass transition, the deformation behaviour of pure bitumen was linear viscous at low stress levels and showed power law creep at high stress levels with a creep exponent of approximately 2.3. The glass transition temperature is the temperature range at which bitumen changes from a glassy to a fluid condition; it usually ranges from -40 ℃ to 0 ℃. Figure 2.6 shows the steady-state stress/strain-rate relationship of pure bitumen. It can be seen that although in the higher half of the stress range the behaviour can still be considered to be power law, it changes gradually to linear behaviour (slop of 1) towards the lower half of the stress range. The transition stress was found to be a measure of the failure strength of the structural linkages in bitumen, and the value was found to be approximately 115kPa.
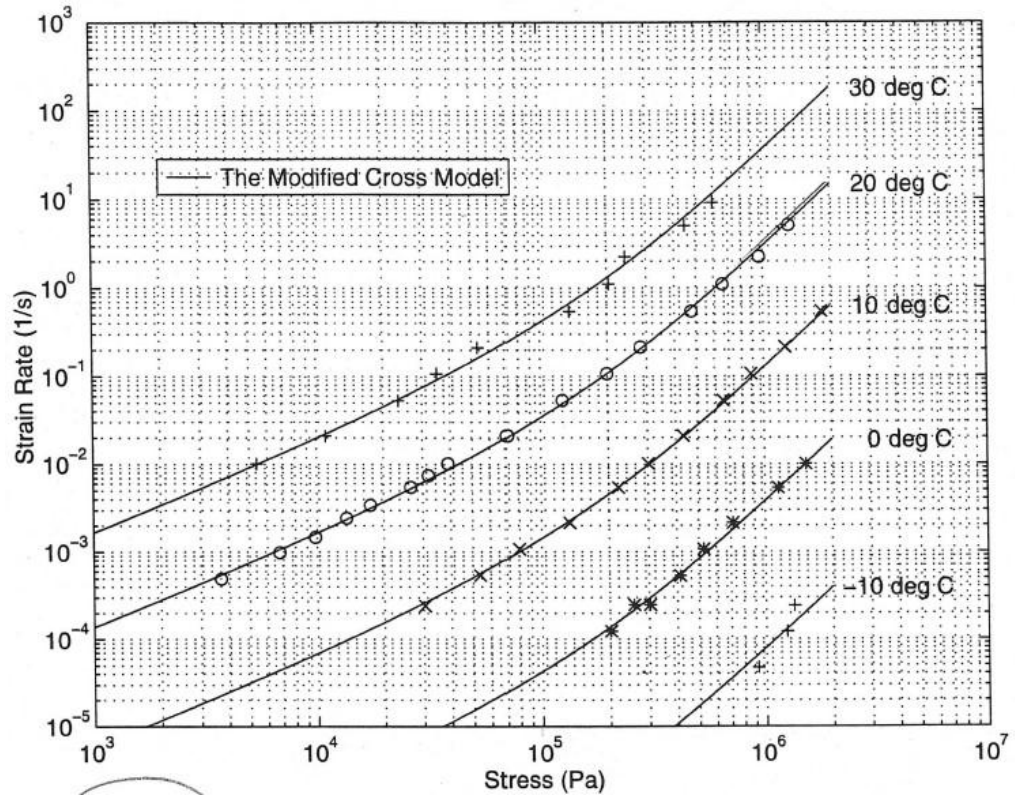
Figure 2.6 Steady-state behaviour of pure bitumen

Khanzada (2000) performed uniaxial tests on HRA mortar, 30/10 HRA and 10mm dense bitumen macadam (DBM) over a range of temperatures and loading stress and found that the steady-state deformation behaviour of asphalt mixtures have the same form as pure bitumen with linear behaviour at low stress levels and nonlinear behaviour at high stress levels. The mixtures were stiffer than pure bitumen. The MCM model Equation (2.7) was modified to give the steady-state behaviour of asphalt mixture:

$$\frac{\sigma_{ss}}{\sigma_0} = \frac{S\dot{\varepsilon}_{ss}}{\dot{\varepsilon}_p}\left(\frac{1}{1+\left(\frac{S\dot{\varepsilon}_{ss}}{\dot{\varepsilon}_p}\right)^m}\right) \tag{2.8}$$

where $\dot{\varepsilon}_{ss}$ is uniaxial strain rate; $\dot{\varepsilon}_p$ is the reference strain rate and S is the stiffening factor due to the presence of aggregate and was found to increase with the volume fraction of aggregate (Khanzada, 2000).

Taherkhani (2006) performed more uniaxial tests on asphalt mixtures over a wide range of conditions and also found that the uniaxial steady-state deformation behaviour of asphalt mixtures were nonlinear power law creep; the temperature dependency of the steady-state deformation behaviour of the mixtures was free volume controlled and can be well captured by the WLF equation (see (Taherkhani, 2006) for further details). The steady-state results from the constant strain rate and constant stress creep tests were found to be complementary.

2.5 Constitutive models for asphalt mixture

Constitutive modelling of an asphalt mixture entails understanding the functional relationship between stresses and strains at different loading conditions. It is much more complex than soil and rock due to the complex behaviour of bitumen. The following features should be included in the constitutive model of an asphalt mixture (Taherkhani, 2006):

- The inelastic, non-homogenous, non-linear, anisotropic, time, loading rate and temperature dependent behaviour of the mixtures
- Dilatancy
- Different properties in tension and compression
- Existence of residual deformations at the end of loading cycles

- The effect of ageing, moisture and air voids content on the permanent deformation

It is difficult to satisfy all the requirements above. Therefore, simplified constitutive models have been developed in recent years. Some of them are listed in the following sections.

2.5.1 **Elastic model**

Burmister (1943) developed elastic layer theory for a two-layer pavement, which was later used for more layers. In this theory, materials are usually assumed to be homogenous isotropic and linear elastic and characterized by time-independent constants of proportionality between stress and strains (Huang, 1967). The loading curve of the elastic material is identical to the unloading curve, and all strains are recovered upon the removal of the applied load. Based on Hooke's law, the relationship between stress and strain for elastic material in three dimensions is given as:

$$\{\sigma\} = [D] \times \{\varepsilon\} \tag{2.9}$$

where $\{\sigma\}$ and $\{\varepsilon\}$ are the stress and the strain tensor, respectively; $[D]$ is the stiffness matrix of elasticity which expressed as a function of Young's modulus E and Poisson's ratio v:

$$[D] = \frac{E}{(1+\upsilon)(1-2\upsilon)} \begin{bmatrix} 1-\upsilon & \upsilon & \upsilon & 0 & 0 & 0 \\ 0 & 1-\upsilon & \upsilon & 0 & 0 & 0 \\ 0 & 0 & 1-\upsilon & 0 & 0 & 0 \\ 0 & 0 & 0 & 0.5-\upsilon & 0 & 0 \\ 0 & 0 & 0 & 0 & 0.5-\upsilon & 0 \\ 0 & 0 & 0 & 0 & 0 & 0.5-\upsilon \end{bmatrix} \tag{2.10}$$

The elastic stiffness of a bituminous layer indicated the ability of the layer to spread load, and reduce the stress per unit area transmitted to the underlying layer (Preston, 1991). It is known that the stiffness of an asphalt mixture varies with loading time and temperature, therefore, the Young's modulus above is replaced by a stiffness modulus (Van der Poel, 1954). The linear elastic model is accurate enough to enable prediction of asphalt mixture behaviour at lower temperatures and short loading times (Eisenmann et al., 1977, Ulliditz et al., 1987). Non-linear elastic models are also used to represent the non-linear behaviour of asphalt mixtures. Hicks, et al, (1972) and Starodubsky, et al (1990) proposed that the stress-strain curves generally show a linear and a non-linear period before reaching their peak value where the non-linear behaviour comes from the development of micro-cracks.

2.5.2 **Linear viscoelastic models**

Asphalt mixture behaviour is linear viscoelastic at low stress and strain levels when subjected to loading. The class of linear materials for which the coefficient functions are time dependent are referred to as linear viscoelastic (Moavenzadeh et al., 1968). When a stress or strain is imposed on a body of asphalt mixture, rearrangement takes place inside the material as a response to that excitation. This rearrangement requires a finite time in any real material. Materials that exhibit significant amounts of time dependent stress strain behaviour are called viscoelastic (Schapery, 1974). Schapery stated that for linear viscoelastic behaviour, the response must satisfy the following two conditions: 1. Proportionality: proportional change in input causes the same proportional change in response. 2. Superposition: response due to independent

inputs acting simultaneously is equal to the sum of the response from each input acting separately. They can be mathematically expressed as

$$R\{cI\} = cR\{I\} \tag{2.11}$$

$$R\{I_a + I_b\} = R\{I_a\} + R\{I_b\} \tag{2.12}$$

where I is the input to a system (e.g. forces), $R\{I\}$ is the response of the system from the input I (e.g. displacement), I_a and I_b are inputs that could be of the same or different time history.

Van der Poel (1954) defined the stiffness modulus of bitumen as a function of loading time and temperature. Thereafter, linear viscoelastic models have been applied to describe the behaviour of asphalt by many researchers. A spring (purely elastic) and a dashpot (purely viscous) are the two main elements used to establish the mechanical model to build the relationship between stress and strain as a function of time. These elements are combined in series as a Maxwell model, and in parallel as a Kelvin model. Ossa et al. (2005) has proved that the characteristics of mechanical models can broadly agree with experimental results under conditions of low stress and strain levels. A Burger's model shown in Figure 2.7 composed of a Maxwell model connected in series to a Kelvin model has been used to exhibit both delayed elasticity and steady creep behaviour. The uniaxial creep response to a step change in stress σ_0 is given by:

$$\varepsilon(t) = J(t)\sigma_0 = \left\{ \frac{1}{k_m} + \frac{t}{C_m} + \frac{1}{K_k}\left[1 - e^{(-t/\tau_1)}\right] \right\}\sigma_0 \tag{2.13}$$

where $J(t)$ is the creep compliance; K_m and K_k are the stiffness of the spring in Maxwell and Kelvin model respectively; C_m and C_k are the viscosity of dashpot in the Maxwell and Kelvin model respectively. $\tau_1 = C_k / K_k$ is the relaxation time (Lee, 2006).
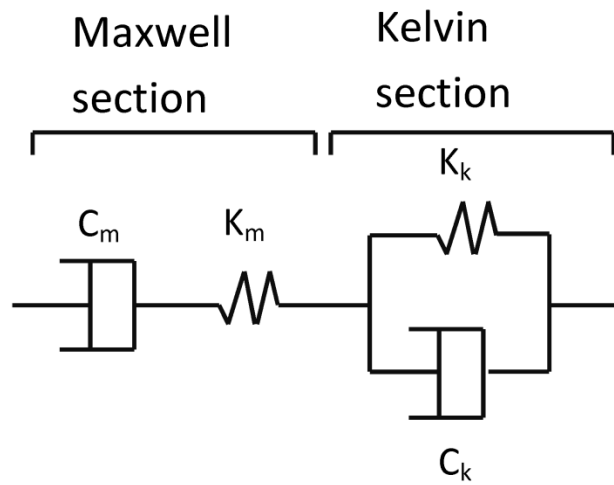
Figure 2.7 Burger's model

The viscoelastic behaviour of Burger's model is illustrated in Figure 2.8. As the figure shows, there is an instantaneous elastic response (strain OA) when the stress is applied then a further delayed elastic strain AB is acquired in time as is a steadily increasing creep strain component BC. When the stress is removed, there is an instantaneous elastic recovery (same in magnitude as OA) and a delayed elastic recovery DE leaving a permanent strain at E which is acquired through the action of creep (Johnson, 1985).
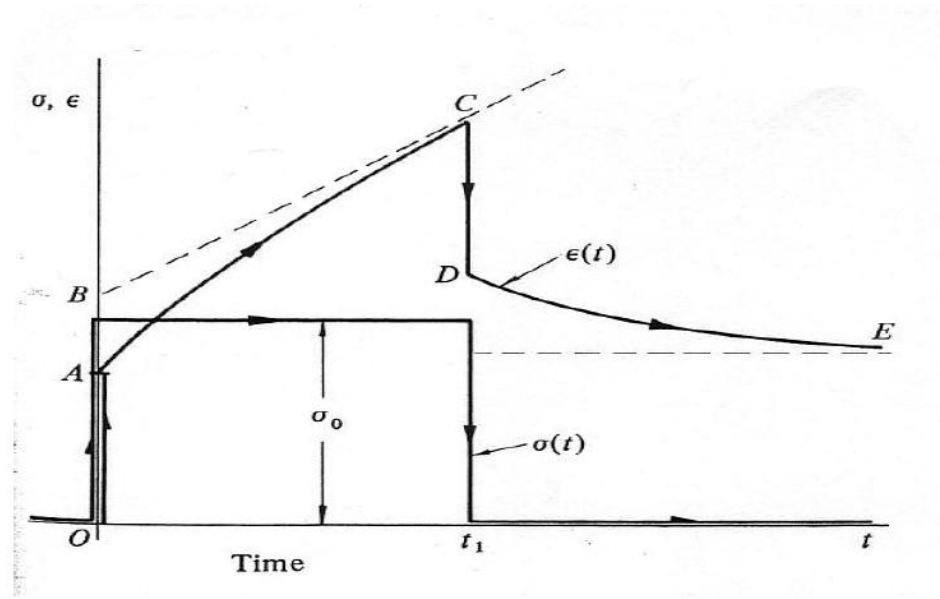
Figure 2.8 Viscoelastic response of stress and strain (Johnson, 1985)

2.5.3 **Nonlinear viscoelastic models**

The behaviour of asphalt mixtures cannot be modelled adequately by linear models at high stress and strain rate levels. Fitzgerald et al. (1973) performed experimental and theoretical investigations to demonstrate that extended nonlinear, homogenous constitutive equations are more readily applicable to defining the mechanical behaviour of a sand asphalt mixture.

Lai et al. (1973) developed a non-linear generalised Kelvin model which consists of a non-linear dashpot connected in series with a non-linear Kelvin chain to represent the non-linear behaviour of asphalt mixtures. In this model, the non-linear dashpot accounts for the time dependent irrecoverable strain (ε_p, viscous flow) and the non-linear Kelvin chain accounts for the power law time dependent recoverable strain (ε_v). They are given by

$$\left\{\begin{array}{l} \varepsilon_p(t) = (b_1\sigma + b_2\sigma^2)t^{n_p} \\ b_1 = 0.0844\times10^{-3} \\ b_2 = -0.454\times10^{-6} \\ n_p = 0.25 \end{array}\right\} \qquad (2.14)$$

$$\left\{\begin{array}{l} \varepsilon_v(t) = (C_1\sigma + C_2\sigma^2)t^{n_v} \\ C_1 = 0.0748\times10^{-3} \\ C_2 = -0.412\times10^{-6} \\ n_v = 0.093 \end{array}\right\} \qquad (2.15)$$

This model has been proved to be satisfactory enough to predict the creep behaviour of an asphalt mixture under multiple step loading and repeated loading.

Judycki (1992) applied non-linear viscoelastic theories to model the non-linear behaviour of asphalt mixtures under three point bending tests. The results show that the non-linear effects increased with stress level and loading time at 10 ℃. The non-linearity function is expressed in the form

$$\log[\Gamma(\sigma,t)] = \sigma\frac{t}{a+bt} \qquad (2.16)$$

where Γ is the non-linearity function dependent upon stress σ and time t; a and b are calculated from experimental results ((Judycki, 1992)).

Harvey (2000) developed a rheological model consisting of Maxwell and Kelvin elements in series, based on linear spring and non-linear dashpots (see Figure 2.9), here the springs are linear and the dashpots are nonlinear with constitutive relations of the power law form (see (Harvey, 2000)). In Figure 2.9, E_1 and E_3 are the spring stiffnesses in series and parallel respectively; n_2 and

n_3 are the power law exponents of the series and parallel dashpot respectively;

σ_{02} and σ_{03} are the reference stress in the power law equations for the series

and parallel dashpots respectively (equation (2.6)); $\dot{\varepsilon}_{02}$ and $\dot{\varepsilon}_{03}$ are the

reference strain rates corresponding to the reference stresses above. This model

was found to be able to represent the tensile behaviour of thin films of bitumen

over a range of temperatures, strain rates and specimen aspect ratios. Harvey

(2000) demonstrated that the non-linear viscoelastic model can successfully

predict the tensile stress-strain response of bitumen when either rupture in thick

ductile films or voiding in thin bitumen films.
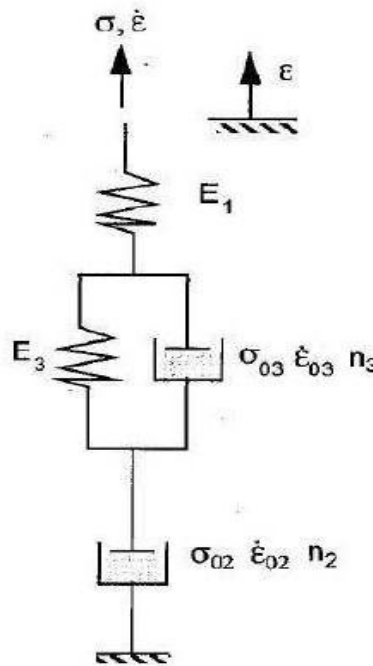
Figure 2.9 Harvey rheological model (Harvey, 2000)

As the non-linear viscoelastic model in practice requires many more calibration

constants and much more complex fitting procedures, the linear viscoelastic

models are still the popular choice in modelling of the constitutive behaviour of

asphalt mixtures.

2.5.4 **Elastic-visco-plastic models**

Perl et al. (1983) developed a constitutive model for asphalt mixtures subjected to repeated loading incorporating elastic, plastic, viscoelastic and viscoplastic strain components. The elastic strain is found to depend solely and linearly on the stress. The plastic strain is linearly proportional to stress and exhibits a power-law dependence on the number of loading cycles. The viscoelastic strain is nonlinear with respect to stress and is governed by a power law of time. The viscoplastic strain component is nonlinear with respect to stress and thus can be represented by the product of a second-order polynomial of stress and two power laws of time and number of cycles. They performed a series of repeated uniaxial creep and creep recovery tests under constant stresses of various magnitudes at 25 °C and found that the total strain includes recoverable and irrecoverable parts, some of which are time dependent and some are time independent

$$\varepsilon_t = \varepsilon_e + \varepsilon_p + \varepsilon_{ve} + \varepsilon_{vp} \tag{2.17}$$

where ε_e is recoverable and time-independent elastic strain, ε_p is irrecoverable and time-independent plastic strain, ε_{ve} is recoverable and time-dependent viscoelastic strain, and ε_{vp} is irrecoverable and time-dependent viscoelastic strain.
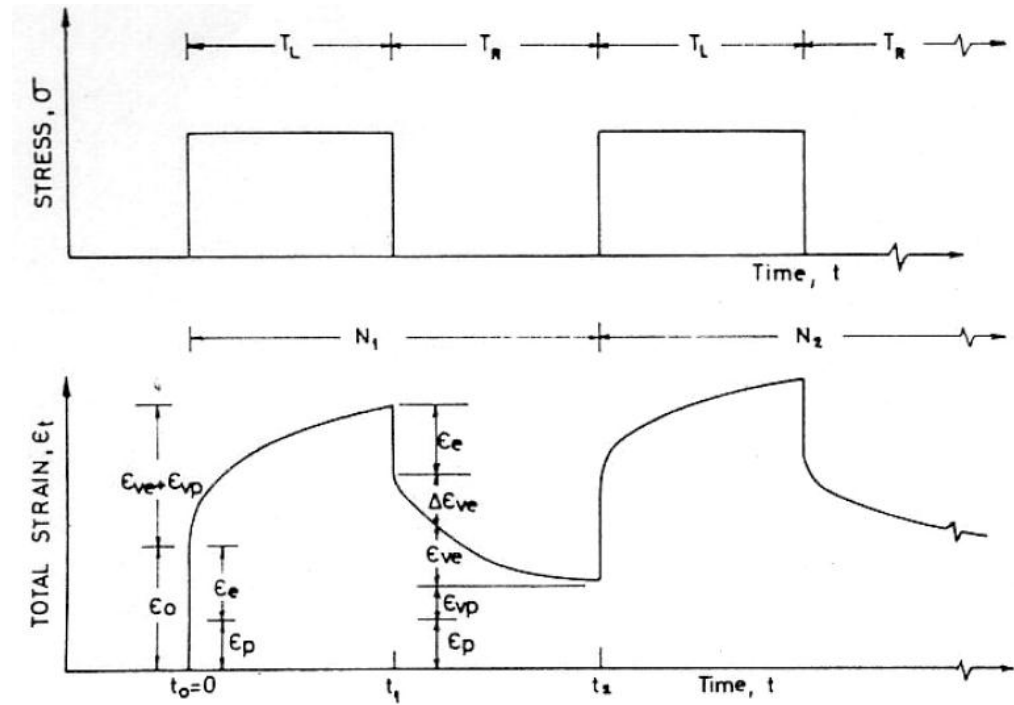
Figure 2.10 Strain components under repeated loading (Perl et al., 1983)

Figure 2.10 shows the schematic representation of strain components under repeated loading. It can be seen that there are instantaneous elastic ε_e and plastic ε_p strains at $t = t_0$ when the load applied. Viscoelastic ε_{ve} and viscoplastic ε_{vp} strains are building up as loading continued from t_0 to t_1. Once the load is removed, at $t = t_1$, the elastic strain ε_e recovered, the viscoelastic strain is recovered gradually over time between t_1 and t_2. At the end of one cycle, the residual strain consists of recoverable plastic and viscoplastic strain components.

2.6 **Uniaxial compression test**

2.6.1 **Introduction**

Laboratory tests are typically performed to understand the deformation behaviour of asphalt mixtures. Uniaxial tests used to measure mixture characteristics for a variety of predictive methods have gained wide acceptance due to ease of specimen preparation, simplicity of test procedures and low cost of test equipment. Typically, uniaxial tests are conducted at either constant stress (creep test) or a constant strain rate in compression or tension. In the uniaxial compression test, the friction reduction system (see Chapter 5) is used between the loading plates and specimen to prevent specimen barrelling due to the lateral constraint from the plate to the specimen.

In a uniaxial creep test, a cylindrical bitumen specimen with flat ends is typically put between two steel platens, one of them fixed and the other acting as the loading platen. A vertical stress is applied rapidly to the specimen through the platen and then held constant. The axial and radial strains as well as axial load are recorded as a function of time. A typical creep curve is shown in Figure 2.11, the curve can be divided into three regions. The primary creep region which comprises the instantaneous strain (occurs upon load application) is also known as the time-independent strain. The initial elastic and the primary creep strain cannot be neglected. They can be treated in much the same way that elastic deflection is allowed for in a structure, the secondary creep region (steady state) in which the strain is time-dependent and the strain rate is constant and tertiary creep region in which the strain rate is increasing.
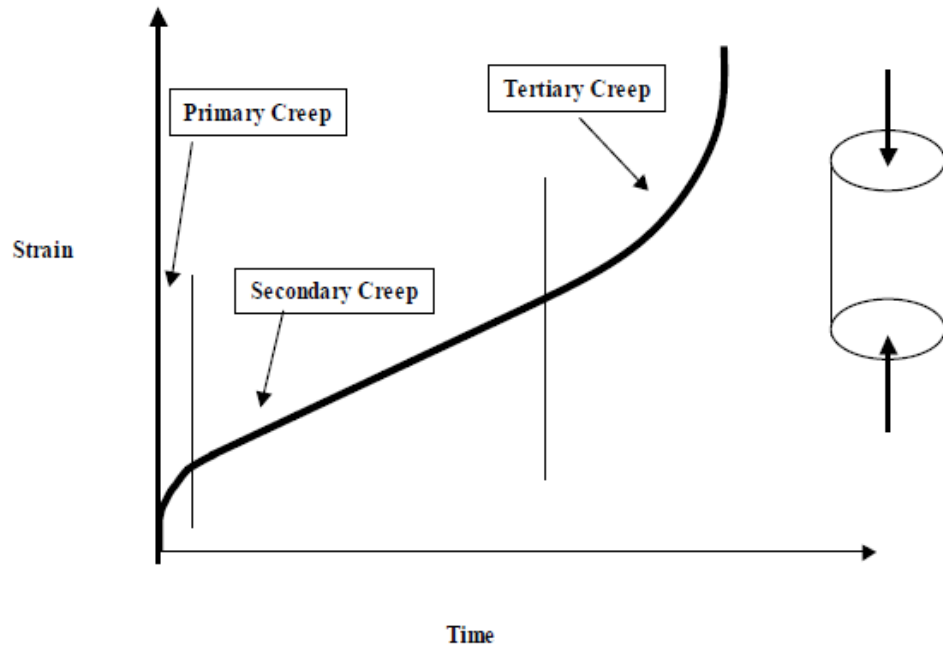
Figure 2.11 Typical creep curve (Taherkhani, 2006)

The constant strain rate test and the creep test are found to be complementary experimental tools for investigation of the steady state deformation behaviour of asphalt mixtures (Cheung, 1995, Deshpande, 1997). In a uniaxial strain-controlled test, constant strain rates are applied to the asphalt mixture and the axial and radial strains as well as the axial stress are measured with time. A typical result from the constant strain rate test where the axial stress is plotted against the strain (axial or radial strains) is shown in Figure 2.12. The stress versus strain relationship consists of linear elastic zone and inelastic hardening zone, up to a peak stress, known as steady state stress, followed by a softening portion.
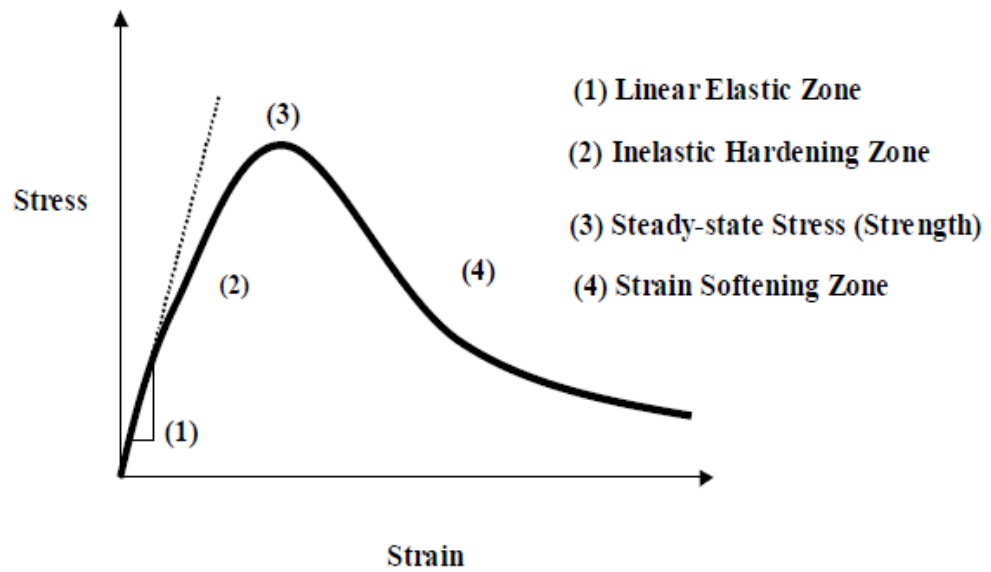
Figure 2.12 Typical results from the constant strain rate test (Taherkhani, 2006)

2.6.2 **Volumetric behaviour**

To study the volumetric behaviour of asphalt mixtures, the radial deformation of the specimens should be measured during the uniaxial compression rate tests. Figure 2.13 shows a typical result from the constant strain rate tests for hot rolled asphalt under test conditions of 0.0005/s and 20 ^{o}C. The axial stress is plotted against the axial and radial strains. As can be seen, the axial strain and radial curves are similar to each other. They all have the four distinct areas as mentioned in section 2.6.1. The Young's modulus of the mixtures was calculated from the axial stress and strain data taken at the beginning of the test.
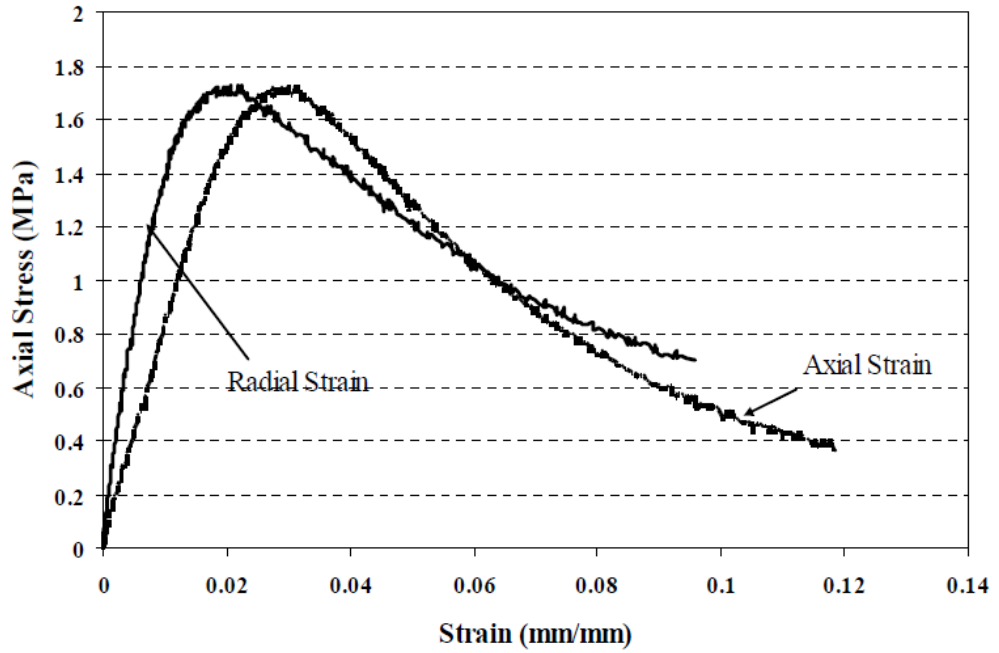
Figure 2.13 A typical constant strain rate test result for hot rolled asphalt at 20°C (Taherkhani, 2006)

Poisson's ratio is defined as the negative ratio of the transverse extension strain to the longitudinal contracting strain in the direction of loading in the elastic region of behaviour, and is given by

$$\upsilon = -\frac{\varepsilon_r}{\varepsilon_a}$$ (2.18)

In this equation, the tensile deformation is considered positive and compressive deformation is considered negative; the Poisson's ratio is a positive value. Most materials have Poisson's ratio values ranging between 0.0 to 0.5. Materials with a Poisson's ratio of exactly 0.5 are incompressible, since the sum of all their strains leads to a zero volume change. Poisson's ratio in a viscoelastic material is time dependent (Taherkhani, 2006). Poisson's ratio of asphalt mixtures has been found to lie somewhere in the range 0.1 to 0.45 (Read, 1996). In the uniaxial compression test, Poisson's ratio is determined as

the average ratio of the radial strain to the axial strain over the short time period in the beginning of the test.

2.7   Micromechanical models of asphalt mixture

The Finite element method has become a well-established method of modelling the mechanical behaviour of asphalt mixtures (Sepehr et al., 1994, Erkens et al., 2002b, Collop et al., 2003b, Sadd et al., 2003, Soares et al., 2003, Dai et al., 2007). In this method, the asphalt mixtures are treated at the macro scale using continuum based approaches. There is a difficulty in using the continuum modelling approach for asphalt mixtures because it cannot explain rutting problems and the considerable movement and rotation of granular particles in the mixture. The micromechanical behaviour of the mixture is not explicitly included in this approach (Kim et al., 1990, Sousa et al., 1993, Collop et al., 1995, Uzan, 1996, Schapery, 1999, Biaauwendraad et al., 2000, Erkens et al., 2002a, Long et al., 2002, Souza et al., 2012). To better understand the constitutive behaviour of asphalt materials at the level of contacting particles, a micromechanical model which can predict the fundamental material properties of a composite based upon the properties of the individual constituents is needed. This approach can provide a clear examination of the micromechanical material behaviour. This section reviews some of the micromechanical models which have been used in the modelling of asphalt mixtures.

2.7.1 Thin film bitumen creep model

Hills (1973) developed a micromechanical model to model the creep behaviour of asphalt mixtures. This model considers bitumen as forming a binder layer

between a pair of adjacent particles (see Figure 2.14) and taking account of the forming of the binder films and the gradation of the aggregate. The macroscopic strain of the mixture is assumed to be accommodated at a microscopic scale by displacements of adjacent particles in both shear and compression which are assumed to be independent of each other. The deformations in the mixture are the result of relative sliding displacements between adjacent mineral particles. The rate of strain is dependent of the magnitude of stresses, the thickness of bitumen (change as a function of time) and the bitumen properties.
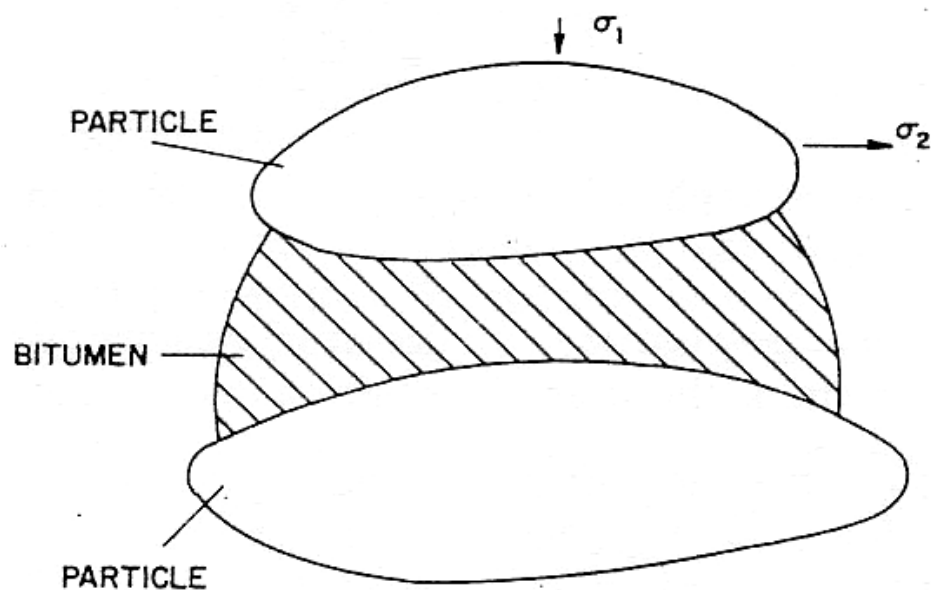
Figure 2.14 Bitumen film separated by to particles (Hills, 1973)

This model has been shown to give good correlation with experimental results and is applicable to the linear, shear and volumetric strains in uniaxial compression tests.

2.7.2 **Microstructure model**

Cheung et al. (1999) suggested an isolated contact model to predict the deformation behaviour of the idealized mix and concluded that the deformation is primarily determined by the distribution of the thin films of bitumen. The evolution of the film distribution is very sensitive to the loading path. More about thin film deformation behaviour can be found in Cheung et al. (1997).

Sadd et al. (2004) indicated that the load carrying behaviour in an asphalt mixture is strongly related to the local load transfer between aggregate particles, and this is taken as the microstructural response. A micromechanical model has been developed to simulate the asphalt microstructure by replacing the aggregate/binder system with an equivalent finite element network that represents the loading carrying behaviour zone between neighbouring particles pair. An elliptical aggregate model (see Figure 2.15(b)) was used to represent the typical asphalt material (see Figure 2.15(a)). Two models were then developed. The first model incorporated a network of frame elements with a special stiffness matrix to predict load transfer between cemented particles (see Figure 2.15(c)). The second model incorporated the commercial ABAQUS finite element code using user defined continuum elements for the binder and rigid elements for aggregate (see Figure 2.15(d)), this model employed four node quadrilateral elements to simulate binder and two-node rigid elements to model aggregate. More detail can be found in Sadd et al. (2004).
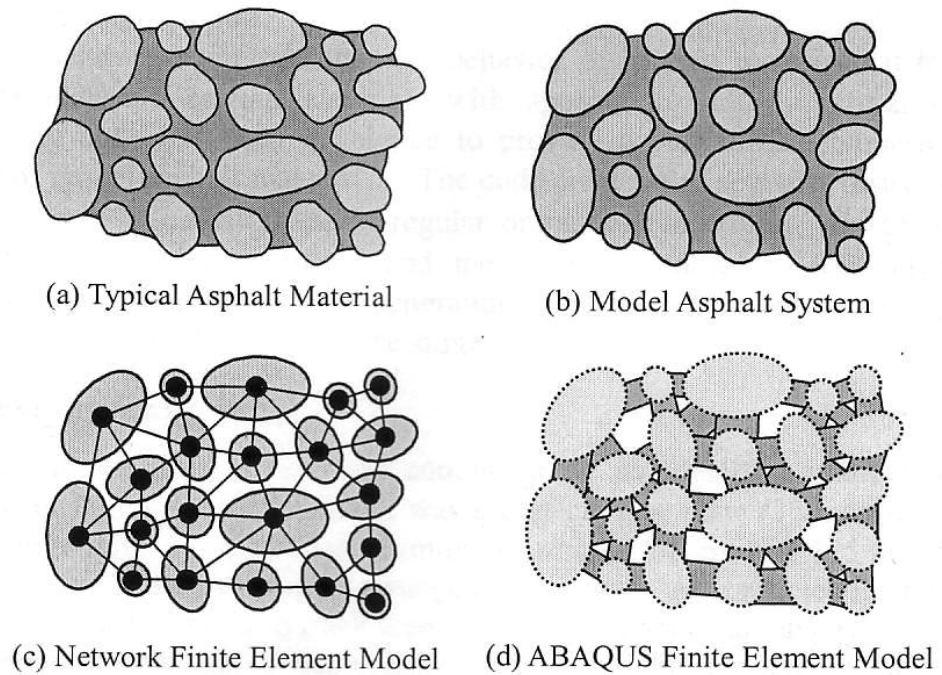
Figure 2.15 Asphalt modelling concepts (Sadd et al., 2004)

2.7.3 **Discrete element model**

The Distinct Element Method introduced by Cundall (1971) for the analysis of rock mechanics problems is a numerical model capable of describing the mechanical behaviour of assemblies of discs and spheres. In this method, the contact forces and displacements of a stressed assembly of particles can be determined. Strictly speaking, the Distinct Element Method refers to rock mechanics models, and Discrete Element Method applies to granular media. However, the distinction between the two has become cloudy in the literature and informally many researchers use the texts interchangeably. The development and application of discrete element method in granular material and asphalt will be reviewed in chapter 3.

2.8 **Summary**

This chapter reviews the three main types of asphalt mixture: Asphalt Concrete (continuously graded), Hot Rolled Asphalt (gap-graded mixtures) and Stone Mastic Asphalt (dense gap-graded). Stone mastic asphalt has been chosen in the project because of its high coarse aggregate content and more discussion can be found in chapter 5.

There are two main types of load failure in an asphaltic pavement: cracking (fatigue) and rutting (permanent deformation). The macro-scale constitutive behaviour of asphalt mixtures is well understood. Asphalt mixture is usually assumed to be linear viscoelastic at small strain rates and/or low stress, non-linear viscoelastic at large strain rates and/or high stress level. It is loading rate and temperature dependent during deformation.

A number of continuum constitutive models are available to describe the behaviour of asphalt mixtures. These models have been reasonably successful although large number of calibration factors are needed in a quantitative analysis of pavement structures. The micromechanical behaviour of asphalt mixtures is not explicitly included in this approach.

Micromechanical models can predict fundamental material properties of a composite based upon the properties of the individual constituents. This approach can provide a clear examination of the micromechanical material behaviour.

3 Discrete element modelling

3.1 Introduction

The previous chapter reviewed the three main types of asphalt mixture, and, the mechanical properties, monotonic constitutive behaviour, constitutive models, the uniaxial compression test and micromechanical models of asphalt mixtures. It was concluded that the traditional approaches are not capable of fully describing the complex behaviour of asphalt mixtures. The Discrete Element Method (DEM) presents a promising method for modelling asphalt at particle scale. DEM has been widely used in soil and rock materials during the past decades and has been concluded to be a promising method for modelling soil at the particle scale. Attempts have been carried out in modelling asphalt mixtures as well and will be discussed is this chapter. Some of the theory and background of Particle flow code in three dimensions are also included in this chapter.

3.2 Application and development of discrete element method

This section reviews the application and development of the DEM in granular materials (section 3.2.1) and asphalt mixtures (section 3.2.2).

3.2.1 **Granular materials**

The Discrete Element Method has been widely applied in soil and rock mechanics (Ergenzinger et al., Robertson et al., 1997, Robertson, 2000, Cheng et al., 2004, Lim et al., 2005). In the early 70's, Cundall (1971) introduced a simple computer program to model the progressive failure of a discrete block system. The interaction between blocks is governed by friction and stiffness. There is no limit to the amount of displacement or rotation of each block and any block is permitted to touch any other block. The basic DEM theory such as the force displacement law, the law of motion and the calculation cycle are introduced and will be discussed later in section 3.3.

In the late 70's, Cundall et al. (1979a) developed a computer program, BALL in two dimensions by incorporating the DEM theory described in Cundall (1971) to model the granular assemblies comprising distinct particles which displace independently and interact only at contact points. In this research, the effects of damping and speed of loading were also investigated. The BALL program was further developed by Cundall et al. (1979b) to simulate the behaviour of assemblies of discs under conditions of loading and unloading. Cundall proved that DEM and BALL were valid tools for research into the behaviour of granular assemblies. In the early 80's, Cundall et al. (1982) further developed the BALL by improving methodologies for measurement of granular assemblies in simulation. The force chains, particle rotations and locked in shear forces were presented at the particle interaction level. In the late 1980's, Cundall (1988a, b) developed a DEM program called TRUBAL to extend the simulation to three dimensional assemblies. A dense random packed

assembly of spheres can be produced to a desired porosity using TRUBAL. The numerical servo-control algorithm used to equilibrate the specimen under the required isotropic stress was also introduced in the paper.

Particle Flow Code in Three Dimensions (PFC3D) for DEM simulations was first released in 1995 by ITASTA Consulting Group Inc. Hazzard et al. (2000) used PFC3D to analyse the crack nucleation and propagation in brittle rock. The micromechanical structures of different rocks have been considered to present the mechanical behaviour of different rocks. They found that the cracking pattern of the crack model agreed with laboratory test results. McDowell et al (2002a, b) used PFC3D to model the fracture of soil grains. They developed an agglomerate of balls bonded together with contact bond to represent the soil particles and demonstrated the possibility of obtaining the correct size effect on specimen strength. They further used PFC3D to model one dimensional normal compression of sand (McDowell et al., 2002b). They concluded that the yield stress reduces as the agglomerate size increases. They also found that the yield stress predicted by the model is lower than the experimental results, probably due to the different shape of the agglomerate. To sum up, they concluded that DEM offers a powerful tool for modelling the behaviour of crushable soil particles and it is capable of providing micromechanical insight into soil behaviour.

Dolezalove et al. (2003) used PFC2D to model medium dense Zbraslav sand. The micro-properties of a synthetic sand model were calibrated based on the macro-scale response of the physical sand. The predicted influence of stress path direction changes on the deformational response of synthetic sand shows good agreement with laboratory results. Furthermore, Particle Flow Code has

been widely used. For example: Wanne (2003) simulated compressive strength testing of anisotropic hard rock, Konietzky et al. (2003) simulated cyclic fatigue of a notched plate under tension and Zhou et al. (2003) simulated shear band simulations on synthetic sand based on biaxial simulations.

Powrie et al. (2005) used PFC3D to capture the essential macro-features of soil behaviour as observed from laboratory tests. In their model, two spheres were bonded permanently to behave as a single rigid particle (see Figure 3.1). Many of the clumped spheres were generated in a predefined area to model the biaxial simulation. They have investigated the effects of loading platen friction, initial specimen porosity and inter-particle friction angle and concluded that the peak effective angle of friction and volumetric dilation of the specimen increases proportionately with the particle shape factor which is defined as $(R+r)/R$ in Figure 3.1. They concluded that a numerical specimen with 10,000 particles (Figure 3.2) comprising pairs of bonded spheres of shaped factor 1.5 and inter-particle friction angle of $26°$ have demonstrated the ability to model the behaviour of soil as observed in the laboratory.
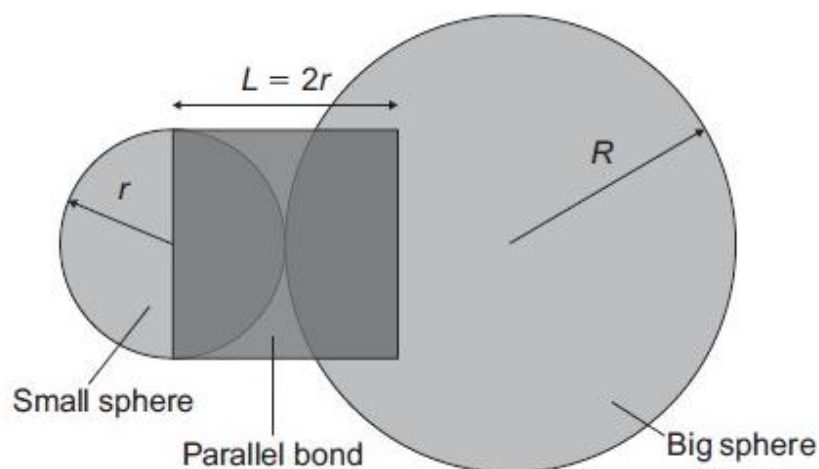
Figure 3.1 Bonded spheres
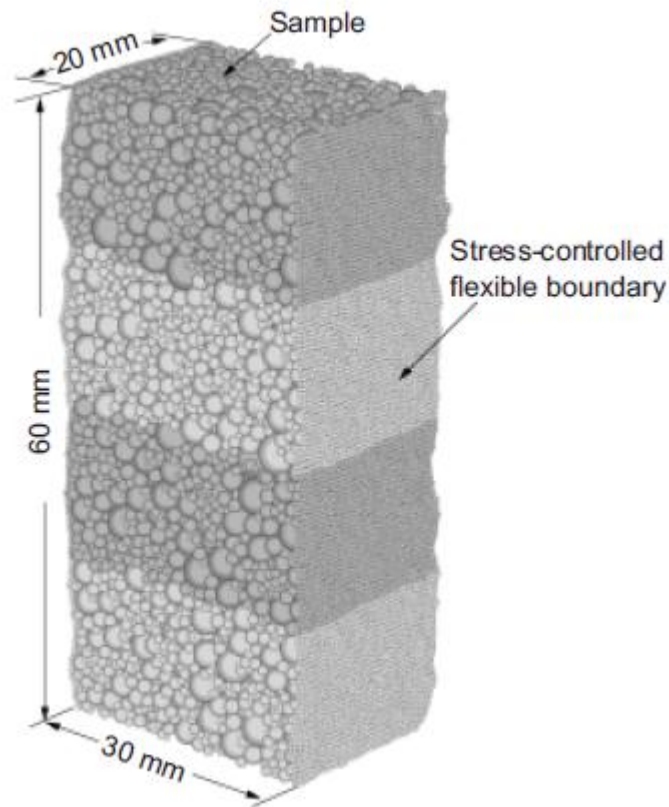
Figure 3.2 Typical specimen with 10 000 particles

McDowell et al. (2006) used PFC3D to model geogrid-reinforced aggregates. In their research, the geogrid was modelled by bonding many small spheres together to form the required geometry. They proved that the peak mobilised resistance and the displacement necessary to mobilise peak pull force can be predicted by using this model in pull-out simulations. Large scale pull-out tests and cyclic triaxial tests were also simulated to examine the zone of influence of the geogrid. They concluded that the DEM holds much promise as a tool for investigating ballast-geogrid composite systems.

Lu et al. (2008) successfully applied DEM in modelling the mechanical behaviour of railway ballast under triaxial conditions. They reported that weak parallel bonds between clumps can be used to represent the effect of particle

shape and inter-particle friction when modelling shear behaviour of ballast. The volumetric change can be modelled by adding breakable asperities to the main body of a particle. They also showded that the monotonic shear behaviour of railway ballast can be correctly modelled under a range of confining pressures, providing micromechanical insight into the behaviour.

3.2.2 **Asphalt mixtures**

The previous section reviews the application and development of DEM in granular materials. In addition, the DEM is an approach capable of modelling the micromechanical behaviour of asphalt mixtures. Rothenburg et al. (1992) invested a micromechanics model of asphalt in which the material is represented as a set of discrete elastic particles bounded by viscoelastic bitumen. Particles are considered as plane elements (disks) that interact by means of contact forces. In this model, the binder is treated as an incompressible fluid. A binder-aggregate interaction model was developed to account for the behaviour of asphalt concrete. They performed a few simulations of creep tests and reached the conclusion that asphalt exhibits steady state creep when the number of frictional contacts is below a certain minimum (Chang et al., 1993). They proved that it is possible to simulate the rutting problems in pavements by using a discrete element model.

Chang et al. (1993) presented a microscopic model, ASBAL, based on the DEM to model the behaviour of asphalt concrete. The rheological analog of viscoelastic bitumen is presented by a linear spring and a dashpot in parallel (Kelvin element). The program has been used to simulate simple triaxial tests under simple loading (Chang et al., 1993) and rutting under repeated loading

(Meegoda et al., 1993). A few simulations were undertaken with different loading conditions and various microscopic parameters to understand how the factors influence the simulations. They have shown that the DEM model is useful tool to study the fundamental properties of asphalt concrete. Meegoda et al. (1994) replaced the Kelvin element with Burger element (Figure 2.7) to simulate the viscoelastic behaviour of bitumen. A few simulations were performed with different microscopic parameters under varied types of loadings. They showed that under monotonic loading, a typical Hot Mix Asphalt test exhibits non-linear behaviour and under cyclic loading, permanent deformation was modelled (Chang et al., 1997).

Buttlar et al. (2001) developed microstructure discrete element modelling (MDEM) to simulate the Stone Mastic Asphalt microstructure and to model the indirect tension test. This approach is a two-dimensional (2D) model extended from the traditional DEM approach. The various material phases (e.g., aggregate, mastic) were modelled with clusters of very small discrete elements and the microstructure was obtained by optically scanning smoothly through test specimens. A high resolution scanner was used to obtain gray-scale images of the sections. The MDEM has all the benefits of traditional DEM and can also model complex aggregate shapes and propagation of cracks around or through aggregates during a test. However, this model has been proved to under-predict mixture stiffness, since each particle (aggregate) is assumed to be coated with matrix material and the calibration technique is not sufficiently accurate.

You et al. (2004) further developed a technique to calibrate the MDEM model with experimental results by expanding aggregates to create additional

aggregate contacts. This improvement was shown to provide better modulus estimates and believed to be more representative of the actual three-dimensional behaviour (You et al., 2004). They used MDEM to predict the asphalt mixture complex modulus in extension/compression across a range of test temperatures and loading frequencies (You et al., 2004), the complex modulus of asphalt aggregate hollow cylinders subjected to internal pressure (You et al., 2005), the compressive dynamic moduli of asphalt mixtures (You et al., 2006) and the creep stiffness of asphalt mixtures (Dai et al., 2007). The results proved to be reasonable and useful when compared with laboratory results. Except, for some fine mixes, the DEM approach provided a lower prediction of the mixture moduli compared with experimental tests. This is due to insufficient aggregate to aggregate contacts in the 2D model.

You et al. (2008) developed a three-dimensional (3D) microstructure based discrete element model of asphalt to study the dynamic modulus from the stress-strain response under compressive load. The 3D microstructure of the asphalt mixture was obtained from a number of 2D images. They demonstrated that the 3D discrete element models were able to predict the mixture moduli across a range of temperatures and loading frequencies.

Collop et al (2003a, 2004) presented a DEM model to investigate the use of PFC3D to simulate the behaviour of a highly idealised asphalt mixture which contained single-sized sand mixed with bitumen in uniaxial and triaxial compression creep tests. The effect of the bitumen was represented by time-dependent normal and shear contact stiffnesses. They found that a specimen containing 4500 particles is required for the Young's modulus and Poisson's ratio to be within 2% of the values calculated using a much larger number of

particles (Collop et al., 2003a, Lee, 2006). They also found that the bulk modulus was linearly dependant on the normal contact stiffness and independent of the shear contact stiffness. Poisson's ratio was found to be dependent on only the ratio of shear contact stiffness to the normal contact stiffness. They stated that the numerical results have all been validated with experimental data (Collop et al., 2004).

Collop et al. (2006) further developed the DEM 3D model to simulate the dilation behaviour of uniaxial creep tests at an axial stress of 400 kPa and triaxial tests for deviator stresses of 400 and 600 kPa at stress ratios of 0.6 and 0.8 in an idealised asphalt mixture. A viscoelastic Burger's model has been adopted in their simulations. They have found that the dilation gradient under uniaxial conditions increases as the ratio of compressive to tensile contact stiffness increases as a function of time in the viscoelastic simulations. The simulation results have been compared to experimental results and a good agreement has been found (Figure 3.3). The comparison between the predicted and measured results has shown that the model is able to predict the effect of stress ratio on dilation. Later, they used the model to simulate the viscoelastic deformation behaviour of an idealized asphalt mixture (Collop et al., 2007). An elastic contact was used for the compressive normal contact stiffness and a viscoelastic contact was used for shear and tensile normal contact stiffness.
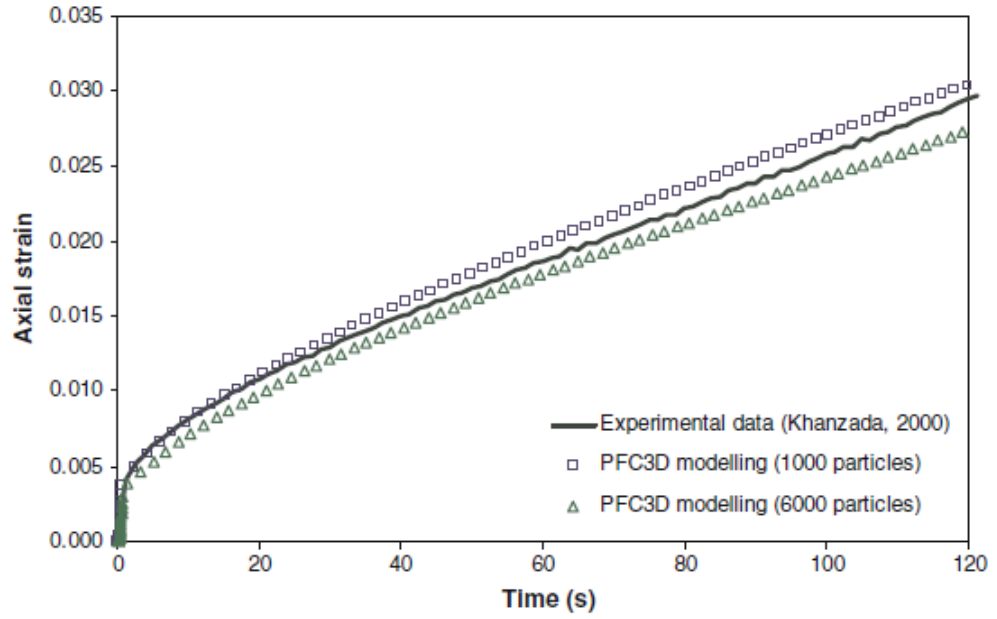
Figure 3.3 Predicted and measured axial strain for uniaxial creep test at 400 kPa as a function of time (Collop et al., 2006)

Abbas et al. (2007) simulated the viscoelastic behaviour of nine asphalt mixtures containing unmodified and modified asphalt binders. Aggregates were modelled as rigid objects (Figure 3.4) and the viscoelastic interaction among the mix constituents was defined using a time-dependent viscoelastic model. Image analysis techniques were used to capture the asphalt mixture microstructure. The image processes can be found in Papagiannakis et al. (2002).
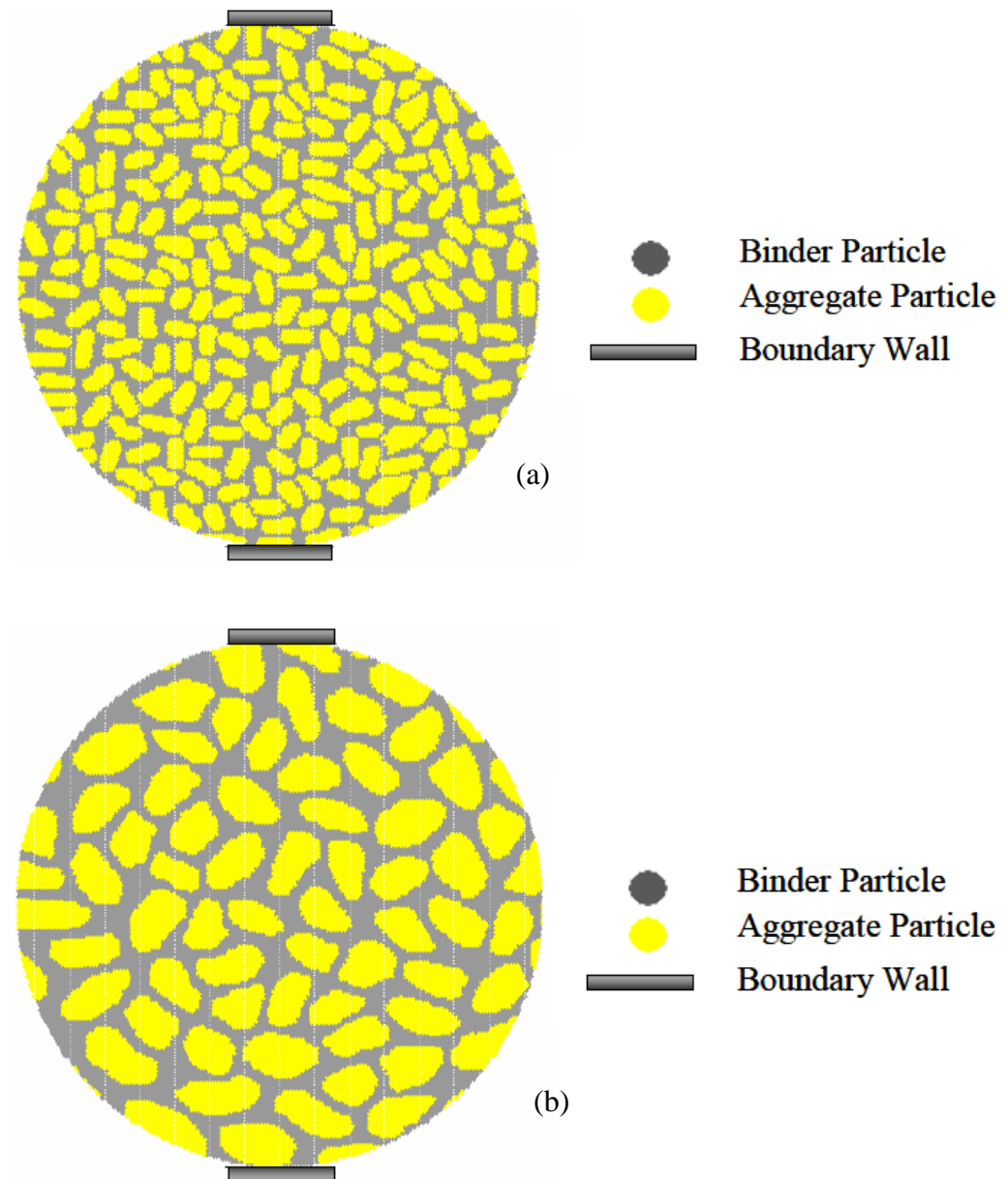
Figure 3.4 Cylindrical specimens containing (a) small size aggregate (b) large size aggregate (Abbas, 2004)

Carmona et al. (2007) extended the two-dimensional discrete element model to capture microscopic failure mechanism relevant for the process of fatigue of asphalt mixtures. They used polygons and beams to represent aggregates and binder respectively. The effect of healing has also been included. Later, Kun et al. (2008) used DEM and a fiber bundle model to study the fatigue fracture of heterogeneous materials based on Basquin's law of fatigue (Basquin, 1910).

Chapter 3 Discrete element modelling

Kim et al. (2008) developed a cohesive zone model (CZM) with viscoelastic properties which was implemented in 2-D DEM and used this model to simulate the fracture behaviour of asphalt concrete in a disk-shape compacted tension test. They concluded that viscoelastic DEM simulations were found to realistically capture rate effects in the fracture of asphalt mixtures at low temperatures and the use of a heterogeneous microstructure combined with a viscoelastic bulk material would lead to better agreement with experimental data (Figure 3.5). The heterogeneous fracture model constituents are composed of three phases: aggregates, asphalt mastic, and the interface between aggregates and asphalt mastic.
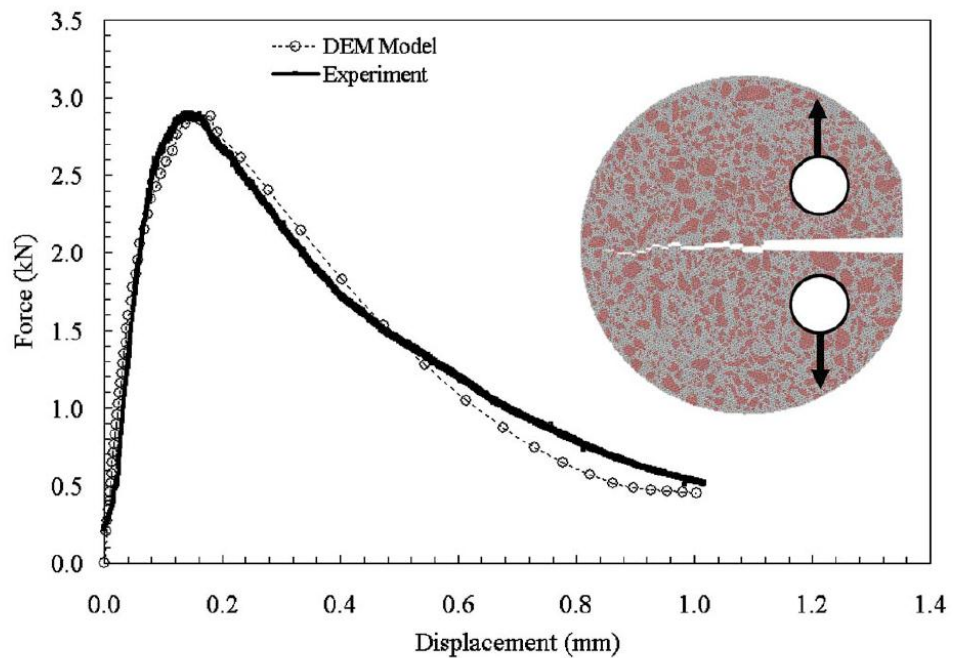
Figure 3.5 Comparison of experimental and simulation results for the heterogeneous fracture model (Kim et al., 2008)

Kim et al. (2009) further used the discrete element cohesive fracture model with heterogeneity subjected to the model-I fracture test configuration to study the various fracture behaviours of asphalt concrete. Numerical simulations with

different nominal maximum aggregate sizes, temperatures and aggregate types were conducted and the results showed excellent agreement with experimental results at different temperatures and with different mixture types. They demonstrated that the heterogeneous discrete element method fracture model could capture the physical crack and stress distribution along with global fracture responses (Figure 3.6).
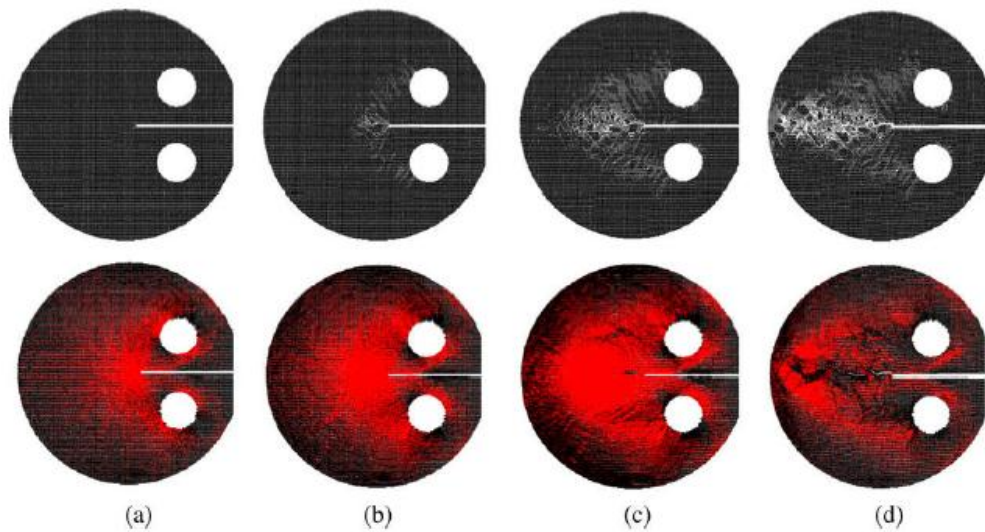
Figure 3.6 Progressive fracture process of the heterogeneous DEM model with crack (top) and stress distribution (bottom) (Kim et al., 2009)

Mahmound (2008) introduced an approach that combines DEM and image processing techniques to model the resistance of asphalt to fracture. This approach was used to determine the internal forces that develop within the aggregate structure under loading. It was concluded that a high rate of increase in forces indicates less breakage of aggregate particles and vice versa. However, their findings are limited to stone-to-stone contact between coarse aggregate particles (e.g HMA) and the simulations were 2 dimensional in nature. More details can be found in Mahmoud et al. (2010).

Chapter 3 Discrete element modelling

Adhikari et al. (2008b) used X-ray Computed Tomography (CT) techniques to capture images of asphalt mixture. By doing this the aggregate orientation, aggregate gradation, sand mastic distribution and air void distribution in the asphalt mixture were analysed. The mixture properties were predicted from X-ray CT images of the aggregate, mastic, and air voids. They monitored the strain response of the asphalt mastic and mixture models under compressive load in both two dimensions and three dimensions. The simulation results were compared with experimental measurements. They concluded that the three-dimensional discrete element models were able to predict the asphalt mixture dynamic modulus, and the prediction is much better than two dimensional models (Figure 3.7). The image based model was believed to be the most accurate model. Many researchers have used the image based models for reconstruction of asphalt mixture microstructures (You et al., 2009). The disadvantage of this using X-ray CT is it is laboratory dependent. Expensive laboratory equipment is needed and well trained technicians are also required. More details about the representation of real particles using X-ray CT can be found in Wang et al. (2007).
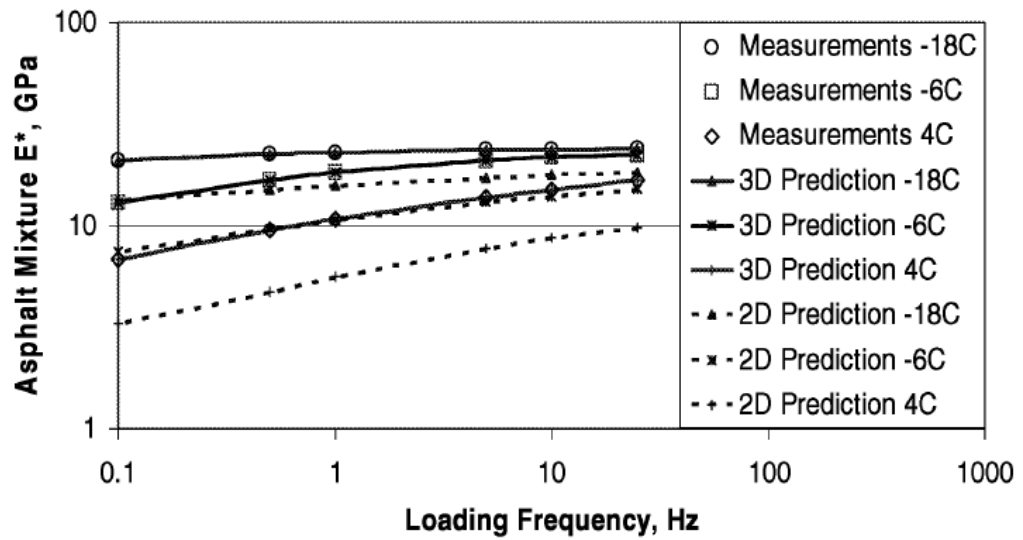
Figure 3.7 Dynamic modulus (E*) prediction using 2D and 3D DEM with laboratory
measurement of the asphalt mixture (Adhikari et al., 2008b)

Liu et al. (2009b) introduced a randomly created polyhedron method where the
aggregates are simulated with randomly created polyhedral specimens
comprising a large number of spherical particles (Figure 3.8). The specimen
preparation method did not require 2D images from experiments and can
partially represent actual geometry of aggregate particles; however, it proved to
be time consuming due to the large number of particles involved.
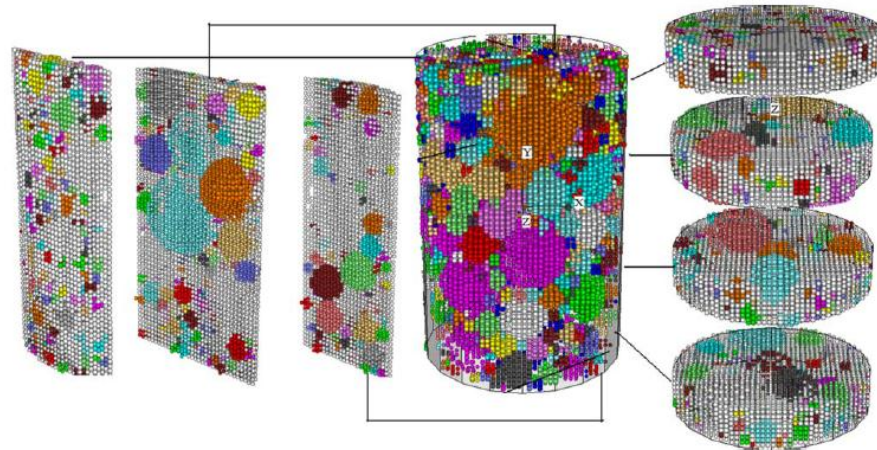
Figure 3.8 Visualization of an asphalt mixture specimen (Liu et al., 2009b)

Wu (2009) continued with the DEM model to investigate the use of PFC3D to simulate the behaviour of a highly idealised asphalt mixture in uniaxial compression creep tests. He concluded that post peak (softening) behaviour was simulated by allowing bond breakage between adjacent particles. The maximum rate of bond breakage occurred at the peak stress (compressive strength), see Figure 3.9. He used a specimen containing 6000 particles with contact normal and shear stiffness of 12 MPa and 1.2MPa, respectively. The mean value of normal and shear bond strength was taken to be 12MN with a Coefficients of Variation (CoVs) 25% and the friction coefficient was chosen to be 0.5 between particles where bonds are broken. The loading speed of 0.01m/s is an optimum speed below which the predicted stress-stain response is not dependent on the loading speed, demonstrating that the dynamic effect has been eliminated during simulations. The result of the specimen with the above parameters showed a qualitatively good agreement with the experimental results in both the pre-peak and post-peak regions of behaviour.
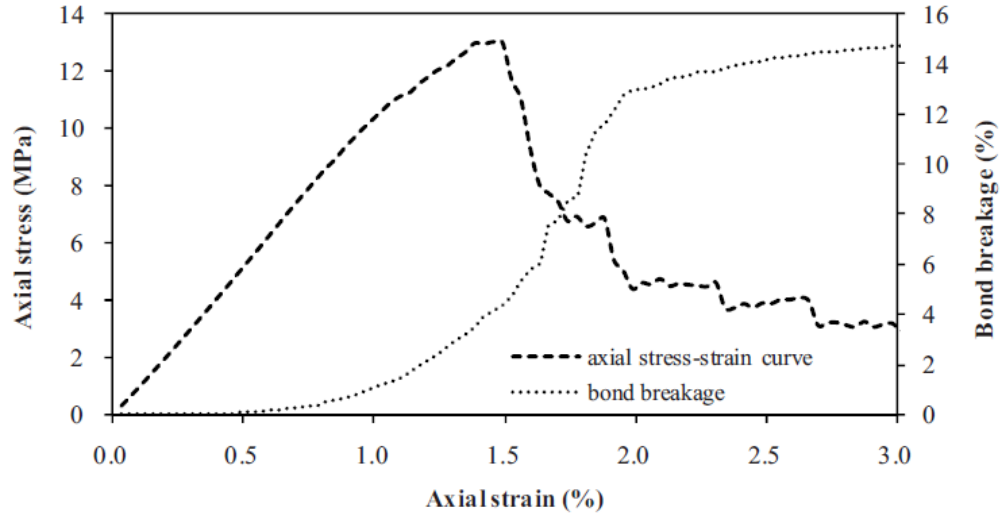
Figure 3.9 Typical result from an elastic simulation at a loading velocity 0.01 m/s

Wu et al. (2011) further used the viscoelastic Burger's Model to give time-dependent shear and normal tensile contact stiffness, while the normal compressive contact stiffness was assumed to be elastic; A computation time optimisation method was developed and demonstrated an acceptable applicability in modelling bonded particles with bond breakage. The compressive strength was found to increase as either the friction coefficient increases or percentage of frictional contacts decreases. A temperature-compensated strain rate effect was included in the DEM simulations; and the bond strength was set as a power-law function of temperature-compensated strain rate as

$$\left(\frac{\sigma_{T,\dot{\varepsilon}}}{\sigma_0}\right) = \left(\frac{\dot{\varepsilon}_T}{\dot{\varepsilon}_0}\right)^n \left(\exp\left(k\left(\frac{1}{T} - \frac{1}{T_0}\right)\right)\right)^n \quad (3.1)$$

where σ_0 is the reference stress; $\dot{\varepsilon}_0$ is the reference strain rate at the reference temperature T_0 and k is the Arrhenius constant; they should be determined according to the loading conditions and experimental results, more details can

65

be found in Wu (2009). It was proved that by using the strain rate dependent bond strength in the DEM simulations, a good agreement with the experimental data in both the pre-peak and post-peak regions of behaviour was obtained (Figure 3.10 - Figure 3.12).
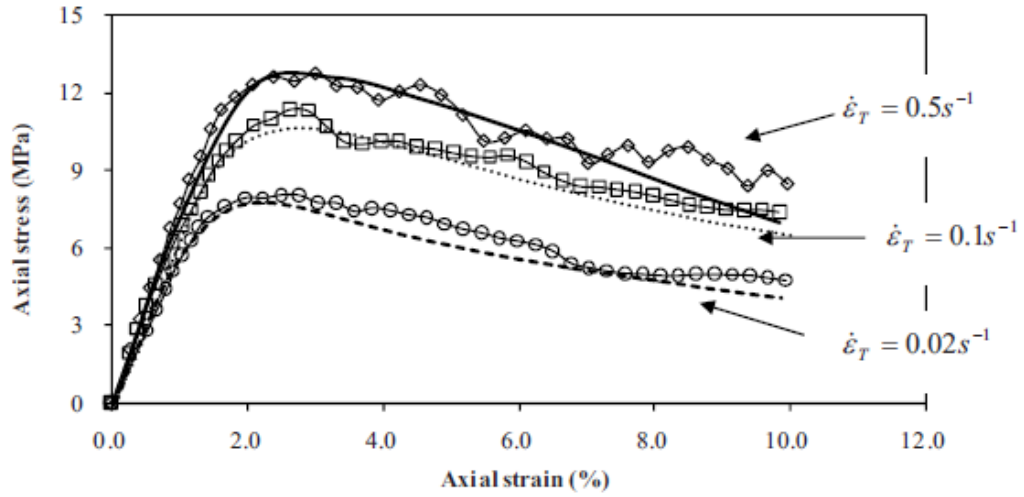
Figure 3.10 Match with experimental data at 10 ^{o}C
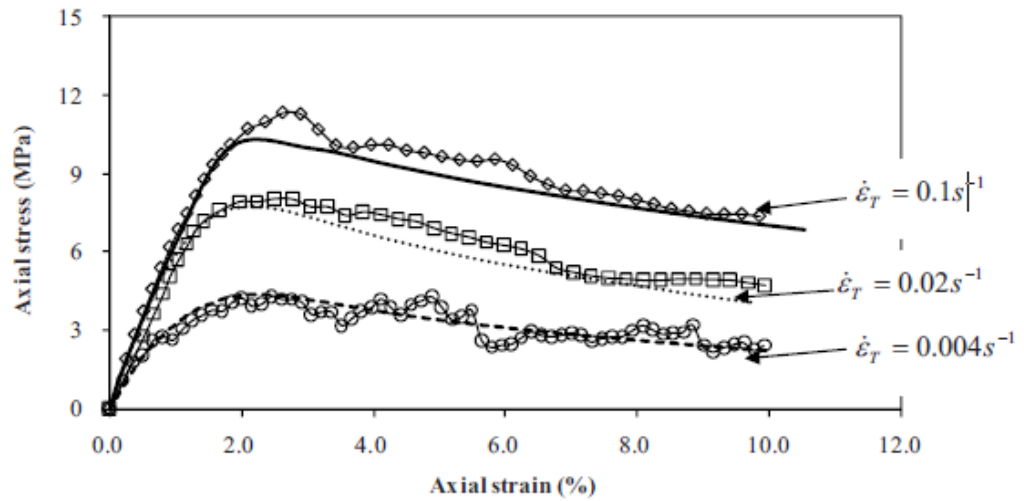
Figure 3.11 Match with experimental data at 20 ^{o}C
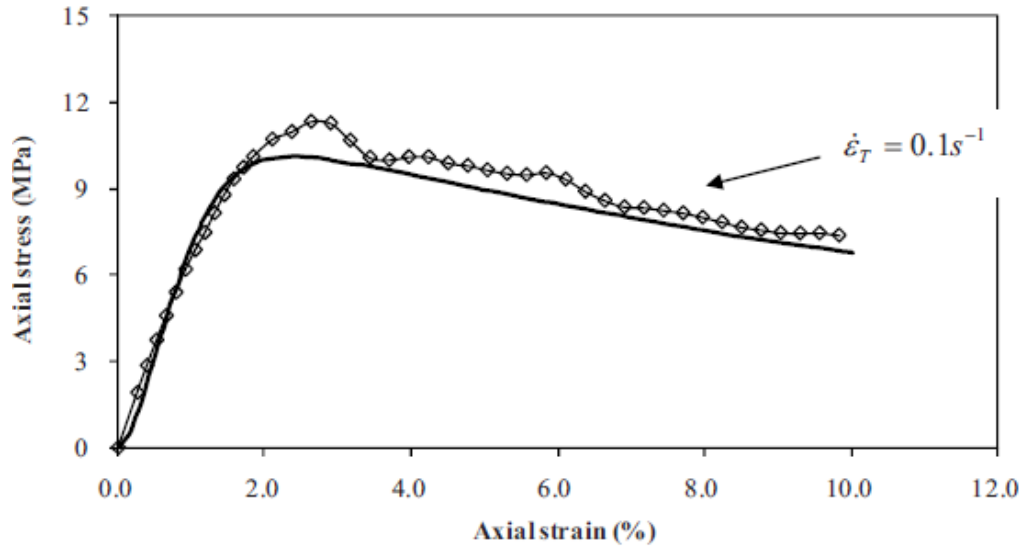
Figure 3.12 Match with experimental data at 0 ^{o}C

3.3 Particle flow code in three dimensions

3.3.1 Introduction

Particle flow code in three dimensions (PFC3D) has been developed by ITASCA Consulting Group Inc. to model movement and interaction of stress in assemblies of rigid spheres. It is classified as a Discrete Element Code by Cundall et al. (1979a) since it allows finite displacement and rotations of discrete bodies.

PFC3D models the dynamic behaviour of assemblies of arbitrarily sized spherical particles. In this approach, each distinct particle displaces independently and interacts with others only at contacts. PFC3D uses the so called 'soft contact approach' whereby the particles are assumed to be rigid but they are allowed to overlap each other at the contact points and the magnitude of the overlap is related to the content force via the force-displacement law. The particle can deform locally at contact points whose behaviour is controlled

by the contact force calculated based on the overlapping magnitude and contact stiffness in the normal and shear directions. The PFC3D model refers to spherical particles as 'balls' and boundaries as 'walls'. Walls allow confinement and compaction by applying a boundary velocity or stress via servo-control. The balls and walls interact with each other via the contact forces between them.

PFC3D allows particles to be bonded together at contact points such that, when pre-defined bond strength is reached, the bond is broken. This allows tensile forces to be developed between particles and includes the formation of micro-cracks in the modelling. Macroscopic behaviour can be modelled by treating a solid as an assembly of many small particles and stress and strain can be measured by averaging these quantities over a representative measurement volume. Typical parameters which need to be defined are the particle normal and shear stiffness and particle bond strengths, the particle coefficient of friction, and the wall coefficient of friction. The stiffness at a contact is calculated assuming that the stiffnesses of the two contacting particles act in series, and the coefficient of friction at a contact is assumed to be the lesser of the coefficients of friction of the contacting objects.

3.3.2 **Basic calculation cycle**

The PFC3D calculation cycle is illustrated in Figure 3.13. The calculation cycle is a time stepping algorithm that requires the repeated application of the law of motion to each particle, a force-displacement law to each contact, and a constant updating of wall positions. Contacts which can exist between two

balls or between a ball and a wall, are formed and broken automatically during the course of the simulations.
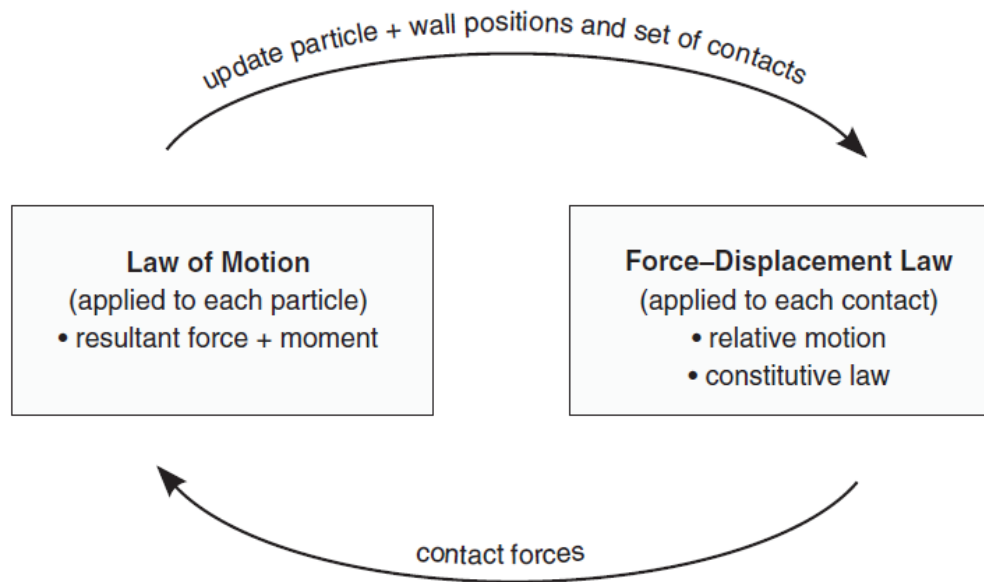
Figure 3.13 Calculation cycle in PFC3D (ITASCA, 2008b)

At the start of each time step, the set of contacts is updated from the known particle and wall positions. The force-displacement law is then applied to each contact to update the contact forces based on the relative motion between the two entities at the contact and the contact constitutive model. Next, the law of motion is applied to each particle to update its velocity and position based on the resultant force and moment arising from the contact forces and any body forces acting on the particle. The wall positions are updated based on the specified wall velocities as well. The calculation performed in each of the two boxes of Figure 3.13 can be done effectively in parallel (ITASCA, 2008b). The force-displacement law and the law of motion are described in the following subsections.

Chapter 3 Discrete element modelling

3.3.2.1   **Force-Displacement Law**

The force-displacement law which describes the contacts between both ball to ball and ball to wall is applied at the start of each cycle at contact to obtain update contact force. The contact force vector F_i is resolved into normal and shear components with respect to the contact plane.

$$F_i = F_i^n + F_i^s \qquad (3.2)$$

Where F_i^n and F_i^s denotes normal and shear components respectively. The normal contact force vector is given by:

$$F_i^n = K^n U^n n_i \qquad (3.3)$$

Where K^n is the normal stiffness [force/displacement], U^n is the overlapping magnitude of two contacting balls and n_i is the unit normal vector.

For ball to ball contact, the normal vector is directed along the line between two ball centres. For ball to wall contact, the normal vector is directed along the line defining the shortest distance between the ball centre and the wall.

It is important to point out that the normal contact stiffness is a secant modulus which relates total displacement and force while the shear contact stiffness is a tangent modulus which relates the incremental displacement and force. When the contact is formed, the shear force is initialised to be zero. Each subsequent relative shear displacement will cause an incremental shear force to be developed and added to its current value to form a new shear force for next cycle. The incremental shear force is calculated using:

$$\Delta F_i^s = -K^s V_i^s \Delta t \tag{3.4}$$

Where k^s is the shear stiffness at contact [force/displacement], V_i^s is the shear component of contact velocity and Δt is the time step. The shear force is then calculated by summing the shear force existing at the start of the time step and the incremental elastic shear force vector.

$$F_i^s = \left\{ F_i^S \right\}^{current} + \Delta F_i^s \tag{3.5}$$

The current shear force $\left\{ F_i^S \right\}^{current}$ is updated every time step and used in the following time step to calculate the acceleration using Newton's Second Law and then integrated to give velocity and displacement to achieve the updated position. This will be described in the following sub-section (ITASCA, 2008b).

3.3.2.2   Law of Motion

The motion of a rigid particle is determined by the resultant force and moment vector acting upon it, which is described in terms of translation motion and rotation motion of particles. The equation of motion is expressed as two vector quantities; one relates the resultant force to the translational motion and the other relates the resultant moment to the rotational motion of the particle. The equation for translational motion is written in vector form:

$$F_i = m\left(\ddot{x}_i - g_i \right) \tag{3.6}$$

where F_i is the resultant force: sum of all externally applied forces acting on the particle, m is the total mass of particle, $\ddot{x}_i$ is the acceleration of particle and g_i is the body force acceleration vector (e.g., gravity loading).

Chapter 3 Discrete element modelling

Also, the equation for rotational motion is given in the vector form as:

$$M_i = I\dot{\omega}_i = \left(\frac{2}{5}mR^2\right)\dot{\omega}_i \tag{3.7}$$

where M_i is the resultant moment acting on the particle, I is the moment of internal of the particle, $\dot{\omega}$ is the angular acceleration of particle and R is the radius of a spherical particle whose mass is distributed uniformly throughout its volume and the centre of the mass coincides with the sphere centre.

The equations of motion given by equations (3.6) and (3.7) are integrated using a centred finite difference procedure involving a time step of Δt. The quantities x_i (velocity), $\ddot{x}_i$, $\dot{\omega}_i$, F_i, and M_i are computed at the primary intervals of $(t \pm \Delta t)$ The translational and rotational accelerations at time t are calculated as

$$\ddot{x}_i^{(t)} = \frac{1}{\Delta t}\left(\dot{x}_i^{(t+\Delta t/2)} - \dot{x}_i^{(t-\Delta t/2)}\right) \tag{3.8}$$

$$\dot{\omega}_i^{(t)} = \frac{1}{\Delta t}\left(\omega_i^{(t+\Delta t/2)} - \omega_i^{(t-\Delta t/2)}\right) \tag{3.9}$$

The translational and rotational velocities at time $(t+\Delta t/2)$ can be solved by inserting equation (3.8) and (3.9) into equation (3.6) and (3.7). Hence,

$$\dot{x}_i^{(t+\Delta t/2)} = \dot{x}_i^{(t-\Delta t/2)} + \left(\frac{F_i^{(t)}}{m} + g_i\right)\Delta t \tag{3.10}$$

$$\omega_i^{(t+\Delta t/2)} = \omega_i^{(t-\Delta t/2)} + \left(\frac{M_i^{(t)}}{I}\right)\Delta t \tag{3.11}$$

Then, the position of particle centre is updated by integrating velocities in equation (3.10) and (3.11) giving

$$x_i^{(t+\Delta t)} = x_i^{(t)} + \dot{x}_i^{(t+\Delta t)}\Delta t \qquad (3.12)$$

The calculation cycle for the law of motion can be summarized as follows. Given the values of $\dot{x}_i^{(t-\Delta t/2)}$, $\omega_i^{(t-\Delta t/2)}$, $\dot{x}_i^{(t)}$, $F_i^{(t)}$, equation (3.10) and (3.11) are used to obtain $\dot{x}_i^{(t+\Delta t/2)}$, $\omega_i^{(t+\Delta t/2)}$. Then, equation (3.12) is used to obtain $x_i^{(t+\Delta t)}$. The values of $F_i^{(t+\Delta t)}$ and $M_i^{(t+\Delta t)}$, to be used in the next cycle, are obtained by application of the force-displacement law (ITASCA, 2008b).

3.3.3 **Mechanical time step**

The PFC3D time-stepping algorithm assumes that velocities and accelerations are constant within each time step. Therefore, the time step chosen in the PFC3D calculation cycle must be small enough so that the disturbance cannot propagate from any particle further that its immediate neighbours during a single time step. The computed solution produced by Equations (3.10),(3.11) and (3.12) will remain stable if the time step does not exceed a critical value. PFC3D has the ability to estimate the critical time step at the start of each calculation cycle and then the actual time step is treated as a fraction of this estimated critical value.

The estimation of the critical time step is determined firstly by considering a one dimensional mass spring system described by point mass (m) and spring stiffness (k). The critical time step is given by Bathe et al. (1976)

$$t_{crit} = \frac{T}{\pi} \qquad (3.13)$$

$$T = 2\pi\sqrt{m/k} \qquad (3.14)$$

where T is the period of the system. Now, consider the infinite series of point masses and spring in Figure 3.14 which illustrates the contacts in the system. When the masses are moving synchronized opposing motion, there is no motion at the centre systems. The motion of a single point mass can be described by the two equivalent systems shown in Figure 3.14b and Figure 3.14c. Therefore, the critical time step in this system is found by using equations (3.13) and (3.14) to be:

$$t_{crit} = 2\sqrt{\frac{m}{4k}} = \sqrt{m/k} \qquad (3.15)$$
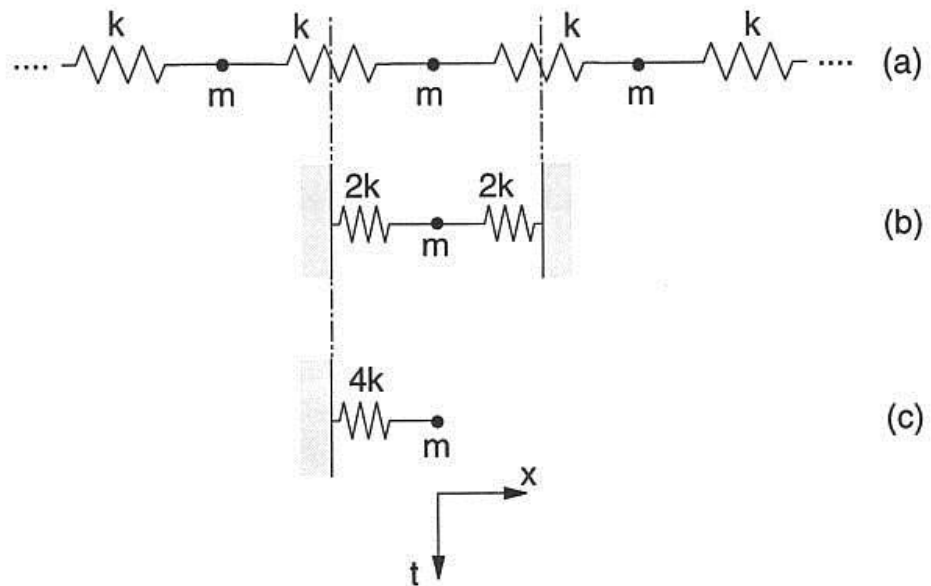
Figure 3.14 Multiple mass spring system (ITASCA, 2008b)

3.3.4 **Elastic contact model**

The elastic contact models for two contacting entities (either ball to wall or ball to ball) subjected to loading in normal and/or shear direction are described in this section. The contact stiffness relates the contact force and relative displacement in the normal and shear directions by the Force-Displacement Law described in section 3.3.2. The normal contact stiffness (secant stiffness) is given in equation (3.16) and the shear stiffness (tangent stiffness) is given in equation (3.17). The contact stiffnesses for the contact model are calculated assuming that the stiffness of two contacting entities act in series giving:

$$K^n = \frac{k_n^{[A]} k_n^{[B]}}{k_n^{[A]} + k_n^{[B]}} \qquad (3.16)$$

$$K^s = \frac{k_s^{[A]} k_s^{[B]}}{k_s^{[A]} + k_s^{[B]}} \qquad (3.17)$$

where superscript [A] and [B] denote the two entities in contact. The parameters of normal stiffness (K_n) and shear stiffness (K_S) of two contacting entities are specified in PFC3D, the contact stiffnesses of two contacting entities are then computed using equation (3.16) and (3.17). This contact stiffness is multiplied by the magnitude of the overlap to obtain the contact force (ITASCA, 2008b).

3.3.5 **Contact bond and slip model**

The contact bond can be envisaged as a pair of elastic springs with constant normal and shear stiffness joining the particles. The contact-bond glue is of a

vanishingly small size that acts only at the contact point and it can only transmit a force. It has been defined that the particles bonded together with a contact bond cannot slip but they can roll over each other. Figure 3.15 shows the rolling between two balls with a contact bond. It can be seen from this figure that two identical balls (A and B) are joined together by a single contact bond. Ball A has rotated about ball B (fixed) without slipping and bond breakages. The contact bond will remain between ball A and ball B when ball A moves to a new position.

The contact bonds have a specified strength in both normal and shear directions. In the normal direction, contact bonds allow tensile forces to develop at contact when the overlapping magnitude between a pair of contacting balls is less than zero. The balls are bonded with normal tensile forces are limited by the normal contact bond strength. If the magnitude of the tensile normal contact force equals or exceeds the normal contact bond strength, the bond breaks and both normal and shear contact forces are set to zero.

In the shear direction, if the magnitude of the shear contact force is equal to or exceeds the shear contact bond strength, the bond breaks but the contact forces are not altered providing the shear force does not exceed the friction limit. A coefficient of friction is set so that the slip model will be activated when the bond breaks; the shear force is resisted if it does not exceed the friction limit (ITASCA, 2008b).
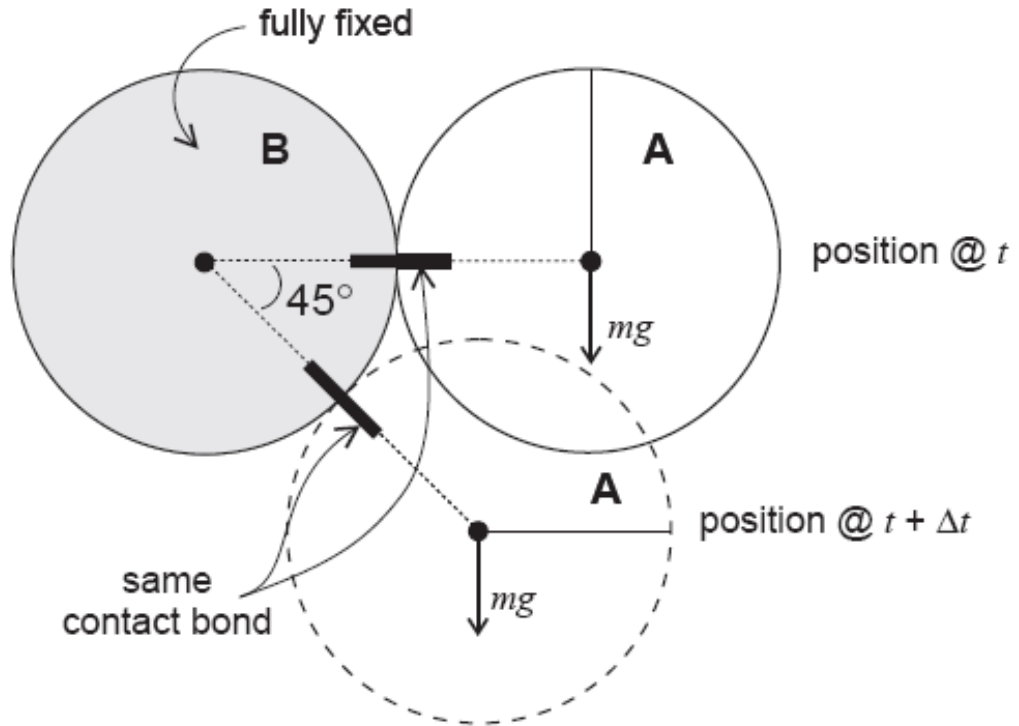
Figure 3.15 Rolling at contact bond (ITASCA, 2008c)

3.3.6 **Parallel bond and moment resistance**

Parallel bond can be envisaged as a set of elastic springs with constant normal and shear stiffnesses, uniformly distributed over a circular disk lying on the contact plane and centred at the contact point; it can transmit both forces and moments between particles. Parallel bonds act in parallel with the slip or contact model described above. The total force and moment acting at each contact where a parallel bond is installed is comprised of a force, F_i, arising from particle to particle overlap, and a force and moment, $\bar{F}_i$ and $\bar{M}_i$, carried by the parallel bond (see Figure 3.16). The constitutive behaviour of each particle to particle contact is described in section 3.3.2. The force and moment carried by a parallel bond can be resolved into normal and shear components with respected to contact plane as

Chapter 3 Discrete element modelling

$$\bar{F}_i = \bar{F}^n n_i + \bar{F}^s t_i \tag{3.18}$$

$$\bar{M}_i = \bar{M}^n n_i + \bar{M}^s t_i \tag{3.19}$$

where $\bar{F}^n$, $\bar{F}^s$ and $\bar{M}^n$, $\bar{M}^s$ denote the axial and shear directed forces and moments, respectively. n_i and t_i are the unit vectors that define the contact plane. These vectors are shown in Figure 3.16. When the bond is formed, $\bar{F}_i$ and $\bar{M}_i$ are initialized to zero. Each subsequent relative displacement and rotational increment at the contact results in an increment of elastic force and moment that is added to the current values. The elastic force increments occurring over a time step of Δt are given as

$$\Delta \bar{F}_i^n = \left(-\bar{k}^n A \Delta U^n \right) n_i \tag{3.20}$$

$$\Delta \bar{F}_i^s = -\bar{k}^s A \Delta U_i^s \tag{3.21}$$

with $\Delta U_i = V_i \Delta t$ and the elastic moment increments are given by

$$\Delta \bar{M}_i^n = \left(-\bar{k}^s J \Delta \theta^n \right) n_i \tag{3.22}$$

$$\Delta \bar{M}_i^s = -\bar{k}^n I \Delta \theta_i^s \tag{3.23}$$

with $\Delta \theta_i = \left(\omega_i^{[B]} - \omega_i^{[A]} \right) \Delta t$ where the contact V_i is the contact velocity, $A = \pi \bar{R}^2$ is the area of the bond disk, $J = \dfrac{1}{2} \pi \bar{R}^4$ is the polar moment of inertia of the disk cross section and $I = \dfrac{1}{2} \pi \bar{R}^4$ is the moment of inertia of the disk cross section about an axis through the contact point and in the direction of $\Delta \theta_i^s$.
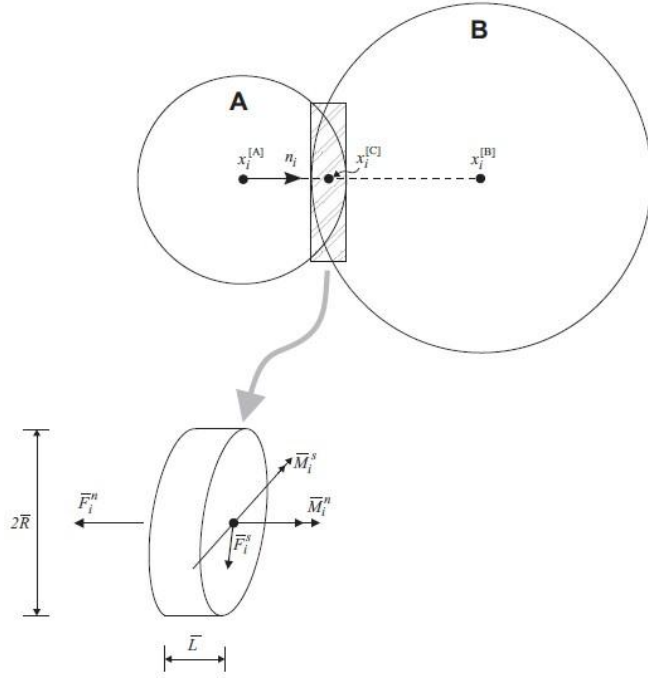
Figure 3.16 Parallel bond (ITASCA, 2008b)

The new force and moment vectors associated with the parallel bond are calculated by summing the old values existing at the start of the time step with the elastic force and moment increment vectors. It should be noted that this needs to be done after shear component vectors have been rotated to account for the motion of the contact plane. The maximum tensile and shear stresses acting on the bond periphery are calculated to be

$$\sigma_{max} = \frac{-\bar{F}^n}{A} + \frac{\left|\bar{M}_i^{\,s}\right|}{I}\bar{R} \tag{3.24}$$

$$\tau_{max} = \frac{\left|\bar{F}_i^{\,s}\right|}{A} + \frac{\left|\bar{M}^{\,n}\right|}{J}\bar{R} \tag{3.25}$$

If the maximum tensile stress exceeds the normal strength, or the maximum shear stress exceeds the shear strength then the parallel bond breaks. Potyondy et al. (2004) developed the bonded particle model for rock (BPM) based on the

parallel bond. They simulated various tests with different micro parameters and proved that the BPM is capable of representing all of the significant behaviour mechanisms in rock.

In real asphalt, there would be rolling and torsional resistance at contacts, as well as in tension and shear. The contact bond can only offer resistance in tension and shear and no resistance to rolling or spinning, which is physically unreasonable. Hence, in this study, for elastic simulations (Chapter 6), the parallel bond has been implemented. For the visco-elastic simulations (Chapter 7), the time-dependent visco-elastic contact bond is used to describe tension, compression and shear. Because it is not possible to allocate time-dependent properties to a parallel bond, a "virtual" parallel bond will be designed for torsional and rolling resistance, in parallel with the time-dependent contact bond, and this is described in Chapter 7.

3.3.7 **Burger's viscoelastic model**

Chang et al. (1997) conducted several simulations where they have used Maxwell, Kelvin and Burger's models (Figure 2.7) to the represented asphalt cement. The Burger's linear viscoelastic model was shown to be the most promising model for modelling bitumen behaviour, based on mechanical response and comparisons with physical experimental results. A Burger's contact model is a user defined contact model implemented in PFC3D to simulate the time dependent behaviour of a material. This contact model is written in C++. The Burger's model is represented in Figure 3.17. This model contains a Kelvin element and Maxwell element connected in series and can be used in both normal and shear directions together at a contact point. The model

Chapter 3 Discrete element modelling

has the following properties: K_k^n, normal stiffness for Kelvin element; C_k^n, normal viscosity for Kelvin element; K_m^n, normal stiffness for Maxwell element; C_m^n, normal viscosity for Maxwell element; K_k^s, shear stiffness for Kelvin element; C_k^s, shear viscosity for Kelvin element; K_m^s, shear stiffness for Maxwell element; C_m^s, shear viscosity for Maxwell element; f_s, friction coefficient.

The total displacement of a Burger's model u (sum of the displacement of the Kelvin element and the Maxwell element) and its first derivative are given by

$$u = u_k + u_{mk} + u_{mc} \tag{3.26}$$

$$\dot{u} = \dot{u}_k + \dot{u}_{mk} + \dot{u}_{mc} \tag{3.27}$$

where u_k is the displacement of the viscoelastic component in the Kelvin element, u_{mk} is the displacement of the elastic component in the Maxwell element and u_{mc} is the displacement of the viscoelastic component in the Maxwell element. The contact force using stiffness (K_k) and viscosity (C_k) of the Kelvin element is given by

$$f = K_k u_k + C_k \dot{u}_k \tag{3.28}$$

the contact forces using stiffness (K_m) and viscosity (C_m) of the Maxwell element are given by

$$f = K_m u_{mk} \tag{3.29}$$

$$\dot{f} = K_m \dot{u}_{mk} \tag{3.30}$$

81

Chapter 3 Discrete element modelling

$$f = C_m \dot{u}_{mc} \tag{3.31}$$

From equation (3.28) the velocity of the Kelvin element is given by

$$\dot{u}_k = \frac{-K_k u_k + f}{C_k} \tag{3.32}$$
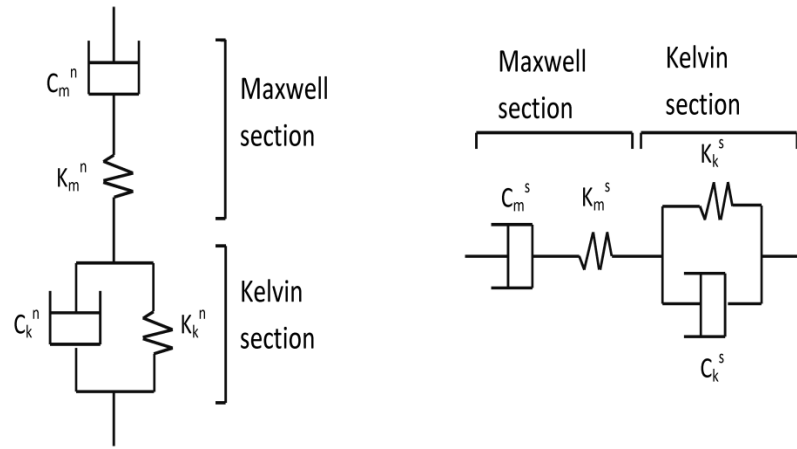
Figure 3.17 Burger's model

Using a central difference approximation of the finite difference scheme for the time derivative and taking average values for u_k and f gives

$$\frac{u_k^{t+1} - u_k^t}{\Delta t} = \frac{1}{C_k} \left[-\frac{K_k(u_k^{t+1} + u_k^t)}{2} + \frac{f^{t+1} + f^t}{2} \right] \tag{3.33}$$

therefore

$$u_k^{t+1} = \frac{1}{A} \left[B u_k^t + \frac{\Delta t}{2C_k} \left(f^{t+1} + f^t \right) \right] \tag{3.34}$$

where

$$A = 1 + \frac{K_k \Delta t}{2C_k} \tag{3.35}$$

$$B = 1 - \frac{K_k \Delta t}{2C_k} \tag{3.36}$$

For the Maxwell element, the displacement and velocity are given by:

$$u_m = u_{mk} + u_{mc} \tag{3.37}$$

$$\dot{u}_m = \dot{u}_{mk} + \dot{u}_{mc} \tag{3.38}$$

Substituting equation (3.30) and (3.31) into (3.37) and (3.38) gives

$$\dot{u}_m = \frac{\dot{f}}{K_m} + \frac{f}{C_m} \tag{3.39}$$

Using central difference approximation of the finite difference scheme and taking the average value for f gives:

$$\frac{u_m^{t+1} - u_m^t}{\Delta t} = \frac{f^{t+1} - f^t}{K_m \Delta t} + \frac{f^{t+1} + f^t}{2C_m} \tag{3.40}$$

therefore

$$u_m^{t+1} = \frac{f^{t+1} - f^t}{K_m} + \frac{\Delta t \left(f^{t+1} + f^t \right)}{2C_m} + u_m^t \tag{3.41}$$

The total displacement and velocity of the Burger's model are given by

$$u = u_k + u_m \tag{3.42}$$

$$\dot{u} = \dot{u}_k + \dot{u}_m \tag{3.43}$$

Chapter 3 Discrete element modelling

Using finite difference scheme for time derivative gives

$$u^{t+1} - u^t = u_k^{t+1} - u_k^t + u_m^{t+1} - u_m^t \qquad (3.44)$$

substituting equation (3.34) and (3.41) into (3.44), the contact force, f^{t+1} , is given by

$$f^{t+1} = \frac{1}{C}\left[u^{t+1} - u^t + \left(1 - \frac{B}{A}\right)u_k^t - Df^t \right] \qquad (3.45)$$

where

$$C = \frac{\Delta t}{2C_k A} + \frac{1}{K_m} + \frac{\Delta t}{2C_m} \qquad (3.46)$$

$$D = \frac{\Delta t}{2C_k A} - \frac{1}{K_m} + \frac{\Delta t}{2C_m} \qquad (3.47)$$

In conclusion, the contact force f^{t+1} can be calculated from known values for u^{t+1}, u^t, u_k^t and f^t. Verification of the Burger's contact model in PFC3D was performed by ITASCA (2008b).

3.3.8 **Servo-control mechanism**

There are some simulations that require stress-control throughout the test (e.g. the constant creep test). The implemented servo-control mechanism is a function that is integrated in PFC3D to maintain a constant stress (axial and confining) throughout the simulation. This function is called on in every calculation cycle to determine the current wall stresses and it then adjusts the wall velocities in such a way as to reduce the difference between measured

stress and required stress. The calculation algorithm for the servo-control mechanism is given by

$$\dot{u}^{(w)} = G\left(\sigma^{measured} - \sigma^{required}\right) = G\Delta\sigma \tag{3.48}$$

where G is the 'gain' parameter estimated using the following reasoning. The maximum increment in wall force arising from wall movement in one time step is given by

$$\Delta F^{(w)} = k_n^{(w)} N_c \dot{u}^{(w)} \Delta t \tag{3.49}$$

where N_c is the number of contacts on the wall and k_n is the average stiffness of these contacts. Hence the change in mean wall stress is given by

$$\Delta\sigma^{(w)} = \frac{k_n^{(w)} N_c \dot{u}^{(w)} \Delta t}{A} \tag{3.50}$$

where A is the wall area. For stability reasons, the change in wall stress must be less than the difference between the measured and required wall stress. To fulfil the stability requirement, a relaxation factor α is introduced such that

$$\left|\Delta\alpha^{(w)}\right| < \alpha\left|\Delta\alpha\right| \tag{3.51}$$

Substituting equation (3.48) and (3.50) into equation (3.51) gives

$$\frac{k_n^{(w)} N_c G\Delta\sigma\Delta t}{A} < \alpha\left|\Delta\alpha\right| \tag{3.52}$$

$$G = \frac{\alpha A}{k_n^{(w)} N_c \Delta t} \tag{3.53}$$

Then, substituting G into equation (3.48) for adjusting the wall velocity to achieve the required wall stress in numerical servo-control (ITASCA, 2008c).

3.3.9 **Micro-properties**

For a cubic array of spheres (in which each sphere has six neighbours), consider an unconfined test to measure Young's modulus. The increment in axial stress, $\Delta\sigma_a$ is related to the increment in axial force, ΔF_a ,as follows

$$\Delta\sigma_a = \Delta F_a / (2R)^2 \tag{3.54}$$

where R is the radius of all spheres.

The increment in strain, $\Delta\varepsilon_a$ is related to the relative normal displacement between two adjacent particles, Δu ,

$$\Delta\varepsilon_a = \Delta u / 2R \tag{3.55}$$

This displacement gives rise to a normal force, recalling that the apparent normal stiffness is the series combination of k_n for both particles:

$$\Delta F_a = \left(\frac{1}{2}k_n\right)\Delta u = \left(\frac{1}{2}k_n\right)(2R\Delta\varepsilon_a) = k_n R\Delta\varepsilon_a \tag{3.56}$$

Substituting from equation (3.54)

$$\frac{\Delta\sigma_a}{\Delta\varepsilon_a} = \bar{\bar{E}} = \frac{k_n}{4R} \tag{3.57}$$

This equation gives the apparent Young's modulus, $\bar{\bar{E}}$, of the cubic assembly in terms of the input normal stiffness, k_n , and the particle radii. Equation (3.57)

is exact only for cubic arrays, but it is a useful first estimate for the Young's modulus of a non-uniform array of particles (ITASCA, 2008c).

Potyondy et al. (2004) suggested that the normal and shear stiffness of the binder are assigned as

$$\bar{k}^s = \frac{\bar{\bar{E}}_c}{R^{(A)} + R^{(B)}} \tag{3.58}$$

$$\bar{k}^n = \frac{\bar{k}^s}{\left(\bar{k}^s / \bar{k}^n\right)} \tag{3.59}$$

where $\bar{\bar{E}}_c$ is the Young's modulus of the binder, $R^{(A)}$ and $R^{(B)}$ is radii of the two particles in contact. The units of parallel bond stiffness in equations (3.58) and (3.59) are Pa/m, so the real parallel bond normal stiffness is given by:

$$K = \bar{k}^n * PI * [\lambda * MIN(R^A, R^B)]^2 \tag{3.60}$$

where $MIN(R^A, R^B)$ is the minimum radius of the two balls, λ is known as the radius multiplier.

3.4 **User defined contact model**

User defined contact constitutive models can be added to PFC3D by writing the model in C++, compiling it as a Dynamic Link Library (DLL) file and loading the DLL into PFC3D whenever needed. Once the model is installed, PFC3D can refer to the specific model names in commands, and the model and associated properties can be manipulated. The source code of contact models used in PFC3D include a header file (modelname.H) which provides the class specification for the model and a source file which contains listings of the

member functions for the model (modelname.CPP). The header and source files are then used to create a DLL by using Microsoft VC++ Verson 7.1. More details about the base class, member functions, registration of models and information passed between the model and PFC3D can be found in ITASCA (2008a). An example of how to implement a DLL model is also provided.

3.5 **Summary**

DEM has been widely used in modelling the behaviour of granular material, whilst a number of programming codes have been developed since the 1970's. Recent developments in the the(Collop et al., 2007)ory and in computer technology have allowed the further investigation of asphalt behaviour from microscopic specimens using DEM. PFC3D is popular among researchers in the field of the DEM.

Over the past two decades, the discrete element method has been used to simulate the microstructure of asphalt mixtures by many researchers. Three main methods were used: a highly idealized method (Collop et al., 2006), a randomly created polyhedron method (Liu et al., 2009a), an image based method (Adhikari et al., 2008a).

In the highly idealized method, the mechanical behaviour of idealized asphalt mixture is modelled. Therefore the grading of aggregate is not considered. Also, the contact bond used to bond the particles cannot provide moment resistance and stop the particles from rolling or spinning. However, this is a necessary step for further development in discrete element modelling of real asphalt

mixtures with more realistic contact models and will be studied in this dissertation.

The randomly created polyhedron method has proved to be time consuming due to the large number of particles involved. This can be avoided in this dissertation using a model specimen which provides realistic time-dependent behaviour at contacts.

The image based method is laboratory dependent; expensive laboratory equipment is needed and well trained technicians are required, this is not required in this study.

The basic calculation algorithms were described in section 3.3. The calculation cycle in PFC3D is a time-stepping algorithm involving the repeated application of the law of motion and force displacement law. The mechanical time-step determination and elastic contact model were also introduced. Both contact bond and parallel bond models were introduced. The parallel bond will be used in the elastic simulations in this project due to the ability to transmit moment and force. The Burger's contact model will be used to give time dependent behaviour. The servo-control mechanism will be introduced to simulate the uniaxial creep test in this project. Finally, the determination of the micro-properties was examed. In conclusion, PFC3D is a very powerful DEM programming code available to model asphalt materials.

4 Numerical specimen preparation procedure

4.1 Introduction

A numerical specimen preparation procedure has been developed to prepare cylindrical specimens with graded particles. The specimens produced need to be initially isotropic with low residual stresses and dense packing. As mentioned in section 2.2.3, the stone mastic asphalt is a dense gap-graded asphaltic mixture with high content of coarse aggregate (>70%) and a binder rich mortar (filler and bitumen). The blue line in Figure 4.1 shows the standard mean grading of 0-10 mm SMA (BS EN 13108-5:2006). It can be seen that, the aggregate sizes in the mixture are ranges from as small as 0.063mm to as large as 14mm, and fines occupy about 18% by mass. Aggregates with less than 2mm diameter are defined as fines. They play a very important role in both micro and macro mechanical behaviour of asphalt mixtures. In DEM, the aggregates are simulated as spheres with required radii, while the binder is not simulated with visible discrete elements but normal and shear contact stiffnesses. Due to the limitation of computer processing capability, it is very difficult in discrete element modelling to model all aggregates. According to Simpson et al. (2008), DEM analyses to date have been limited to about 10^5 particles. In order to save computational time in modelling, new stone mastic asphalt was re-produced by removing aggregates which could pass a sieve size of 2mm. The new asphalt mixture comprised coarse aggregate (size bigger than

Chapter 4 Numerical specimen preparation procedure

2mm), filler, binder and air. The grading curve of the aggregate for this mixture is shown by the red line in Figure 4.1. This new grading curve has been used for the preparation of both laboratory and numerical specimens.

This chapter presents the procedures to produce an initially isotropic numerical specimen to mimic the test specimen in the laboratory, the measurement methods for strains, porosity and number of contacts and the numerical servo-control used in simulating the uniaxial constant creep test by adjusting the wall velocity to reduce the difference between measured requested stresses.
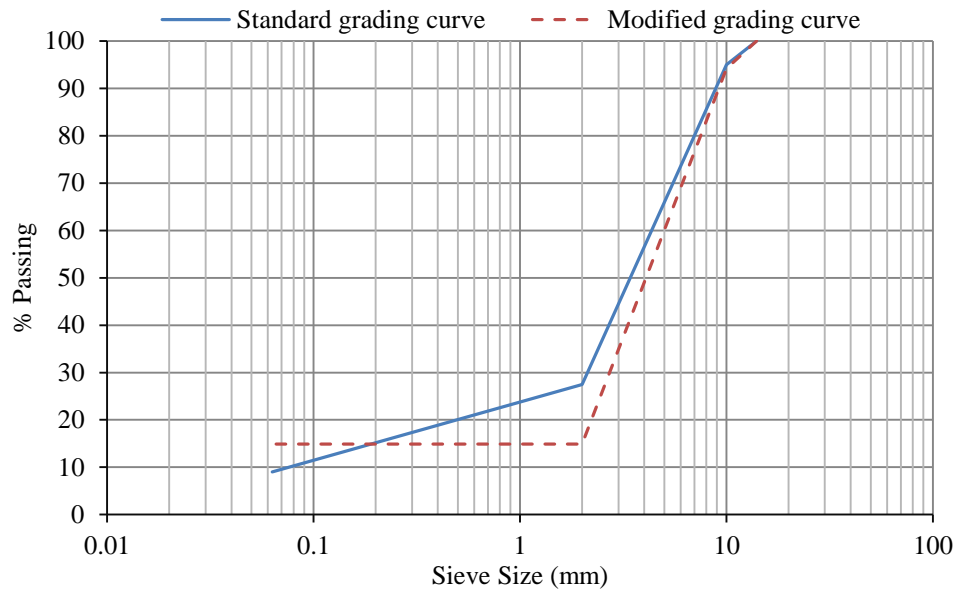
Figure 4.1 Grading curves (the modified grading curve will be used for both experimental and numerical specimens)

4.2 **Review of the packing characteristic of spheres**

There are two important issues regarding the packing characteristic of the numerical specimen. Firstly, the specimen needs to be initially stress free and isotropic, secondly, the specimen need to be densely packed. Lee (2006) and

Wu (2009) had shown that the packing density (percentage by volume of solids) of 0.63 give a dense random packing for the single-size particles specimen. The asphalt mixture used in this research comprises different sizes of aggregates mixed with bitumen and filler. The packing density should be higher than the single-sized particle specimen as particle sizes are variable and smaller particles can fit into the void spaces between the larger particles. The following procedures have been developed to generate an isotropic numerical specimen to simulate the uniaxial compression tests.

4.3   Numerical specimen preparation

4.3.1 Boundary and particle generation

To generate a numerical specimen, a set of confining boundaries are needed to constrain the assembly and restrict the movement of particles across the boundaries. The wall in PFC3D acts as boundary constraint for the assembly and restricts the movement of particles. It has arbitrarily defined contact properties for interaction with particles. Contact forces between particles and walls are calculated via the force displacement law, as for particle-particle contacts (see section 3.3.2.1). For the simulation of uniaxial compression, the top and bottom walls are used to simulate the loading platens. And a cylindrical wall shown in Figure 4.2 is used to confine the specimen during preparation and is removed before loading.
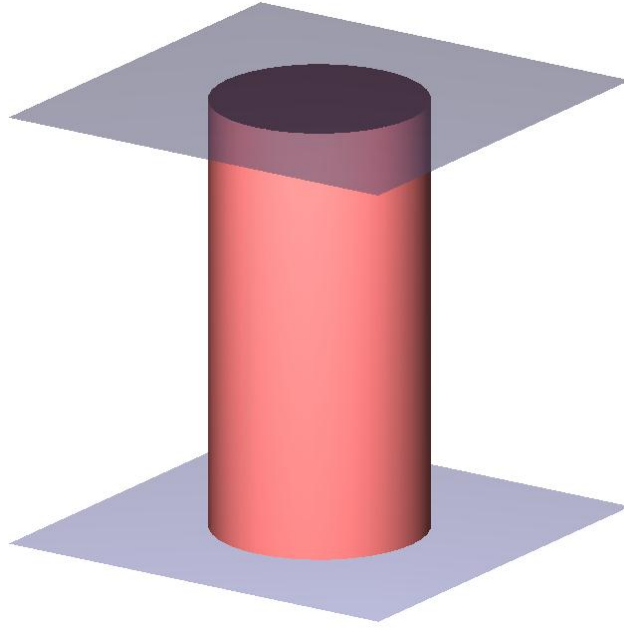
Figure 4.2 Boundaries in PFC3D

The other fundamental geometric entity for the Discrete Element Model is the particle. These are generated after the walls. The desired number of particles for each diameter is based on the mixture design of asphalt mixture and grading of aggregate. It is given by

$$N = \frac{3 \times PV(p_{n+1} - p_n)}{4\pi(\frac{r_{n+1} + r_n}{2})^3} \tag{4.1}$$

where range of particles radii is divided into n sub-ranges with lower and upper limits of r_n and r_{n+1} respectively; N is the number of particle (with radius of $(r_{n+1} + r_n)/2$) to be generated, P is the volume percentage of aggregate particles in asphalt mixture, V is the total volume of the asphalt mixtures, p_{n+1} and p_n is the percentage passing (by volume) of the aggregate through sieve size $2r_{n+1}$ and $2r_n$, respectively.

Particles are generated with random centroid coordinates to give an irregular packing type with no discernible pattern in the arrangement of particles. Particles are first generated with a small radius such that no two particles overlap. The particle radii are then increased gradually to the target value. The initially generated radius r is calculated by

$$r = \frac{R}{m^n} \qquad (4.2)$$

where R is the target (real) particle radius. The particle radius is increased by a factor of m each time and up to n times. During the process, particles are allowed to re-arrange until the residual stress within the specimen is approximately isotropic. It should be noted that during cycling the wall and particle friction coefficients are set to zero temporarily to facilitate the re-arrangement process.

4.3.2 Isotropic equilibrium state

The numerical specimen generated from the above procedures has a high level of isotropic stress (about 10MPa) due to the large amount of overlap at contact points between particles. However, the numerical specimen must be initially isotropic and essentially free from internal stresses before being used to simulate the uniaxial compression test. ITASCA (2008b) suggested that the initial isotropic stress should be less than 1% of the uniaxial compressive strength (peak stress obtained from experimental data). This can be achieved by slightly reducing the radii by 1-2 % of the radius values for all particles until the isotropic stress is less than the pre-set value which is determined from

the experimental data (1% of peak stress). By doing this, the magnitude of overlap between particles decreases leading to a reduction in contact forces in the specimen. The particles are also allowed to re-arrange each time after decreasing the radii.

A uniformly distributed contact force is shown in Figure 4.3. Each cylindrical pipe represents the compressive force and the radius of each cylinder corresponds to the magnitude of contact force generated.
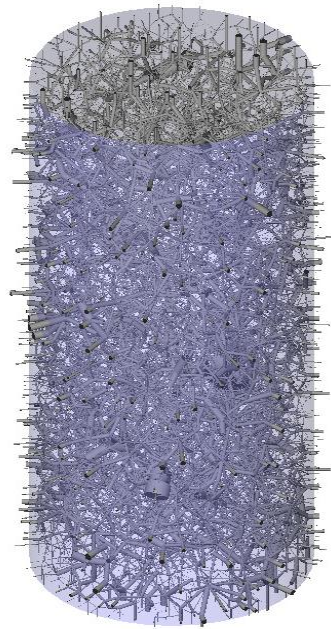
Figure 4.3 Contact force

4.3.3 **Preparation of bonded particles**

Potyondy et al. (2004) successfully used parallel bonds to simulate the cement behaviour. The bitumen in this simulation is also represented by the bond model in PFC3D but not simulated with a visible discrete element. In PFC3D bonds are installed at existing contacts and between all proximate balls (those that are within a distance d of one another where d is equal to 10^{-6} times the

mean radius of the two balls). A sufficient coordination number is very important in using agglomerates to simulate crushable particles in the DEM, reported by Lim et al. (2007). Typically, there are about 10-15% of particles with less than four contacts in the specimen at this stage. Figure 4.4 shows the particles with less than four contacts in the specimen produced by the above method.
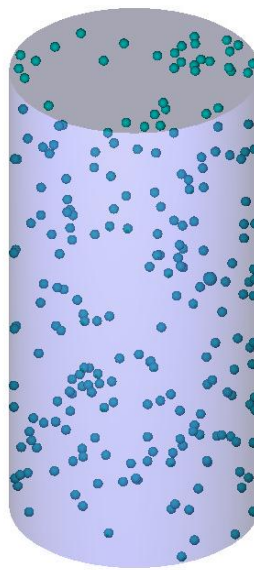
Figure 4.4 Particles with less than four contacts inside a typical numerical specimen

Rothenburg et al. (1992) suggested that a particle assembly needs at least four contacts per particle on average to carry the load. Collop et al. (2004) also showed that a minimum of 4 contacts per particle on average is needed to model the internal contact structure of a sand asphalt mixture. To create a specimen with a good contact bond network, the following processes have been developed

- Fix the positions of all the particles and set their velocities to zero

- Scan all the particles in the specimen to detect those with less than four contacts

- Release those particles (one by one); each released particle is taken in turn and expanded in increments of 0.1% to create additional contacts with neighbouring particles until four contacts are obtained, this particle is allowed to re-arrange to reach equilibrium each time after increase the radius, then the next released particle follows the same procedure.

By following the above procedures, a dense randomly packed specimen with low isotropic internal stresses and a minimum of four contacts per particle is generated. Figure 4.5 shows a typical specimen. The specimen is 120 mm in height and 30 mm in radius and contains 6000 particles; the average number of contacts per particle for the specimen is 5.5 and particles occupy 70% of the total volume (same as laboratory specimens – Chapter 5); the coloured particles represent different sizes of particles. The particles are then bonded and used to simulate the uniaxial compression test. Figure 4.6 shows the specimen particles bonded by parallel bonds (light blue represents the parallel bond).
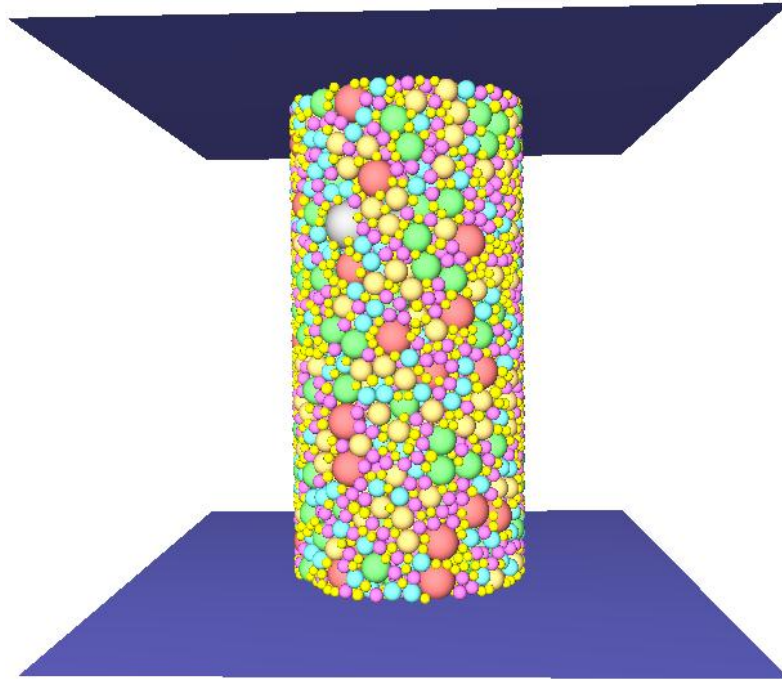
Figure 4.5 A specimen of aggregate
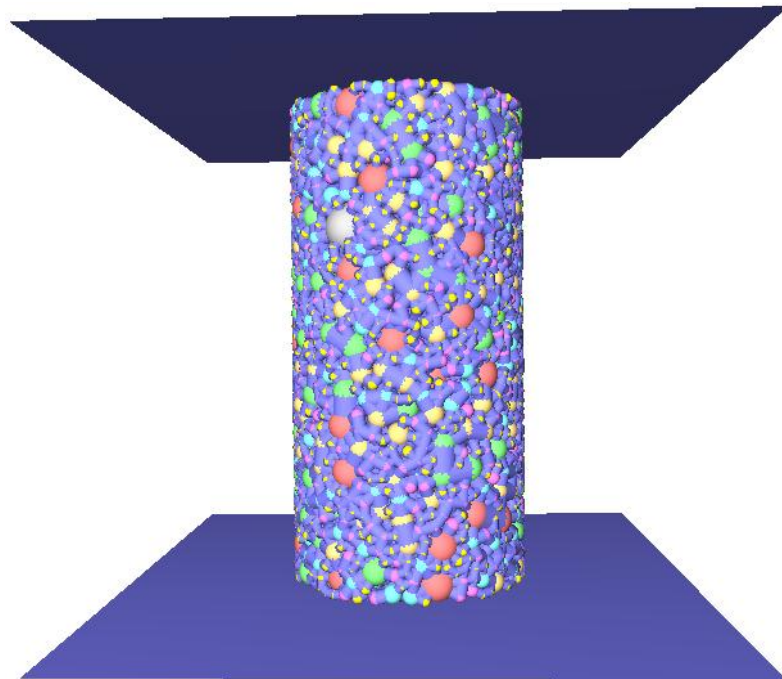
Figure 4.6 A specimen of bonded particles

4.3.4 **Preparation of uniaxial simulations**

To simulate the uniaxial compression test, the top and bottom walls used are as the loading platens (bottom wall fixed) while the lateral wall is removed to give zero confinement to the specimen. The lateral wall can be used as confining wall in a triaxial test. The bonded specimen prepared using the above procedures is at a lower isotropic internal stress; therefore, the removal of the lateral wall will result in unloading which leads to a self-equilibrating set of compressive and tensile unbalanced forces. However, the unbalanced forces are usually less than 0.01% of the average force in the specimen at peak strength. Hence, the locked in forces can be considered as negligible. To reduce the unbalanced force due to particle radius enlargement as well as the removal of the lateral wall, the bonded specimen can be allowed to reach a steady state before uniaxial compression by the 'solve' command in PFC3D. During the uniaxial compression simulations, the bottom wall is fixed whilst the top wall acts as the loading platen.

4.4 **Method of measurement**

4.4.1 **Measurement Sphere**

A measurement sphere is defined as a specified measurement volume in PFC3D and is capable of measuring properties such as the coordination number, porosity, stresses and strain rates. This specified 3D volume of space is usually a sphere, so is referred to as a "measurement sphere". A measurement sphere with a specified radius can be installed at any point within a specimen.

Chapter 4 Numerical specimen preparation procedure

The porosity of a numerical specimen means the air void content of the specified volume of space. It is defined as the ratio of total void volume within the measurement sphere to measurement sphere volume.

$$n = \frac{V_{void}}{V_{sphere}} = \frac{V_{sphere} - V_{ball}}{V_{sphere}} = 1 - \frac{V_{ball}}{V_{sphere}} \qquad (4.3)$$

where V_{sphere} is the volume of the measurement sphere, V_{void} is the volume of void within the measurement sphere and V_{ball} is the volume of the measurement sphere occupied by balls and is defined by

$$V_{ball} = \sum_{N_p} (V_p) - V_{overlap} \qquad (4.4)$$

where N_p is the number of balls that intersect the measurement sphere and $V_{overlap}$ is the volume of overlapping particles contained within the measurement sphere.

According to equation (4.4), the measurement sphere accounts for the volume of particles overlapping, therefore, it can be concluded that the measurement sphere is able to measure the porosity of a synthetic material in a numerical simulation with great accuracy. This measurement method will be used in the later simulations to measure the porosity of the numerical specimen.

The Coordination Number C_n is defined as the average number of contacts per particle. It can also be measured from the measurement sphere. The coordination number will be calculated for particles with their centroids contained within the measurement sphere, using

$$C_n = \frac{\sum\limits_{N_b} n_c^{(b)}}{N_b}$$

(4.5)

where N_b is the number of particles with centroids contained within the measurement sphere and $n_c^{(b)}$ is the number of contacts between balls. In this project two measure spheres (see Figure 4.7) were used to measure the porosity of the specimen s as 30%.
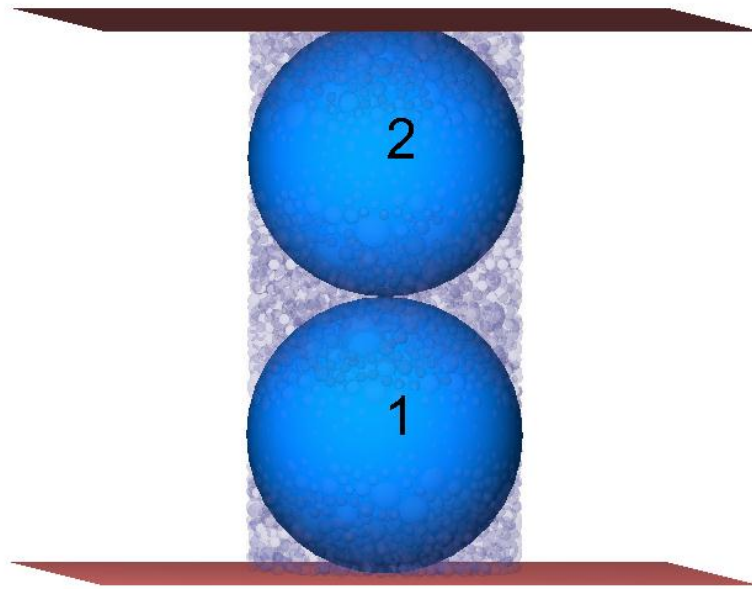
Figure 4.7 Specimen with measurement spheres

4.4.2 **Measurement of Axial Stress and axial and radial Strain**

The axial stress, axial strain and radial strain were recorded during the simulation. The axial stress was calculated from the contact forces between the particles in contact with the loading platens divided by the area. It should be

mentioned that in order to compare with laboratory results, a constant platen area has been used, to calculate the nominal stress. The original coordinates of the top and bottom loading platens are recorded in computer memory prior to testing. The platen coordinates are then updated regularly during the simulation. The axial strain of the specimen is calculated based on the relative change in position of the loading platens before and after simulation. It should be noted that the extent of overlapping (under compression) of the wall and adjacent balls is relatively small compared to the axial displacement of the specimen and hence it is negligible. Radial strain can be calculated as the average radial strain for all the particles on the circumference of the specimen. This can be achieved by:

- Detect particles which are in contact with the lateral wall (before being deleted) and record their distance to the axis of the cylinder; the average distance is recorded as the initial radius

- During the simulation, constantly detect the distance of those particles to the axis of the cylinder; the average distance is taken as the new radius.

In addition, the bond breaking time, position and pattern (normal or shear breaks) can be detected and recorded in PFC3D during the simulation (ITASCA, 2008b).

4.5 Modified servo control

During the creep test simulation, a constant load is applied to the specimen. This can be achieved by servo control in PFC3D. The default servo control

method (section 3.3.8) is applied for elastic material only. For viscoelastic material, equation (3.49) does not apply. For each particle contacting with loading plates, the wall to particle force arising from wall movement in one time step can be obtained from equation (3.45) (see section 3.3.7) and is given by

$$\Delta F_i = \frac{1}{C}[\dot{u}_i^{(w)}\Delta t + (1-\frac{B}{A})u_{k_i}^t - (D+C)f_i^t]\qquad(4.6)$$

The wall force arising from wall movement can be added from all the particles contacting with the loading platen

$$\Delta F = \frac{1}{C}[N\dot{u}^{(w)}\Delta t + (1-\frac{B}{A})\sum_{i=1}^{N}u_{k_i}^t - (D+C)\sum_{i=1}^{N}f_i^t]\qquad(4.7)$$

where N is the number of particles contacting with the wall. The change in mean wall stress is then given by

$$\Delta\sigma^{(w)} = \frac{1}{ZC}[N\dot{u}^{(w)}\Delta t + (1-\frac{B}{A})\sum_{i=1}^{N}u_{k_i}^t - (D+C)\sum_{i=1}^{N}f_i^t]\qquad(4.8)$$

where Z is the wall area. Substituting equation (3.48) and equation (4.8) into equation (3.51), the gain can be determined by

$$G = \frac{ZA\alpha|\Delta\sigma| - (1-\frac{B}{A})\sum_{i=1}^{N}u_{k_i}^t - (D+C)\sum_{i=1}^{N}f_i^t}{N\Delta\sigma\Delta t}\qquad(4.9)$$

where $\Delta\sigma$, $\sum_{i=1}^{N}u_{k_i}^t$ and $\sum_{i=1}^{N}f_i^t$ can be recorded easily in PFC3D by using user define contact model. Then, substituting G into equation (3.48) for adjusting the wall velocity to achieve the required wall stress in numerical servo-control.

4.6 **Summary**

This chapter presents the numerical specimen preparation procedures to produce an isotropic numerical specimen to mimic the test specimen in the laboratory. The produced numerical specimens satisfy the following requirements:

- The particle grading curve is the same as laboratory specimen (the modified grading curve in Figure 4.1).

- The specimen has dense and random packing with a volume fraction of solids equal to 70% which is approximately the same packing characteristics as a realistic mixture.

- Initially isotropic and approximately stress free.

- A minimum of four contacts per particles to carry the load.

The specimen is then ready to be bonded and used to simulate the laboratory tests. For a uniaxial compression simulation, the cylindrical boundary of the specimen is removed to give zero confinement to the specimen. Using DEM, the interaction of material components, such as particle displacements and rotations, can be monitored during the simulation. The porosity is measured by using two measurement spheres positioned one above another.

The axial strain is measured from the relative displacement of the loading platens. Radial strain is measured based on the displacement of particles on the circumference of the specimen. Axial stress is calculated from the contact forces between the particles in contact with the loading platens divided by the area. The numerical servo-control is used in simulating the uniaxial creep test by adjusting the wall velocity to reduce the difference between measured and

requested stresses. A constant speed is applied to the top wall to simulate the uniaxial constant strain rate test.

5 Experimental work

5.1 Introduction

Asphalt mixture is a composite material comprising mineral aggregate, bitumen and air. The micromechanical behaviour of the asphalt mixture is still not well understood. Computer modelling has been proven to be a powerful and economic method to develop understanding of the constitutive relationships. Laboratory research can offer valuable information to explain the damage mechanism of asphalt mixture. This section presents the laboratory work involved in this project. The results are used to calibrate and compare results from computer modelling.

5.2 Asphalt mixture

5.2.1 Material selection

As introduced in Chapter 4, it is hard to model the fine particles in an asphalt mixture because of the limitation of computer processing ability. Hence, a modified Stone Mastic Asphalt is produced in this research. It has been mentioned in Section 2.2.3, that stone mastic asphalt includes more coarse aggregate and less fines compared to other mixtures. Also, it is important to prepare an artificial numerical specimen to replicate the asphalt mixture. The previous chapter presented the numerical specimen preparation procedures to produce cylindrical bonded specimen s which are initially isotropic and with low residual stresses and dense packing. Based on the numerical specimens

produced, the asphalt mixture used in the laboratory comprises aggregate with particles larger than 2mm in diameter, filler, bitumen and air. The target design aggregate grading for the new asphalt mixture is shown in Figure 4.1 (Red line). The aggregates were sieved out by using 10mm, 8mm, 6.3mm, 5mm, 4mm, 2.8mm and 2mm sieves from 10mm, 6mm granite and dust. The filler used in this project is limestone with simple grading (approximate 95% passing the 63um sieve). The bitumen used is 40/60 penetration grad bitumen with a softening point of 51 ℃. Several Schellenberg tests have been done to obtain the required binder content with different constituents of aggregate, bitumen and filler. The Schellenberg test describes a method for determining binder drainage of bituminous mixtures. It is applicable to asphalt materials that are not porous asphalt or for those porous asphalts incorporating fibers. It can be used either for determining the binder drainage for different binder contents, or with a single binder content, eliminating successive repetitions. It also enables the effects of varying fine aggregate types or including any anti-draining additive to be quantified.

The mixture design was determined as shown in Table 5.1. Both laboratory and numerical specimens were prepared based on the mixture design. The target air void content was set as 5 %. The maximum density was also measured in the laboratory as 2453 kg/m3. The maximum density of the mixture was used in calculating the bulk density of the mixtures required in the mixture design.

Constituent		Percentage (Mass)	Percentage (Volume)
Aggregate (mm)	10	5.5	70
	8	18.6	
	6.3	15.8	
	5	12.1	
	4	9.3	
	2.8	11.2	
	2	7.5	
Filler		14	12
Bitumen		6.0	13
Air voids		0	5

Table 5.1 Mixture design

5.2.2 **Specimen preparation**

The mixing of the aggregate, bitumen and filler is accomplished by the hot mix method and the procedures are similar to those outlined by the Asphalt Institute (BS EN 12697-35:2004). The mixing temperature is chosen to equal a bitumen viscosity of 170 ± 20 centistokes within a limited time in order to reduced mechanical degradation of aggregate. The mechanical behaviour of asphalt mixture largely depends on the mechanical behaviour of bitumen, the aggregate content and air voids (BS EN 12697-35:2004). To prepare a mixture for manufacturing a specimen, the required aggregate batches were sorted in accordance with the predetermined gradations, placed in a tray and heated in a thermostatically controlled oven within ± 5 ^{o}C of the pre-selected temperature range to remove moisture. At the same time, the bitumen was also heated within ± 5 ^{o}C of the required mixing temperature to reduce the viscosity. The aggregate and bitumen were then maintained at the required temperature for approximately four hours. Before mixing the aggregate and bitumen, the heated aggregate was placed in a preheated sun-and-planet mixer. A small hollow was

made in the aggregate into which the required mass of bitumen was added. The aggregate and the bitumen were then mixed for approximately two minutes.

Slabs were compacted by the Nottingham roller compactor; see Figure 5.1. The roller compactor consists of a roller wheel of 900 mm diameter, which is loaded vertically by a pneumatic actuator and a trolley which is powered by a horizontal actuator. The slab mould needs to be pre-heated and sprayed with a silicone lubricant to reduce adhesion between the mould and specimen. The slab mould is placed on the trolley; the mass of material to go to the mould for each slab was calculated to give the required density (based on the maximum density). When compacting, the trolley moves to and fro at a constant speed of travel. Simultaneously, the vertical roller sector compacts the mixture in the slab. After compaction, the slabs were left to cool before removal from the moulds. The end of the slabs were trimmed by using a masonry saw. The finished slabs had the dimensions of 305mm by 305 mm in plane with a thickness of 85 mm.

Figure 5.1 Laboratory roller compactor (Taherkhani, 2006)

Cylindrical specimens were used in the uniaxial compression tests. Harvey et al. (2000) suggested that test specimens compacted in the laboratory must have specimen dimensions of 4 to 6 times the maximum aggregate size to minimise boundary effects. To avoid confinement effects in the specimen due to the friction between specimen and loading platens, the aspect ratio (ratio of height to diameter) of the specimen is usually chosen to equal a value of 2 (Erkens et al., 2002a). When the aspect ratio is 2, it is assumed that there is no confinement in the middle third of the specimen and that part is under pure uniaxial compression. Therefore, reliable values of strain and stress can be obtained. As will be discussed in Section 6.3, the minimum specimen dimensions to give reasonably accurate estimates of bulk material properties in computer modelling are about 60mm in diameter and 120mm in height (6000 particles numerical specimens). Based on the conditions above and the

diameter of available coring drills in the laboratory, the dimension of the test specimen in the laboratory was determined as 70 mm in diameter and 140 mm high. The specimens were made by coring through the width of the slabs (using a wet diamond-tipped core drill) into three pieces of 70 mm by 305 mm cores, then two 70 mm by 140 mm specimens were cut from each core. An ideal specimen would have a uniform air void distribution. This is controlled by the compaction effort, method of compaction, viscosity of bitumen, aggregate gradation and aggregate. To prevent ageing and distortion at ambient temperatures, all the specimens were stored in a cold room with a temperature set at 5 ^{o}C. Six hours before the test, the temperature of the testing cabinet was brought to the desired value; the specimen to be tested was kept inside the temperature controlled cabinet before the start of the test.

5.3   Uniaxial compression test

5.3.1 Test equipment

The equipment used for the uniaxial tests undertaken in this project is shown in Figure 5.2. The cabinet mounted on INSTRON (a servo-hydraulic test apparatus) loading frame is temperature controllable with a -5 ^{o}C to 50 ^{o}C operating range. The equipment consists of a 100 kN servo hydraulic actuator with $\pm$ 50 mm movement, an axially mounted load cell, the specimen and its instrumentation. The loading frame is operated by a 'Rubicon' digital servo control system. An external pump supplies the hydraulic power for the equipment. A desktop computer is used for data acquisition.

Figure 5.2 Uniaxial tests equipment – INSTRON (Taherkhani, 2006)

5.3.2 **Test protocol**

For a uniaxial constant strain rate test, a monotonic compression displacement is applied to the specimen through the hydraulic actuator which passes through an opening in the underside of the temperature controlled cabinet. A Linear Variable Differential Transformer (LVDT) is connected to the actuator piston to monitor the movement of the crosshead stroke and provides a feedback signal for the control system. The control system then compares the signals with the required signal and the difference is fed to the servo-valve which reduces the difference by adjusting the oil flow to the actuator. The axially mounted load cell, monitors the load applied to the specimen and, is connected to the specimen through a ram passing through an opening through the roof of the temperature cabinet. For a uniaxial creep test, a constant load is quickly

applied to the specimen through movement of the hydraulic actuator. The load monitored by the load cell is transferred to the control system. The control system then compares this feedback signal with the required signal and the difference is fed to the servo-valve, which reduces the difference between the input and output signals by adjusting the oil flow.

In uniaxial compression tests, the axial and radial deformations were measured at pre-set intervals during testing by the axial and radial Linear Variable Differential Transformers (LVDTs) mounted on the specimen. LVDTs are inductive sensing devices that produce an AC output voltage proportional to the mechanical displacement of a small iron core. LVDTs have high resolution and can measure movements as small as a few millionths of a millimetre up to a few centimetres by suitable conditioning hardware and high resolution data acquisition.

The axial displacement of the specimen is measured using two ± 5 mm LVDTs diametrically opposite each other. They were fixed vertically on supporting arms and placed on the top platen, see Figure 5.3. The axial strain is then calculated from the average of these two measurements. A 90 mm diameter collar was made for measuring the radial deformation of the specimen. An ± 5 mm LVDT was mounted on the collar at the middle height of specimen; see Figure 5.3.
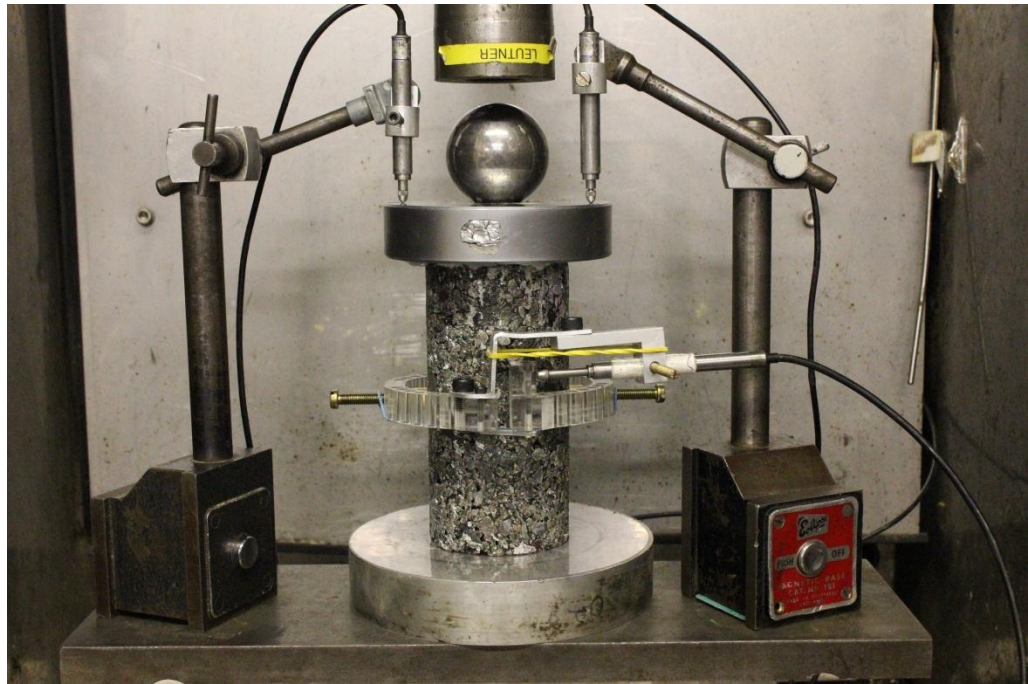
Figure 5.3 Uniaxial compression test setting up

Before setting up the LVDTs, calibration is very vital to ensure accurate results. To calibrate the LVDTs, a calibration caliper is used as shown in Figure 5.4 and Figure 5.5 for the calipers of LVDTs. At first, the caliper was set to just compress the LVDTs (reference position), then the LVDTs were compressed repeatedly at 0.25mm intervals. The output of the LVDTs is plotted against the displacement. This provides a linear relationship and is used to calibrate the testing data.
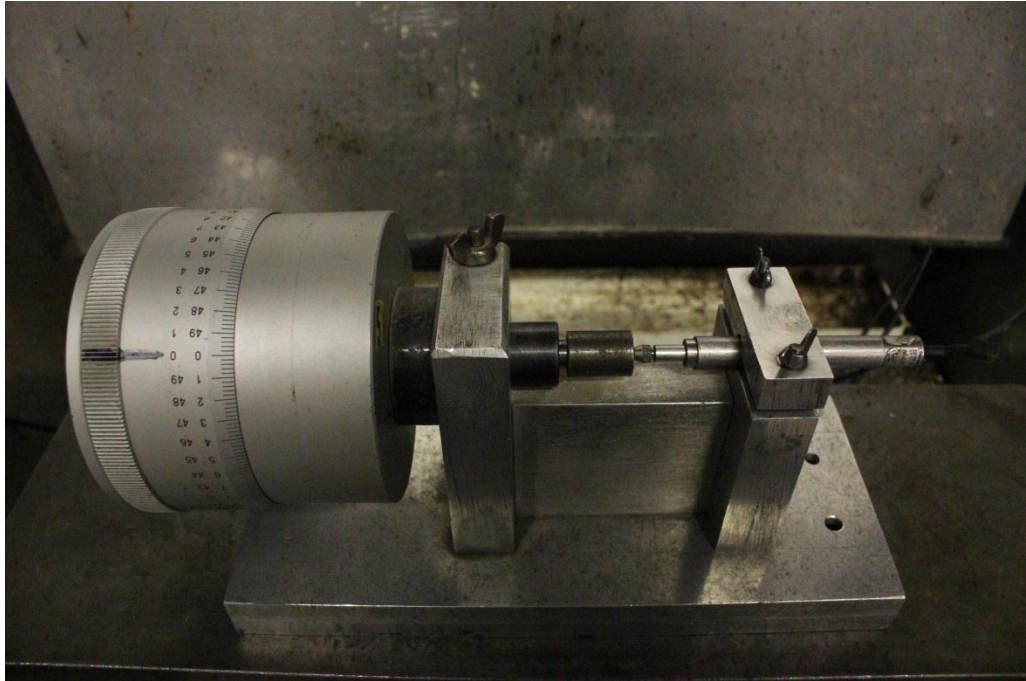
Figure 5.4 Caliper used to calibrate the LVDTs (axial strain)

Figure 5.5 Caliper used to calibrate the LVDTs (radial strain)

The influence of friction between the specimen and loading platens on compression test results is well documented (Erkens et al., 2002a). It is known that, by inducing large lateral forces, the platens confine the top and bottom of

the specimen, which restrains the radial deformation and results in a barrel shape deformation of the specimen. To minimise the confinement and achieve a uniform deformation in the specimen, the friction between specimen and the platens must be eliminated. This has been done by using a plastic film of silicone in combination with two thin layers of Vaseline, one between the foil and the loading platen, and one between the foil and the ends of the specimen. During some tests, sliding of the specimen was experienced. This was caused by using a specimen which had not been properly trimmed or in which the air void distribution across the diameter was not uniform, these results have been discarded.

5.4   Experimental results analysis

Using the equipment and instrumentation described above, uniaxial constant strain rate and creep tests were undertaken under the conditions listed in Table 5.2. The following subsection presents the results and analysis for constant strain rate and creep test respectively.

Test	Temperature	Loading
Constant strain rate	20 ^{o}C	0.005, 0.0005, 0.00005 (s^{-1})
Constant stress creep	20 ^{o}C	400, 500, 600, 1000 (kPa)

Table 5.2 Uniaxial compression test conditions

5.4.1 Constant strain rate

The axial stress against axial and radial strains for the three loading speeds at 20 ^{o}C for the modified stone mastic asphalt are plotted in Figure 5.6 and Figure

Chapter 5 Experimental work

5.7. From these figures, it can be seen that: the peak stress increases as the strain rate increases. In addition, an increase in Young's modulus can be observed with increase in the strain rate. The Young's modulus of the mixture is calculated from the axial stress and strain data which are taken at the beginning of the test (up to 0.5% axial strain). The axial strain level corresponding to the peak stress decreases with increasing strain rate.
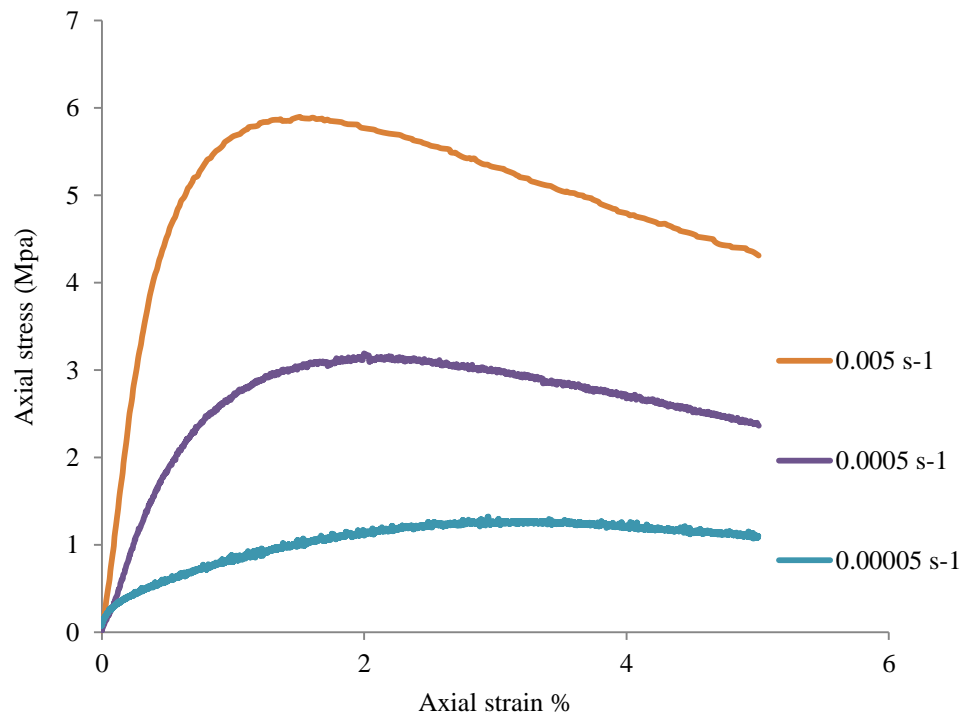
Figure 5.6 Axial stress versus axial strain of constant strain rate tests
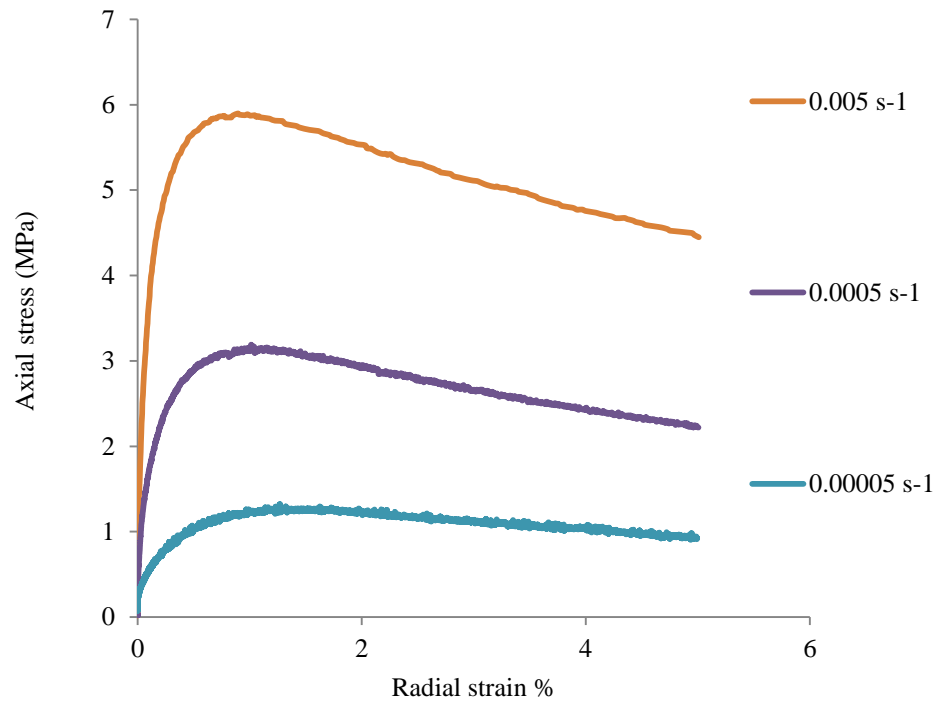
Figure 5.7 Axial stress versus radial strain of constant strain rate tests

The results for the constant strain rate of 0.005/s and 20 ^{o}C are shown in Figure 5.8. The axial stress is plotted against the axial and radial strains. As can be seen from both curves, the axial stress to axial and radial strain relationships are similar. It consists of hardening portion up to a peak stress which it is followed by a softening portion. As introduced in Section 2.6.2, the plot can be divided into four distinct regions: an initial linear region, an inelastic strain hardening region, the peak stress and the descending strain softening. The onset of dilation occurs when the magnitude of the radial strain (expansion) reaches half the axial strain in compression, based on equation (5.1)

$$\varepsilon_v = \varepsilon_a + 2\varepsilon_r \tag{5.1}$$

where ε_v is the volumetric strain; ε_a is axial strain and ε_r is radial strain.
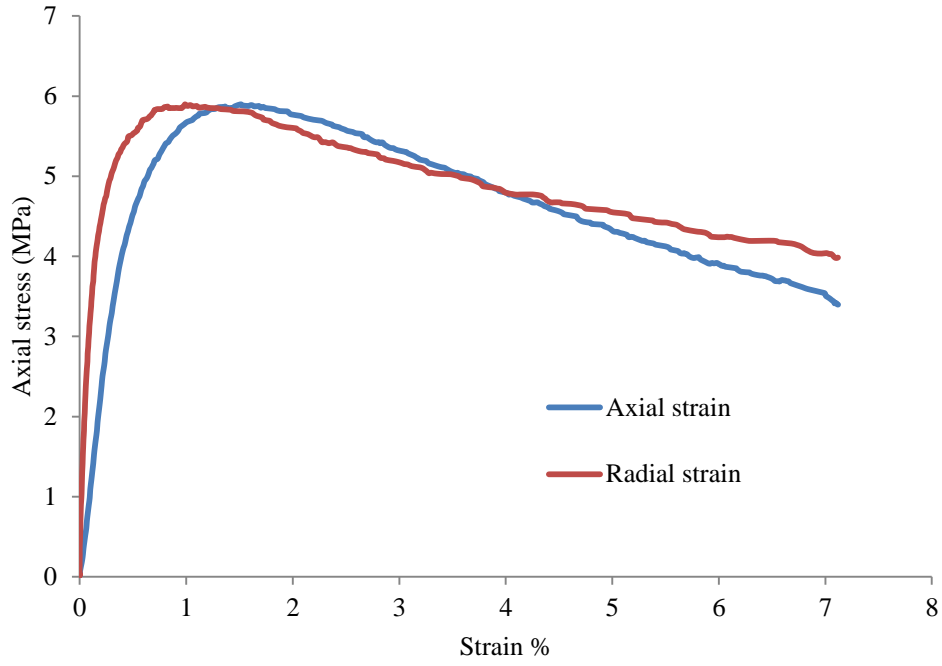
Figure 5.8 A typical strain rate result at 20 $^{\circ}$C

Figure 5.9, Figure 5.10 and Figure 5.11 summarise the axial strain at peak stress (ε), peak stress (σ) and initial stiffness ($\bar{\sigma}$) a function of strain rates on double logarithmic scales for different strain rates. It can be seen that the peak stress is approximately proportional to strain rate when plotted on double logarithmic scales with a gradient of approximately 0.325. This can be expressed by the Power Law relationship as

$$\left(\frac{\sigma}{\sigma_0}\right) = \left(\frac{\dot{\varepsilon}}{\dot{\varepsilon}_0}\right)^n \tag{5.2}$$

where $n = 0.325$, σ_0 is the reference stress (3.19 MPa at 20 $^{\circ}$C), $\dot{\varepsilon}_0$ is the reference strain rate (0.0005 s^{-1} at 20 $^{\circ}$C). The gradients of $q = 0.3874\,0.3874$ (equation (5.4)) and $m = -0.1447$ (equation (5.3)) are observed from Figure 5.11 and Figure 5.9, respectively.

119

Chapter 5 Experimental work

$$\left(\frac{\varepsilon}{\varepsilon_0}\right) = \left(\frac{\dot{\varepsilon}}{\dot{\varepsilon}_0}\right)^m \qquad (5.3)$$

$$\left(\frac{\bar{\sigma}}{\bar{\sigma}_0}\right) = \left(\frac{\dot{\varepsilon}}{\dot{\varepsilon}_0}\right)^q \qquad (5.4)$$

The gradients observed from Figure 5.10 will be used in the numerical viscosity simulations to scale the contact normal and shear bond strengths (Chapter 7).
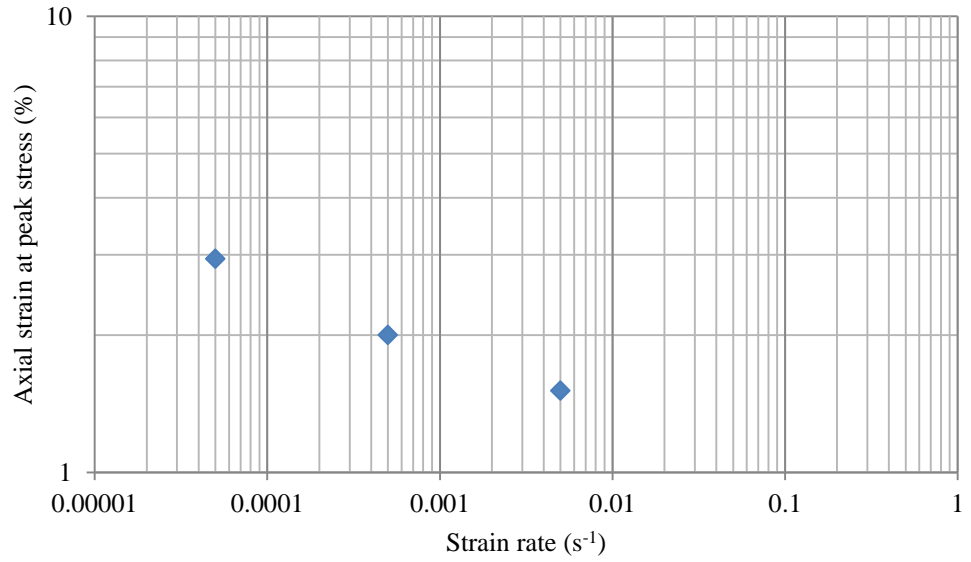
Figure 5.9 Axial strain at peak stress plotted against strain rate in a double logarithmic scale at 20 °C
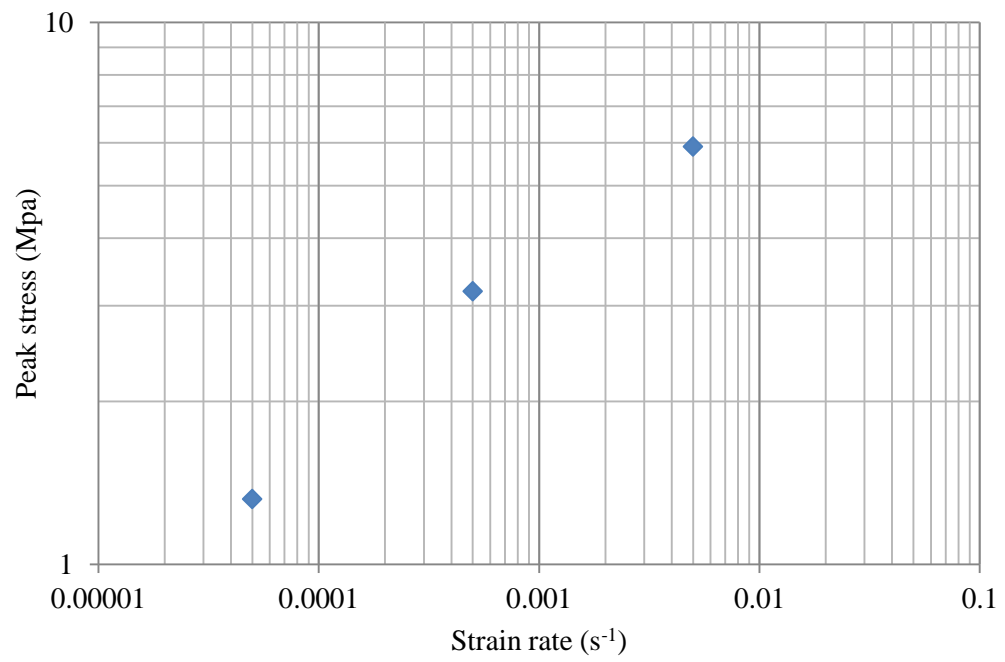
Figure 5.10 Peak stress plotted against strain rate in a double logarithmic scale at 20 ^{o}C
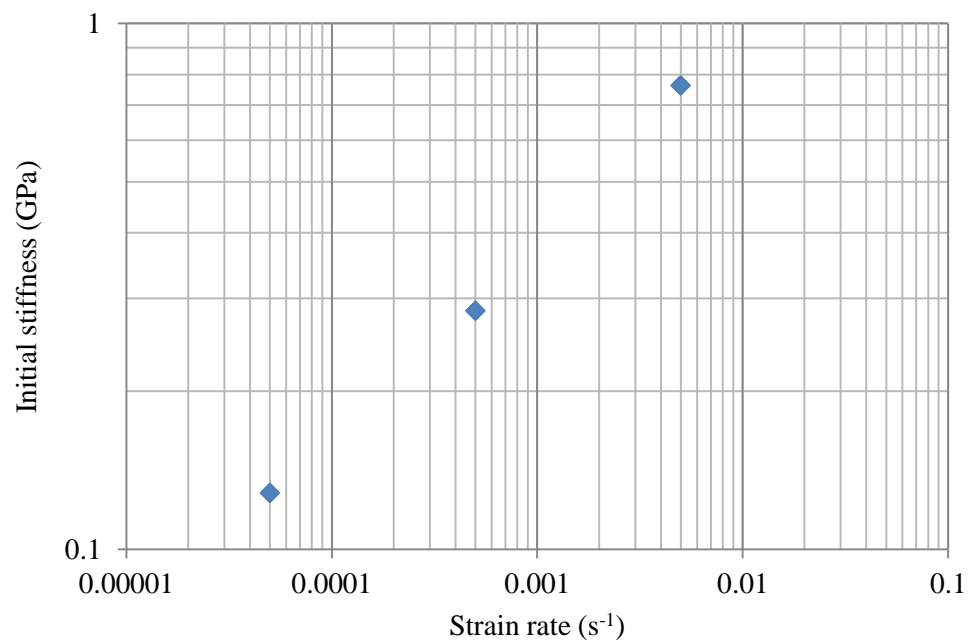
Figure 5.11 Initial stiffness plotted against strain rate in a double logarithmic scale at 20 ^{o}C

5.4.2 **Creep test**

The results of the uniaxial creep test at 400kPa, 500kPa, 600kPa and 1,000kPa for the modified stone mastic asphalt at 20°C are shown in Figure 5.12. The axial strain is plotted against the time elapsed following the application of the target load. As can be seen, the creep curve can be divided into three parts: a primary creep region where the strain rate decreases, a secondary creep region where the strain rate is almost constant, also known as steady-state strain rate and a tertiary creep region where the strain rate increases rapidly as the specimen approaches failures. At the same loading time, the axial strain increases as the stress level increases. The specimen tends to rupture earlier and quicker as the stress increases. The aggregates (granite) used for these specimens are from Mountsorrel quarry.
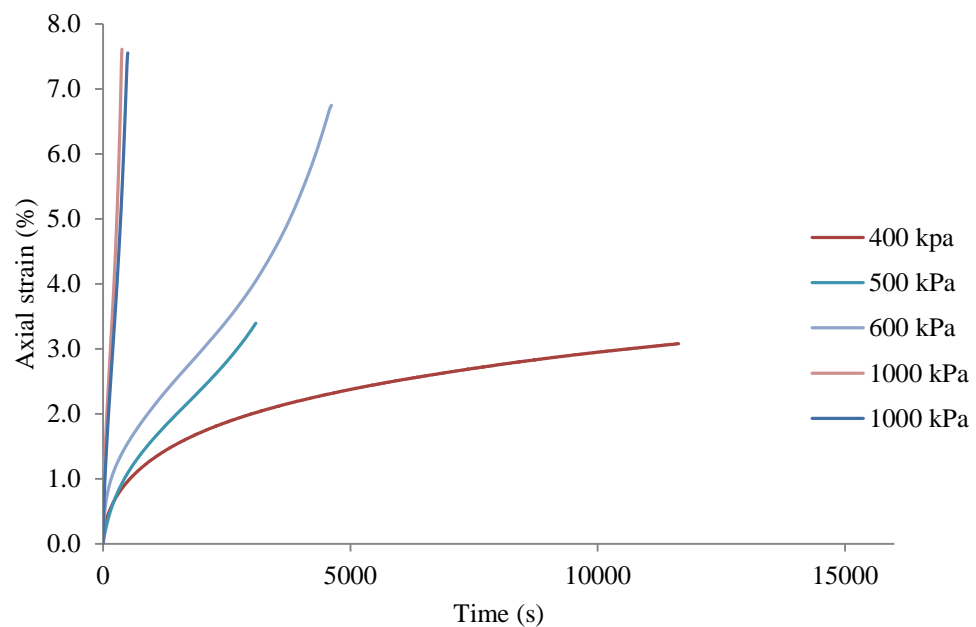
Figure 5.12 Results of creep tests

Two more creep tests were undertaken under 400kPa and 500kPa with aggregates from Bardon Hill quarry. The results are shown in Figure 5.13. As can be seen, even for the same material, different sources lead to large variability of the test results. In addition, the variability can also be caused by the variation of air void content in the slab. Figure 5.14 shows four of the specimens used in this project. As can be seen, in some places, it is porous, while in others, it is quite dense. This variability can be reduced by using a gyratory compactor to make the specimens, but, in this case, the specimens would need to be made one by one which would mean that more material would be wasted and takes longer to make the specimens. The new stone mastic asphalt only comprises aggregate larger than 2mm in diameter, filler and bitumen. The absence of the fines can also cause variations of in the sizes of the air voids. The shape of the particles is another factor giving rise to variability in the test results.
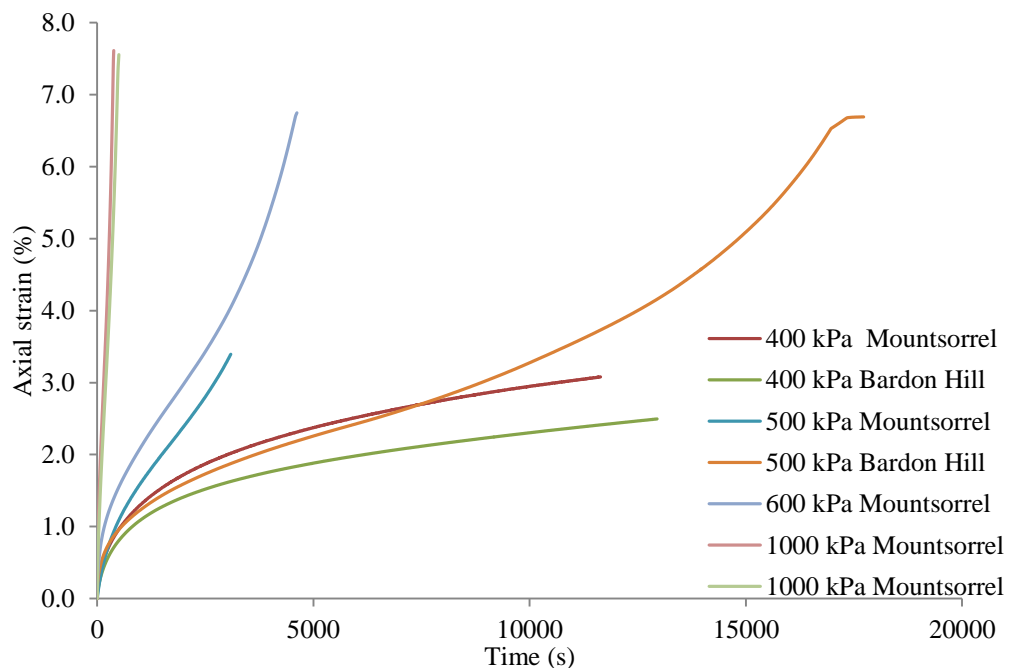
Figure 5.13 Results for creep tests for the specimens with different aggregate sources

Figure 5.14 Laboratory specimens

5.5 Summary

The chapter presents the laboratory tests undertaken in this project. The material selection and specimen preparation have been introduced. The new stone mastic asphalt which has a nominal minimum aggregate size of 2.0mm was produced. This was obtained by eliminating all the aggregate smaller than 2.0mm from the 1-10mm size stone mastic asphalt's gradation. The test equipment and test protocol were introduced afterwards.

A series of constant strain rate and creep tests were performed. The axial stress in the constant strain rate tests was shown to be dependent on the strain rate. The axial strain at peak stress and peak stress for constant strain rate tests is strain-rate dependent. The axial strain for the creep tests is dependent on the stress level. The rupture appears earlier as the stress level increases. These results are similar to those for bitumen and other types of asphalt mixtures that

were reviewed (see Section 2.6) and will be used for comparison with the simulation results.

The variability of test results can be caused by the sources of the aggregate; the way in which the specimen is made; the absence of fine aggregates and by the differences in the particle shapes.

6 Elastic modelling

6.1 Introduction

Bitumen is a viscoelastic material, the response of which depends on loading time and temperature. This chapter investigates the elastic response of bitumen. Elastic simulations are necessary for further develop of Discrete Element Model in asphalt mixtures. In the elastic modelling, the effect of bitumen is represented by a set of elastic springs with constant normal and shear stiffness and moment resistance using a "parallel bond" in PFC3D. Aggregate particles are represented as balls.

The following sections include an introduction to the properties selection and an example of an elastic simulation of a loading and unloading test. The chapter also investigates the effect of the number and positions of particles, loading speed, ratio of normal to shear contact stiffness and parallel bond radius on bulk properties.

6.2 Model properties and simulation

A parallel bond (Figure 3.16) is defined by the following five parameters: normal and shear stiffness, $\bar{k}_n$ and $\bar{k}_s$ (stress/displacement); normal and shear strength, σ and τ (stress); and bond disk radius, $\bar{R}$. The stiffness of balls and parallel bonds were calculated from equation (3.57) and (3.58), respectively. A specimen with 6000 particles was generated by using the specimen preparation procedures introduced in chapter 4. The numbers of particles were calculated

using equation (4.1) based on Figure 4.1 and Table 5.1. The Young's modulus of the particle and parallel bond were taken as 4.5GPa. The values were chosen arbitrarily so that a general trend for elastic simulations could be established. For simplicity, the ratio of normal to shear stiffness for particle and parallel bond are set equal to one. To simulate the behaviour of asphalt as a bonded material, the particle normal and shear bond strengths were taken to be large to avoid bond breakage during the simulation. To obtain fully elastic behaviour, the friction coefficient for each ball was set to zero, to give zero energy dissipation by sliding. The uniaxial constant strain rate compression tests were simulated by applying a velocity of 0.01m/s to the top platen, fixing the bottom platen and deleting the lateral platen. This velocity has been selected to ensure that the stresses on both the top and bottom walls are approximately the same. The specimen was loaded and simulation was stopped at an axial strain of 0.4%. No bond breakage was detected during the loading simulations. Figure 6.1 shows the axial stress versus axial strain. Figure 6.2 shows the radial strain versus axial strain. As can be seen, linear relationships are found. A Young's modulus of 6GPa and Poisson's ratio of 0.27 for the specimen can be determined from the gradients of the curves shown in Figure 6.1 and Figure 6.2.

The simulation was then continued with an unloading simulation by giving the top platen a velocity of -0.01 m/s and terminating when the top platen reached the initial height. The axial strain versus number of cycles for loading and unloading simulation is shown in Figure 6.3. As the plot shows, the loading curve is identical to the unloading curve, and all the strains are recovered, and hence are elastic.

Chapter 6 Elastic modelling

Several parameters are involved in the elastic simulation. It is important to understand how each parameter affects the simulation results. The following subsections provide more simulation results with various parameter combinations to offer guidance on further parameter determination.
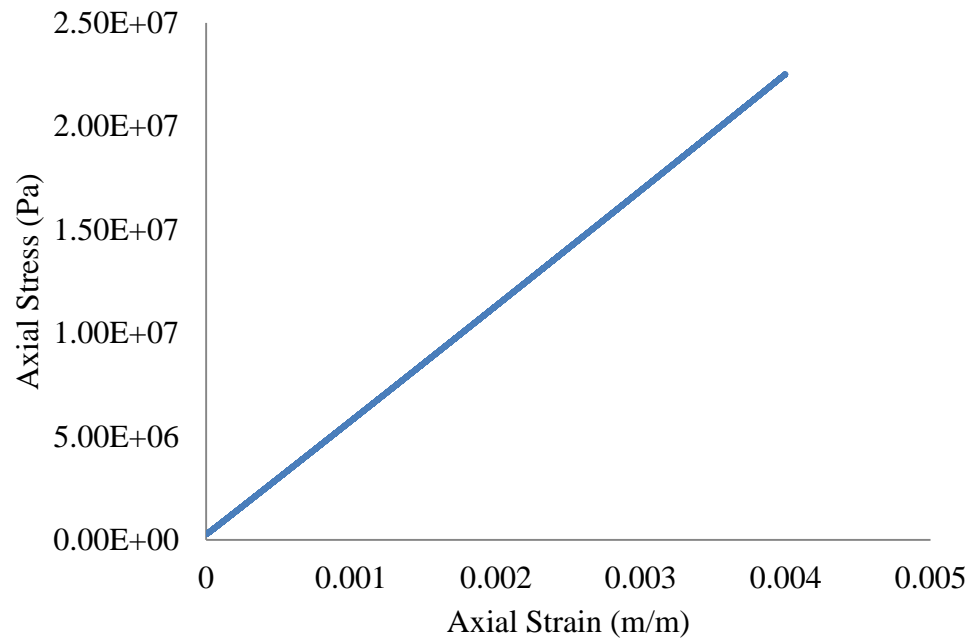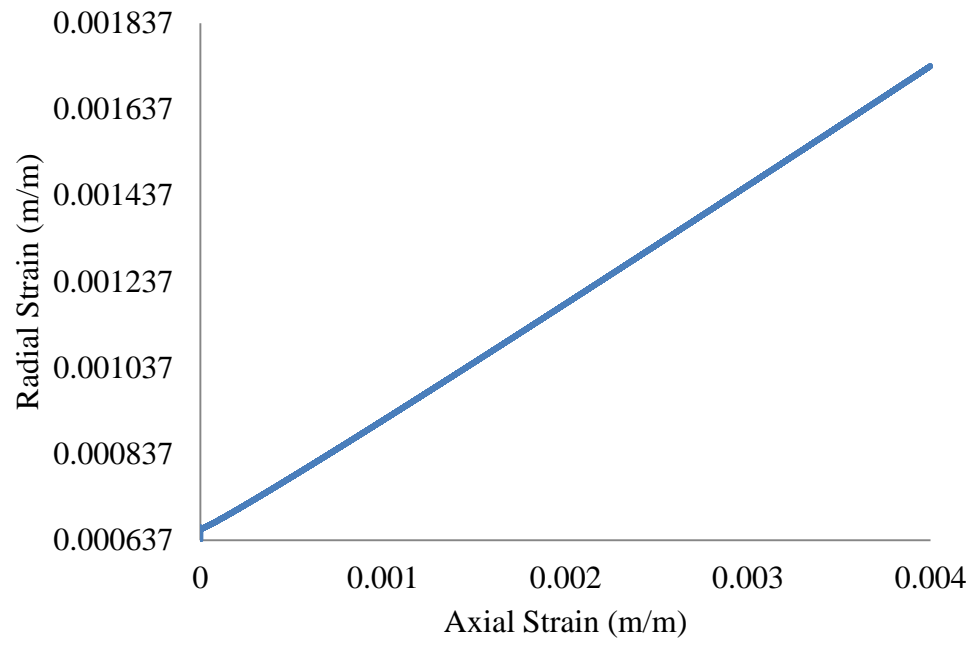

Figure 6.1 Axial stress versus axial strain

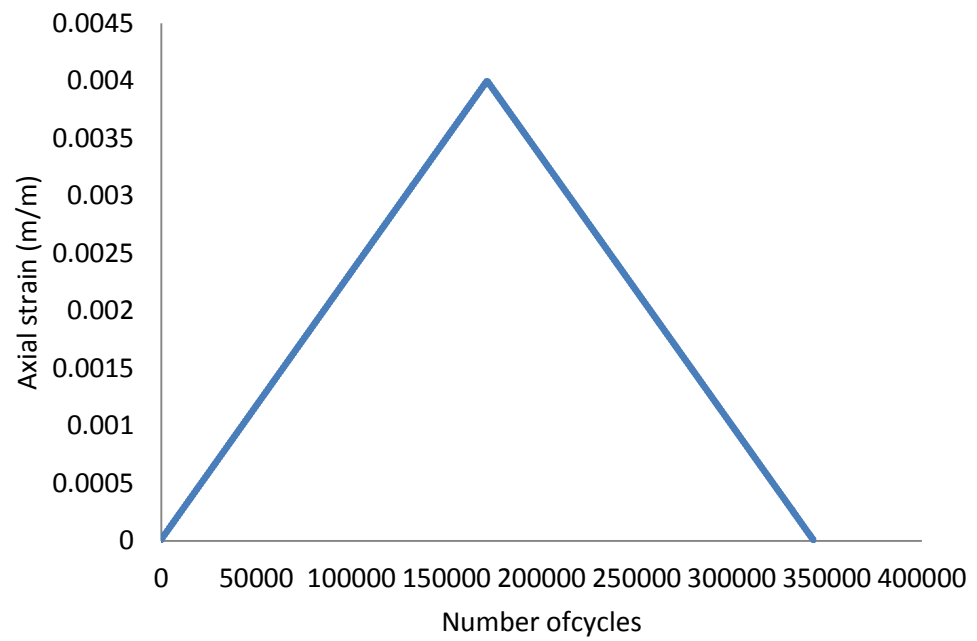Figure 6.2 Radial strain versus axial strain

Figure 6.3 Axial strain verses time step for the loading and unloading simulation

6.3   Effect of number and position of particles

The main purpose of examining the effect of the number of particles was to choose a specimen size which is large enough to fully represent the behaviour of the material but small enough to minimise the computation time. A series of uniaxial simulations was performed on six specimens generated with different numbers of particles. The loading speed was set as 0.01 m/s. The material properties are the same as for the previous loading and unloading test. The dimensions of all specimens are shown in Table 6.1, the ratio of specimen height to specimen diameter was kept constant at 2:1 for all specimens. The number of particles for each radius is calculated by Equation (4.1) based on Table 5.1 and Figure 4.1 (see Table 6.2). The Young's modulus and Poisson's ratio of the specimens were then calculated (see Figure 6.4). It can be seen that the general trend is for Young's modulus to increase and Poisson's ratio to decrease as the number of particles increase, tending towards constant values. Therefore, it can be concluded from Figure 6.4 that at least 6000 particles are required for the results to be close to the results as using 10000 particles.

Four separate simulations have also been performed with 6000 particles in different random positions. The particle and parallel bond parameters were set to be the same as in previous the loading and unloading simulations. The resulting Young's modulus and Poisson's ratios are shown in Figure 6.5. It can be seen that the variability caused by the random positions of the particles is negligible. Therefore, at least 6000 particles are required in the simulation to obtain reasonable estimates of bulk elastic modulus and Poisson's ratio.

Number of particles	Specimen diameter (mm)	Specimen height (mm)
1000	33.11	66.22
3000	47.75	95.50
4500	54.66	109.32
6000	60.16	120.32
8000	66.21	132.42
10000	71.33	142.66

Table 6.1 Dimensions of the specimen with different numbers of particles

Sieve sizes (mm)	Number of particles for each size range					
	1000	3000	4500	6000	8000	10000
10 - 14	3	9	14	19	25	31
8 - 10	24	72	108	144	192	240
6.3 - 8	42	125	188	250	334	417
5 - 6.3	63	190	285	380	507	634
4 - 5	100	301	452	602	803	1003
2.8 - 4	272	814	1221	1629	2171	2714
2 - 2.8	496	1489	2232	2976	3968	4961

Table 6.2 Number of particles for each size at different size specimens
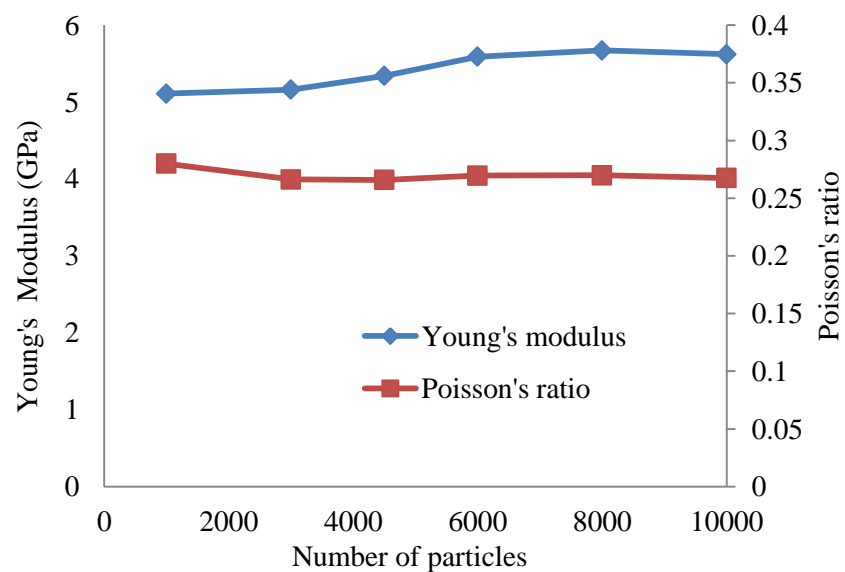
Figure 6.4 Effects of the number of particles on bulk elastic properties
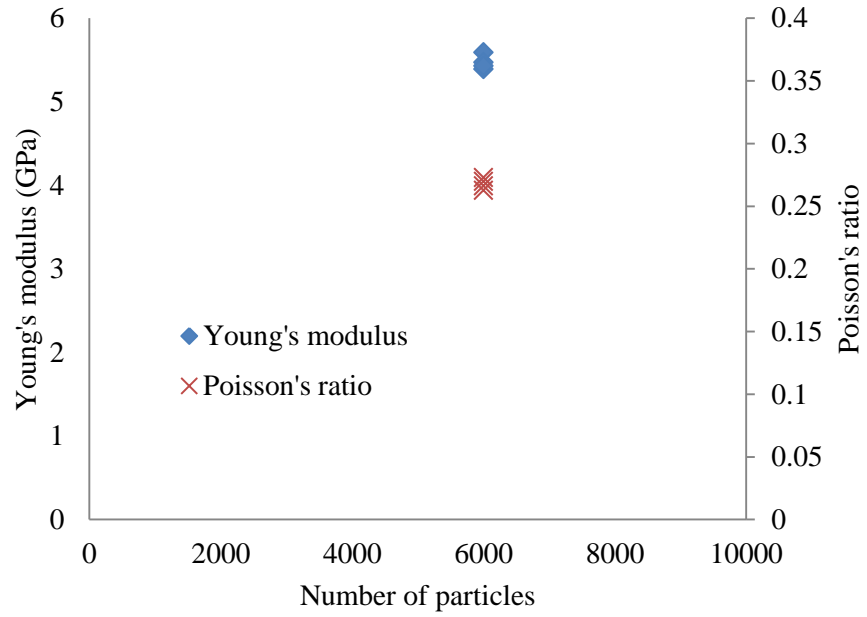
Figure 6.5 Effect of position of particles on the bulk elastic properties

6.4 **Effect of loading rate**

It is necessary to make sure that the loading rate in the numerical simulation is low enough to avoid dynamic effects but high enough to reduce the computation time. An optimum loading rate is required to maintain the accuracy of the simulations. A series of uniaxial simulations was performed by using a specimen of 6000 particles with different loading rates range from 0.0001m/s to 5m/s. The specimen of 6000 particles is the same as in the previous loading and unloading tests. The specimen properties were also set to be the same as for the previous loading and unloading tests.

The stresses on the top and bottom loading platens were recorded at 0.5% axial strain in the simulations. Figure 6.6 shows a plot of the stresses on the top and bottom platens at the different loading rates. It can be seen from this figure that the difference between the stresses on the top and bottom walls increases at the

higher loading rates. This indicates that by applying a lower loading rate (0.02m/s) dynamic effects could be avoided. This can also be explained by Figure 6.7 and Figure 6.8. It can be seen from Figure 6.7 that at a loading rate of 0.5 m/s, the stresses on both walls fluctuate. This clearly indicates the effect of dynamic stress wave propagation within the specimen at the higher loading rates. However, it can also be seen from Figure 6.8 that the loading of 0.02 m/s resulted in a virtually identical linearly increasing stress on the plates. Therefore, it was decided that a loading rate of 0.02m/s could be used during the simulations
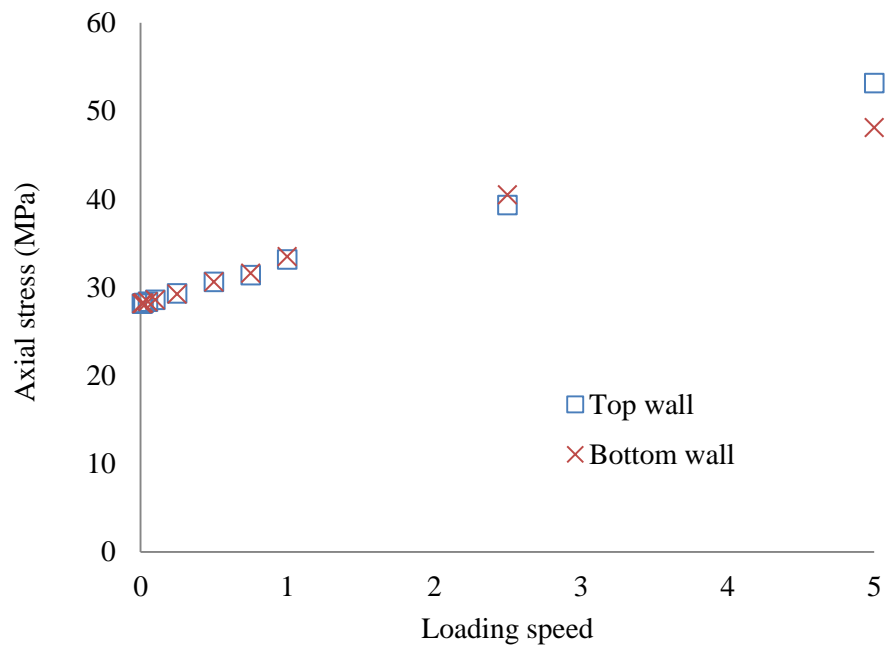

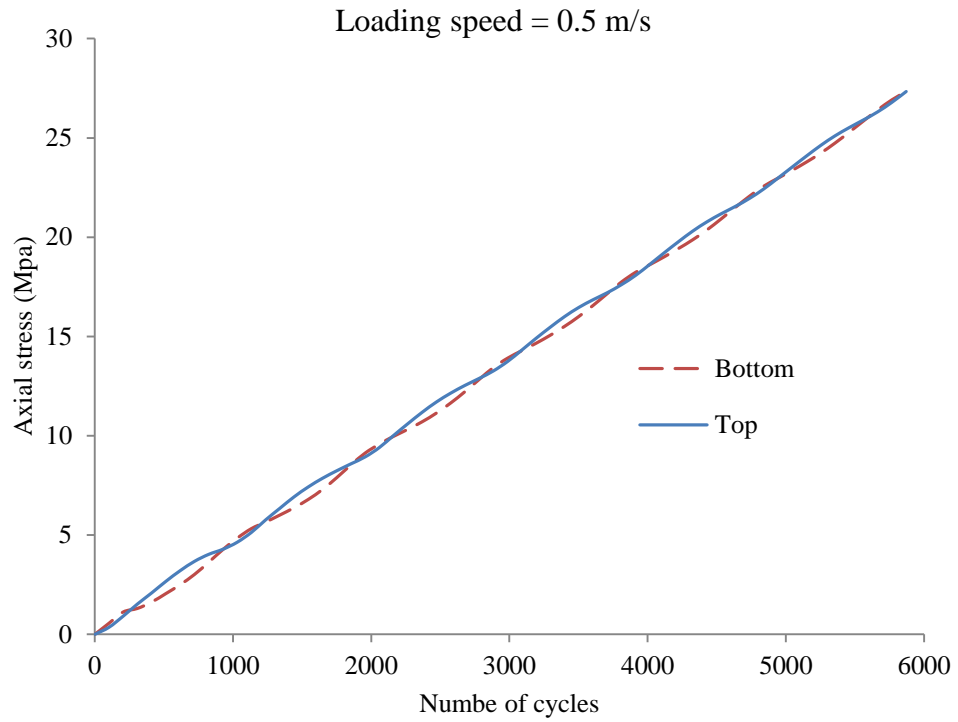Figure 6.6 Stresses on loading platens at different loading rates

Loading speed = 0.5 m/s

Figure 6.7 Stresses on top and bottom walls at 0.5 m/s
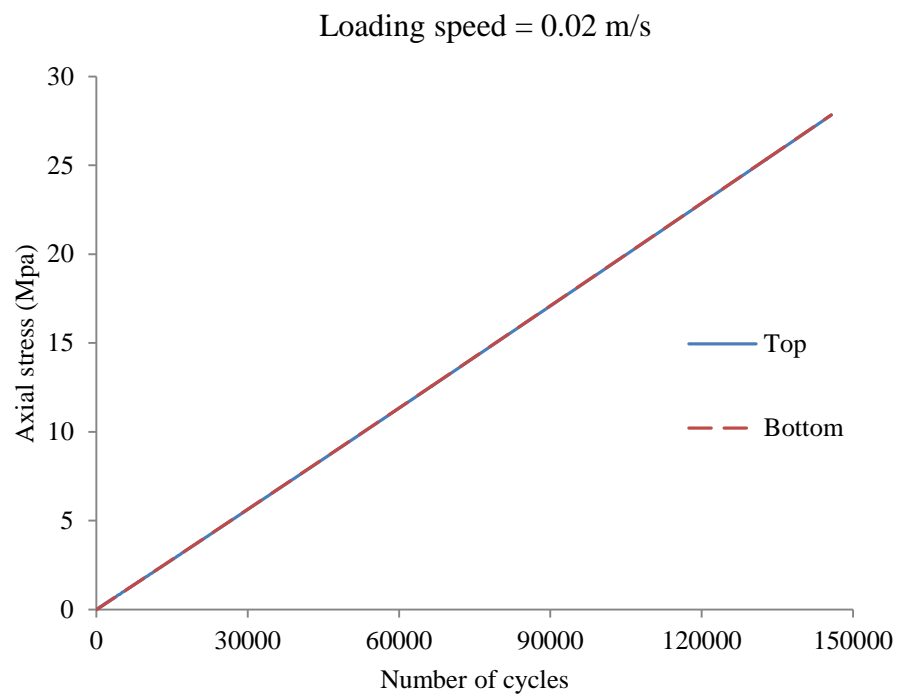
Loading speed = 0.02 m/s

Figure 6.8 Stresses on top and bottom walls at 0.02 m/s

6.5 **Effect of the normal and shear contact stiffness on bulk properties**

To investigate how the bulk material properties depend on the normal and shear contact stiffnesses of the particles and parallel bonds, a series of uniaxial simulations were performed over a range of contact stiffnesses and the ratio of normal to shear contact stiffness of the particles and parallel bonds in the specimen.

A specimen containing 6000 particles was used and compressed at a loading rate of 0.01m/s. For simplicity, the Young's modulus of particles and parallel bonds were set to be the same. Figure 6.9 shows a plot of Poisson's ratio corresponding to numerical Young's moduli of 0.45Gpa and 4.5Gpa respectively, ie. E and $\bar{E}$ in equations (3.57) and (3.58) are identical in calculating the ball stiffness and the equivalent direct tensile or compression stiffness of the parallel bond, respectively; the shear contact stiffnesses were calculated from equation (3.58) and (3.57), the normal contact stiffnesses were varied so that the ratios of normal to shear contact stiffnesses range from 1 to 10. It can be seen from this figure that the Poisson's ratio of the specimen increases as the ratio is increased and it depends on only the ratio of contact stiffness and not their absolute values. It should be mentioned that, to minimise dynamic effects, a smaller time step (lower loading speed) is required for a higher stiffness. However, in order to save computational time, the same loading speed (0.01 m/s) has been used for all the simulations with a different ratio of normal to shear contact stiffness; hence, the discrepancy in Poisson's ratios at higher ratios of normal to shear contact stiffness.

Figure 6.10 shows the relationship between Young's modulus and the ratio of normal to shear contact stiffness for a range of shear contact Young's moduli. It can be seen from this figure that the Young's modulus of the specimen depends on both normal and shear contact stiffness.
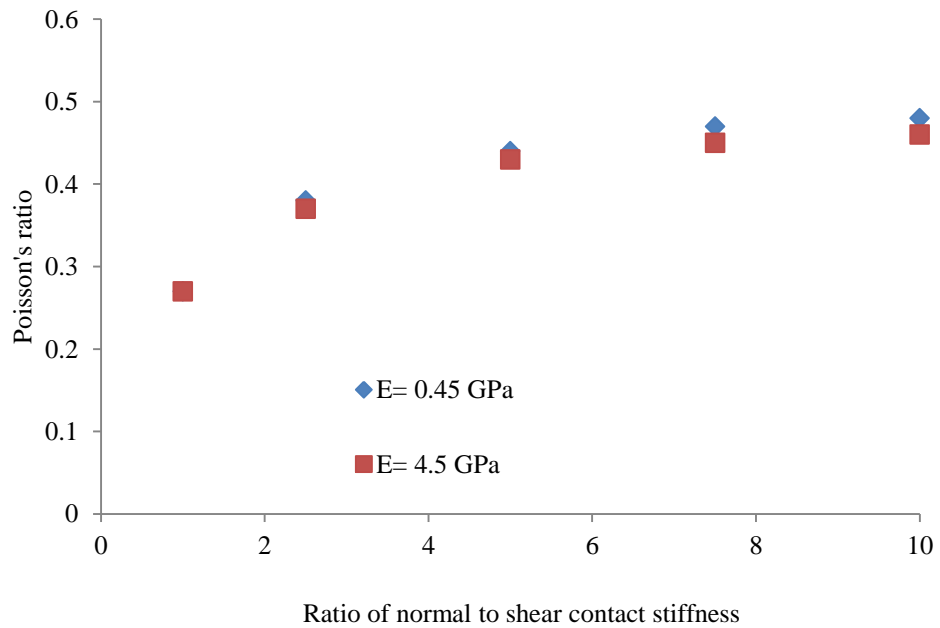
Figure 6.9 Effect of the ratio of normal to shear contact stiffness on Poisson ratio
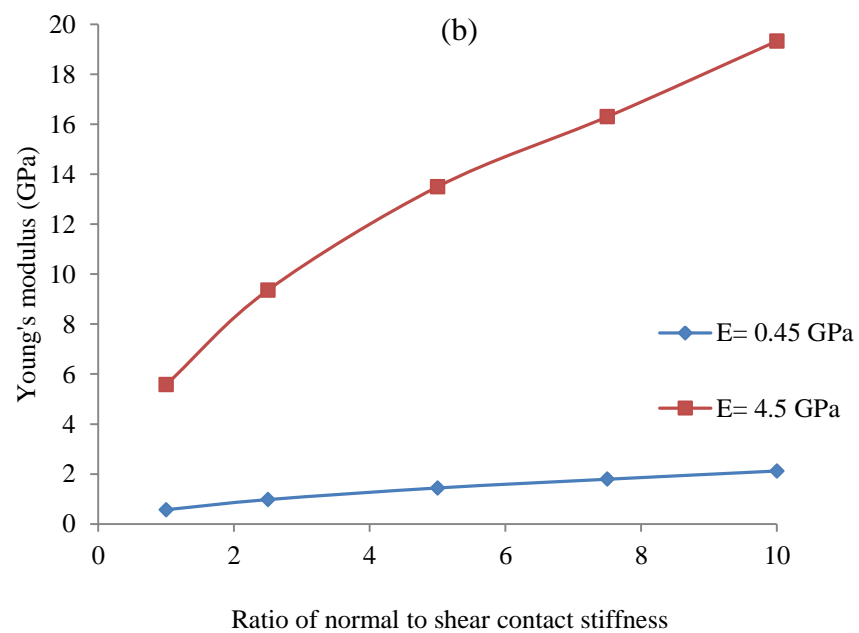
Figure 6.10 Effect of the ratio of normal to shear contact stiffness on Young's modulus

6.6 **Effect of parallel bond radius**

According to equation (3.60) the parallel bond stiffness is related to the bond radius multiplier, so it is necessary to understand how the bond radius multiplier affects the bulk modulus of the specimen. A specimen with 6000 particles was used and simulated at a loading rate of 0.01m/s. Figure 6.11 shows the Young's modulus and Poisson's ratio with a different parallel bond radius multiplier. It needs to be mentioned that the Young's modulus of the parallel bond was changed according to the bond radius multiplier so that the equivalent contact stiffnesses in direct tension and compression were the same (equation (3.60)). It can be seen from Figure 6.11 that the bond radius has little effect on the Young's modulus, and that as the radius increases the Poisson's ratio decreases. This is the expected result since for the same equivalent contact stiffness of parallel bonds, larger radii can carry more moment resulting in a smaller Poisson's ratio and an approximately constant Young's modulus.
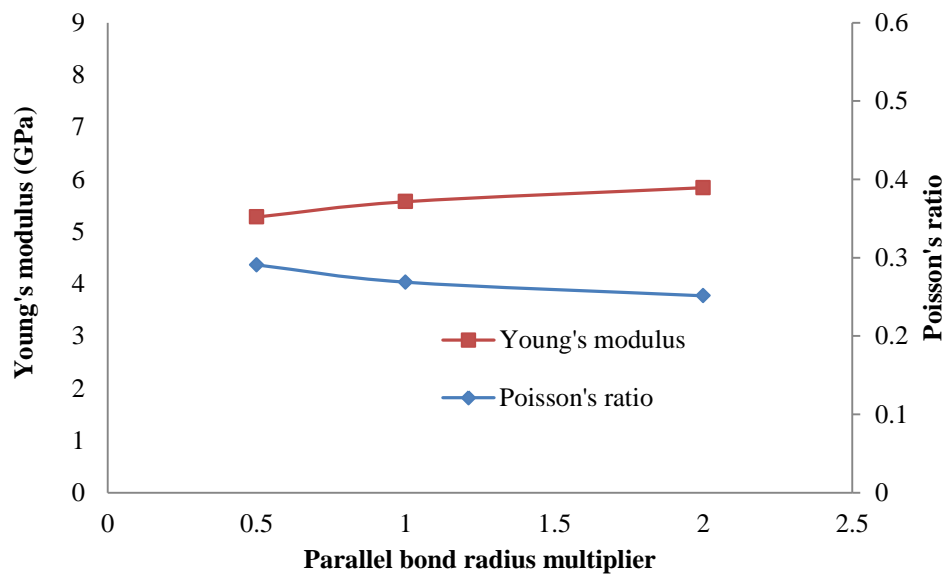
Figure 6.11 Effect of parallel bond radius multiplier on the bulk modulus of specimen

6.7 **Summary**

The following conclusions can be drawn from this chapter:

- Discrete element modelling can be used to model realistic asphalt mixtures under elastic conditions (high loading speed or low temperature).

- A numerical specimen preparation procedure has been produced to obtain a specimen which is similar to the real specimen.

- Elastic properties of asphalt mixtures can be modelled by a specimen of bonded particles.

- A minimum of 6000 particles is needed to obtain a reliable Young's modulus and Poisson's ratio.

- A maximum of 0.02 m/s loading speed is used to avoid dynamic stress wave propagation within the specimen for tests in this dissertation.

- Poisson's ratio was found to increase with the ratio of normal to shear contact stiffness but was independent of the stiffnesses (neglecting the effect of stiffness on required loading velocity).

- The Young's modulus was found to be dependent on both normal and shear stiffnesses.

- When the parallel bond radius increases, the Young's modulus is approximately constant and Poisson's ratio decreases.

7 Viscoelastic modelling

7.1 Introduction

Visco-elastic simulations are necessary for further development of discrete element modelling of asphalt mixtures. Viscoelasticity describes the time-dependent stress-strain behaviour. It is well known that asphalt mixtures are loading-rate and temperature dependent exhibiting elastic, delayed elastic and viscous behaviour. To capture the time-dependent behaviour, a viscoelastic model is required. The Burger's model introduced in section 3.3.7 can be used to capture the time-dependent properties of bitumen.

This chapter presents the use of a modified Burger's model which provides moment and torsional resistance at contacts to model the uniaxial compression test under different loading conditions. The results are compared with experimental results on the same material based on the grading curve (Figure 4.1) and mix design (Table 5.1); see chapter 5 for the details of the laboratory tests.

7.2 Modified Burger's contact model

The stiffness in the Burger's model is given by:

$$K = \left[\frac{1}{K_m} + \frac{t}{C_m} + \frac{1}{K_k}\left(1 - e^{-t/\tau}\right) \right]^{-1} \qquad (7.1)$$

where t is the loading time and $\tau = C_k / K_k$ is the relaxation time. Equation (7.1) shows that the contact stiffness will reduce as a function of loading time. In reality, the time-dependent behaviour of an asphalt mixture will be significantly more complicated. However, this simple approach is the necessary precursor to the introduction of more complex modelling which can be achieved in PFC3D by a user-defined contact model.

The Burger's model in PFC3D can transmit only force when the contact bond is installed which means the particles can roll over each other easily; see section 3.3. However, in reality aggregate particles do not roll over each other in bonded aggregates. For this purpose, an alternative approach was developed. The Burger's model was activated as the stiffness of the contact bond in tension and compression, and a "virtual" parallel bond was introduced to give a Burger's model in a moment resistance and torsional resistance at a contact. The word "virtual" is used because the bond doesn't sustain direct tension or compression (this is given by the contact bond), nor can the virtual bond break; the contact bond governs breakage. If the current stiffness of the contact bond is k_c, and the radius of the virtual parallel bond is R, and distributed stiffness k_p per unit area, then the stiffness of the virtual parallel bond was taken as equation (7.2) through all simulations, and values for the parameters quoted in this chapter are the equivalent k_c values.

$$k_p \pi R^2 = k_c \tag{7.2}$$

Chapter 7 Viscoelastic modelling

For the moment resistance, each subsequent relative rotation increment at contacts produces an increment of moment and adds to the current value. This can be imagined as a circular disk lying on the contact plane and centered at the contact point. This disk has the properties in bending and torsion giving by the Burger's stiffness over a chosen radius. The total moment at a contact can be resolved into respective normal (torque M^n) and shear ("moment" M^s) components with respect to the contact plane as

$$M = M^n n_i + M^s t_i \qquad (7.3)$$

where n_i is the unit normal to the contact plane and t_i is a unit vector in the contact plane. The bending moment acts along the contact plane and the torsion moment acts normal to the contact plane. The increment of torque ΔM^n (unit normal in contact normal direction) and bending moment ΔM^s (unit normal in the contact plane) are given by

$$\Delta M^n = -(k^s J \Delta \theta^n) n_i \qquad (7.4)$$

$$\Delta M^s = -k^n I \Delta \theta^s \qquad (7.5)$$

where k^n, k^s are the Burger's stiffnesses for bending and torsion respectively; $\Delta \theta^n$, $\Delta \theta^s$ are rotation increment due to the torque and moment, respectively. I and J are the moment of inertia and polar moment of inertia of the imaged cross section, respectively. And they are given by

$$I = \frac{1}{4} \pi R^4 \qquad (7.6)$$

$$J = \frac{1}{2} \pi R^4 \qquad (7.7)$$

$$R = \lambda * \min(R^A, R^B) \tag{7.8}$$

where R is the radius of the imagined circular disk; λ is known as the radius multiplier; R^A and R^B are the radii of particles in contact. It should be noted that the relative angular velocity which is used to calculate the rotation increment is stored as a vector in global coordinates in PFC3D. It must be updated to account for the contact motion before the calculation. Finally, the calculated moment needs to be updated in terms of global coordinates.

An example simulation has been done with 6000 particles at a strain rate of 0.07×10^{-4} s^{-1}. The model parameters were chosen arbitrarily so that the magnitude and shape of the axial stress versus axial strain curve was similar to the experimental result (up to axial strain level of 0.01) shown in Figure 7.1. The normal and torsion contact parameters were taken to be K_k^n = 3.5MN/n, C_k^n = 35MNs/m, K_m^n = 3.5MN/n, C_m^n = 35MNs/m and the shear and bending contact parameters were taken to be a factor of 1.75 smaller than the normal contact parameters so that the Poisson's ratio is 0.32 based on Figure 6.9. The inter-particle friction coefficient was set to be 0.7. The radius multiplier was set as 1.

The predicted axial stress versus axial strain curve is shown as the dotted line in Figure 7.1. It can be seen that the strain softening is more pronounced, compared to that in the laboratory result. This is due to the particle shape not being considered. A two ball clump of same volume as the previous sphere shown in Figure 7.2 was then used to replace the sphere in the specimen and the result is shown as the dashed line in Figure 7.1, demonstrating that the particle shape is important in the simulation of strain softening. However the

effects of the particles shape will not be the main objective for this research, all the following simularions will based on numerical specimens containing polydisperse spheres only.
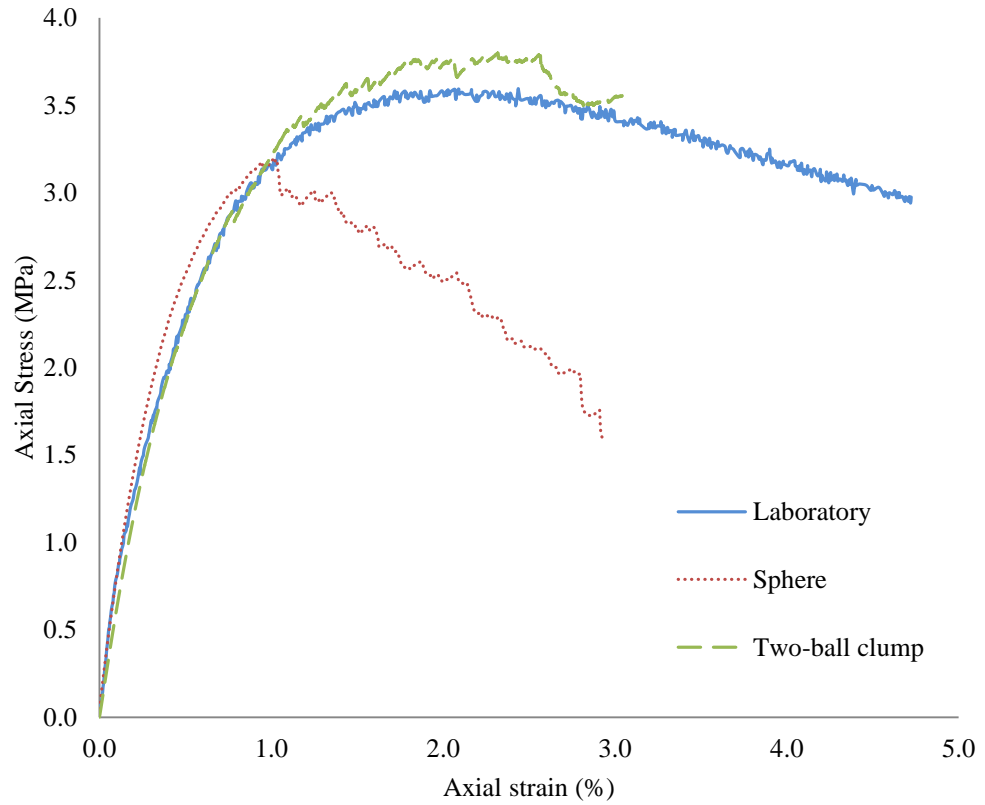

Figure 7.1 Axial stress versus axial strain at a strain rate of 7×10^{-4} s^{-1}
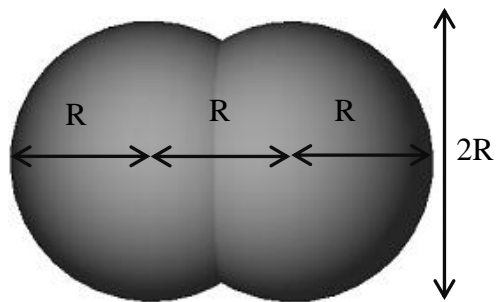

Figure 7.2 Two-ball clump

7.3 **Effect of modified Burger's model parameters**

As can be seen from the example simulation (Section 7.2), there are a number of parameters involved in the modified Burger's model: ie. the Maxwell stiffness and viscosity, the Kelvin stiffness and viscosity, the friction coefficient, the ratio of normal to shear Burger's model parameters and the radius multiplier. The distribution of bond strengths is also a factor influencing the behaviour. Therefore, it is important to understand how each parameter affects the simulation results before using it to simulate the laboratory test under various loading conditions.

A typical three dimensional microstructural-based discrete element viscoelastic modelling process is extremely time-consuming. McDowell et al. (2009) found a scaling method by using dimensional analysis for viscosity and velocity in discrete element modelling of strain-controlled tests on asphalt. They have proved that the effect of scaling applied velocity is the same as that of scaling both Kelvin and Maxwell viscosities by the same factor. This scaling method, which offers great benefit in saving computer simulation time, has been used for the strain-controlled simulations in this project. A factor of 100 was used for scaling the loading speed (in the laboratory) and both viscosities (in DEM) for all the constant strain rate simulations.

To make it clear the following symbols are used to represent the parameters.

K_m^n Maxwell normal stiffness (MN/m)

C_m^n Maxwell normal viscosity (MNs/m)

K_k^n Kelvin normal stiffness (MN/m)

C_k^n Kelvin normal viscosity (MNs/m)

N / S Ratio of normal to shear Burger's contact parameters

λ Radius multiplier

f Friction coefficient

The properties of the first uniaxial compression constant strain rate simulation are shown in Table 7.1. The strain rate before scaling was taken to be 0.005s-1. Both normal and shear contact bond strengths were chosen to be equal to 37 N. The following subsections describe the results of the simulations based on the first simulation and changing one parameter only each time. The axial stress versus axial and radial strains plots are shown for each case.

Burger's model parameters				N / S	λ	f
K_m^n (MN/m)	C_m^n (MNs/m)	K_k^n (MN/m)	C_k^n (MNs/m)			
9	170	8	170	11	1	0.7

Table 7.1 Properties for the first constant strain rate test

7.3.1 **Effect of Maxwell stiffness**

Two simulations with higher Maxwell stiffnesses (see Figure 3.17) were simulated; the results are shown in Figure 7.3 and Figure 7.4. From the figures, it can be seen that pre-peak slope of the stress-strain plot increases as the Maxwell stiffness increases. In addition, a wider range of post peak softening

behaviour is predicted as Maxwell stiffness decreases. This is because the Maxwell stiffness works as the elastic component in Burger's model; increasing the Maxwell stiffness will lead to an increase in the elastic stiffness of the material. The peak stress is shown to be approximately independent of the Maxwell stiffness.
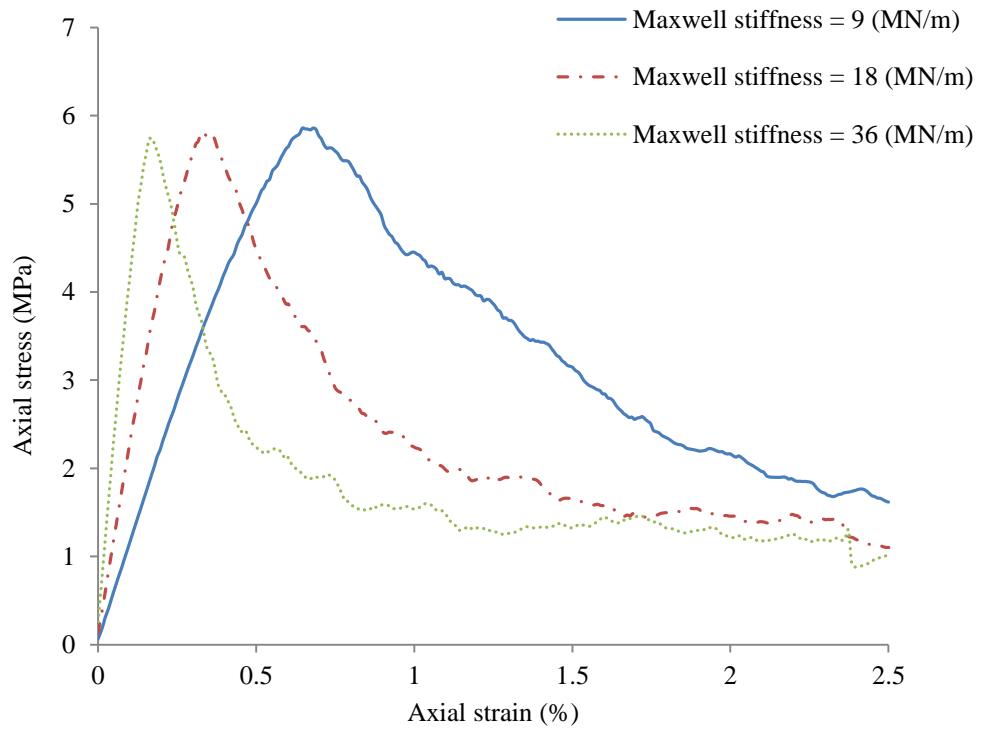

Figure 7.3 Axial stress versus axial strain for different Maxwell stiffnesses based on Table 7.1 at strain rate of 0.005 s^{-1}
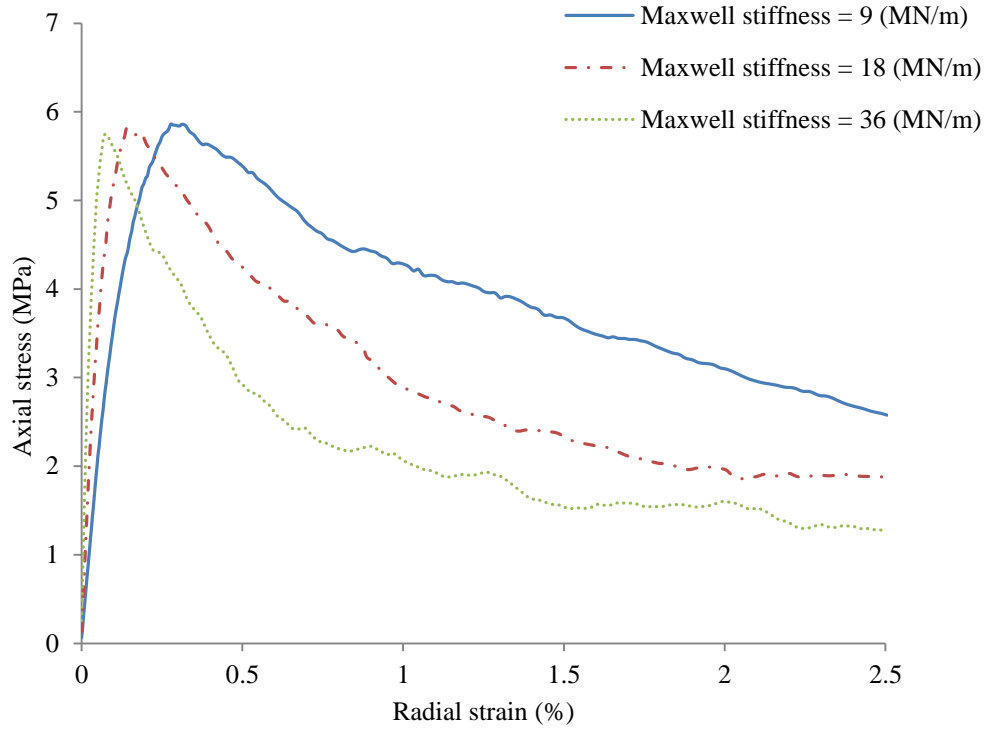
Figure 7.4 Axial stress versus radial strain for different Maxwell stiffnesses based on Table 7.1 at a strain rate of 0.005 s^{-1}

7.3.2 **Effect of Maxwell viscosity**

Two simulations with higher Maxwell viscosities (see Figure 3.17) were performed; the axial stress verses axial and radial strain plots are shown in Figure 7.5 and Figure 7.6. As can be seen, the axial stress is approximately independent of the Maxwell viscosity at a strain rate of 0.005 s^{-1}. The difference in behaviour appearing after the peak stress is due to contact bond breakage. According to equation (7.1), for a contact, different Maxwell viscosity values will result in different contact forces and therefore contact bonds break at different times and positions. In addition the Maxwell viscosity will influence post-elastic behaviour even if no bond breakage occurs.
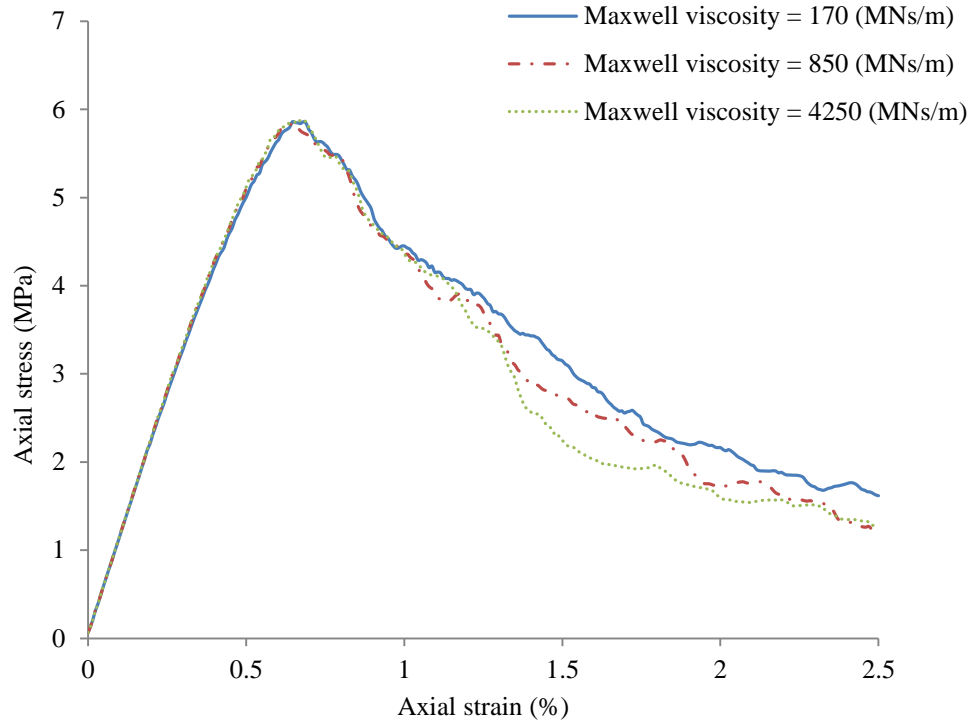
Figure 7.5 Axial stress versus axial strain for different Maxwell viscosities based on Table 7.1 at a strain rate of 0.005 s^{-1}
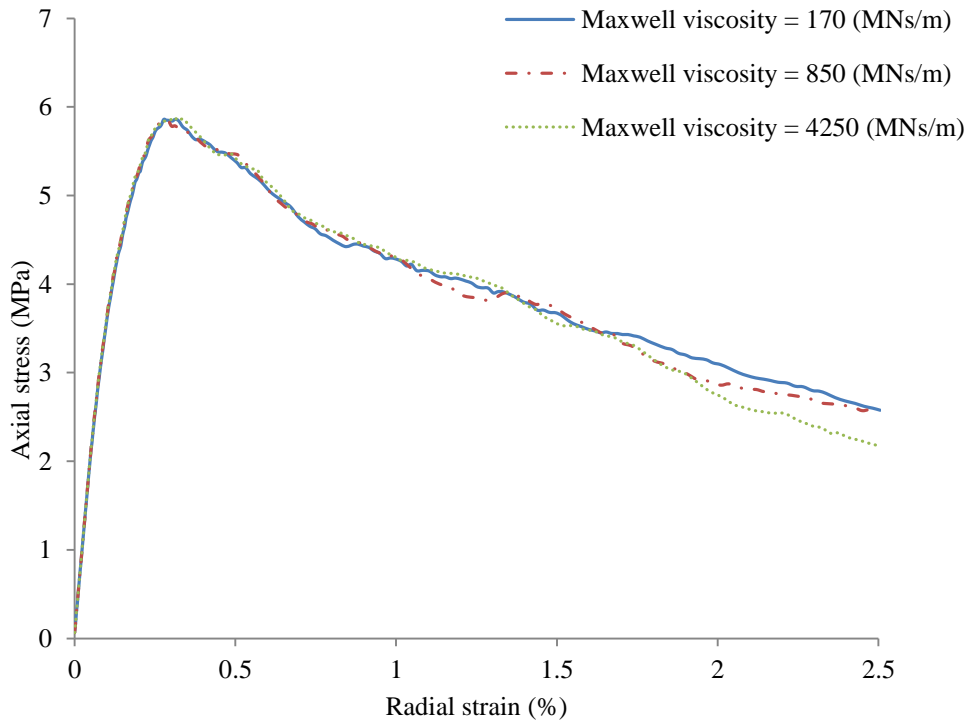

Figure 7.6 Axial stress versus radial strain for different Maxwell viscosities based on Table 7.1 at a strain rate of 0.005 s^{-1}

Three simulations were also performed at a strain rate of 0.00005 s^{-1} for the three different Maxwell viscosities. The results are shown in Figure 7.7 and Figure 7.8. It can be seen that at lower strain rate (0.00005 s^{-1}), the slope just before the peak stress of the stress-strain plot increases as the Maxwell viscosity increases. The peak stress appears earlier when the Maxwell viscosity increases. It can be seen that the behaviour becomes more brittle as the strain rate or Maxwell viscosity increases. This would be expected for a time-dependent brittle material. For this DEM material containing time-dependent contact stiffness and bonds, it would be anticipated that a lower loading rate or Maxwell viscosity would lead to more ductile behaviour due to the lower contact forces, according to equation (3.45). It will be shown in section (7.4.2) that the peak strength occurs at the maximum rate of bond breakage and this will also be shown to be true under creep conditions (section 7.5.3), where tertiary creep rupture is shown to be coincident with a rapid onset of bond breakage.

The difference between the stress-strain curves for the Maxwell viscosities of 170 MNs/m and 850 MNs/m becomes more obvious when the strain rate reduces from 0.005s^{-1} to 0.00005s^{-1}, which suggests that a more obvious difference between the stress-strain curves for the Maxwell viscosities of 850 MNs/m and 4250 MNs/m would be obtained at a much lower strain rate (less than 0.00005 s^{-1}).
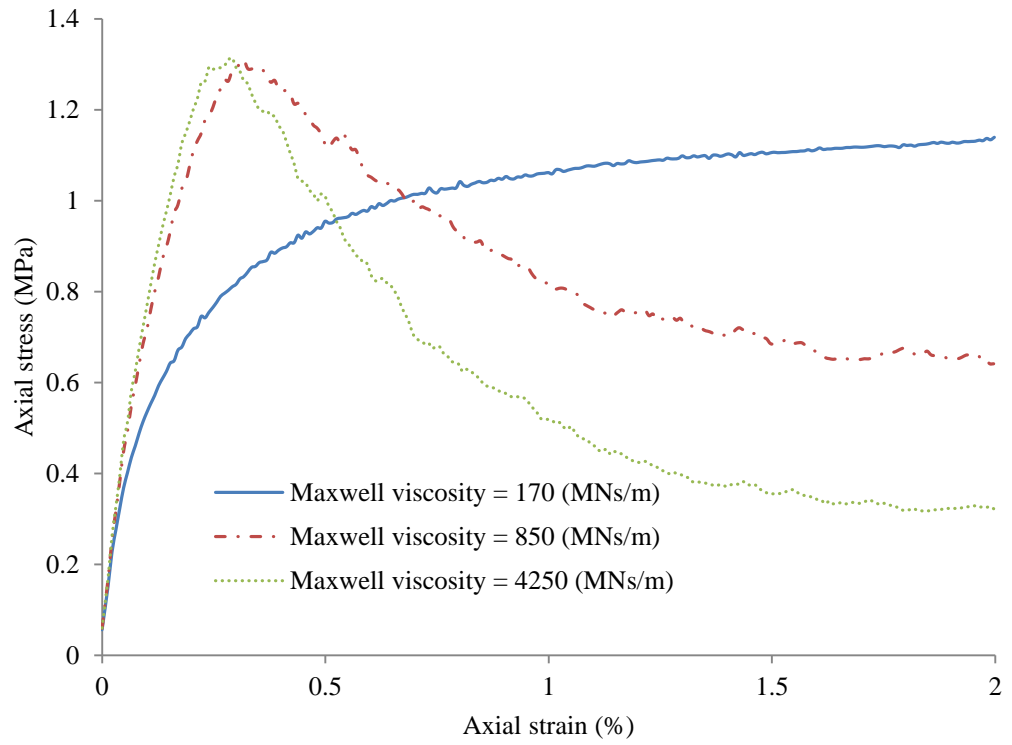
Figure 7.7 Axial stress versus axial strain for different Maxwell viscosities based on Table 7.1 at a strain rate of 0.00005 s^{-1}
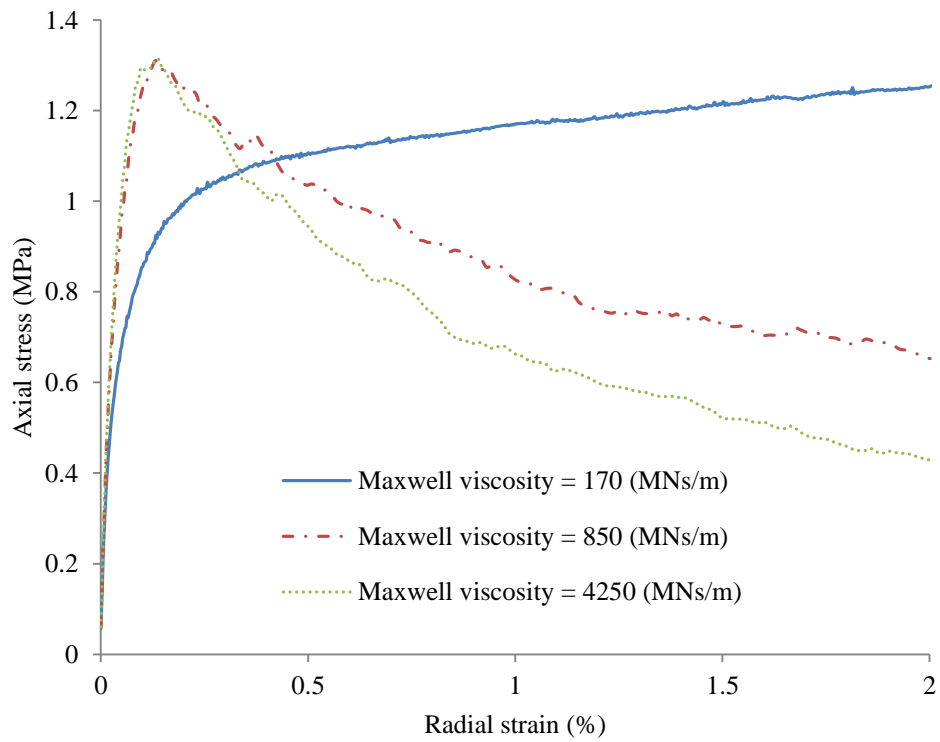

Figure 7.8 Axial stress versus radial strain for different Maxwell viscosities based on Table 7.1 at a strain rate of 0.00005 s^{-1}

7.3.3 **Effect of Kelvin stiffness**

Two simulations with higher Kelvin stiffnesses (see Figure 3.17) were simulated; the axial stress verses axial and radial strain plots are shown in Figure 7.9 and Figure 7.10. The same pattern was observed as for the three different Maxwell viscosities at the constant strain rate of 0.005 s^{-1}. Three simulations with the same Kelvin stiffnesses at a constant strain rate of 0.00005s^{-1} were performed. The results are shown in Figure 7.11 and Figure 7.12. It can be seen that the axial stresses for the three cases differ in behaviour after the elastic phase and then reach the same steady-state.

Figure 7.9 Axial stress versus axial strain for different Kelvin stiffnesses at a strain rate of 0.005 s^{-1}

Figure 7.10 Axial stress versus radial strain for different Kelvin stiffnesses at a strain rate of 0.005 s^{-1}
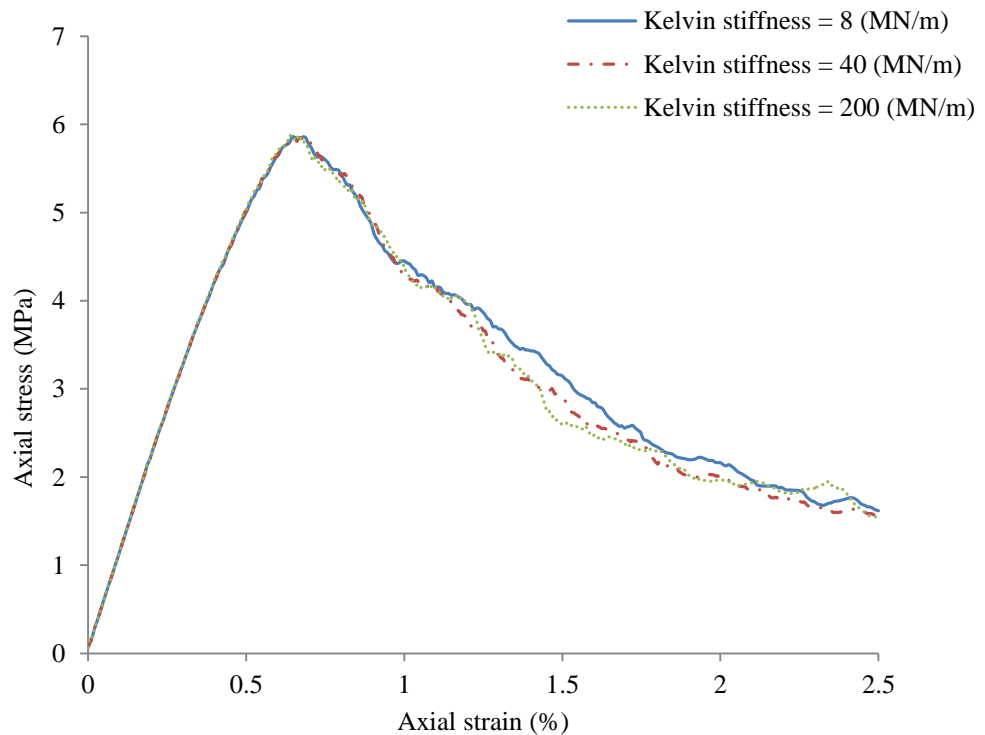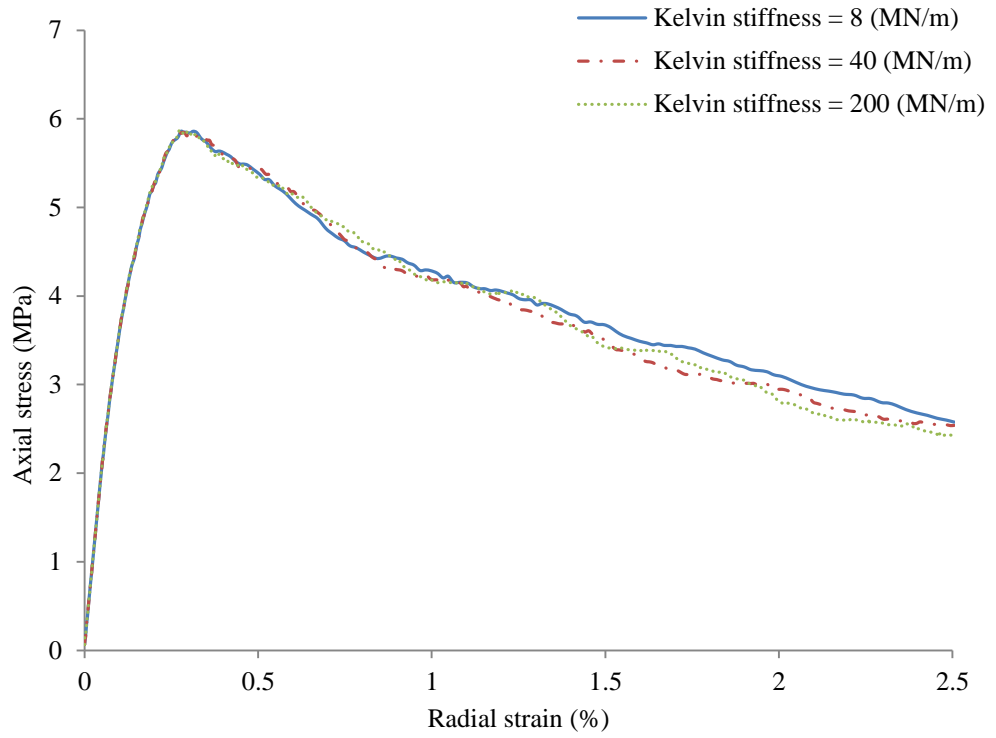

Figure 7.11 Axial stress versus axial strain for different Kelvin stiffnesses at a strain rate of 0.00005 s^{-1}

Figure 7.12 Axial stress versus radial strain for different Kelvin stiffnesses at a strain rate of 0.00005 s^{-1}

7.3.4 **Effect of Kelvin viscosity**

Six simulations with different Kelvin viscosities (see Figure 3.17) based on Table 7.1 were simulated at the constant strain rates of 0.005 and 0.00005 s^{-1}; the axial stress verses axial and radial strain plots are shown in Figure 7.13, Figure 7.14, Figure 7.15 and Figure 7.16. It can be seen that the effect of Kelvin viscosity on the constant strain rate simulations at a higher strain rate (0.005 s^{-1}) is not as obvious as the effect at a lower strain rate (0.00005 s^{-1}). The stress-strain curve reaches the steady-state at an earlier stage with higher Kelvin viscosity for a constant strain rate of 0.00005 s^{-1}.

Figure 7.13 Axial stress versus axial strain for different Kelvin viscosities at a strain rate of 0.005 s-1
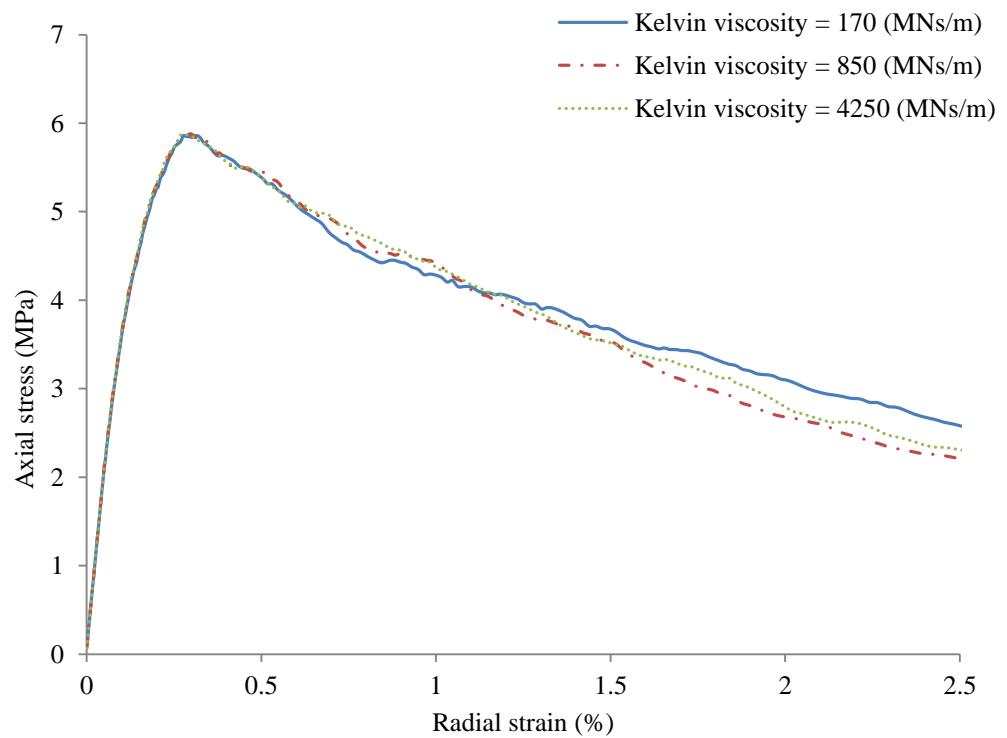
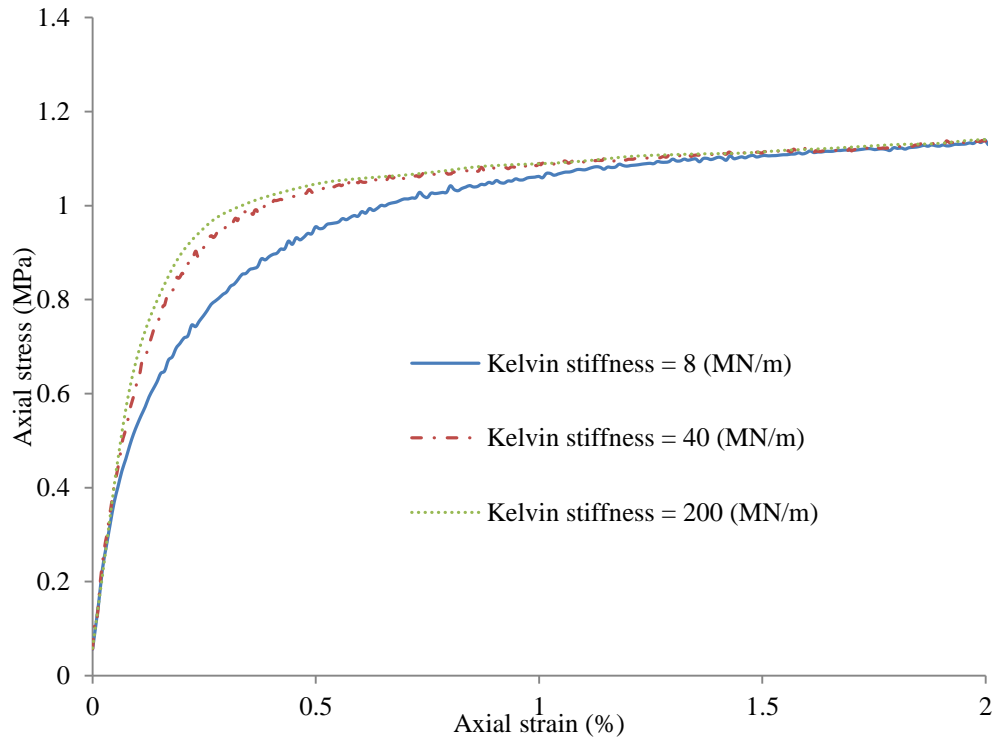Figure 7.14 Axial stress versus radial strain for different Kelvin viscosities at a strain rate of 0.005 s-1

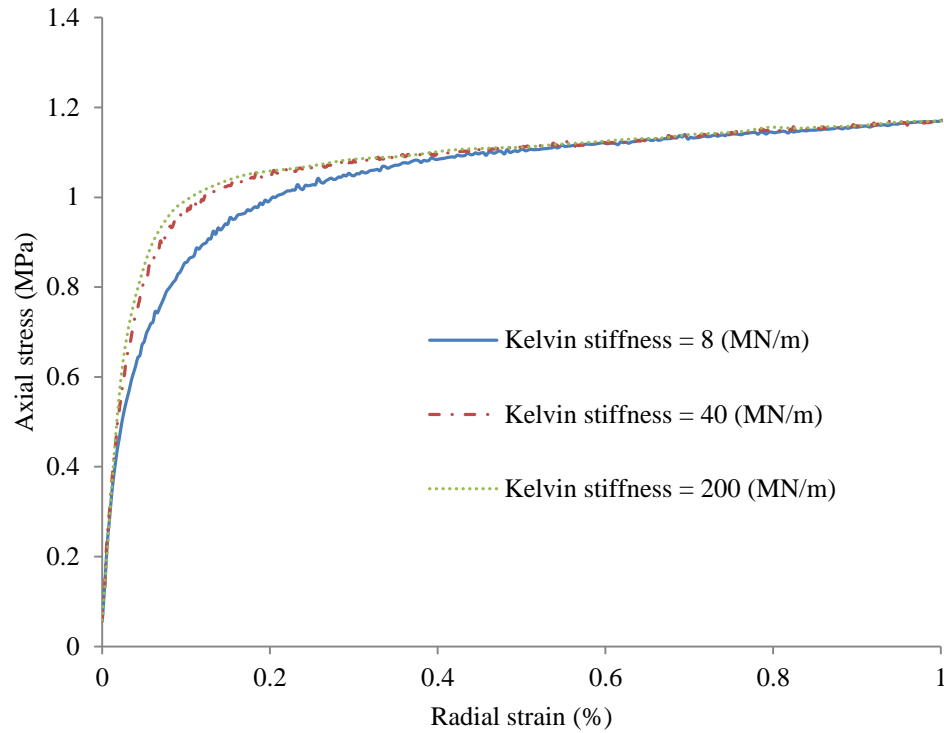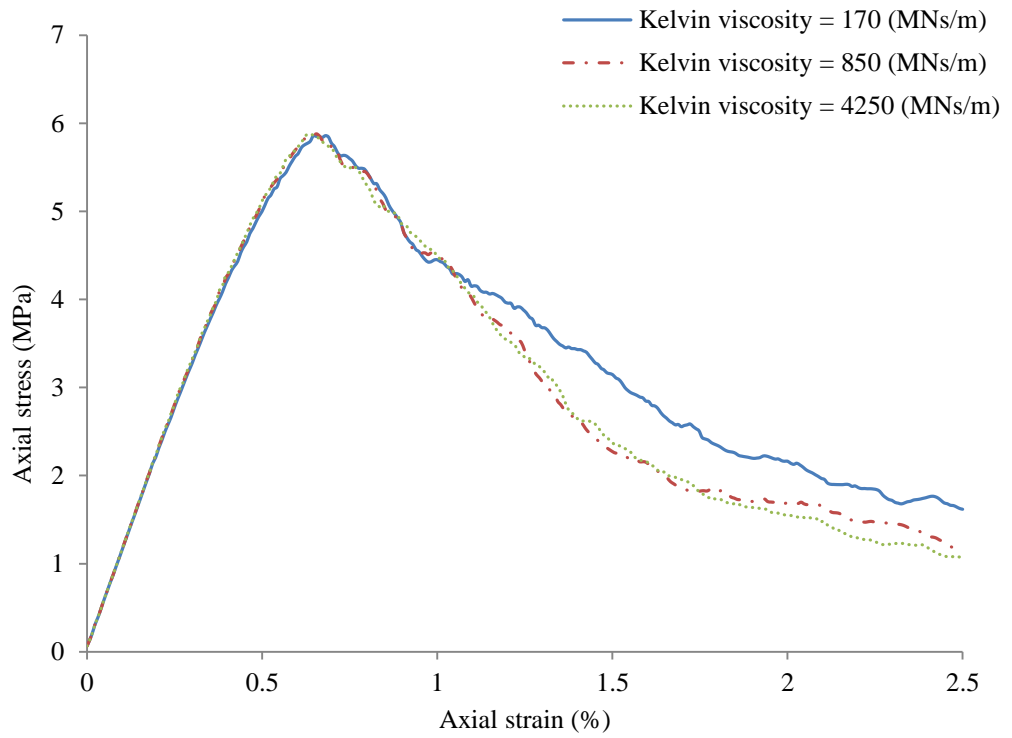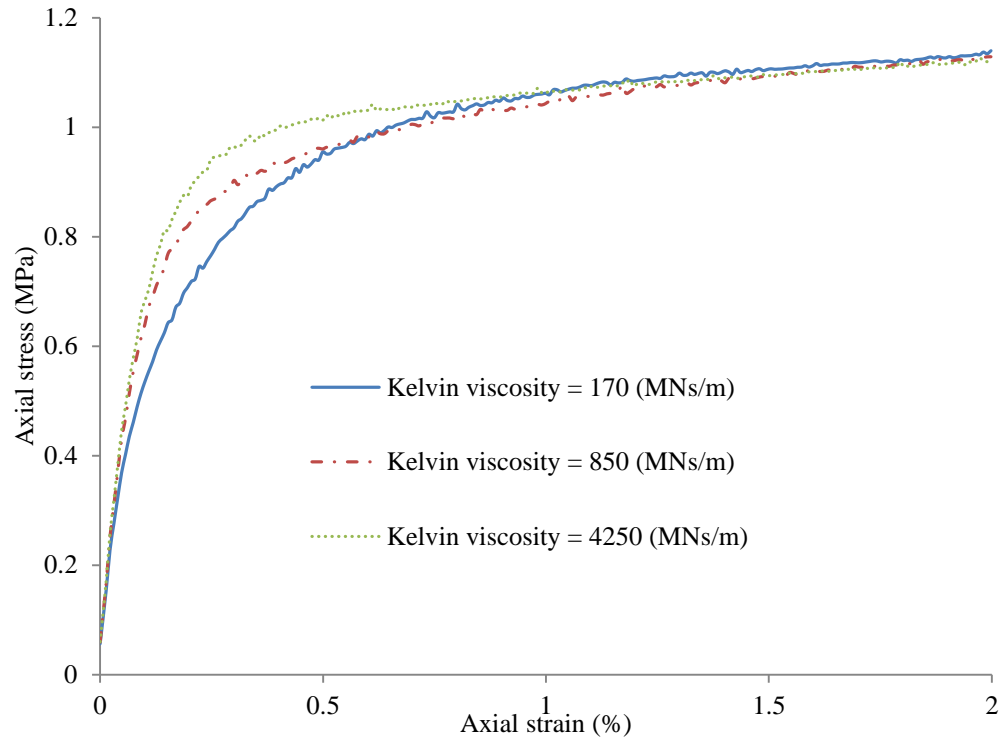Figure 7.15 Axial stress versus axial strain for different Kelvin viscosities at a strain rate of 0.00005 s^{-1}
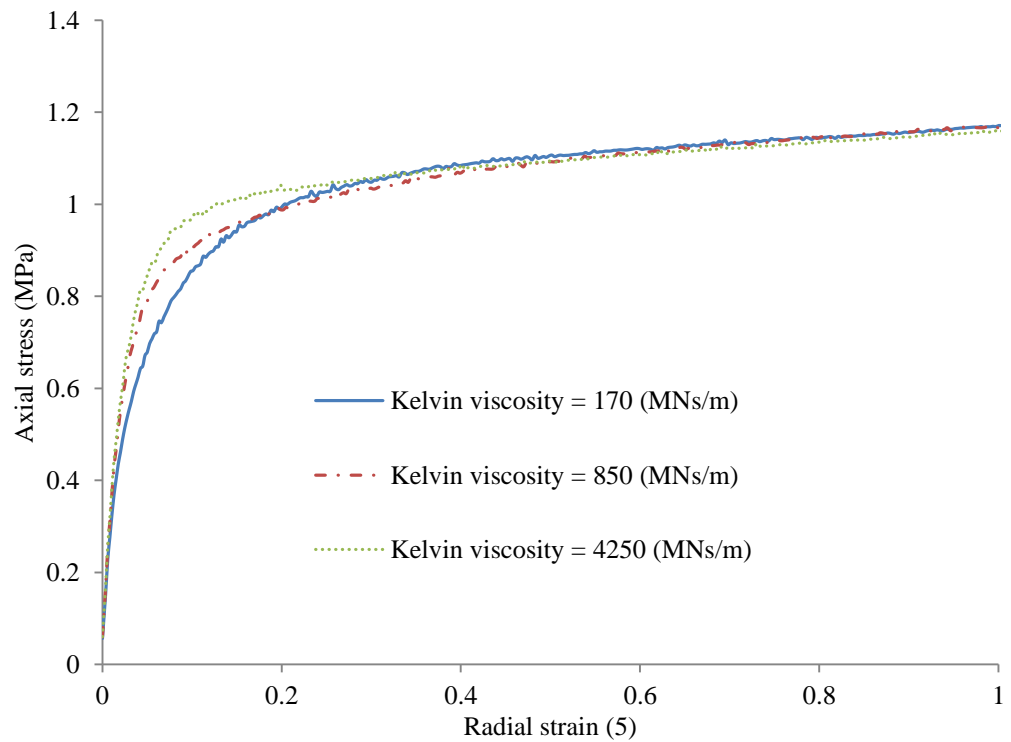
Figure 7.16 Axial stress versus radial strain for different Kelvin viscosities at a strain rate of 0.00005 s^{-1}

7.3.5 Effect of the ratio of normal to shear Burger's parameters

Two simulations with different ratios of normal to shear Burger's model parameters were simulated. The contact normal and calculated bending (equation (7.2)) parameters were kept the same as in Table 7.1 while the contact shear and calculated torsional (equation (7.2)) parameters were varied so that the ratios of normal to shear (and bending to torsional) contact parameters were different in each of the three simulations. The axial stress versus axial and radial strains plots are shown in Figure 7.17 and Figure 7.18. As can be seen, the pre-peak slope of the stress-strain curve reduces and the peak stress reduces slightly as the normal to shear contact property ratio increases. This is because with a reduced shear contact stiffness the particles tend to move in shear instead of in the normal direction. A wider range of post peak softening behaviour was predicted, due to a different contact bond breakage pattern.
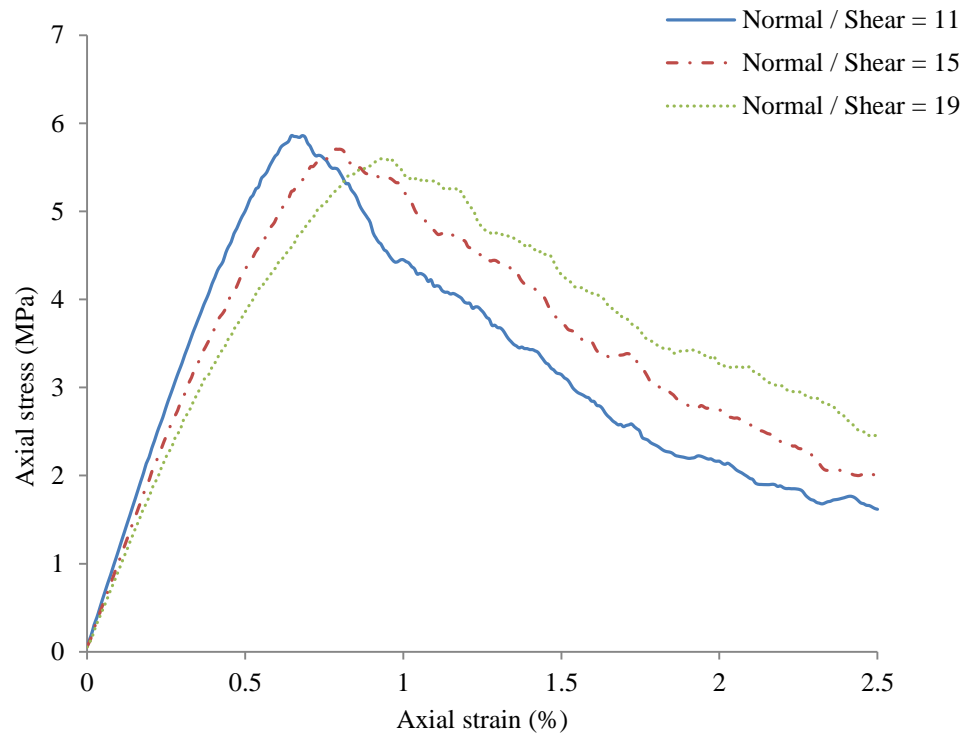
Figure 7.17 Axial stress versus axial strain for different ratios of normal to shear Burger's model parameters based on Table 7.1
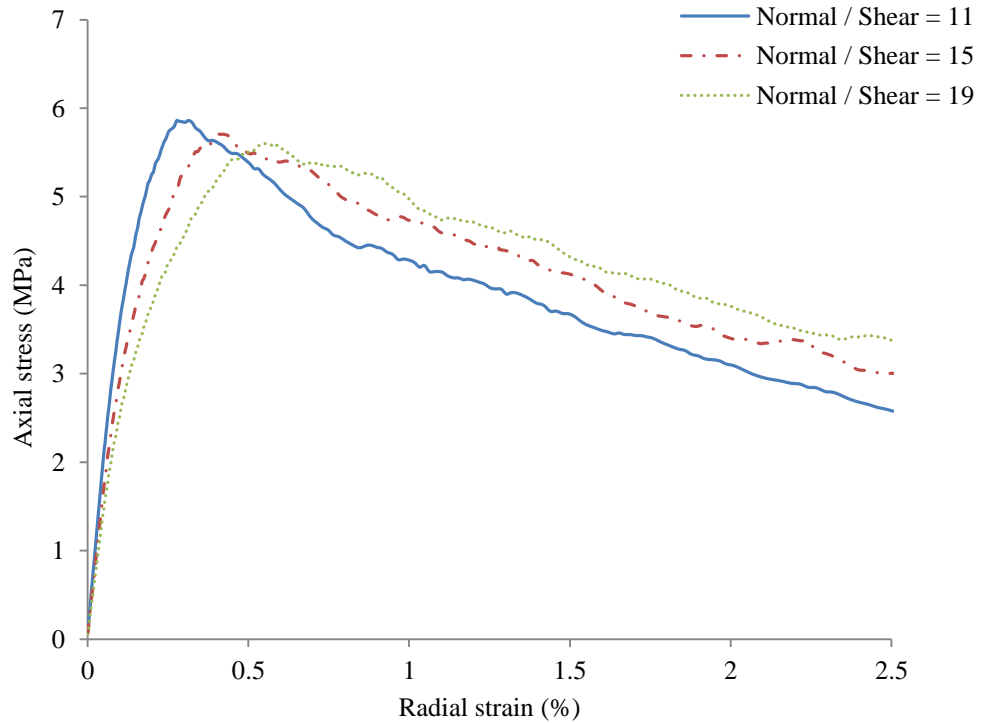
Figure 7.18 Axial stress versus radial strain for different ratios of normal to shear Burger's model parameters based on Table 7.1

7.3.6 **Effect of radius multiplier**

As mentioned in section 7.2 the modified Burger's model with moment and torsion resistance can be imagined as a virtual circular disk (with no strength characteristics) lying on the contact plane and centered at the contact point. This disk has the properties of bending and torsion Burger's stiffness distributed over a chosen radius. To understand the effect of the radius, two simulations with different radius multipliers were simulated (equation (7.8)). The Burger's contact properties were set to be the same as in Table 7.1 (k_p remaining according to equation (7.2)). The axial stress versus axial and radial strains plots are shown in Figure 7.19 and Figure 7.20. It can be seen that the slope just before the peak stress of the stress-strain curve and the peak stress reduces slightly as the radius multiplier reduces. Based on equations (7.4) and (7.5), smaller radius causes a lower increment in normal (torsion) and shear (bending) moments while the stiffnesses and rotation increments are kept the same, hence, wider post peak softening behaviour.
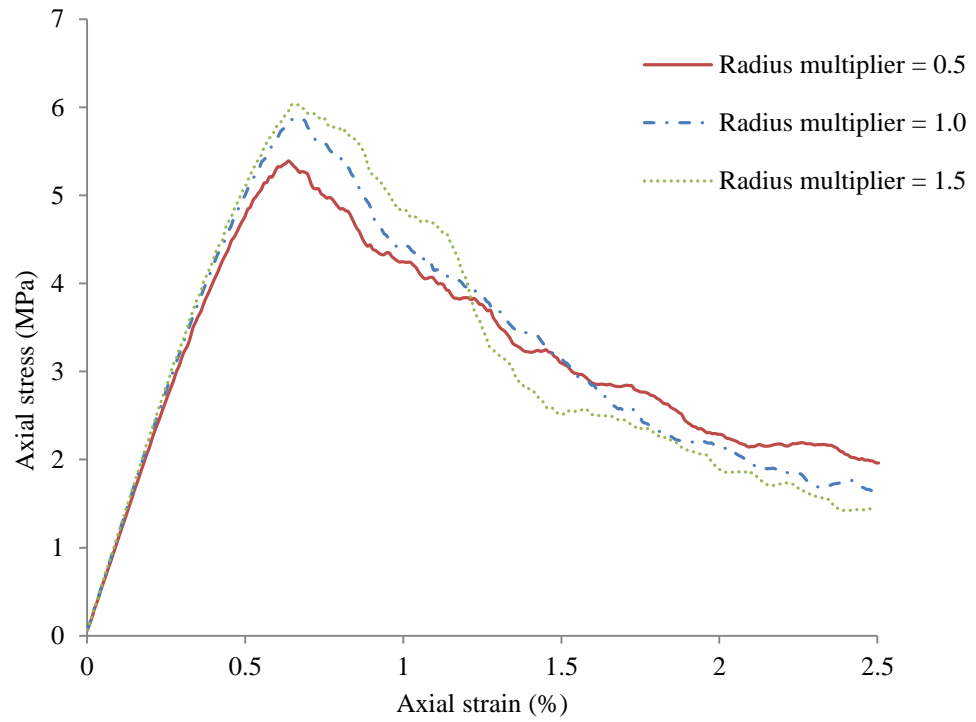
Figure 7.19 Axial stress versus axial strain for different radius multiplier based on Table 7.1
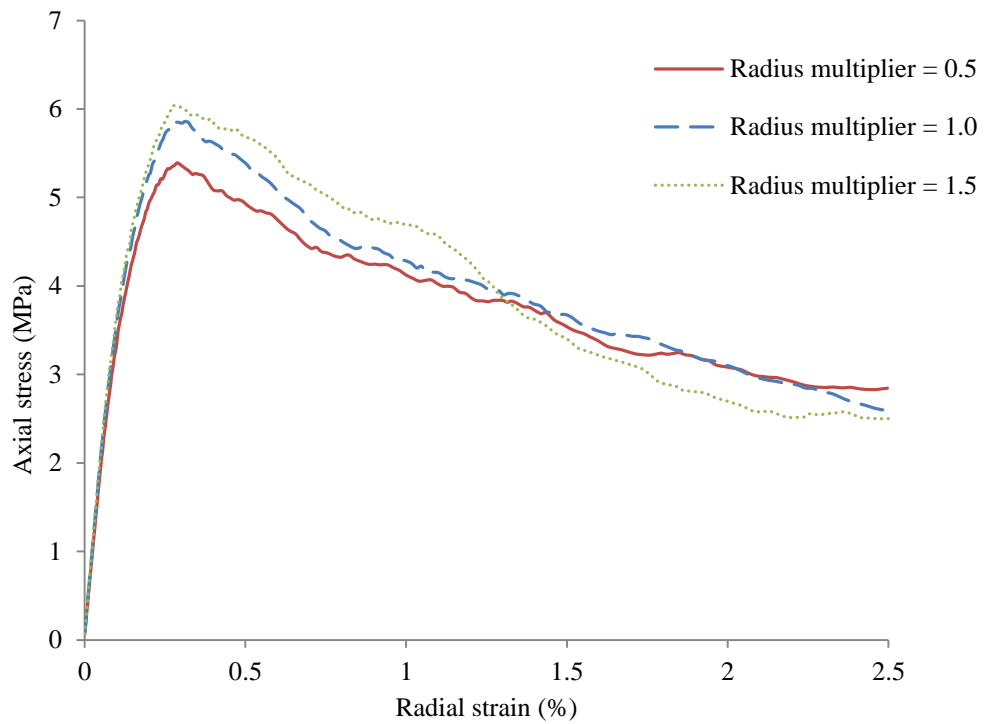
Figure 7.20 Axial stress versus radial strain for different radius multiplier based on Table 7.1

7.3.7 **Effect of friction coefficient**

Two simulations with different friction coefficients were performed; results are shown in Figure 7.21 and Figure 7.22. As can be seen, the initial "elastic" axial stress is independent of friction. The peak stress increases as the friction coefficient increases. This is due to the slip model in PFC3D. As the friction coefficient decreases the maximum allowable shear contact force decreases which leads to particles slipping more easily. Also, a higher friction coefficient causes more energy dissipation, hence, a wider post peak behaviour.
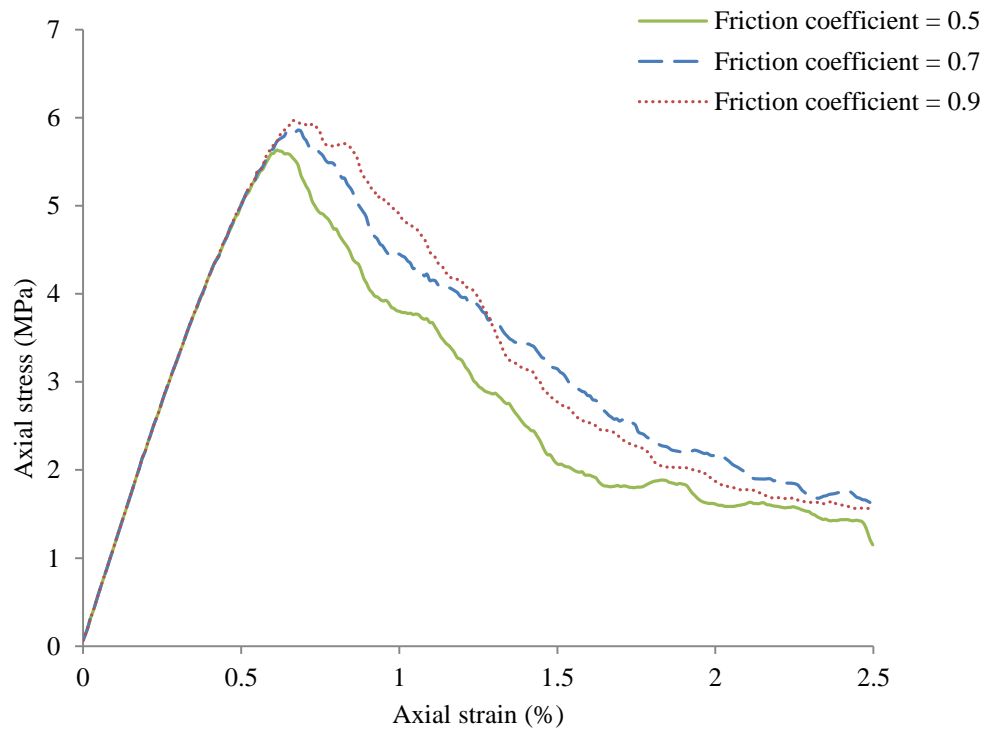
Figure 7.21 Axial stress versus axial strain for different friction coefficient
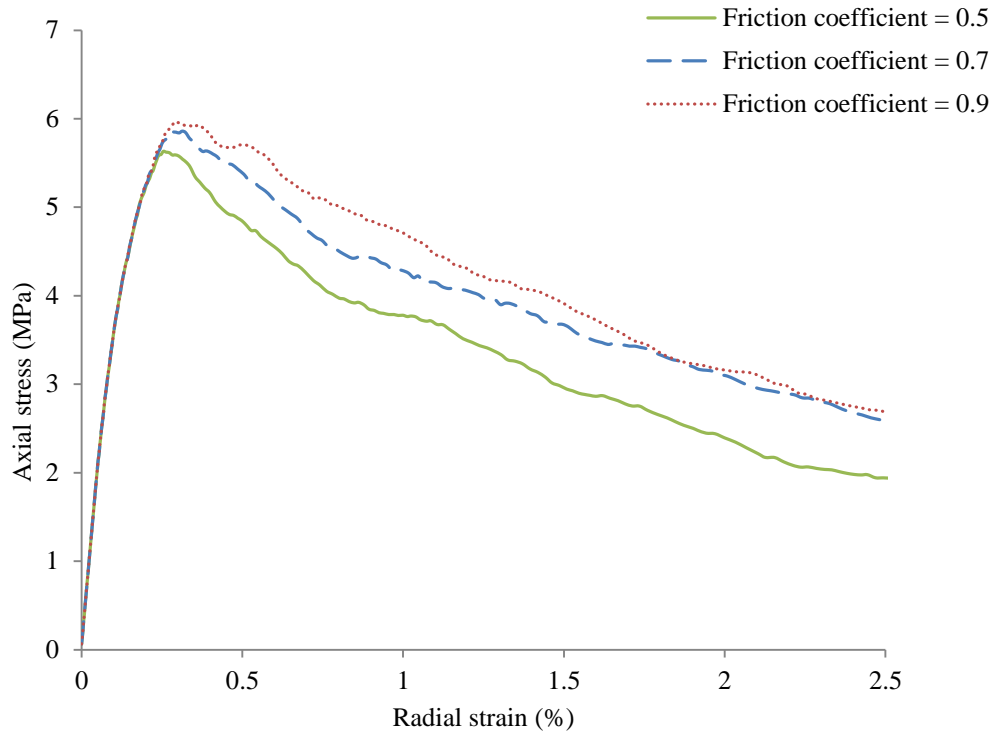
Figure 7.22 Axial stress versus radial strain for different friction coefficient

7.3.8 **Effect of bond strength distribution**

As noted from the above simulations, a single value of contact bond strength was used. However, in reality there is likely to be variation in bond strength. This section investigates the effect of different bond strength distributions. Three types of distributions were investigated: uniform distribution, normal distribution and Weibull distribution. The average values of bond strength of the following simulations have been set to be the same as for viscoelastic simulations (37 N).

7.3.8.1 **Uniform distribution**

Two simulations with a uniform distribution of bond strength were simulated with bond strength in the range of [0, 74] N and [17, 57] N, so that the average

bond strength is equal to 37. The simulation results for the uniform distributions are shown in Figure 7.23 and Figure 7.24. It can be seen that the slope just before the peak stress of the stress-strain curve reduces as the bond strength changes from a single value to uniform distribution. This is because for a uniform distribution of bond strengths, there will be some weaker bonds which break easily leading to the decrease of pre-peak slope of the stress-strain curve and peak stress. A wider post peak behaviour can be observed when the bond strength changes from a single value to a uniform distribution and is wider at a higher standard deviation for uniaxial simulations. In addition, a lower slope just before the peak stress of stress-strain curve can be observed at a higher standard deviation for uniform distributions.

Figure 7.23 Axial stress versus axial strain for uniform distribution
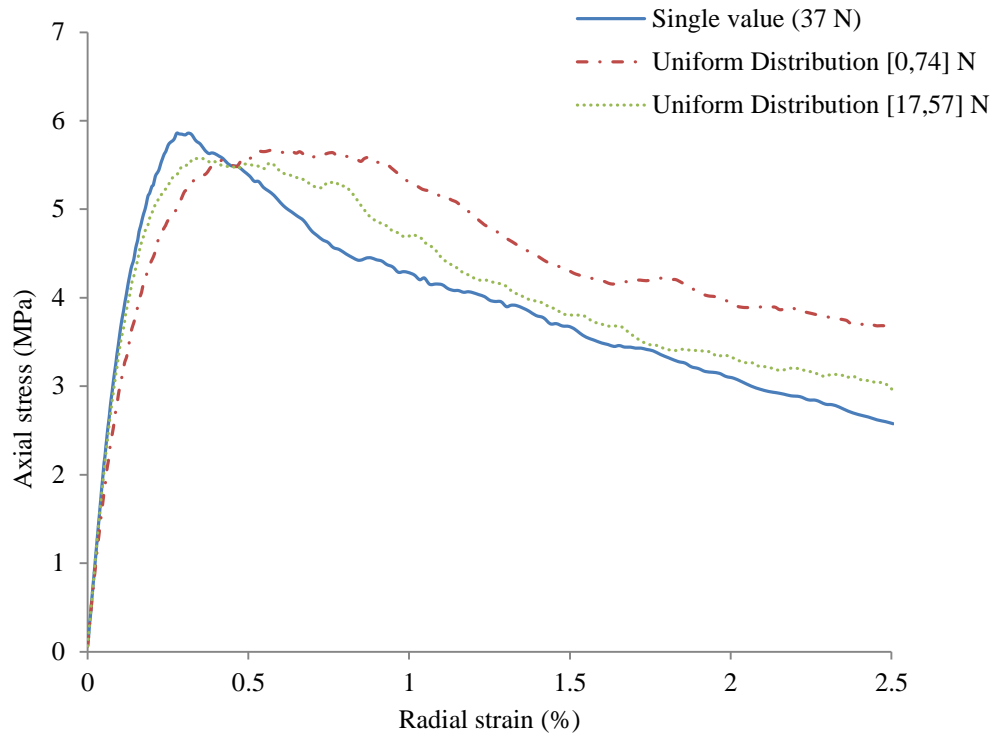
Figure 7.24 Axial stress versus radial strain for uniform distribution

7.3.8.2   **Normal distribution**

Two simulations with a normal distribution of bond strengths were performed

with a mean equal to a value of 37 N and standard deviations equal to 20 N and

40 N, respectively; see Figure 7.25. In PFC, when the bond strength value is set

to be less than zero, no contact bond will be created; in this case the bond

strength is not normally distributed any more. After consideration of the bond

strength values less than zero and replacing these strengths with zero values,

the bond strengths are now in distributions with mean equal to 37.09 N and

40.63 N and standard deviation equal to 19.58 N and 34.22 N, respectively.

The axial stress versus axial and radial strains are shown in Figure 7.26 and

Figure 7.27. As can be seen from the figures, the slope just before the peak

stress of the stress-strain curve decreases as the bond strength changes from

single value to a normal distribution. This is because when there is a

distribution of bond strengths, some contact bonds will be weaker or even have no contact bond where the bond strength is less than zero. A wider range of post peak softening behaviour is observed for a normal distribution of bond strengths. The post-peak behaviour becomes wider as the standard deviation increases.
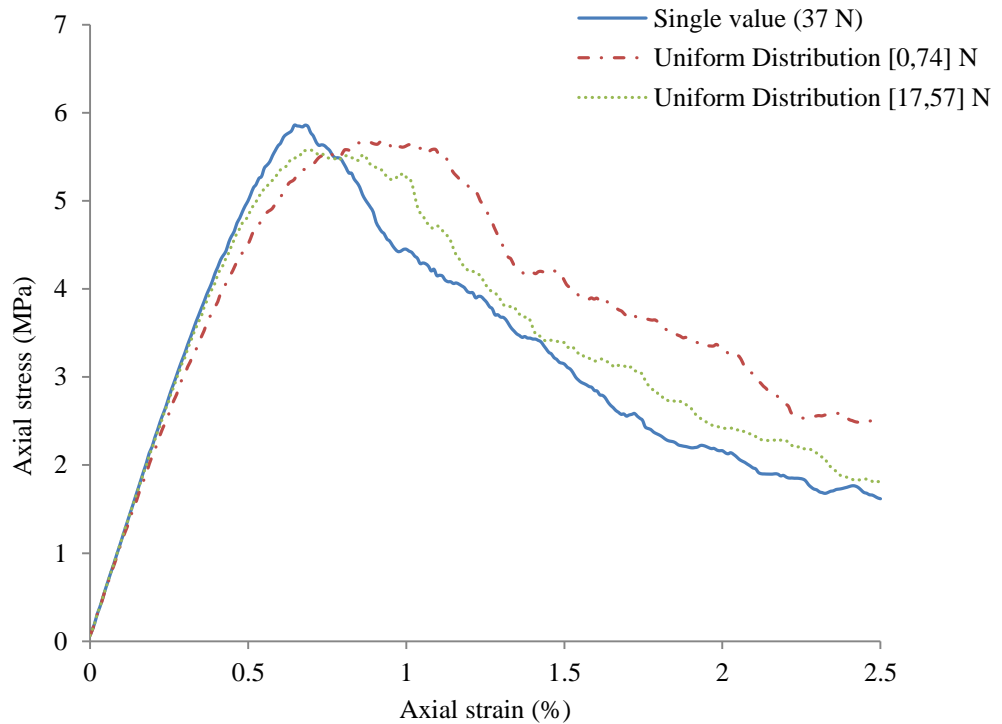

Figure 7.25 Normal distributions

Figure 7.26 Axial stress versus axial strain for normal distribution
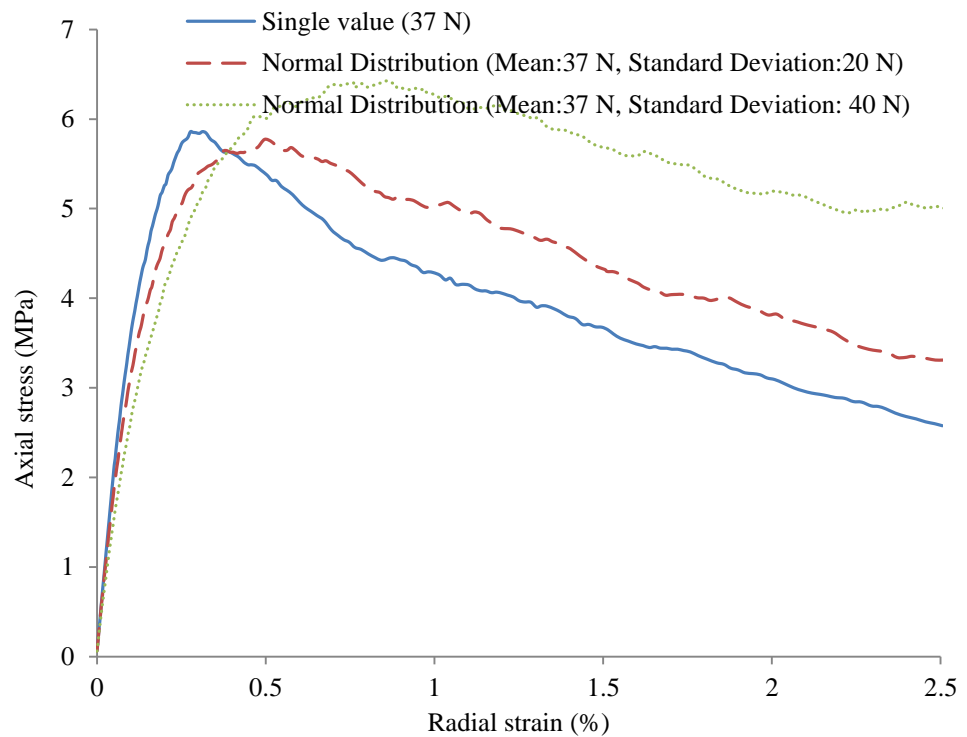
Figure 7.27 Axial stress versus radial strain for normal distribution

7.3.8.3 **Weibull distribution**

The probability density function of a Weibull distribution is given by (Weibull (1951)):

$$f(x;\alpha,m) = \frac{m}{\alpha}(\frac{x}{\alpha})^{m-1} e^{-(x/\alpha)^m} \quad x \geq 0 \tag{7.9}$$

where $m > 0$ is the shape factor relating to the coefficient of variation and $\alpha > 0$ is the scale factor (proportional to mean). McDowell et al. (2009) applied the Weibull statistics to tensile failure of soil grains compressed between flat platens. They proved that Weibull can reasonably be applied to the tensile failure of soil grains, thus validating the use of Weibull as a tool in the analysis of particle crushing

Two simulations with Weibull distributions of bond strength were simulated with a mean equal to 37 N and the modulus was set as 0.9 and 1.4, respectively, see Figure 7.28. The results have been plotted in Figure 7.29 and Figure 7.30. It can be seen that the slope just before the peak stress of the stress-strain curve decreases when the bond strength changes from single value to a Weibull distribution and increases as the modulus increases. This is for the same reasons as uniform and normal distributions. A wider range of post peak softening is also predicted compared with the single value of bond strength. The post-peak behaviour becomes wider as the modulus decreases.
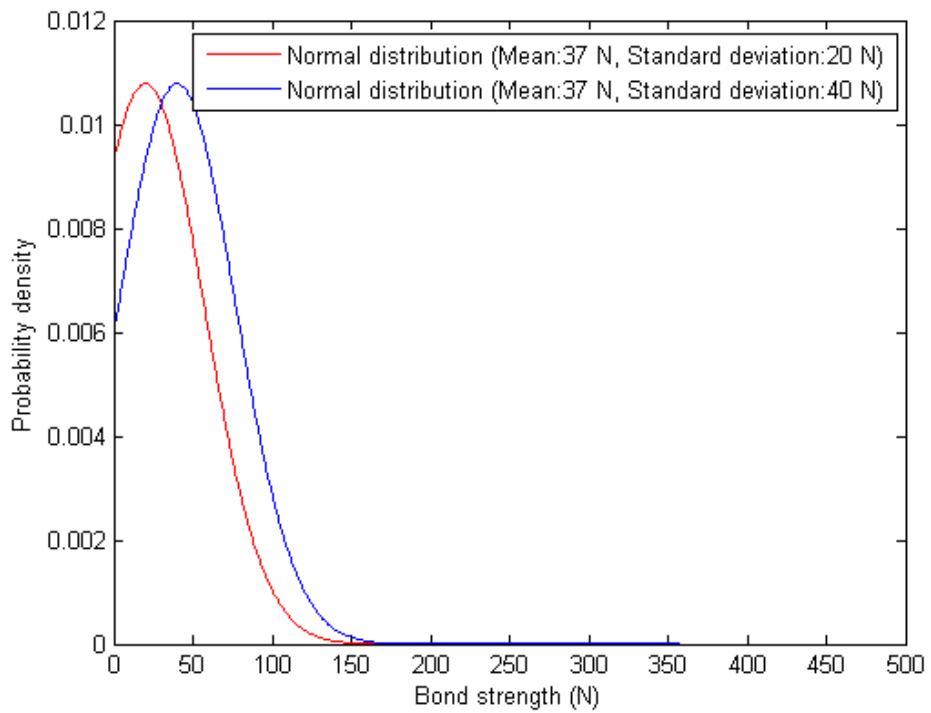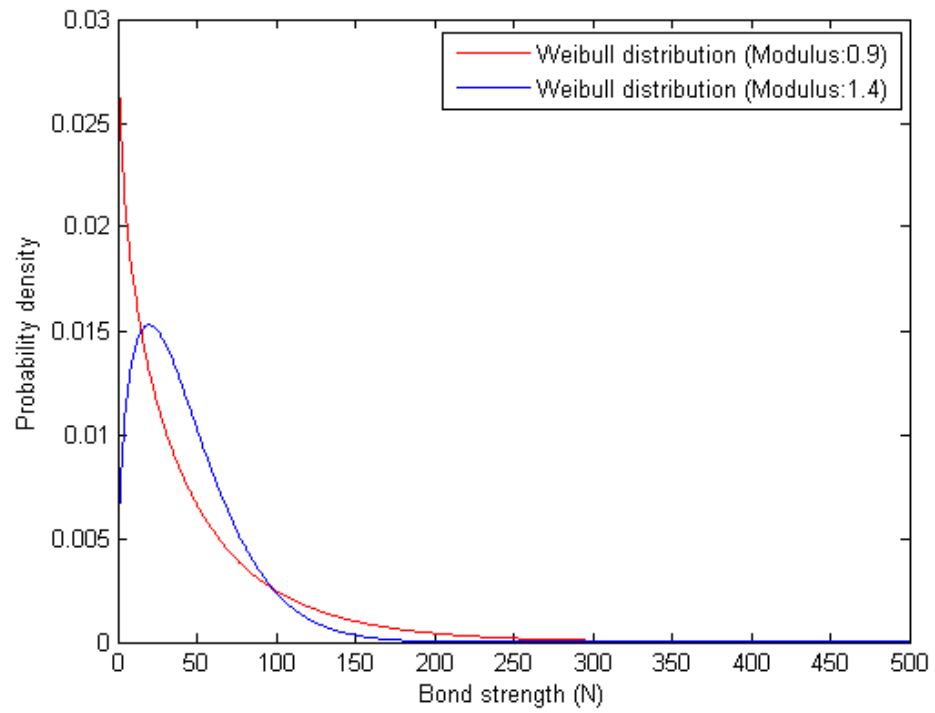
Figure 7.28 Weibull distributions
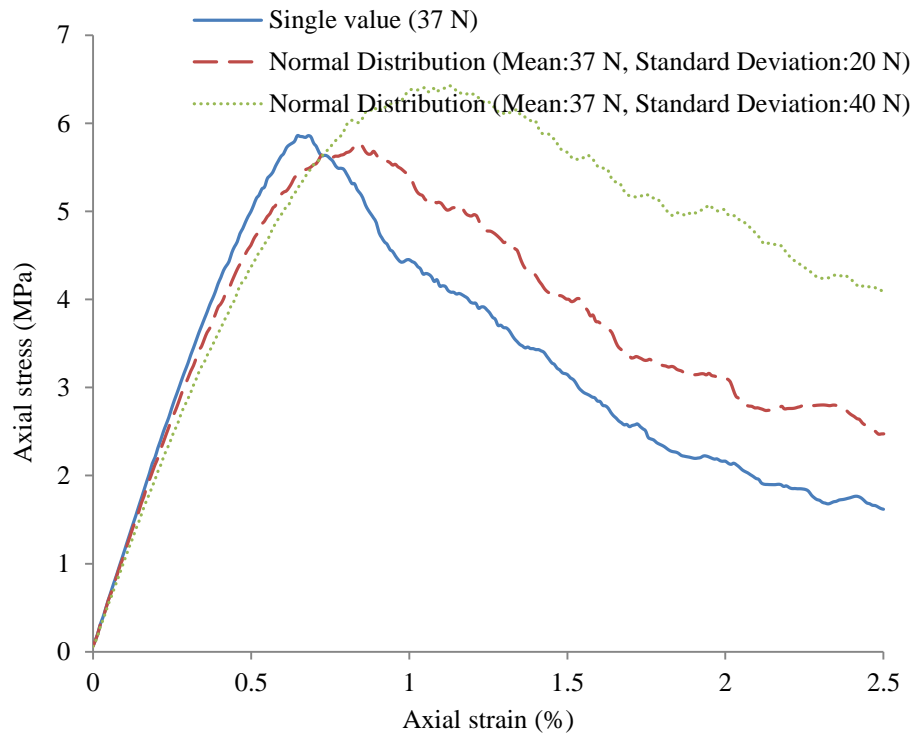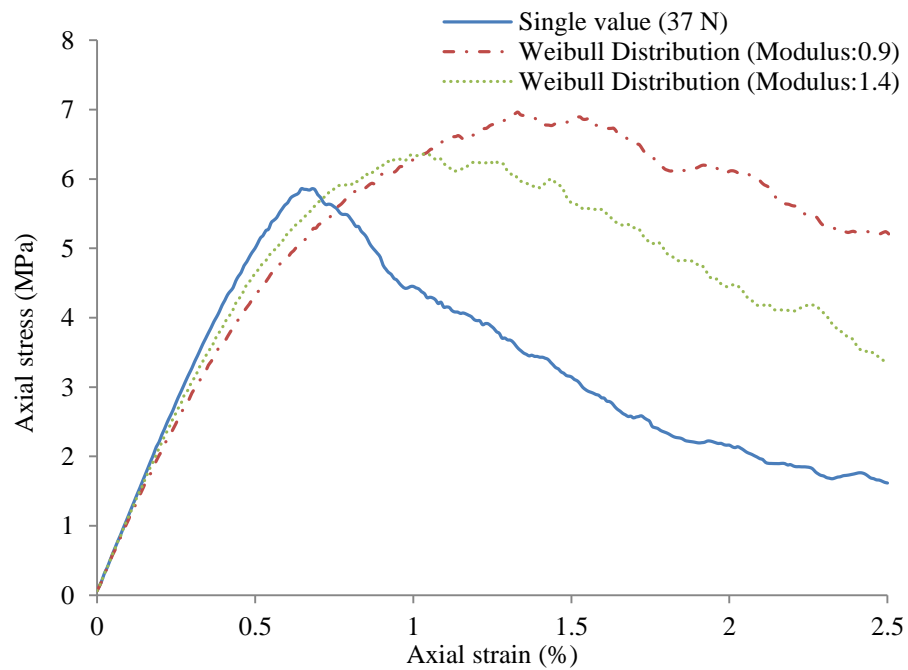

Figure 7.29 Axial stress versus axial strain for Weibull distribution
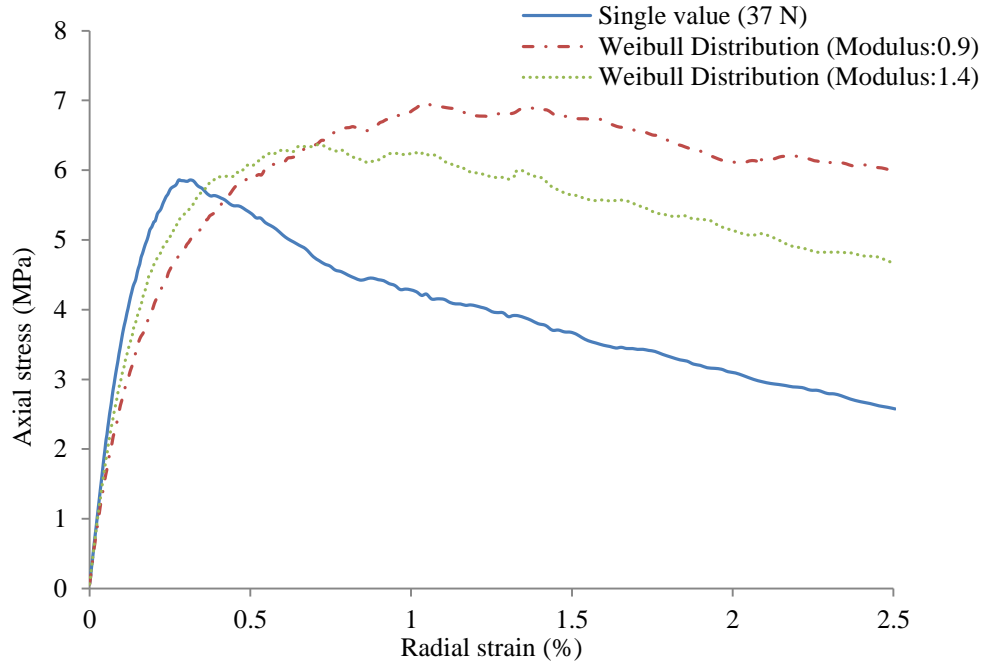
Figure 7.30 Axial stress versus radial strain for Weibull distribution

Based on the parametric study mentioned above, the modified Burger's model can be adjusted to simulate the uniaxial compression tests in the laboratory. Both the normal and Weibull distributions can be adjusted to simulate the pre-peak and post-peak behaviours for the stress-strain behaviour.

7.4 Constant strain rate test

The previous section presented the effects of the parameters on the behaviour of asphalt mixtures at constant strain rates. The modified Burger's model was shown to be suitable for the simulation of uniaxial constant strain rates. This section presents the use of the modified Burger's model to simulate the constant strain rate tests and the comparison with the laboratory results (chapter 5).

7.4.1 **Comparison with experimental results**

In the constant strain rate simulations, the normal and Weibull distribution have been used for the contact bond strengths. The mean and standard deviation for normal distribution were set as 50 N and 50 N, respectively. After consideration of all the bond strength values less than zero and replacing these strengths with zero values, the mean and standard deviation of this final distribution are calculated as 54 N and 44 N, respectively (Figure 7.31). This distribution will still be referred to as the normal distribution even through the non-zero part has effectively been replaced by an impulse function at zero strength. The modulus (shape parameter, m) and alpha (scale parameter, α) for Weibull distribution (Section 7.3.8.3) were set as 1.1 and 60 N, respectively, see Figure 7.31.
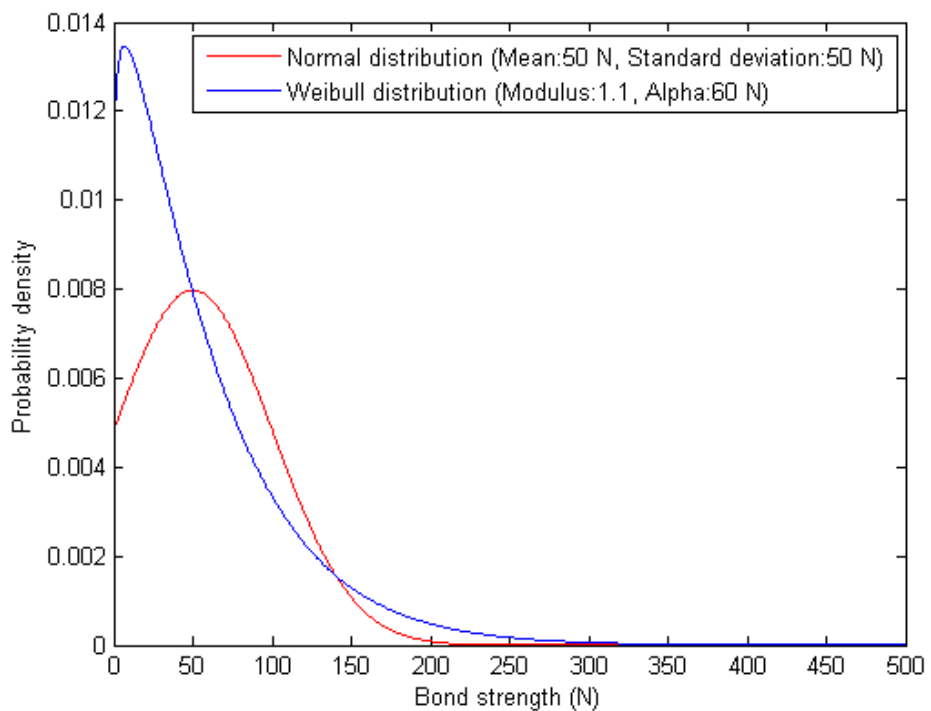
Figure 7.31 Bond strengths distributions

Chapter 7 Viscoelastic modelling

A factor of 100 was used to scale the loading speed and both viscosities for constant strain rate of $0.005s^{-1}$ simulations. The Burger's model parameters are shown in Table 7.2. These values were chosen based on the previous parametric study to produce reasonable numerical results similar to previously presented experimental data at a constant strain rate of $0.005s^{-1}$ (Figure 5.6) The Burger's parameters could have been calibrated at a different strain rate, and the then applied to the other two strain rates; however it is reassuring that in this case the chosen parameters have captured the essential features of the behavior across the three strain rates, even though the simulations do not match exactly the experimental over a large range of strain.

Burger's model parameters				N / S	λ	f
K_m^n (MN/m)	C_m^n (MNs/m)	K_k^n (MN/m)	C_k^n (MNs/m)			
110	680	0.8	170	11.	0.25	0.7

Table 7.2 Properties for the constant strain rate simulation

Based on the earlier reviews, asphalt is a viscoelastic material, the deformation behaviour of which depends on loading speed. Previous laboratory constant strain rate test results (see section 5.4.1) show that the peak stress is a function of strain rate and can be expressed by the a power-law formation equation (equation (5.2)). In the constant strain rate test simulations, the previously justified power-law exponent (n) of 0.325 has been used in scaling both the normal and shear bond strengths in the modelling for different loading speeds given by:

$$\left(\frac{\bar{\sigma}}{\bar{\sigma}_0}\right) = \left(\frac{\dot{\varepsilon}}{\dot{\varepsilon}_0}\right)^n \qquad (7.10)$$

where $\bar{\sigma}_0$ is the reference strength at the reference strain rate $\dot{\varepsilon}_0$.

A numerical specimen containing 6000 particles was generated according to the specimen preparation procedures as described previously in chapter 4. The stress-strain response for the simulations under three loading speeds were recorded as shown in Figure 7.32 and Figure 7.33 with the laboratory results. In the simulations, for lower strain rates (0.0005 and 0.00005 s^{-1}), both viscosities have been scaled instead of loading rate, because if both are scaled by the same factor as the strain rate, then this is equivalent as shown by dimensional analysis by McDowell et al. (2009). The results show good agreement between laboratory and simulations with bond strengths having normal and Weibull distortions (Figure 7.31). The quantitative differences between the numerical specimens and the experimental result for the softening behavior at a strain rate 0.005s-1 may result from the fact that in the numerical specimens, when a bond breaks the visco-elastic behavior at the contact vanishes and visco-elastic behavior is only possible in compression and shear if the contact reforms; however, in the laboratory specimens bitumen is present after bond breakage and thus visco-elastic behavior may still occur in compression, shear and torsion (not tension) if the adjacent particles should come into contact.
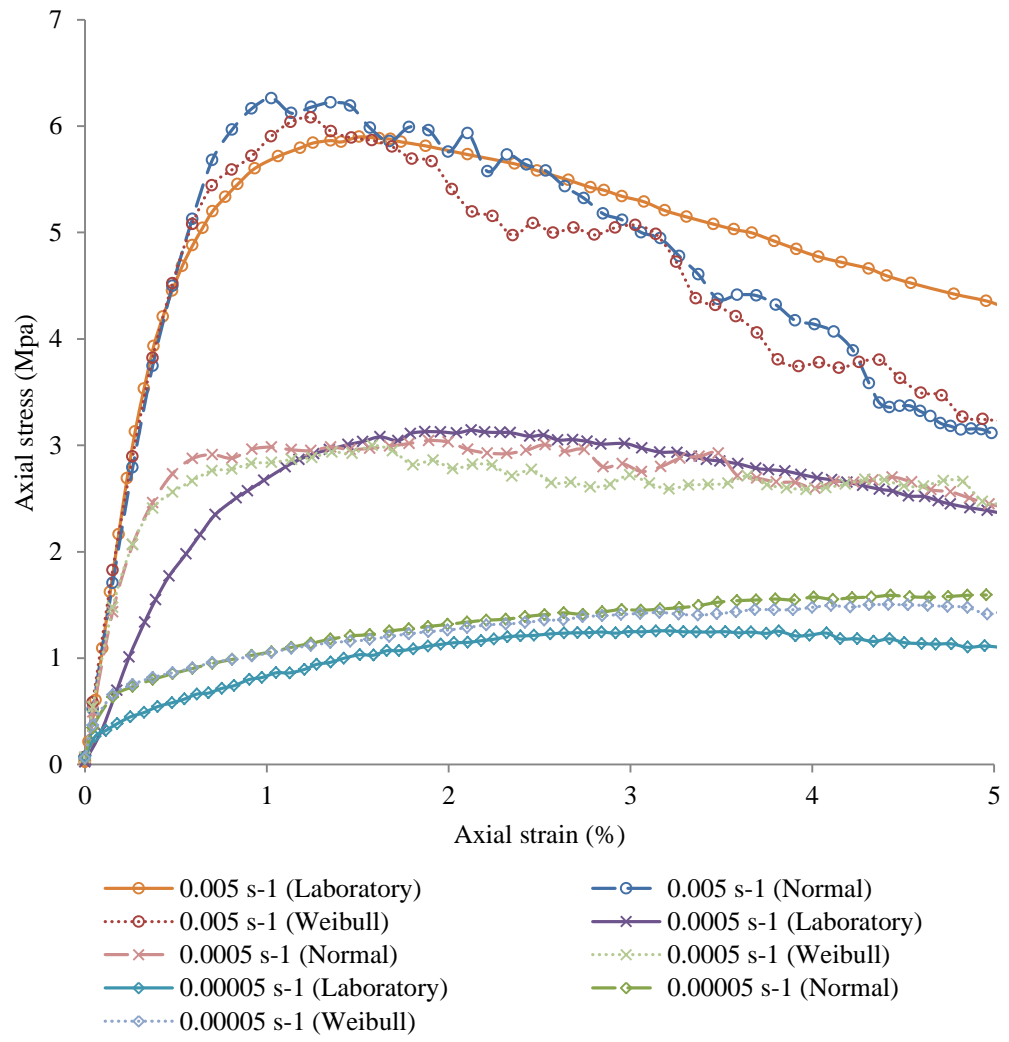
Figure 7.32 Axial stress versus axial strain curves for different bond strength distributions see Figure 7.31
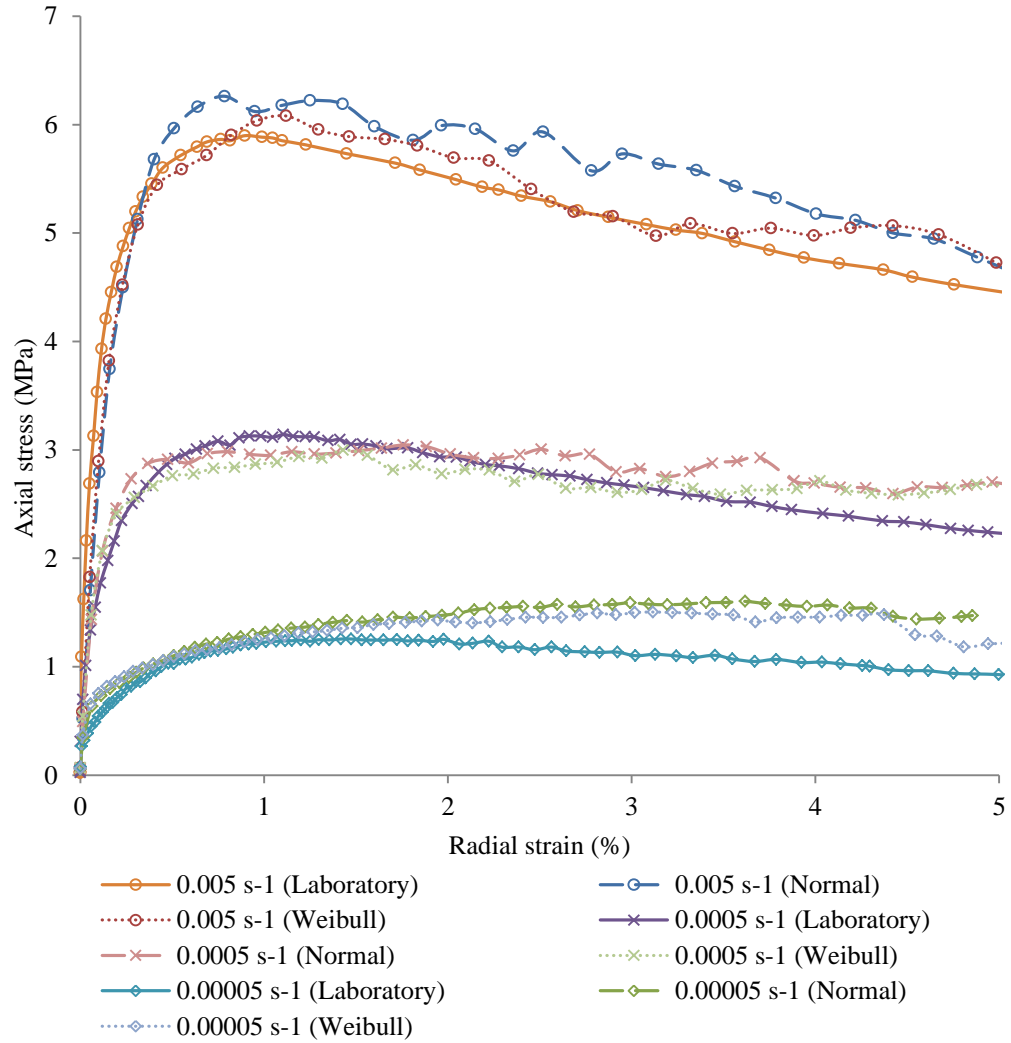
Figure 7.33 Axial stress versus radial strain curves for different bond strength distributions see Figure 7.31

7.4.2 **Bond breakage**

The percentages of the normal, shear and total bond breakage can be recorded during the simulations. Figure 7.34 to Figure 7.39 show the bond breakage for normal and Weibull bond strength distributions (Figure 7.31) at three strain rates. As can be seen, for all the strain rates, the bond breakage increases as the axial strain increases and the maximum rate of bond breakage occurs just before peak strength and the peak strength appears to coincide with the maximum curvature of the bond breakage versus axial strain plot. At lower

loading rates ($0.00005s^{-1}$) fewer bond breakages are observed. This is consistent with Figure 7.7 and Figure 7.8, in the sense that if peak strength corresponds to max rate of bond breakage, a higher loading rate or viscosity leads to larger contact forces, more bond breakage and more brittle behaviour.
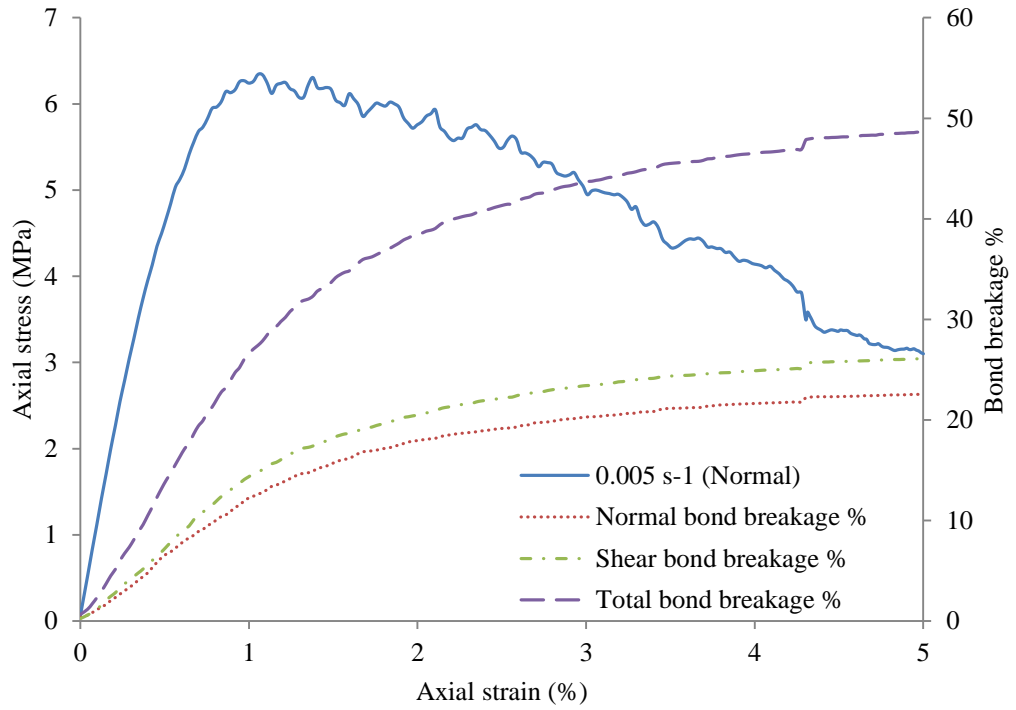
Figure 7.34 Bond breakage for normal distribution of bond strengths (Figure 7.31) at $0.005s^{-1}$
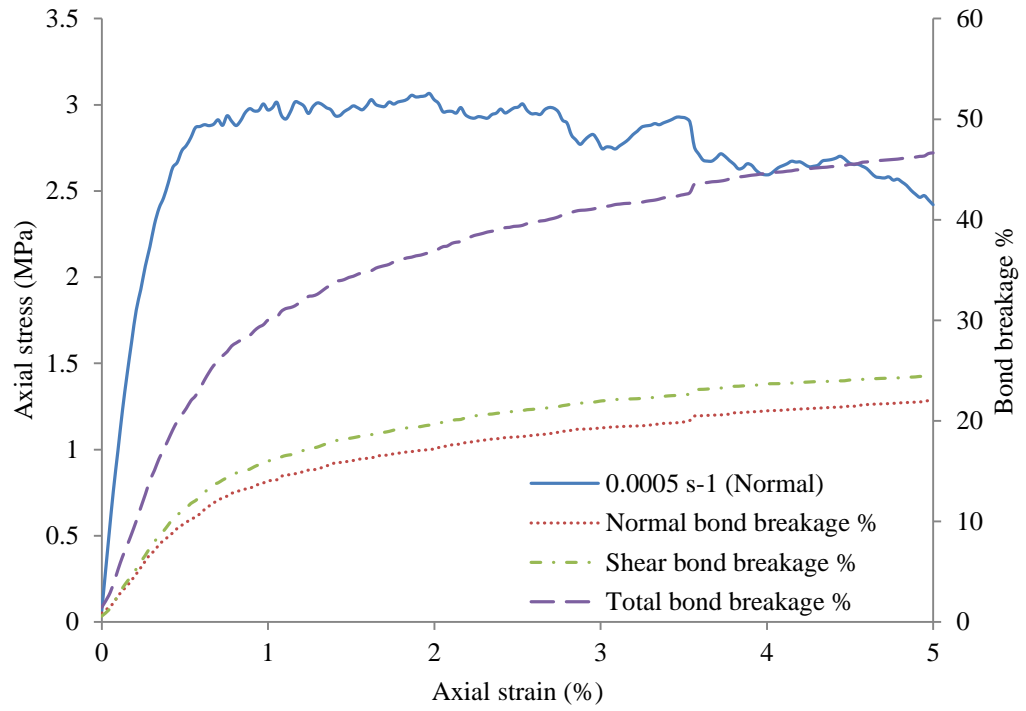
Figure 7.35 Bond breakage for normal distribution of bond strengths (Figure 7.31) at 0.0005s^{-1}
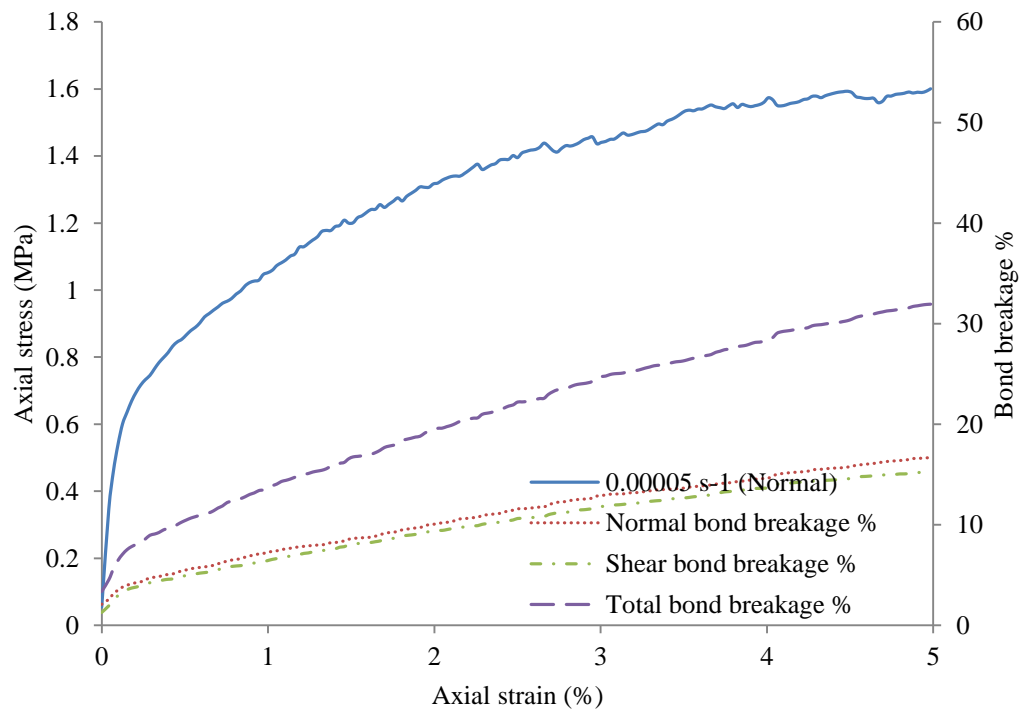
Figure 7.36 Bond breakage for normal distribution of bond strengths (Figure 7.31) at 0.00005s^{-1}
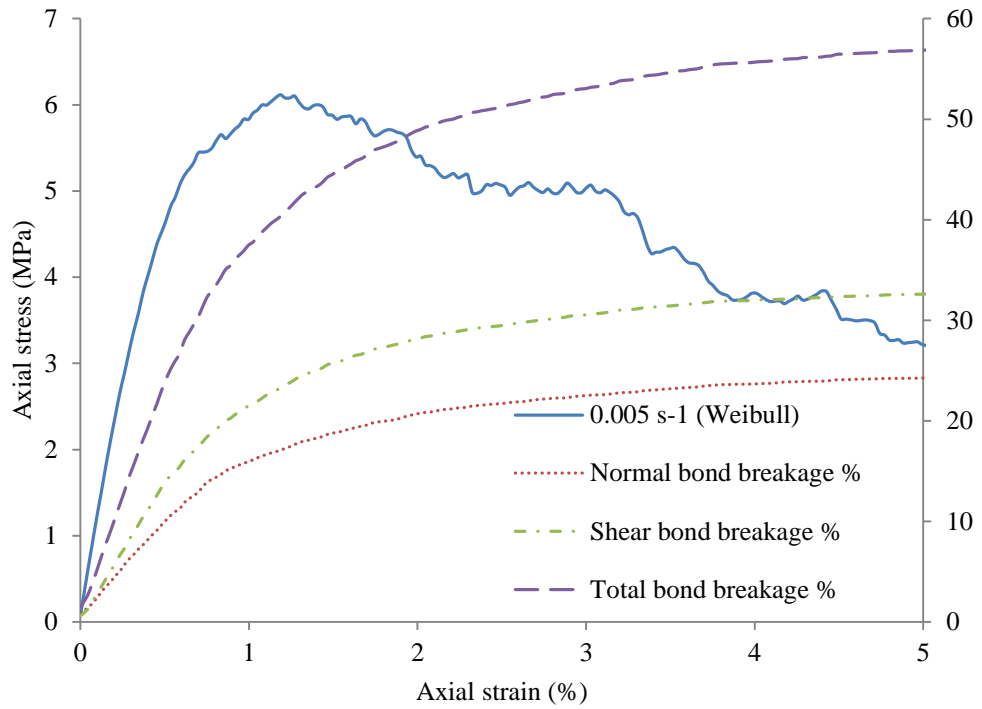
Figure 7.37 Bond breakage for Weibull distribution of bond strengths (Figure 7.31) at 0.005s^{-1}
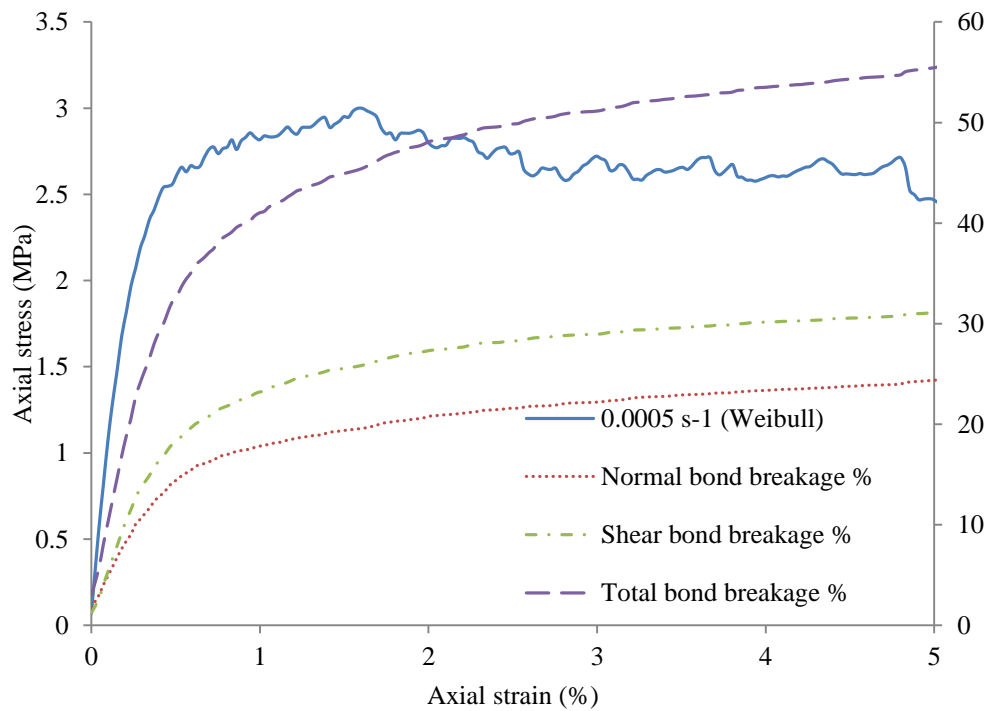
Figure 7.38 Bond breakage for Weibull distribution of bond strengths (Figure 7.31) at 0.0005s^{-1}
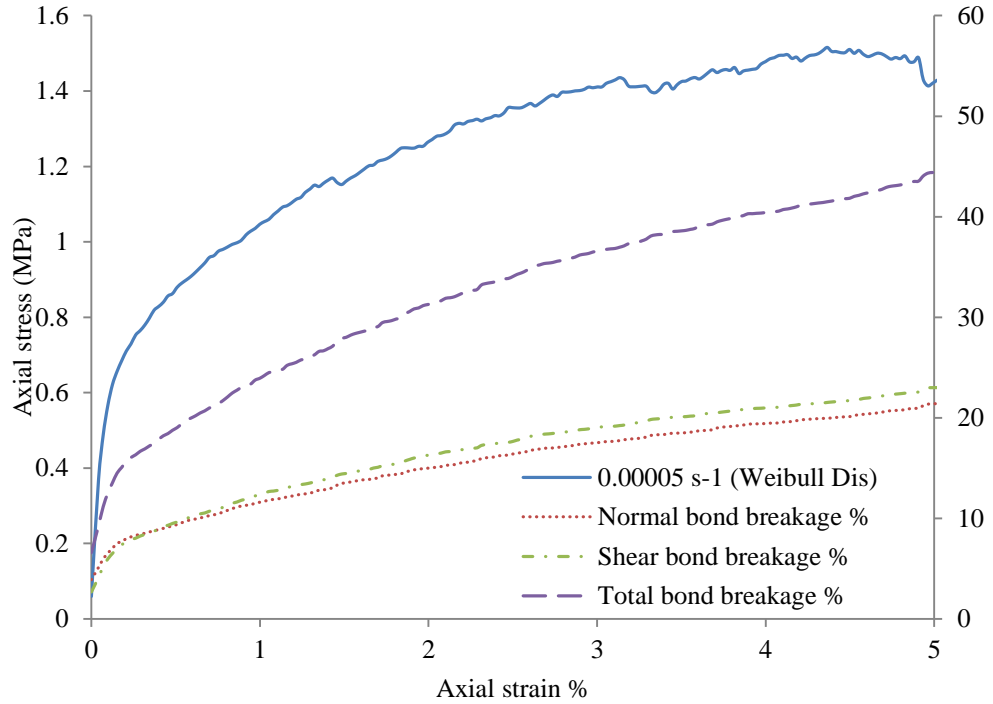
Figure 7.39 Bond breakage for Weibull distribution of bond strengths (Figure 7.31) at
0.00005s^{-1}

Figure 7.40 shows the damage modes and locations of broken bonds at different axial strain levels for a constant strain rate of 0.005 s^{-1} with a normal distribution of bond strengths (Figure 7.31). A red circle represents the bond breaking in the normal direction and a black circle represents the bond breaking in the shear direction.

As can be seen, the micro-cracks in both normal and shear damage modes are uniformly distributed throughout the specimen. An increase in the number of micro-cracks can be observed as the axial strain increases. Few micro-cracks (individual bond breakages) are observed at an axial strain of 0.5%, indicating that the damage to the specimen at this level of strain is largely internal. However, at an axial strain of 1% a dramatic increase in the number of micro-cracks is observed indicating that macroscopic cracks (a number of adjacent

bond breakages) are forming in the specimen where it is associated with onset of the post peak softening region in Figure 7.34.

Axial strain = 0.5%   Axial strain = 1%

Axial strain = 1.5%   Axial strain = 2%
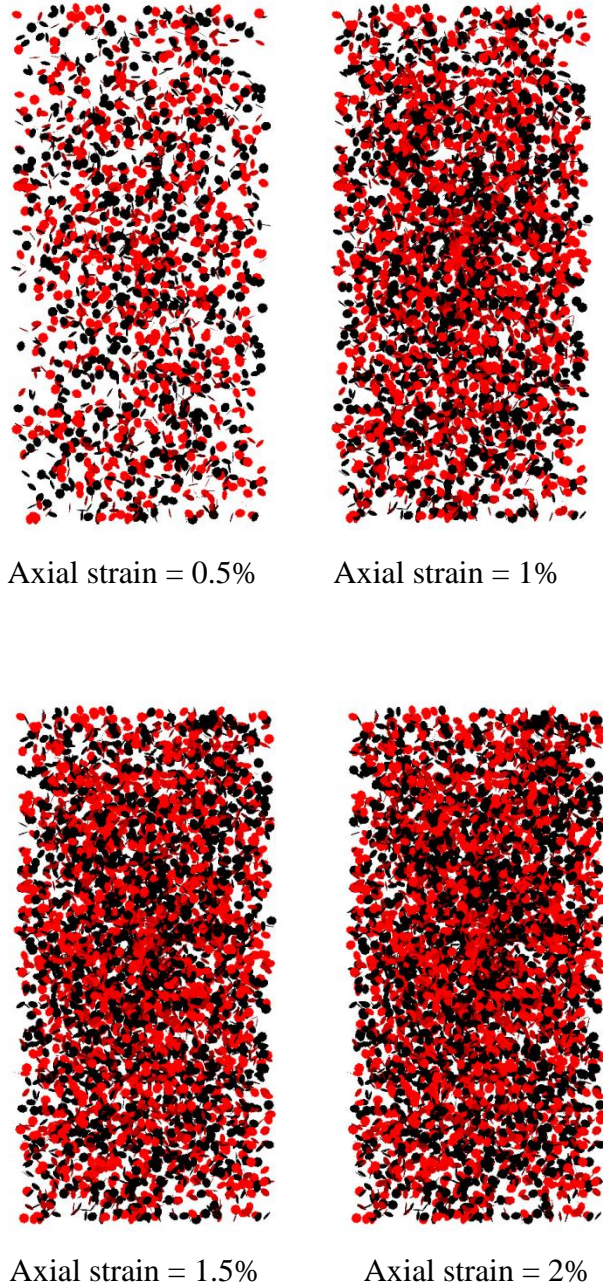
Figure 7.40 A front view of bond breakage throughout the specimen at different axial strain
(red- normal breakage; black- shear breakage)

7.4.3 **Effect of random bond strength distribution**

As mentioned before, the bond strengths follow alternative normal and Weibull distributions. During the simulations, values of bond strengths are randomly chosen from the normal or Weibull distributions using a random number seed. Therefore, even for the same distribution, different bond strength values could be applied to the same contacts in different simulations with a different seed. To understand the effect of the variability in the bond strengths, two more simulations with the same normal and Weibull bond strength distributions (Figure 7.31) but different random values were modelled. The results are shown in Figure 7.41, Figure 7.42, Figure 7.43 and Figure 7.44. As can be seen, the axial stress is approximately independent of the variability of the bond strengths for each strain rate. The small differences in behaviour appearing after the peak stress is due to contact bonds breaking at different times and positions due to the variability of bond strengths.
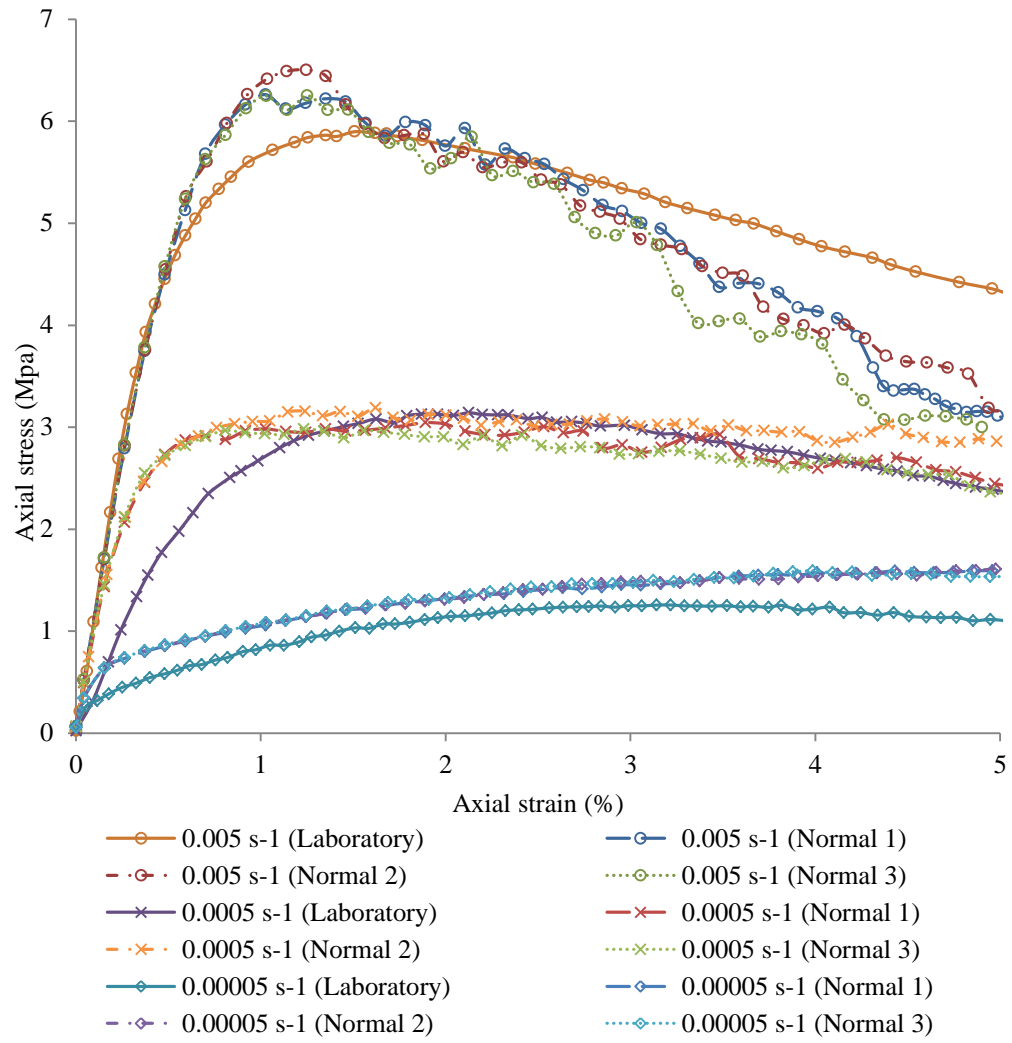
Figure 7.41 Axial stress versus axial strain for three normal distributions of bond strengths (Figure 7.31) and laboratory tests
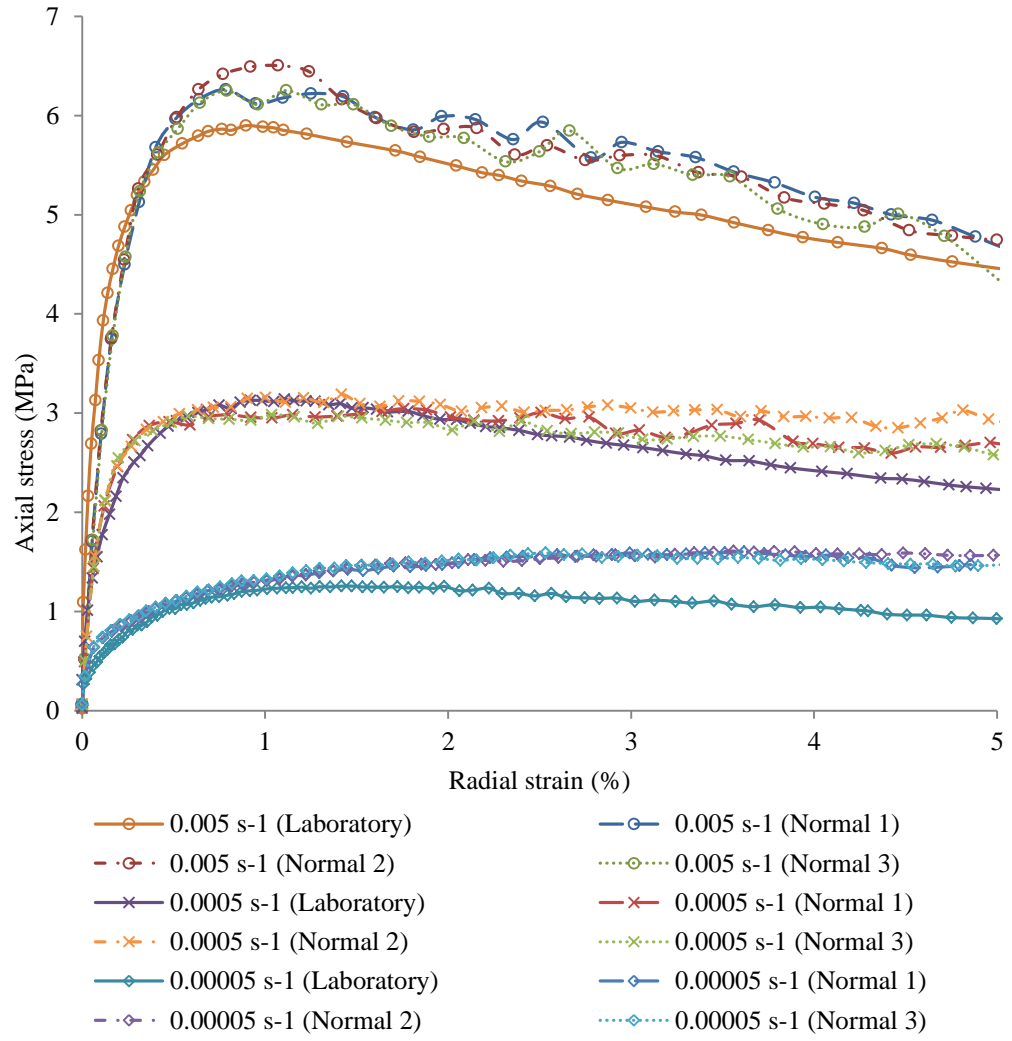
Figure 7.42 Axial stress versus radial strain for three normal distributions of bond strengths (Figure 7.31) and laboratory tests
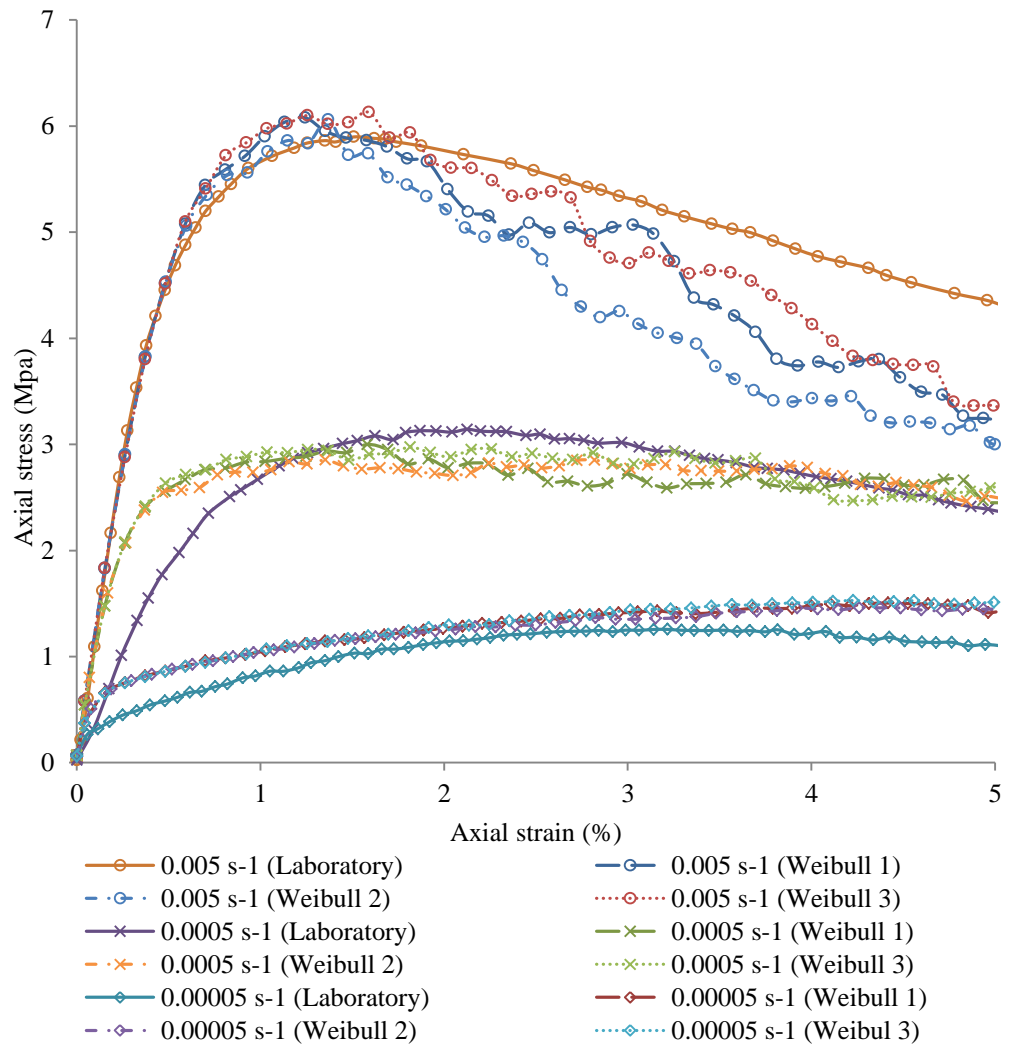
Figure 7.43 Axial stress versus axial strain for three Weibull distributions of bond strengths (Figure 7.31) and laboratory tests
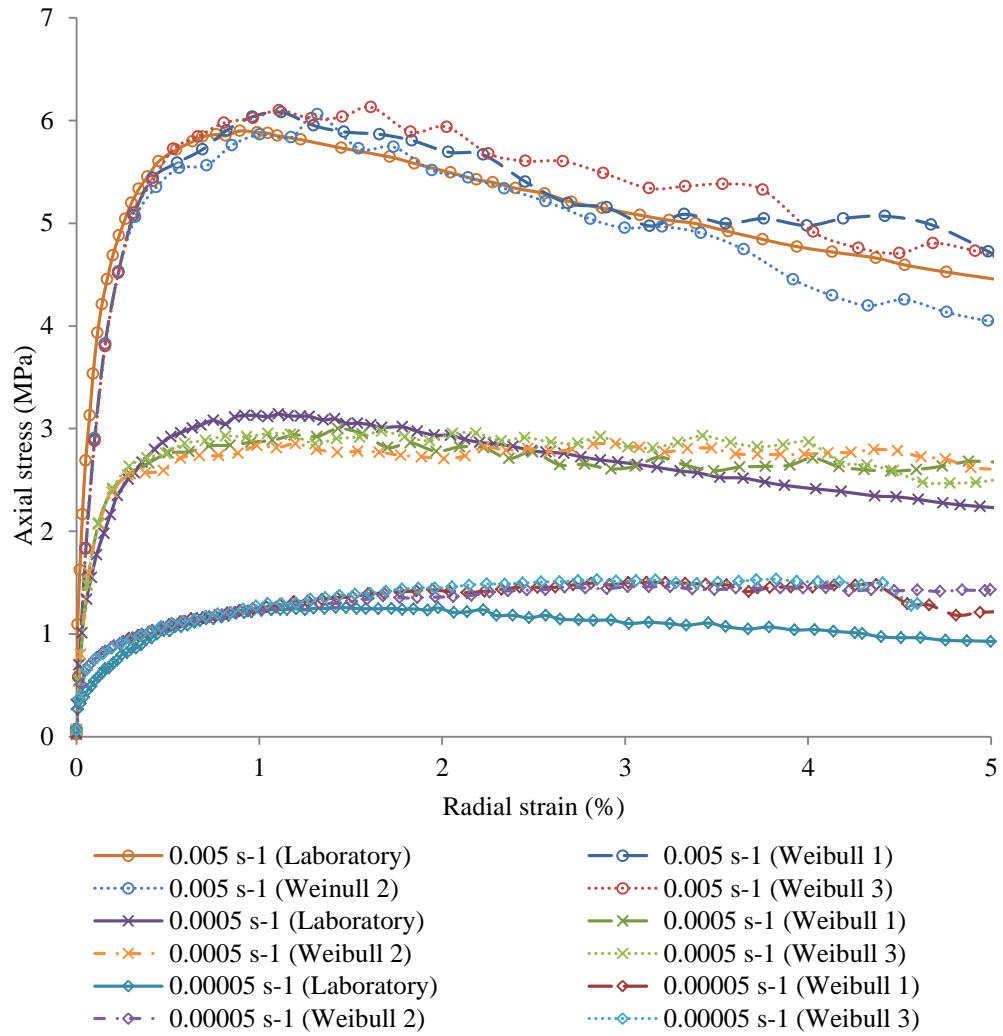
Figure 7.44 Axial stress versus radial strain for three Weibull distributions of bond strengths (Figure 7.31) and laboratory tests

7.4.4 **Effect of particle positions**

The numerical specimen preparation method randomly places the particles in a pre-defined area using a random number seed. Several separate constant strain rate simulations have been performed with 6000 particles in different random positions, at strain rates of $0.05s^{-1}$ $0.0005s^{-1}$ and $0.00005s^{-1}$ for both the normal and Weilbull distributions of bond strengths in Figure 7.31. The specimen Burger's model parameters were set to be the same as in previous sections (Table 7.2). The results of axial stress as a function of axial strain and radial

strain are shown in Figure 7.45, Figure 7.46, Figure 7.47 and Figure 7.48. It can be seen that the variability in the stress-strain behaviour caused by the random positions of the particles in constant strain rate simulations is negligible for each strain rate.
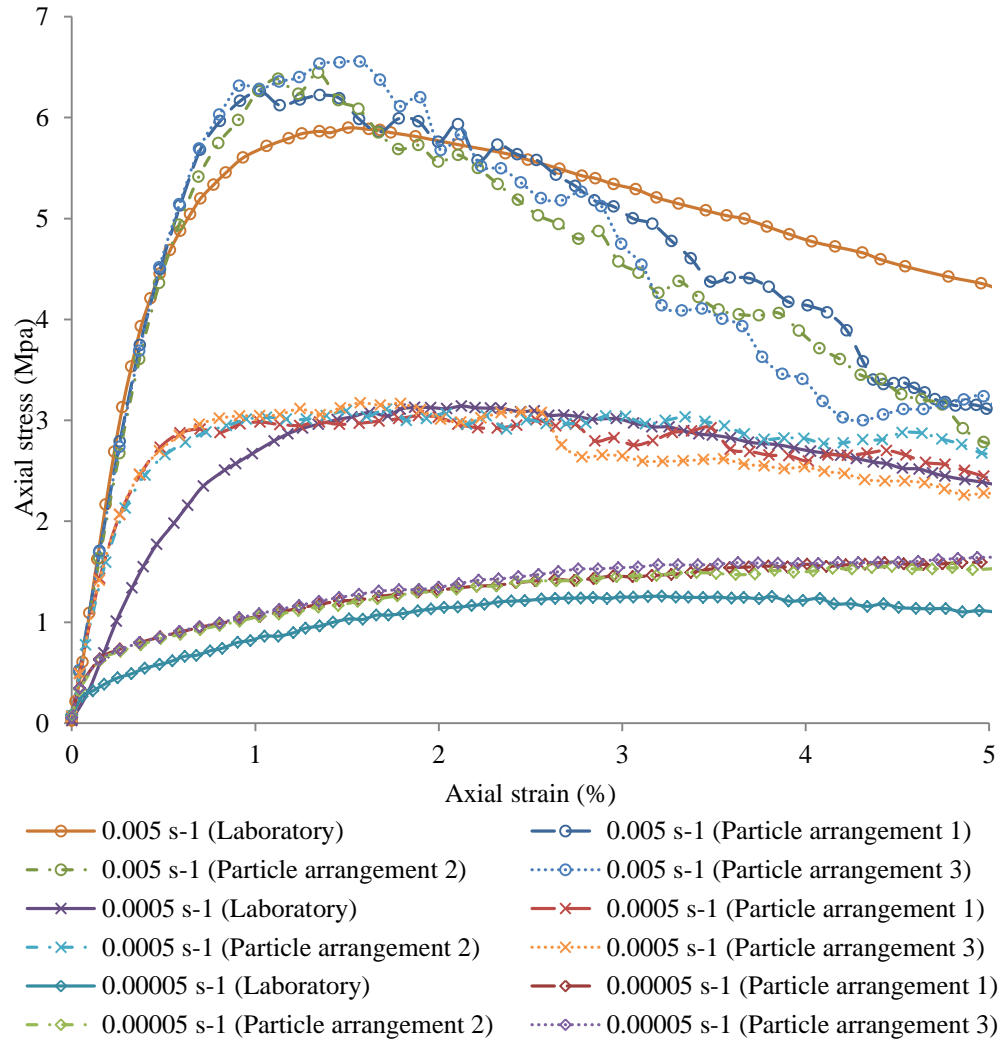
Figure 7.45 Effect of particle positions for normal distribution of bond strengths (Figure 7.31) on axial stress vs axial strain
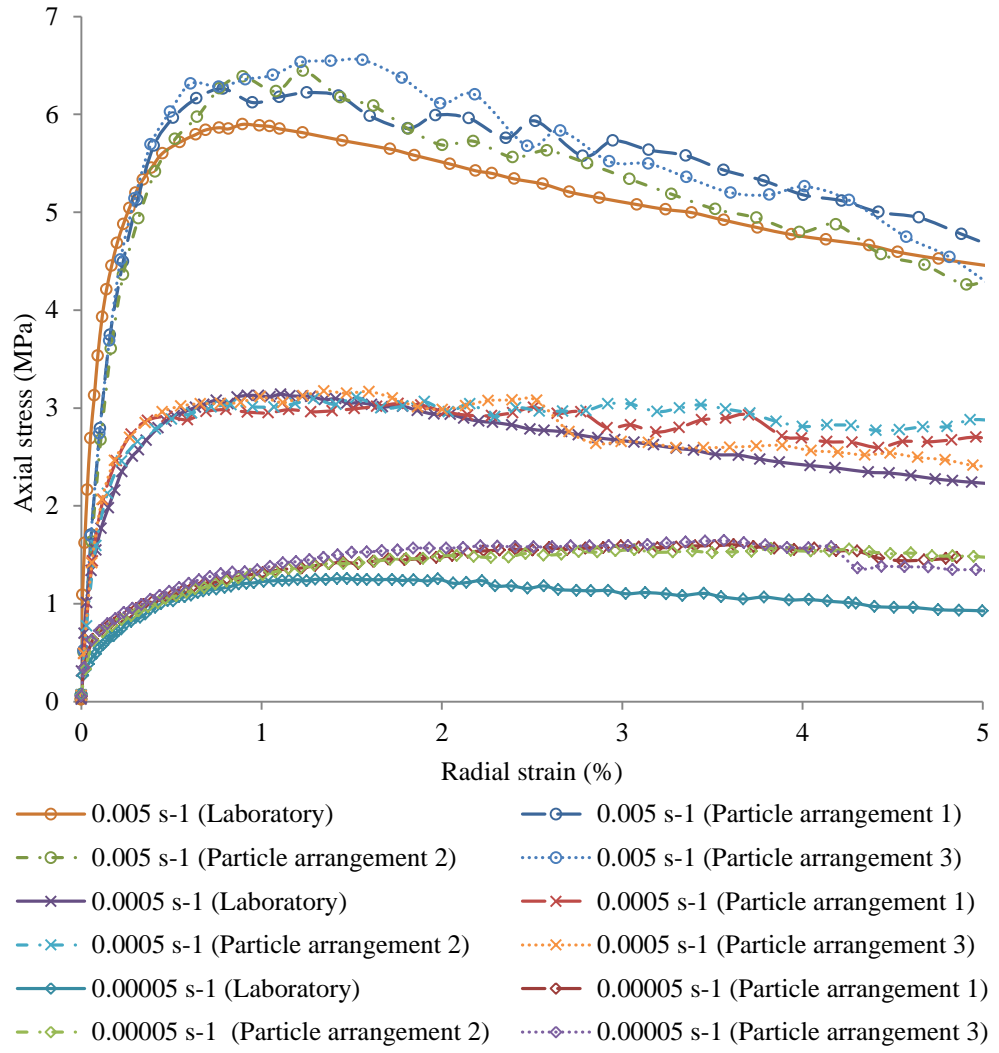
Figure 7.46 Effect of particle positions for normal distribution of bond strengths (Figure 7.31) on axial stress vs radial strain
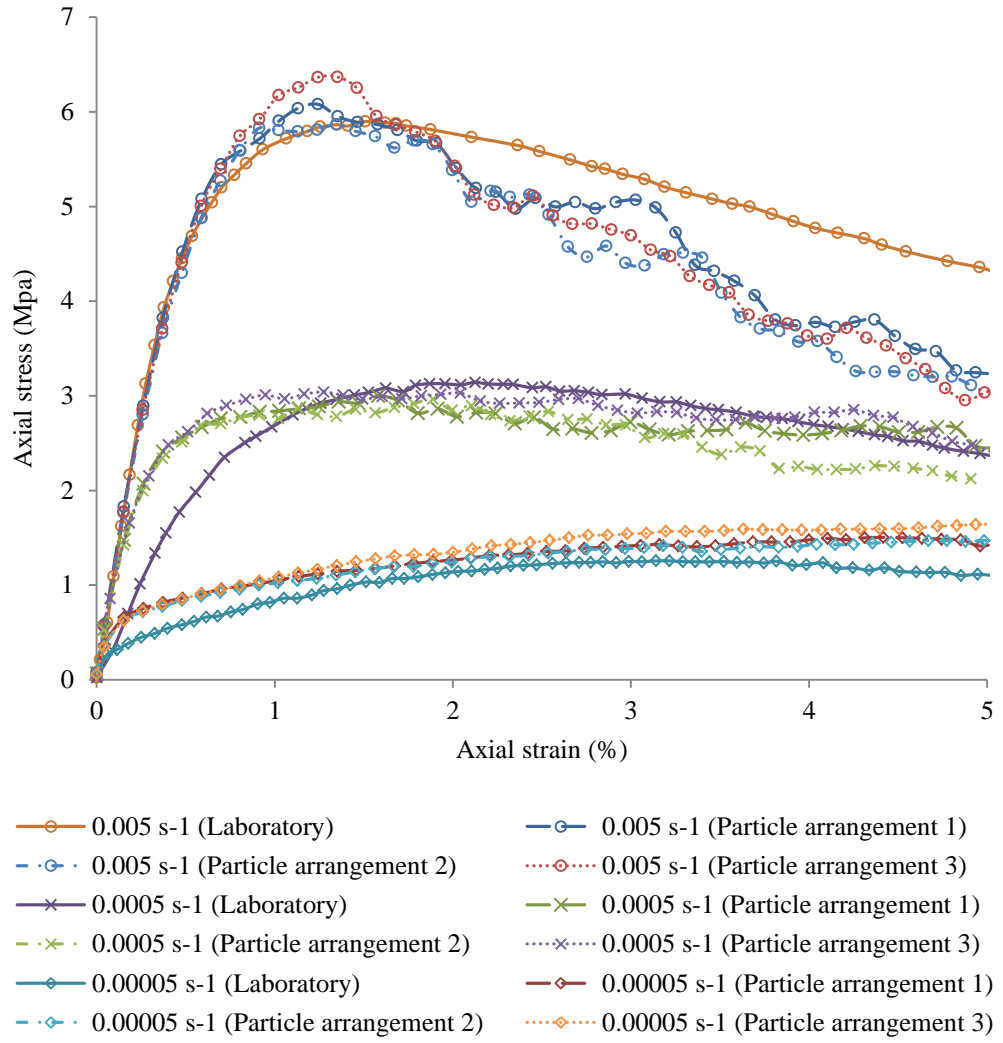
Figure 7.47 Effect of particle positions for Weibull distribution of bond strengths (Figure 7.31) on axial stress vs axial strain
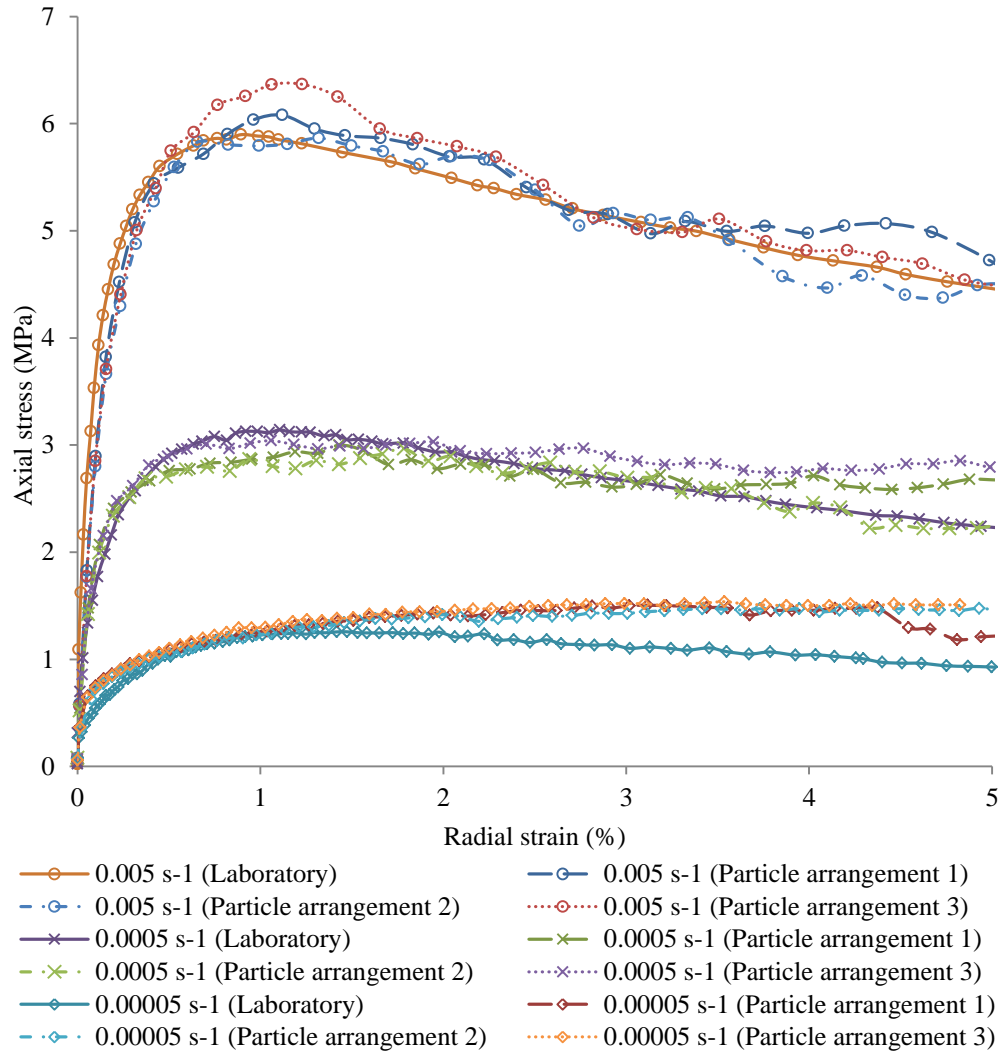
Figure 7.48 Effect of particle positions for Weibull distribution of bond strengths (Figure 7.31) on axial stress vs radial strain

7.4.5 **Effect of number of particles**

As introduced in section 6.3, a minimum of 6000 particles are required in the simulation to obtain reasonable estimates of bulk elastic modulus and Poisson's ratio. To understand the effect of the number of particles on the stress-strain behaviour in the viscoelastic simulations, two simulations were performed for a numerical specimen with 10000 particles produced by the method mentioned in chapter 4. The Burger's contact parameters were set as in Table 7.2. The bond strengths followed either the normal or Weibull distributions used previously

(Figure 7.31). The simulations are shown in Figure 7.49 and Figure 7.50. It can be seen that 6000 particles are enough to obtain a reasonable prediction of the stress-strain behaviour of constant strain rate tests on asphalt mixtures.
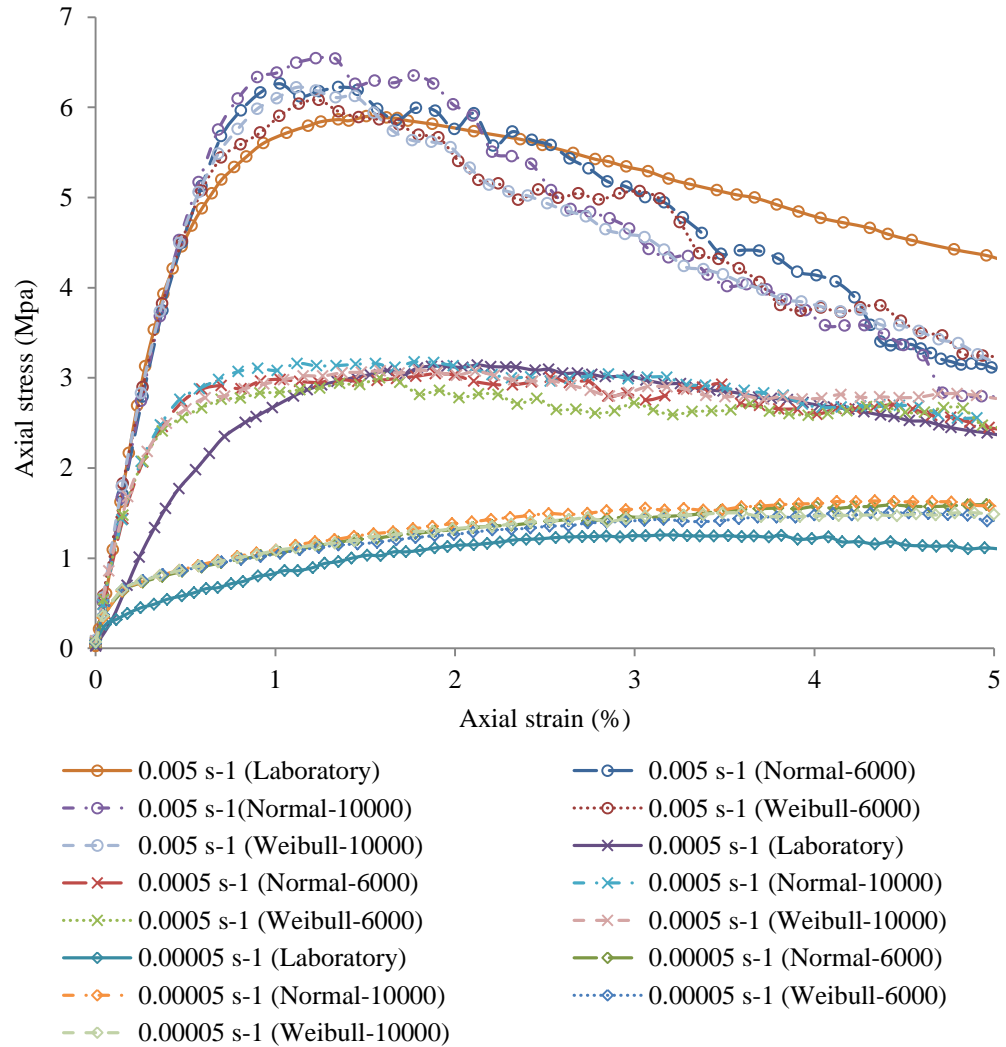
Figure 7.49 Axial stress against axial strain for different numbers of particles, compared to laboratory tests
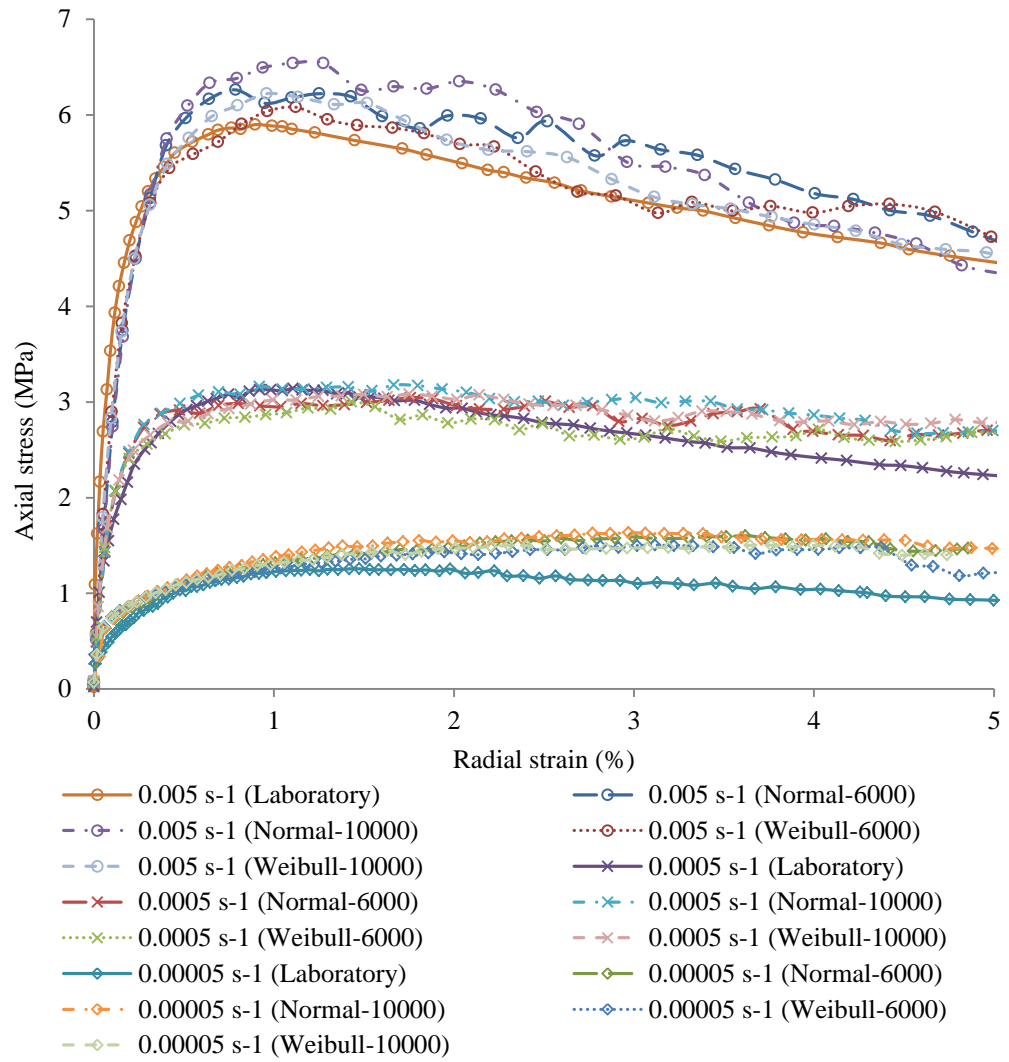
Figure 7.50 Axial stress against axial strain for different numbers of particles, compared to laboratory tests

7.5   Creep test

The previous section presented the use of the modified Burger's model to simulate the uniaxial constant strain rate test. A good agreement between laboratory and simulation results was observed. This section represents the use of the modified Burger's model and the same numerical specimen and parameters as the constant strain rate test, to simulate creep tests, in order to ascertain if the same numerical specimens can give creep behaviour which is in agreement with experimental data.

7.5.1 **Dimensional analysis**

It has been noted earlier that DEM is very time consuming. It is highly desirable to develop new methods which are sufficient to describe the 3D mechanical behaviour but which keeps computational time to a minimum. McDowell et al. (2009) derived a scaling method by using dimensional analysis for viscosities and velocity in DEM of strain control tests on asphalt. They proved that the effect of scaling applied velocity is the same as that of scaling both viscosities in the Burger's model by the same factor. For a creep test, the dimensional analysis can also be used to accelerate the DEM simulations.

The analytical expression for the time-deformation response captured by the Burger's model to a force F_0 applied at time $t = 0$ is given by:

$$\delta(t) = F_0 \left[\frac{1}{K_m} + \frac{t}{C_m} + \frac{1}{K_k} \left(1 - e^{-tK_k/C_k} \right) \right] \tag{7.11}$$

Based on equation (7.11), the deformation can be written as a function of the following 6 physical parameters:

$$\delta(t) = f(K_k, K_m, C_k, C_m, F, t) \tag{7.12}$$

As indicated, the six parameters contain three physical dimensions: Length L, mass M, and time T. Based on the dimensional analysis, the physics of the problem can be described in terms of one dependent dimensionless group and three independent dimensionless groups. One of the possibilities is:

$$\frac{uK_k}{F} = G\left(\frac{K_m t}{C_m}, \frac{K_k t}{C_k}, \frac{C_m}{C_k}\right) \tag{7.13}$$

It is now evident that if C_k and C_m are both increased/decreased by the same factor x, then this is equivalent to scaling time by $1/x$.

The displacement calculated from equation (7.11) is plotted against time in Figure 7.51 using the parameters given in Table 7.3. Figure 7.52 shows the analytical solution for the case which scales down both viscosities by a factor of 10. From Figure 7.51 and Figure 7.52, it can see that, for the same displacement (0.3m), the unscaled case takes 2000s while the scaled case only needs 200 s. Figure 7.53 shows the analytical solution for unscaled parameters and time and both viscosities scaled by a factor of 10. The two curves are identical, demonstrating that equation (7.13) is correct.

You et al. (2011) developed an approach to reduce the computational time with a Time-Temperature Superposition (TTS) principle. They also proved that the same creep compliance can be determined by scaling the Burger's viscosities and by scaling time. This scaling method will be used in the creep simulations in this project to reduce the computational time.

Maxwell stiffness kN/m	Maxwell viscosity kNs/m	Kelvin stiffness kN/m	Kelvin viscosity kNs/m
80	680	50	680

Table 7.3 Burger's contact parameters for dimensional analysis
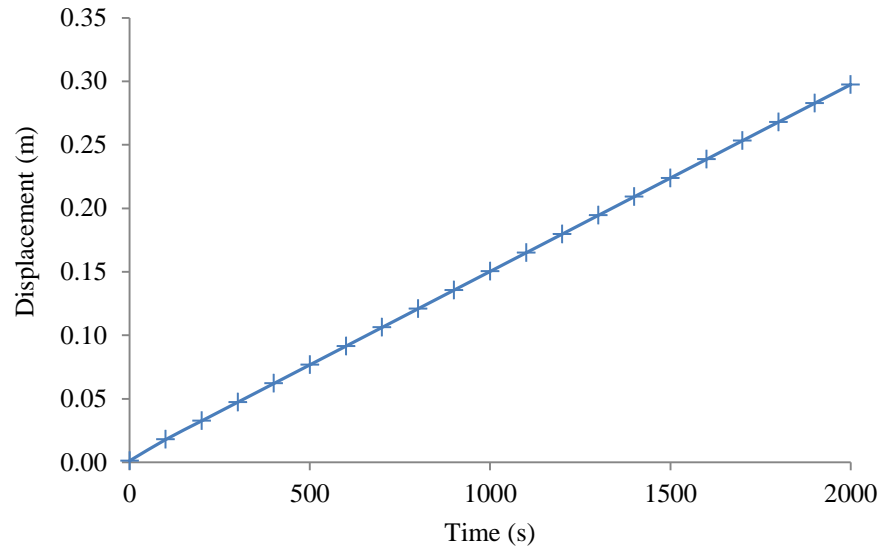
Figure 7.51 Analytical solution for Burger's model properties shown in Table 7.3
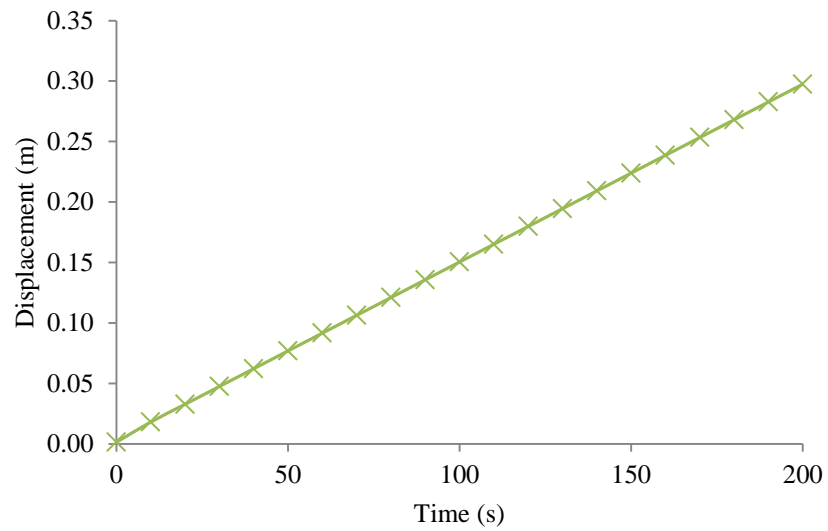
Figure 7.52 Analytical solution for Burger's model properties with both viscosities reduced by a factor of 0.1 according to Table 7.3
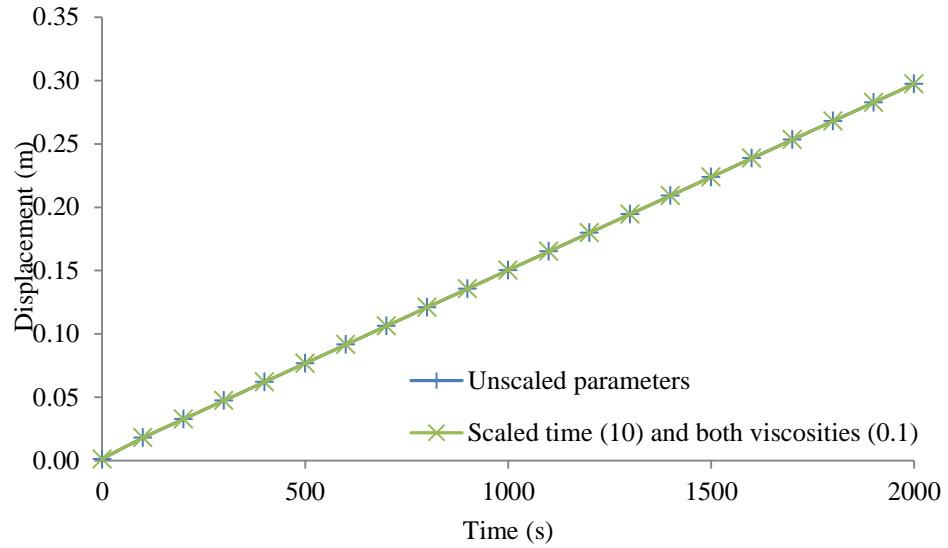
Figure 7.53 Analytical solution for Burger's model parameters in Table 7.3 compared with increasing time by a factor of 10 and reducing both viscosities by the factor of 0.1

7.5.2 **Comparison with experimental results**

Creep simulations under 400 kPa, 500 kPa, 600 kPa, and 1,000 kPa were performed. The specimen parameters are the same as the constant strain rate tests (Table 7.1) and the bond strengths followed the previous normal and Weibull distributions (Figure 7.31). During the simulations, the bond strength has been set as a power-law function of strain rate (see equation (5.2)). The results are shown in Figure 7.54 and Figure 7.55. Three simulations were modelled for each loading condition: the same bond strength distribution but with different number seeds. As can be seen, at higher stresses (500, 600 and 1000 kPa) the bond strength variability can cause rupture at different times. Hence, the bond strengths play an important role in the rupture of the specimen. However at lower stress conditions (400 kPa) the effect of bond strength variability is negligible. This is because at higher loadings, the bonds tend to break earlier. No rupture can be observed at lower stress levels. These

observations show similar patterns of behaviours, comparing with the laboratory results; see Figure 5.13 in section 5.4.2.
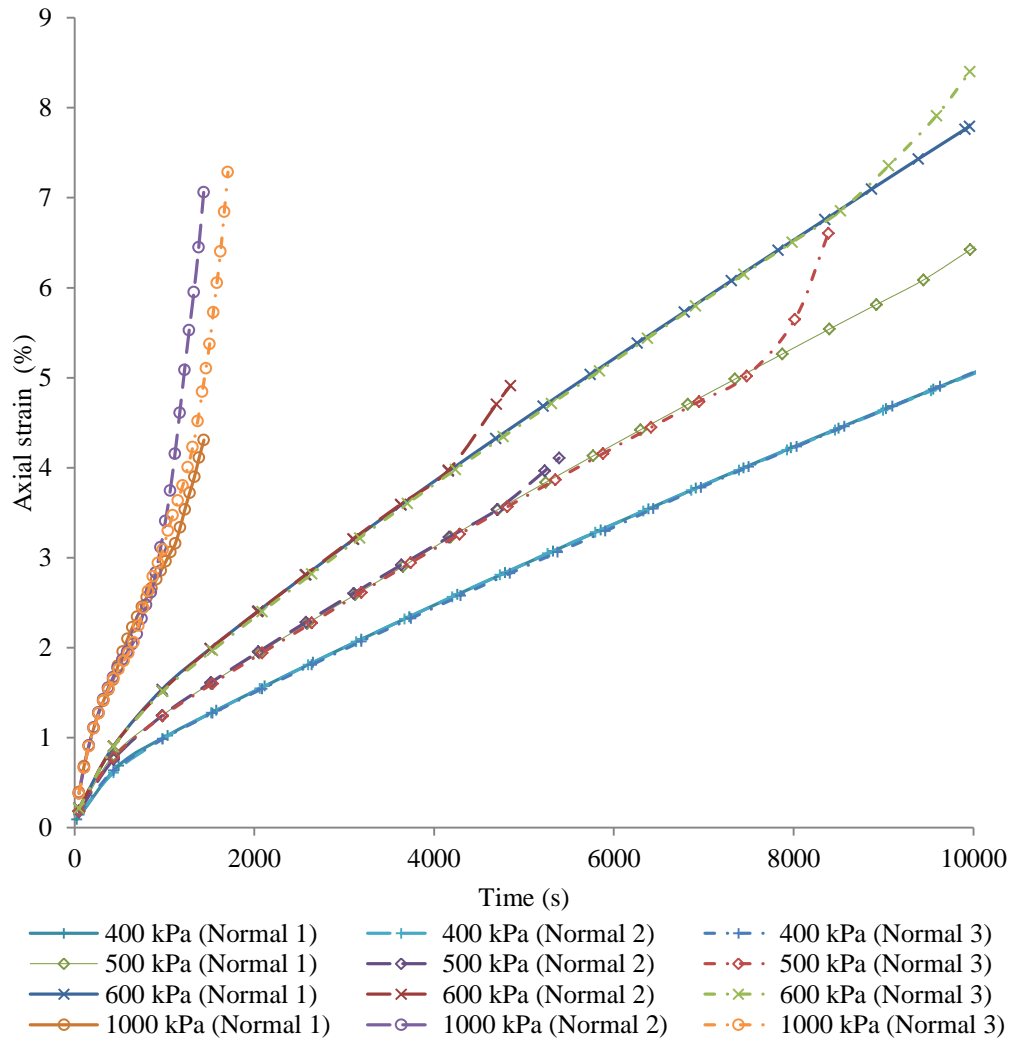
Figure 7.54 Creep simulations with normal distributions of bond strengths
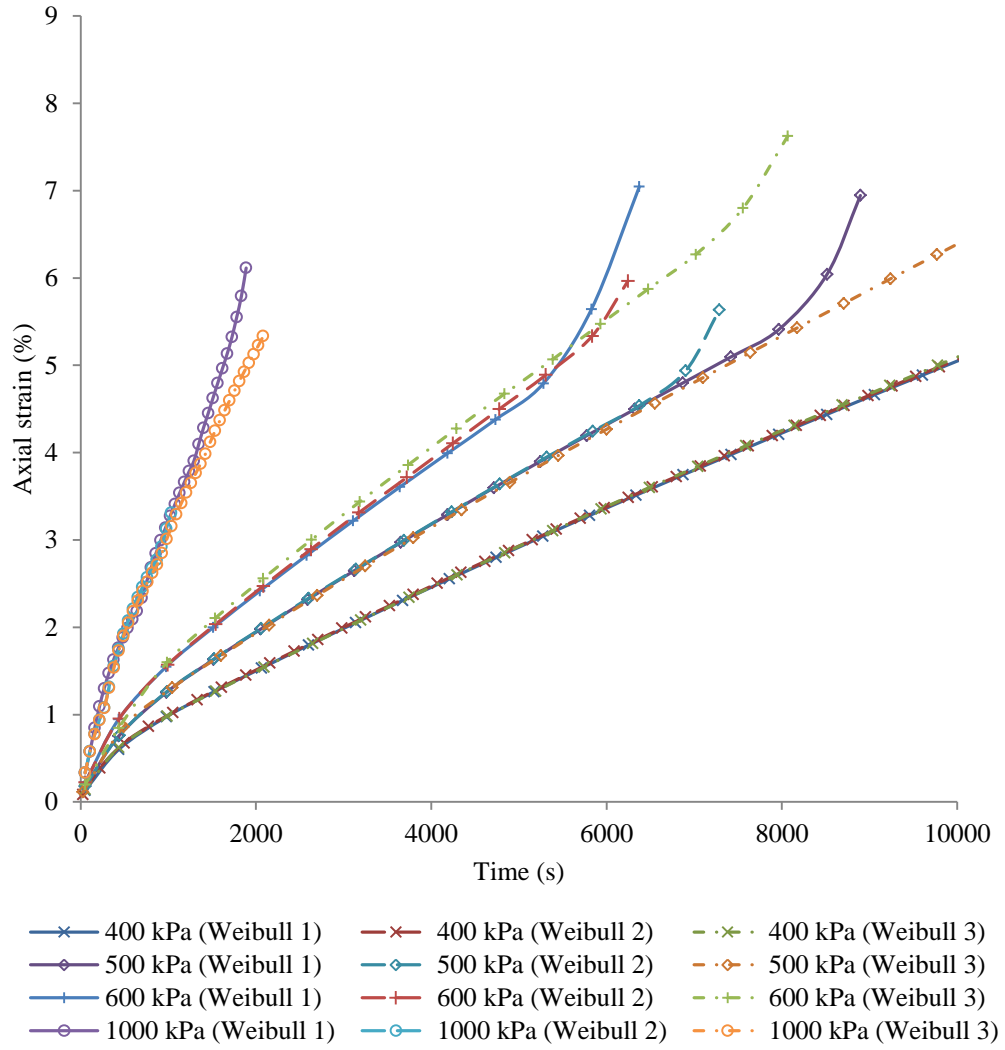
Figure 7.55 Creep simulations with Weibull distributions of bond strengths

The effect of the positions of the particles was also investigated. Two further simulations were performed, with 6000 particles in different random positions for each loading condition. Specimen parameters were set to be the same as for the constant strain rate tests (Table 7.1). Bond strengths followed the previous normal and Weibull distributions (Figure 7.31). The results are shown in Figure 7.56 and Figure 7.57. As can be seen, the positions of the particles has an effect at higher stresses (500, 600 and 1,000 kPa). Rupture can occur at different times and the axial strain can be different at the same loading time. This could also partly explain the variability of the creep results in the

laboratory. As mentioned before, the Burger's model is loading speed dependent. In the creep simulations, bond strengths change as the strain rate changes which can lead to a different bond breakage pattern. At lower stresses (400 kPa) the effect of the positions of the particles is negligible.
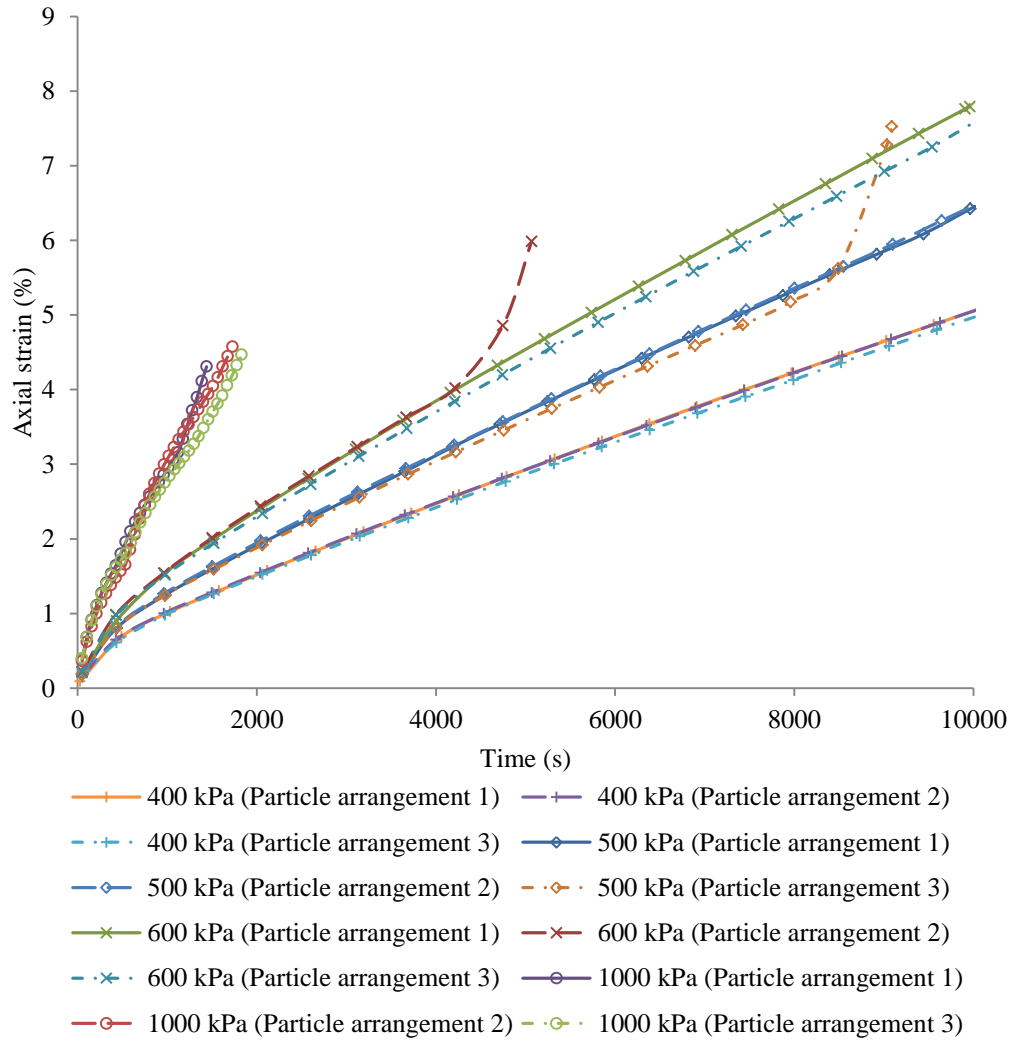
Figure 7.56 Effect of position of the particles with normal distributions of bond strengths
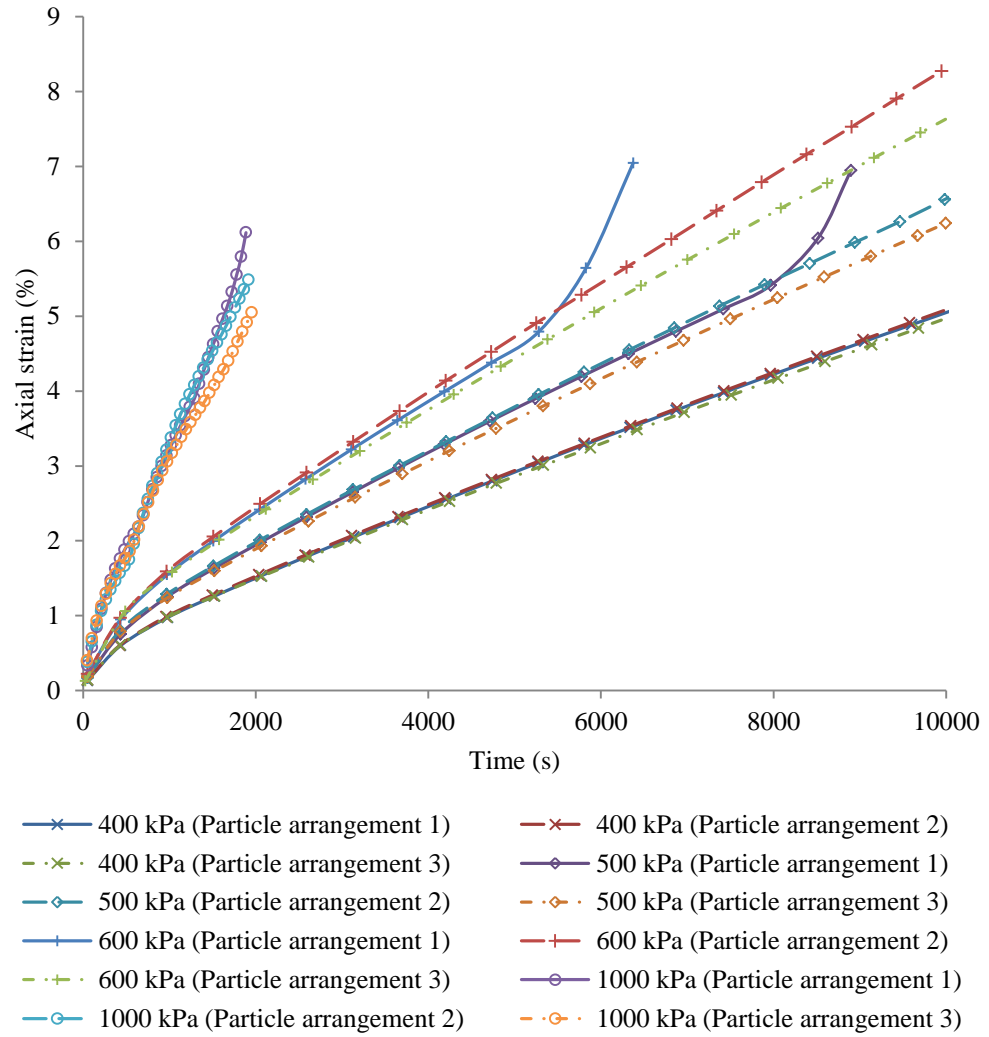
Figure 7.57 Effect of position of the particles with Weibull distributions of bond strengths

7.5.3 **Bond breakage**

The bond breakages were also recorded during the creep simulations and are shown in Figure 7.58 to Figure 7.65. As can be seen, at a lower stress level (400 kPa), only a few bonds break after applying the load. This agrees well with laboratory results: no rupture was observed at lower stress levels. At higher stress levels, the rupture behaviour corresponds to the highest bond breakage rate; see for example, Figure 7.64. These behaviours consistent with that observed in Figure 7.7, Figure 7.8 and Figure 7.34; in those simulations a

197

higher strain rate resulted in more brittle behaviours; in the creep simulations, a higher stress results in well-defined creep rupture when there is a rapid onset of bond breakage.

Based on the bond breakage curves below , the following general trend can be observed; bond breakage rate increase at the primary creep stage (see Figure 2.11), and keeps almost at constant at the secondary creep stage and increases again rapidly at the tertiary creep stage, see for example Figure 7.63 and Figure 7.64.
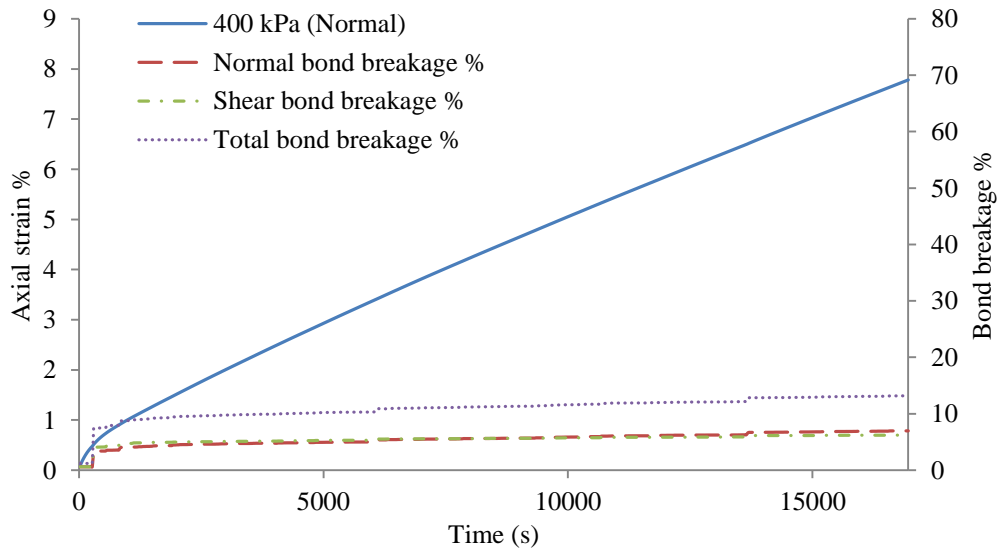
Figure 7.58 Bond breakage for 400 kPa creep simulation with normal distribution of bond strengths
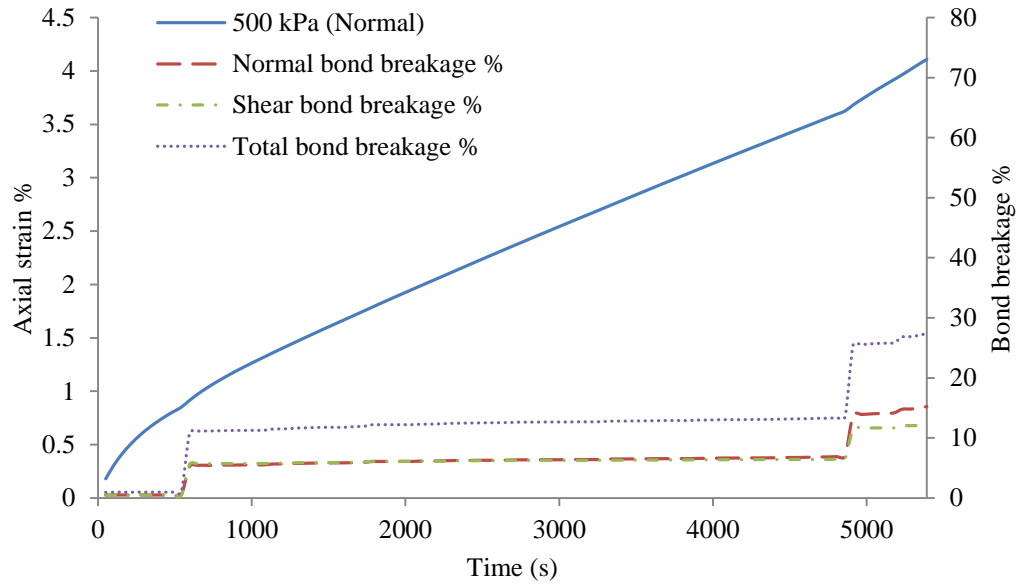
Figure 7.59 Bond breakage for 500 kPa creep simulation with normal distribution of bond strengths
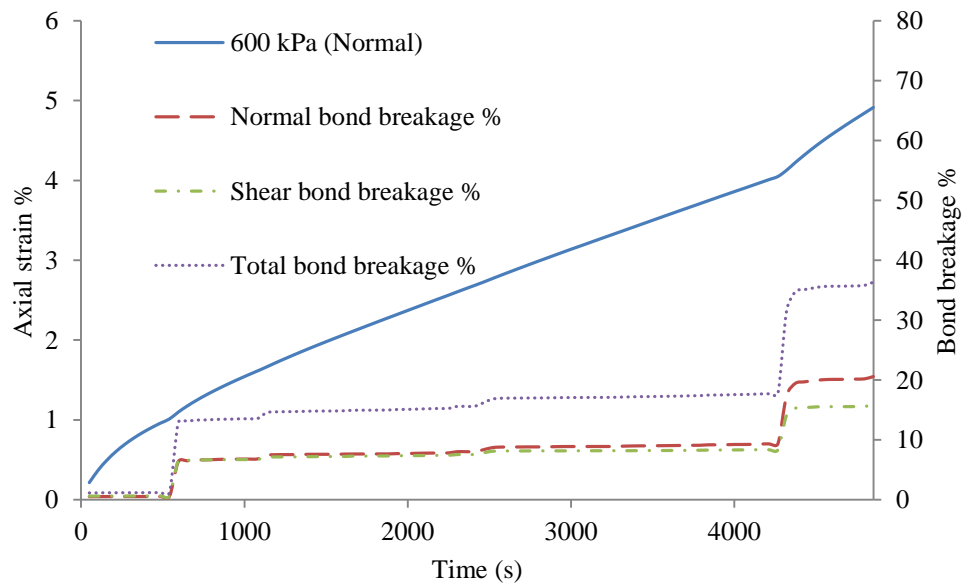
Figure 7.60 Bond breakage for 600 kPa creep simulation with normal distribution of bond strengths
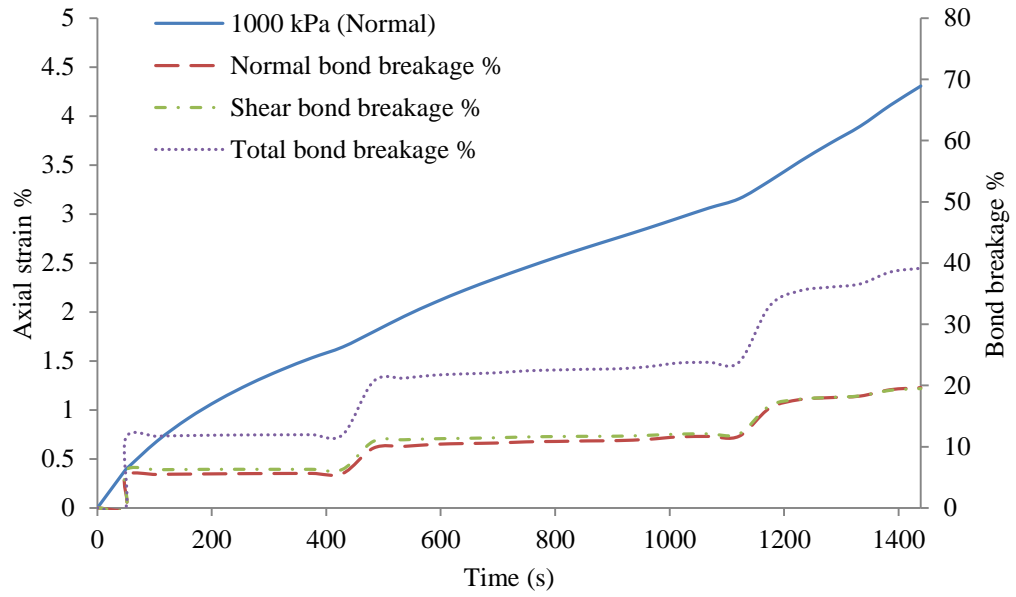
Figure 7.61 Bond breakage for 1000 kPa creep simulation with normal distribution of bond strengths
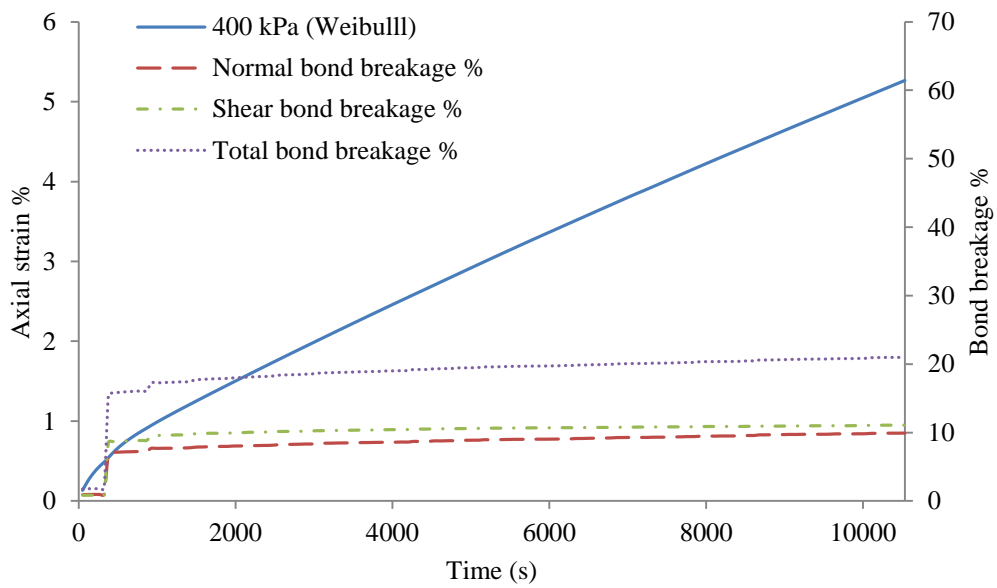
Figure 7.62 Bond breakage for 400 kPa creep simulation with Weibull distribution of bond strengths
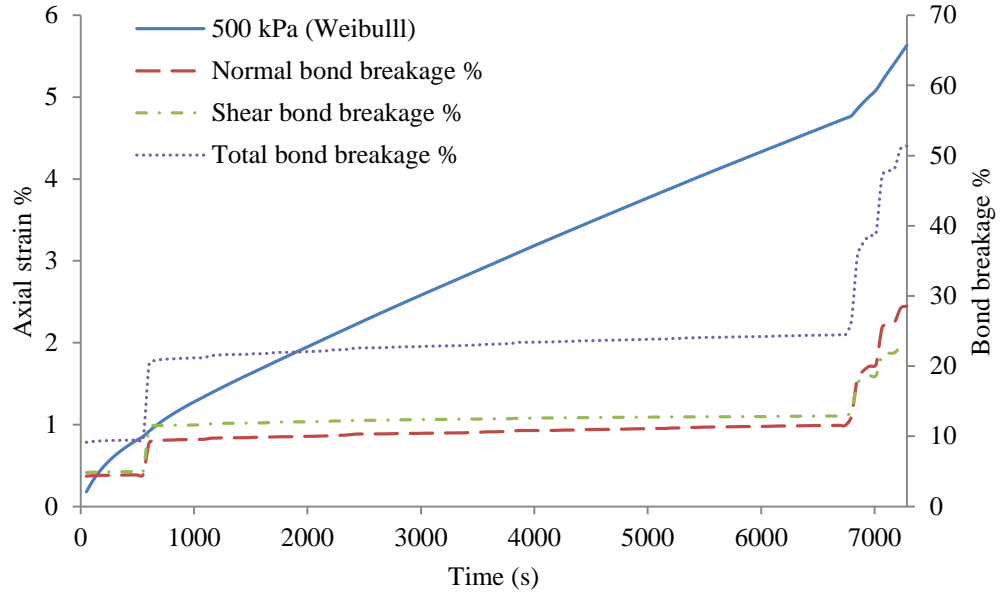
Figure 7.63 Bond breakage for 500 kPa creep simulation with Weibull distribution of bond strengths
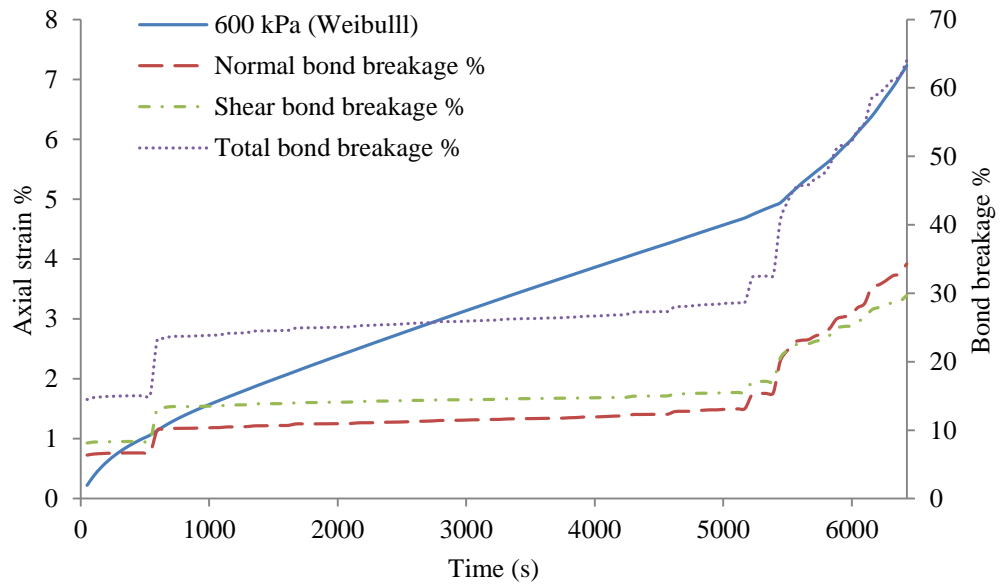
Figure 7.64 Bond breakage for 600 kPa creep simulation with Weibull distribution of bond strengths
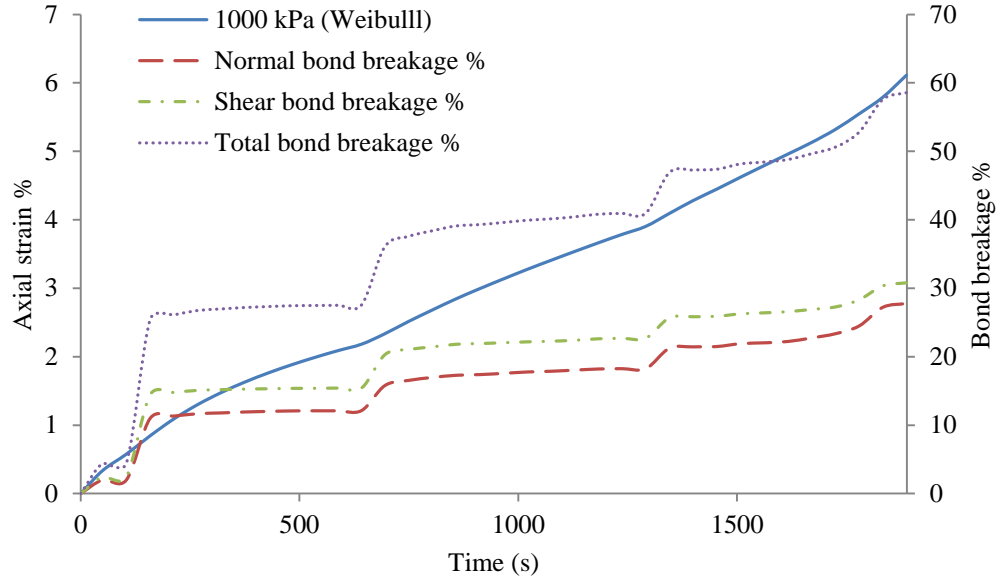
Figure 7.65 Bond breakage for 1000 kPa creep simulation with Weibull distribution of bond strengths

7.6 **Summary**

The Burger's model was implemented to give moment and torsional resistance as well as in direct tension and compression. This chapter presents the use of the modified Burger's model to simulate uniaxial compression tests on graded asphalt mixtures. The effects of various parameters on the simulation results were investigated. The axial stress as a function of strain depends on the Maxwell stiffness, the ratio of normal to shear contact parameters and the bond strength distribution. The peak stress is dependent on the normal to shear contact parameters, the friction coefficient and the bond strength distribution. As the radius multiplier decreases the peak stress decreases and a wider post peak softening behaviour was also observed.

Both normal and Weibull distributions have been used for the bond strength. In the modelling, the bond strength has been set to be power-law function of strain rate. Both constant strain rate and creep test simulations have shown

good agreement with laboratory results. Six thousands particles are enough to give a reasonable prediction of the stress-strain behaviour of asphalt mixtures. Bond breakage was recorded during the simulations and used to investigate the micro-mechanical deformation behaviour of the asphalt mixtures. The constant strain rate test results are approximately independent of the variability of the bond strength and the positions of the particles for each of the constant strain rate tests, while the creep tests are dependent on the variability of the bond strengths and the positions of the particles. An approach was presented based on dimensional analysis to reduce the computational time during the creep simulations. The simulations performed in this project show the potential of DEM as a useful tool in the study of the fundamental properties of asphalt mixtures.

8 Conclusions and recommendations

8.1 Introduction

The mechanical behaviour of an asphalt mixture has been investigated experimentally and modelled numerically. The DEM (PFC3D) has been used to model uniaxial compression tests on the asphalt mixture. This chapter summarises the main conclusions of this thesis and also provides recommendations for future research in this area.

8.2 Conclusions

Stone mastic asphalt has been selected for this project because of its high content of coarse aggregate and binder rich mortar. A new stone mastic asphalt mixture was developed by using aggregate with more than a diameter of 2mm. The new grading curve of aggregate and mix design for the mixture were determined in the laboratory.

A numerical specimen preparation procedure was developed to produce numerical specimens that replicate laboratory test specimens with the same distribution of particle sizes. A dense randomly packed specimen was generated with graded particles. A procedure of preparing the specimen to an equilibrium state with low isotropic stress has been presented.

A parallel bond model has been used to simulate the elastic behaviour of the asphalt mixture. It was found that 6000 particles are required for reasonably accurate estimation of bulk material properties. The variability caused by the

random positions of the particles is negligible. A loading rate of 0.02 m/s was an optimum speed low enough to avoid dynamic effects but high enough to reduce the computation time. The Poisson's ratio was found to be dependent on only the ratio of normal to shear contact stiffness. The Young's modulus was found to be dependent on both normal and shear contact stiffness. The bond radius has little effect on the Young's modulus, and as the radius increases the Poisson's ratio decreases.

A series of uniaxial constant strain rate and creep tests were performed under various loading conditions in the laboratory. A power-law equation was shown to give good prediction of the constant strain rate data obtained at various strain rates in the laboratory experiments.

The Burger's model was used to capture the time dependent behaviour of the graded asphalt mixture. The modified Burger's model was developed to give moment and torsional resistance at contacts. The effects of each parameter were investigated. The bond strength distributions were introduced to model the post peak softening behaviour of the asphalt mixture.

The numerical specimen was calibrated against experimental data for a constant strain rate at one particle value. It was found that the micromechanical model was able to capture the behaviour of the specimen under different rates, so that good agreement with experimental data was obtained.

The numerical model for the constant rate tests was then subjected to creep loading using the same micro mechanical parameters. To reduce the computation time during the creep simulation an approach was presented based on dimensional analysis. The results for the creep tests showed some

dependence on particle locations and distribution of bond strengths, giving some variability in results for a particular stress level. This was found to agree with similar variability in the experimental creep tests at higher stress levels. The bond breakage was recorded during the simulation to assist the investigation of the micromechanical behaviour of asphalt mixtures. It was found that a well-defined rupture at higher stress levels coincided with the maximum rate of bond breakage. It can therefore be concluded that by introducing a new time-dependent model for torsional and bending resistance at particle contacts, with a single set of parameters, both constant strain rate and creep tests can be correctly modelled. This dissertation has therefore shown that DEM is a powerful tool for modelling the time-dependent behaviour of asphalt mixtures.

8.3   Recommendations for future work

The numerical specimens produced in this project comprised graded particles ranging from 2 mm to 12 mm. However, in reality a wider range of particle grading is observed. Future work can focus on the development of numerical specimens with wider aggregate grading and denser packing.

In DEM, models are usually based on certain assumptions with a view to simplifying the problems within an acceptable approximation. This approach results in a lack of precision in describing the real behaviour. For example, in the DEM, a particle is considered as a non-deformable sphere. This assumption is reasonable when the applied stress level is low but it is not suitable at high stress levels, where particle deformation or breakage may occur (McDowell et al., 1998, McDowell et al., 2002a). Therefore, it is important to recognise that

numerical models can only play a partial role in understanding the reality. Real sand particles are much more complex and cannot be simply represented by a two-ball clump either. Particle shape dramatically affects particle rotation and overall specimen strength. It is possible to bond more particles together to form a more realistic shape (Ferellec et al., 2008), or use clumps.

The clumps in PFC3D are assumed not to be subject breakage. However, in reality, particle crushing could occur under high loading stress. Future modelling should take into consideration the crushing of the particles in the aggregate.

Asphalt mixtures are usually assumed to be linear viscoelastic at small strain rates and/or low stress levels. At large strain rates and/or high stress levels the behaviour of asphalt mixtures are non-linear viscoelastic and cannot be directly modelled by a linear viscoelastic approximation. Future research should focus on the development of new contact models with more complex properties. In addition, the developed model should be able to simulate the uniaxial compression tests on asphalt mixtures over a broader range of testing conditions such as various temperatures, higher strain rates and stress levels and repeated loading.

As a first step to model fatigue cracking of asphalt mixture, the compression behaviour of asphalt mixtures has been satisfactorily modelled. The post-peak softening behaviour and the micro-cracks of the asphalt mixture under various strain rates and stress levels were also successfully simulated. Future research should focus on further developing the model to simulate the fatigue of asphalt mixture under cyclic loading. This can be achieved by experimental

investigation and numerical modelling. Eventually, the DEM is expected to help with the development of constitutive models and performance based models to solve highway industry problems like rutting and fatigue.

The creep tests simulation results show that the mechanical behaviour of asphalt mixture is dependent on the bond strength distribution and variability. X-ray techniques can be used to capture the internal structure of asphalt mixtures. The data obtained by X-ray techniques can be used to define the bond strength in numerical simulation. Using this approach, the internal damage within the asphalt mixtures under various loading conditions could be correctly measured in experiments and used to refine the modelling of bond breakage within the numerical specimens.

The bond breakage curves for both constant strain rate and creep simulations show that the time-dependent material behaviour becomes more brittle as the strain rate or viscosity increases. This can be a new approach to under asphalt mixture form micro scope prospective and it is worth to further research.

9 **REFERENCES**

Abbas Ala (2004). Simulation of the Micromechanical Behavior of Asphalt Mixture Using the Discrete Element Method, *Department of Civil and Environmental Engineering Washington State University* vol PhD.

Abbas Ala, Masad Eyad, Papagiannakis Tom and Harman Tom (2007). Micromechanical Modeling of the Viscoelastic Behavior of Asphalt Mixtures Using the Discrete Element Method, *International Journal of Geomechanics* vol 7, pp. 131-139.

Adhikari S., Civil Michigan Technological University. and Engineering Environmental (2008a). Simulation of Mechanical Behavior of Asphalt Concrete: Two-Dimensional and Three-Dimensional Micromechanics-Based Discrete Element Models, Michigan Technological University.

Adhikari Sanjeev and You Zhanping (2008b). 3D Microstructural Models for Asphalt Mixtures Using X-ray Computed Tomography Images, *International Journal of Pavement Research and Technology*, vol 1, pp. 94-99.

Basquin O.H. (1910). The Exponential Law of Endurance tests, *Proceeeding of American Society for Testing Materials*, vol 10, pp. 628-630.

Bathe K.J. and Wilson E.L. (1976). Numerical Methods in Finite Element Analysis, *Englewood Cliffs: Prentice-Hall*.

Bellin P. (1992). Use of Stone Matrix Asphalt in German - State of the Art, *Report Prepared for the A2F02 Committee, Transportatio Research Board* Washington,D.C.

Biaauwendraad J. and Scarpas A (2000). 3D Finite Element Simulation of Damage in Asphalt Concrete Pavement, MCCI '2000-International Symposium on Modern Concrete Composites & Infrastructures', vol I, Beijing, China, pp. 11-16.

British Standards Institution Method for Determination of the Indirect Tensile Stiffness Modulus of Bituminous Materials, *Draft for Development*,

British Standards Institution Bituminous Mixtures. Test Methods for Hot Mix Asphalt. Binder Drainage, *BS EN 12697-18:2004*,

British Standards Institution Bituminous Mixtures. Test Methods for Hot Mix Asphalt. Laboratory Mixing, *BS EN 12697-35:2004*,

British Standards Institution Bituminous mixtures. Material specifications. Asphalt concrete, *BS EN 13108-1:2006*,

REFERENCE

British Standards Institution Bituminous Mixtures. Material Specifications.Hot Rolled Asphalt, *BS EN 13108-4:2006*,

British Standards Institution Bituminous Mixtures. Material Specifications.Stone Mastic Asphalt, *BS EN 13108-5:2006*,

Brown S.F., et al. (1992). Bituminous Pavements: Materials, Design and Evaluation, *Residential Course Lecture Notes*, *School of Civil Engineering, University of Nottingham, UK*

Burmister D.M. (1943). The Theory of Stresses and Displacements in Layered Systems and Applications to Design of Airport Runways, *Highway Research Board*, vol 23, pp. 126-144.

Buttlar William and You Zhanping (2001). Discrete Element Modeling of Asphalt Concrete: Microfabric Approach, *Transportation Research Record: Journal of the Transportation Research Board*, vol 1757, pp. 111-118.

Carmona HA, Kun F, Andrade Jr JS and Herrmann HJ (2007). Computer Simulation of Fatigue under Diametrical Compression, *Physical Review E*, vol 75, p. 46115.

Chang G.K. and Meegoda N.J. (1993). Simulation of the Behaviour of Asphalt Concrete Using Discrete Element Method, *2nd International Conference On Discrete Element Methods*.

Chang Kuo-Neng G. and Meegoda Jay N. (1997). Micromechanical Simulation of Hot Mix Asphalt, *Journal of Engineering Mechanics*, vol 123, pp. 495-503.

Cheng Y. P., Bolton M. D. and Nakata Y. (2004). Crushing and Plastic Deformation of Soils Simulated using DEM, *GEOTECHNIQUE -LONDON-*, vol 54, pp. 131-142.

Cheung C. Y. (1995). Mechanical Behaviour of Bitumens and Biuminous Mixes, *Department of Engineering*, *University of Cambridge, UK*.

Cheung C. Y. and Cebon D. (1997). Thin Film Deformation Behaviour of Power-Law Creeping Material, *Journal of Engineering Mechanics*, vol 123, pp. 1138-1152.

Cheung C. Y., Cocks A. C. F. and Cebon D. (1999). Isolated Contact Model of an Idealized Asphalt Mix, *International Journal of Mechanical Sciences* vol 41, pp. 767-792.

Collop A. C., McDowell G. R. and Lee Y. (2006). Modelling Dilation in an Idealised Asphalt Mixture using Discrete Element Modelling, *Granular Matter*, vol 8, pp. 175-184.

REFERENCE

Collop A. C., McDowell G. R. and Lee Y. (2007). On the use of Discrete Element Modelling to Simulate the Viscoelastic Deformation Behaviour of an Idealized Asphalt Mixture, *Geomechanics and Geoengineering: An International Journal*, vol 2, pp. 77 - 86.

Collop AC, Cebon D and Hardy MSA (1995). Viscoelastic Approach to Rutting in Flexible Pavements, *Journal of Transportation Engineering*, vol 121, pp. 82-93.

Collop Andrew C., McDowell Glenn R. and Lee York W. (2003a). Modelling the Behaviour of an Idealised Asphalt Mixture using the Discrete Element Method, TRB 83rd Annual Meeting, Washington D.C.

Collop Andrew C., McDowell Glenn R. and Lee York W. (2004). Use of the Distinct Element Method to Model the Deformation Behavior of an Idealized Asphalt Mixture, *International Journal of Pavement Engineering* vol 5, pp. 1-7.

Collop Andrew, Scarpas A., Kasbergen Cor and de Bondt Arian (2003b). Development and Finite Element Implementation of Stress-Dependent Elastoviscoplastic Constitutive Model with Damage for Asphalt, *Transportation Research Record: Journal of the Transportation Research Board*, vol 1832, pp. 96-104.

Cundall P. A. (2001). A Discontinuous Future for Numerical Modelling in Geomechanics?, *Geotechnical Engineering*, vol 149, pp. 41-47.

Cundall P. A. and Strack O. D. L. (1979a). A Discrete Numerical Model for Granular Assemblies, *Geotechnique*, vol 29, pp. 47-65.

Cundall P.A, Drescher A. and Strack O.D.L. (1982). Numerical Experiment on Granular Assemblies; Measurements and Observations, *Deformation and Failure of Granular Materials*, pp. 355-370.

Cundall P.A. (1971). A Computer Model for Simulating Progressive, Large-scale Movement in Blocky Rock System, *Proceeding of the Symposium International Society for Rock Mech*.

Cundall P.A. (1988a). Computer Simulation of Dense Sphere Assemblies, *Micromechanics of granular materials*, pp. 113-123.

Cundall P.A. (1988b). Formulation of a Three-Dimensional Distinct Element Model - Part1. A Scheme to Detect and Represent Contacts in a System Composed of Many Polyhedral Blocks, *International Journal of Rock Mechanics and Mining Sciences & Geomechanics Abstracts*, vol 25, pp. 107-116.

Cundall Peter A. and Strack Otto D. L. (1979b). The Development of Constitutive Laws for Soil Using the Distinct Element Method, *SAE Preprints*, vol 1, pp. 289-298.

REFERENCE

Dai Qingli and You Zhanping (2007). Prediction of Creep Stiffness of Asphalt Mixture with Micromechanical Finite-Element and Discrete-Element Models, *Journal of Engineering Mechanics*, vol 133, pp. 163-173.

Deshpande V.S. (1997). Steady-State Deformation Behaviour of Bituminous Mixes, *Engineeing Department, University of Cambridge, UK*.

Dolezalove M., P.Cezen and F.Havel (2003). Micromechanical Modeling of Stress Path Effects Using PFC2D Code, *Numerical Modeling in Micromechanics Via Particle Methods*.

Eisenmann J., Lempe U. and Leykauf G. (1977). Methods for the Structural Design of Asphalt Pavement, *4th International Conference on the Structural Design of Asphalt Pavements*.

Ergenzinger Christian, Seifried Robert and Eberhard Peter A Discrete Element Model to Describe Failure of Strong Rock in Uniaxial Compression, *Granular Matter*, vol 13, pp. 341-364.

Erkens S, Liu X, Scarpas A, Molenaar AAA and Blaauwendraad J (2002a). Asphalt Concrete Response: Experimental Determination and Finite Element Implementation, *Proceeding of the 9th International Conference on Asphalt Pavements*.

Erkens S.M.J.G., Liu X and Scarpas A (2002b). 3D Finite Element Model for Asphalt Concrete Response Simulation, *International Journal of Geomechanics* vol 2, pp. 305-330.

Ferellec J. F. and McDowell G. R. (2008). A Simple Method to Create Complex Particle Shapes for DEM, *Geomechanics and Geoengineering*, vol 3, pp. 211-216.

Fitzgerald J. and Vakili J. (1973). Nonlinear Characterization of Sand-Asphalt Concrete by Means of Permanent-Memory Norms, *Experimental Mechanics* vol 13, pp. 504-510.

Gibb John Michael (1996). Evaluation of Resistance to Permanent Deformation in the Design of Bituminous Paving Mixtures, *Deapartment of Civil Engineering, University of Nottingham,UK* vol PhD.

Harvey J. A. F. (2000). Bitumen Films in Tension, *University of Cambridge*.

Harvey J., Guada I. and Long F (2000). Effects of Material Properties, Specimen Geometry, and Specimen Preparation on Asphalt Concrete Tests for Rutting, *Journal of Association of Asphalt Paving Technologists*, vol 69.

REFERENCE

Hazzard J.F., Young R.P. and Maxwell S.C. (2000). Micromechanical Modelling in Cracking and Failure of Brittle Rocks, *Journal of Geophysical Research* vol 105, pp. 16683-16697.

Heukelom W. and Klomp A.J.G. (1964). Road Design and Dynamic Loading, *Proceeding Association of Asphalt Paving Technologists*, vol 33, pp. 92-125.

Hicks R.G. and Monismith C.L. (1972). Prediction of Resilient Response of Pavements Containing Granular Layers using non-linear Elastic Theory, *Proceeding 3rd International Conference on the Structural Design of Asphalt Pavements*.

Hills J. F. (1973). The Creep of Aaphalt Mixes, *Journal of the Institute of Petroleum*, vol 59, pp. 247-262.

Hofstra A. and Klomp A.J.G. (1972). Permanent Deformation of Flexible Pavements under Simulated Road Traffic Conditions, *Proceedings of 3rd International Conference on the Structural Design of Asphalt Pavements*, pp. 613-621.

Huang Y.H. (1967). Deformation and Volume Change Characteristics of a Sand Asphalt Mixture Under Constant Direct Triaxial Compressive Stresses, *Highway Research Record*, vol 178, p. 60.

ITASCA (2008a). Particle Flow Code in Three Dimensions, Optional Features, Itasca Consulting Group Inc., Minnesota.

ITASCA (2008b). Particle Flow Code in Three Dimensions, Theory and Background., Itasca Consulting Group Inc., Minnesota.

ITASCA (2008c). Particle Flow Code in Three Dimensions, User's Guide, Itasca Consulting Group Inc., Minnesota.

Johnson K. L. (1985). Contact Mechanics, Cambridge University Press.

Judycki J. (1992). Non-linear Viscoelastic Behaviour of Conventional and Modified Asphaltic Concrete under Creep, *Materials and Structures* vol 25, pp. 95-101.

Khanzada R. (2000). Permanent Deformation in Bituminous Mixtures, *Department of Civil Engineering*, *University of Nottingham, UK*.

Kim Hyunwook and Buttlar William G. (2009). Discrete Fracture Modeling of Asphalt Concrete, *International Journal of Solids and Structures* vol 46, pp. 2593-2604.

Kim Hyunwook, Wagoner Michael P. and Buttlar William G. (2008). Simulation of Fracture Behavior in Asphalt Concrete Using a Heterogeneous Cohesive Zone Discrete Element Model, *Journal of Materials in Civil Engineering* vol 20, pp. 552-563.

213

REFERENCE

Kim Y. Richard and Little Dallas N. (1990). One-Dimensional Constitutive Modeling of Asphalt Concrete, *Journal of Engineering Mechanics*, vol 116, pp. 751-772.

Konietzky H, Kamp L. te and Bertrand G (2003). Modeling of Cyclic Fatigue Under Tension with PFC, *Numerical Modeling in Micromechanics via Particle Methods*, pp. 101-105.

Kun F., Carmona H. A., Andrade J. S., Jr. and Herrmann H. J. (2008). Universality behind Basquin's Law of Fatigue, *Physical Review Letters* vol 100, p. 094301.

Lai J.S. and Anderson D. (1973). Irrecoverable and Recoverable Nonlinear Viscoelastic Properties of Asphalt Concrete, *Highway Research Record*, vol 468, pp. 73-88.

Lee York W. (2006). Discrete Element Modelling of Idealised Asphalt Mixture, *Department of Civil Engineering University of Nottingham, UK*.

Lim W. L. and McDowell G. R. (2005). Discrete Element Modelling of Railway Ballast, *Granular Matter*, vol 7, pp. 19-29.

Lim W. L. and McDowell G. R. (2007). The Importance of Coordination Number in Using Agglomerates to Simulate Crushable Particles in the Discrete Element Method, *Geotechnique*, vol 57, pp. 701-705.

Liu Yu (2011). Discrete Element Mwthod for Asphalt Concrete: Development and Application of User Defined Microstructural Models and a Viscoelastic Micromechanical Model, *Department of Civil and Environment Engineering, Michigan Technological University*.

Liu Yu, Dai Qingli and You Zhanping (2009a). Viscoelastic Model for Discrete Element Simulation of Asphalt Mixtures, *Journal of Engineering Mechanics*, vol 135, pp. 324-333.

Liu Yu and You Zhanping (2009b). Visualization and Simulation of Asphalt Concrete with Randomly Generated Three-Dimensional Models, *Journal of Computing in Civil Engineering*, vol 23, pp. 340-347.

Long F, Govindjee S and Monismith CL (2002). Permanent Deformation of Asphalt Concrete Pavements: Development of a nonlinear Viscoelastic Model for Mix Design and Analyses.

Lu M. and McDowell G. R. (2008). Discrete Element Modelling of Railway Ballast under Triaxial Conditions, *Geomechanics and Geoengineering: An International Journal*, vol 3, p. 14.

REFERENCE

Mahmoud Enad, Masad Eyad and Nazarian Soheil (2010). Discrete Element Analysis of the Influences of Aggregate Properties and Internal Structure on Fracture in Asphalt Mixtures, *Journal of Materials in Civil Engineering* vol 22, pp. 10-20.

Mahmound E. (2008). Discrete Element Modelling of Aggregate Graduation and Aggregate Properties of Fracture in Asphalt Mixes, *Zachry Department of Civil Engineering Texas A&M Univeristy, College Station, TX.*

McDowell G. R., Collop A. C. and Wu J. W. (2009). A Dimensional Analysis of Scaling Viscosity and Velocity in DEM of Constant Strain Rate Tests on Asphalt, *Geomechanics and Geoengineering*, vol 4, pp. 171-174.

McDowell G. R. and Harireche O. (2002a). Discrete Element Modelling of Soil Particle Fracture, *Geotechnique*, vol 52, pp. 131-135.

McDowell G. R. and Harireche O. (2002b). Discrete Element Modelling of Yielding and Normal Compression of Sand, *Geotechnique*, vol 52, pp. 299-304.

McDowell G. R., Harireche O., Konietzky H., Brown S. F. and Thom N. H. (2006). Discrete Element Modelling of Geogrid-Reinforced Aggregates, *Proceedings of the Institution of Civil Engineers: Geotechnical Engineering* vol 159, pp. 35-48.

McDowell GR and Bolton MD (1998). On the Micromechanics of Crushable Aggregates, *Geotechnique*, vol 48, pp. 667-679.

Meegoda Jay Namunu. and Chang G.Kuo-neng. (1993). A Novel Approach to Develop a Performance Based Test for Rutting of Asphalt Concrete, *Airport Pavement Innovations - Theory to Practice*, pp. 126-140.

Meegoda N.J. and Chang G.K. (1994). Modeling of Viscoelastic Behaviour of Hot Mix Asphalt (HMA) Using Discrete Element Method, *Proceeding of 3rd ASCE Materials Engineering Conference*, pp. 804-811.

Moavenzadeh F. and Soussou J. (1968). Viscoelastic Constitutive Equation for Sand Asphalt Mixtures, *Highway Research Record*, vol 256, pp. 36-52.

Ossa E. A., Deshpande V. S. and Cebon D. (2005). Phenomenological Model for Monotonic and Cyclic Behavior of Pure Bitumen, *Journal of Materials in Civil Engineering* vol 17, pp. 188-197.

Papagiannakis AT, Abbas A and Masad E (2002). Micromechanical Analysis of Viscoelastic Properties of Asphalt Concretes, *Transportation Research Record: Journal of the Transportation Research Board*, vol 1789, pp. 113-120.

REFERENCE

Partl M. N., Vinson T. S. and Hicks R. G. (1994). Mechanical Properties of Stone Mastic Asphalt, *Proceeding of the Third Materials Engineering Conference*, pp. 849-858.

Perl M., Uzan J. and Sides A. (1983). Visco-Elasto-Plastic Constitutive Law for a Bituminous Mixtures under Repeated Loading, *Asphalt Materials, Mixtures, Construction, Moisture Effects and Sulfur, Transportation Research Record*, vol 911, pp. 20-27.

Potyondy DO and Cundall PA (2004). A Bonded-Particle Model for Rock, *International Journal of Rock Mechanics and Mining Sciences* vol 41, pp. 1329-1364.

Powrie W., Ni Q., Harkness R. and Zhang X. (2005). Numerical Modelling of Plane Strain Tests on Sands Using a Particulate Approach, *Getechnique*, vol 55, pp. 297-306.

Preston J.N. (1991). The Design of Bituminous Concrete Mixes, *Department of Civil Engineering*, *University of Nottingham, UK*.

Qiu Y. F. and Lum K. M. (2006). Design and Performance of Stone Mastic Asphalt, *Journal of Transportation Engineering*, vol 132, pp. 956-963.

Read J.M. (1996). Fatigue Cracking of Bituminous Paving Mixtures, *Department of Civil Engineering*, *University of Nottingham, UK*.

Read John and Whiteoak D. (2003). The Shell Bitumen handbook, Shell UK Oil Products Limited.

Robertson D. (2000). Numerical Simulations of Crushable Aggregates, *University of Cambridge,UK*.

Robertson D., Bolton M. D. and McDowell G. R. (1997). A Numerical Representation of Fracturing Granular Materials, *International journal for numerical and analytical methods in geomechanics.*, vol 21, p. 825.

Rothenburg L., Bogobowicz A., Haas R., Jung F.W. and Kennepohl G. (1992). Micromechanical Modelling of Asphalt Concrete in Connection with Pavement Rutting Problems, *7th International Conference on Asphalt Pavements*, pp. 230-245.

Sadd Martin, Dai Qingli, Parameswaran Venkit and Shukla Arun (2003). Simulation of Asphalt Materials Using Finite Element Micromechanical Model with Damage Mechanics, *Transportation Research Record: Journal of the Transportation Research Board*, vol 1832, pp. 86-95.

Sadd Martin H., Dai Qingli, Parameswaran Venkitanarayanan and Shukla Arun (2004). Microstructural Simulation of Asphalt Materials: Modeling and Experimental Studies, *Journal of Materials in Civil Engineering* vol 16, pp. 107-115.

REFERENCE

Schapery R.A. (1974). Viscoelastic Behavior and Analysis of Composite Materials, Sedeckyj (Ed.) Mechanics of Composite Materials New York, pp. 86-168.

Schapery R.A. (1999). Nonlinear Viscoelastic and Viscoplastic Constitutive Equations with Growing Damage, *International Journal of Fracture* vol 97, pp. 33-66.

Sepehr K., Svec O.J., Yue Z.Q. and Elhussein H.Mohamed (1994). Finite Element Modelling of Asphalt Concrete Microstructure, *3rd International Conference of Computer-Aided Assessment and Control Localized Damage*.

Simpson B. and Tatsuoka F. (2008). Geotechnics: the Next 60 Years, *Geotechnique*, vol 58, pp. 357-368.

Soares J.B., Colares de Freitas F.A and Allen D.H. (2003). Crack Modeling of Asphalt Mixtures Considering Heterogeneity of the Material, *82nd of Transportation Research Board Meeting*.

Sousa J, Weissman SL, Sackman JL and Monismith CL (1993). Nonlinear Elastic Viscous with Damage Model to Predict Permanent Deformation of Asphalt Concrete Mixes.

Souza Leonardo T., Kim Yong-Rak, Souza Flavio V. and Castro Leandro S. (2012). Experimental Testing and Finite-Element Modeling to Evaluate the Effects of Aggregate Angularity on Bituminous Mixture Performance, *Journal of Materials in Civil Engineering* vol 24, pp. 249-258.

Starodubsky S., Belchman I. and Livneh M. (1990). Stress-strain Relationship for Asphalt Concrete in Compression, *RILEM, Materials and Structures*, vol 27, pp. 474-482.

Stroup-Gardiner Mary, Newcomb David, Olson Roger and Teig Jerry (1997). Traffic Densification of Asphalt Concrete Pavements, *Transportation Research Record: Journal of the Transportation Research Board*, vol 1575, pp. 1-9.

Taherkhani Hasan (2006). Experimental Characterisation of the Compressive Permanent Deformation Behaviour in Asphalt Mixtures, *Deaprtment of Civil Engineering The University of Nottingham,UK*.

Thom Nick (2008). Principles of Pavement Engineering, Thomas Telford Publishing Ltd

Todd Kevin B. and Kulakowski Bohdan T. (1989). Simple Computer Models for Predicting Ride Quality and Pavement Loading for Heavy Trucks, *Transportation research record.*

REFERENCE

Ulliditz P., Battiato G., Larsen B.K. and Stubstad R.W. (1987). Verification of Analytical-empirical Method of Pavement Evaluation Based on FWD Testing, *Proceeding 6th International Conference on the Structural Design of Asphalt Pavements*.

Uzan J (1996). Asphalt Concrete Characterization for Pavement Performance Prediction, *Asphalt Paving Technology*, vol 65, pp. 573-607.

Van der Poel C. (1954). A General System Describing the Visco-elastic Properties of Bitumens and its Relation to Routine Test Data, *Journal of Applied Chemistry* vol 4, pp. 221-236.

Van der Poel C. (1955). Time and Temperatures Effects on the Deformation of Asphaltic Bitumens and Bitumen-Mineral Mixtures, *Journal Society of Petroleum Engineers*, pp. 47-53.

Wang L, Park JY and Fu Y (2007). Representation of Real Particles for DEM Simulation using X-ray Tomography, *Construction and Building Materials*, vol 21, pp. 338-346.

Wanne T (2003). PFC3D Simulation Procedure for Compressive Strength Testing of Anistropic Hard Rock, *Numerical Modeling in Micromechanics Via Particle Methods*, pp. 241-249.

Weibull W. (1951). A Statistical Distribution Function of Wide Applicability, *Journal of Applied Mechanics*

Wu Junwei (2009). Discrete Element Modelling of Compression Tests for an Idealised Aspahlt Mixture, *Deapartment of Civil Engineering*, *University of Nottingham,UK* vol PhD.

Wu Junwei, Collop Andrew C. and McDowell Glenn R. (2011). Discrete Element Modeling of Constant Strain Rate Compression Tests on Idealized Asphalt Mixture, *Journal of Materials in Civil Engineering* vol 23, pp. 2-11.

You Z., Adhikari S. and Dai Qingli (2008). Three-Dimensional Discrete Element Models for Aspahlt mixtures, *Journal of Engineering Mechanics*, vol 134, pp. 1053-1063.

You Z. and Buttlar W. G. (2004). Discrete Element Modeling to Predict the Modulus of Asphalt Concrete Mixtures, *Journal of Materials in Civil Engineering* vol 16, pp. 140-146.

You Zhanping, Adhikari Sanjeev and Emin Kutay M. (2009). Dynamic Modulus Simulation of the Asphalt Concrete using the X-ray Computed Tomography Images, *Materials and Structures* vol 42, pp. 617-630.

REFERENCE

You Zhanping and Buttlar William (2005). Application of Discrete Element Modeling Techniques to Predict the Complex Modulus of Asphalt-Aggregate Hollow Cylinders Subjected to Internal Pressure, *Transportation Research Record: Journal of the Transportation Research Board*, vol 1929, pp. 218-226.

You Zhanping and Buttlar William (2006). Micromechanical Modeling Approach to Predict Compressive Dynamic Moduli of Asphalt Mixtures Using the Distinct Element Method, *Transportation Research Record: Journal of the Transportation Research Board*, vol 1970, pp. 73-83.

You Zhanping, Liu Yu and Dai Qingli (2011). Three-Dimensional Microstructural-Based Discrete Element Viscoelastic Modeling of Creep Compliance Tests for Asphalt Mixtures, *Journal of Materials in Civil Engineering* vol 23, pp. 79-87.

Zhou J and Chi Y (2003). Shear-band of Sand Simulated by Paticle Flow Code, *Numerical Modeling in Micromechanics Via Particle Methods*, pp. 205-210.